Title
Engineering Reconnaissance of the 24 August 2016 Central Italy Earthquake. Version 2

Author
GEER Association

Publication Date
2016-11-22

DOI
10.18118/G61S3Z

Data Availability
The data associated with this publication are available at: http://www.geerassociation.org/index.php/component/geer_reports/?view=geerreports&layout=build&id=76

Engineering Reconnaissance of the 24 August 2016 Central Italy Earthquake. Version 2

GEER Team Leaders: Giuseppe Lanzo and Jonathan P. Stewart

Report Editors:

Paolo Zimmaro and Jonathan P. Stewart

DOI:10.18118/G61S3Z

Geotechnical Extreme Events Reconnaissance Association

Report No. GEER-050B

22 November 2016

GEER Team Members

Leader: Jonathan P Stewart, University of California Los Angeles (UCLA)

Co-Leader: Giuseppe Lanzo, Sapienza University of Rome

Stefano Aversa, Università degli studi di Napoli Parthenope

Francesca Bozzoni, Eucentre

Shideh Dashti, University of Colorado Boulder

Luigi Di Sarno, Maria Giovanna Durante, Armando L Simonelli, Augusto Penna, University of Sannio, Reluis Consortium

Sebastiano Foti, Filiberto Chiabrando, Nives Grasso, Vincenzo Di Pietra Politecnico di Torino

Kevin Franke, Brandon Reimschiissel, Brigham Young University

Fabrizio Galadini, Emauela Falcucci, Stefano Gori, Istituto Nazionale di Geofisica e Vulcanologia (INGV)

Robert E Kayen, US Geological Survey (USGS)

Tadahiro Kishida, Pacific Earthquake Engineering Research Center (PEER), University of California, Berkeley

George Mylonakis, Elpida Katsiveli, University of Bristol, University of Patras

Alessandro Pagliaroli, Silvia Giallini University of Chieti-Pescara

Panagiotis Pelekis, School of Pedagogical and Technological Education Athens

Ioannis Psycharis, Elisavet Vintzilaiou, Michalis Fragiadakis, National Technical University of Athens

Giuseppe Scasserra, Filippo Santucci de Magistris, Massimina Castiglia, Tony Fierro, Luciano Mignelli, University of Molise

Anastasios Sextos, Nicholas Alexander, Raffaele De Risi, University of Bristol

Stefania Sica, Michele Mucciacciaro, University of Sannio

Francesco Silvestri, Anna d'Onofrio, Anna Chiaradonna, Filomena De Silva, University of Naples Federico II

Paolo Tommasi, Consiglio Nazionale delle Ricerche

Giuseppe Tropeano, University of Cagliari

Paolo Zimmaro, University of California Los Angeles (UCLA)

Acknowledgements

The work of the GEER Association, in general, is based upon work supported in part by the National Science Foundation through the Geotechnical Engineering Program under Grant No. CMMI-1266418. Any opinions, findings, and conclusions or recommendations expressed in this material are those of the authors and do not necessarily reflect the views of the NSF. The GEER Association is made possible by the vision and support of the NSF Geotechnical Engineering Program Directors: Dr. Richard Fragaszy and the late Dr. Cliff Astill. GEER members also donate their time, talent, and resources to collect time-sensitive field observations of the effects of extreme events.

Sponsorship of GEER activities was also provided by the B. John Garrick Institute for the Risk Sciences at UCLA and the NSF I/UCRC Center for Unmanned Aircraft Systems (C-UAS) at BYU under Project BYU13-03.

The Italian Department of Civil Protection (DPC) is gratefully acknowledged. In particular, the support of Prof. Mauro Dolce is greatly appreciated. Engs. Paola Pagliara and Paola Bertuccioli from the DPC are also gratefully acknowledged for the continuous assistance and for valuable help in obtaining the authorization in flying UAV. The Italian Geotechnical Society (AGI) is also thanked for its participation in this effort. Support for the Italian participants was partially provided by the ReLUIS Consortium (Italian University Network of Seismic Engineering Laboratories). The technical support by ReLUIS Consortium, headquarted in the University of Naples Federico II, Italy, and the Department of Engineering of University of Sannio, Benevento, Italy, is also acknowledged.

We thank Maria Luisa Bello and Maria Elena Sanseverino, master's students at University of Sannio for their contribution to damage to building strutures data collection.

Support for one team member was provided by EUcentre (European Centre for Training and Research in Earthquake Engineering; Pavia, Italy).

Politecnico di Torino (Italy) kindly provided the technical and financial support for his personnel involved in the reconnaissance.

Finally, the Authors greatly acknowledge Dr. Maranci and the assistance of ENEL staff during the inspection on the dam sites

Contents

List of figures

List of tables

1.0 Introduction

Giuseppe Lanzo, Paolo Zimmaro, Jonathan P. Stewart

1.1 Event Overview and Organization of Reconnaissance Activities

An earthquake with a moment magnitude reported as 6.0 from INGV (Istituto Nazionale di Geofisica e Vulcanologia; http://cnt.rm.ingv.it/en) occurred at 03:36 AM (local time) on 24 August 2016 in the central part of Italy. As shown in Figure 1.1, the epicenter was located at the borders of the Lazio, Abruzzi, Marche and Umbria regions, about 2.5 km north-east of the village of Accumoli and about 100 km from Rome. The hypocentral depth was about 8 km (INGV).

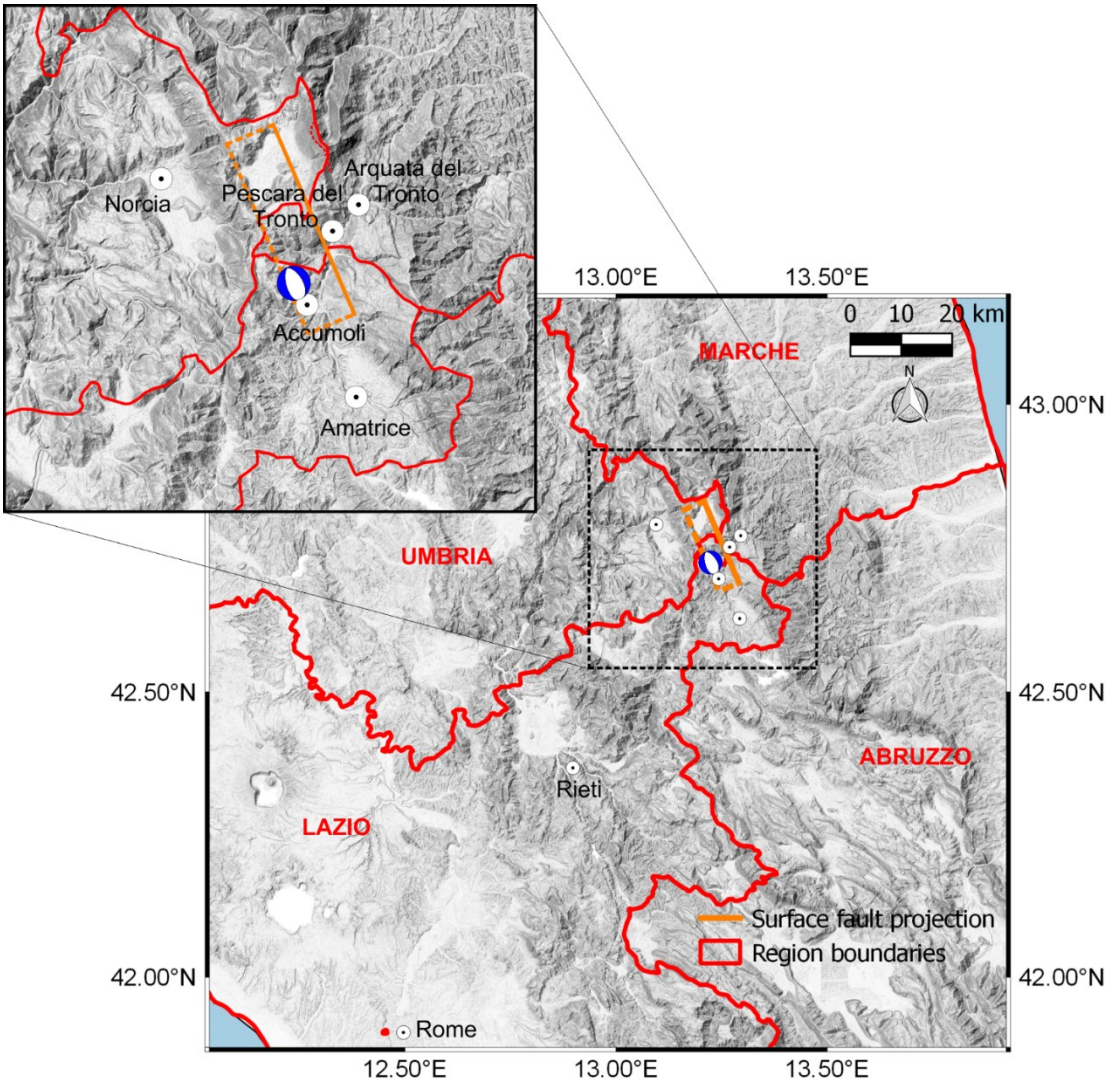

Figure 1.1. Location of the epicentre of the 2016 M6.0 earthquake occurred on August 24, 2016, along with the surface fault projection and administrative boundaries.

The earthquake was located in a gap between two earlier damaging events, the 1997 M6.1 Umbria-Marche earthquake to the north-west and the 2009 M6.1 L'Aquila earthquake to the

south-east. This gap had been recognized prior to the event as a zone of elevated risk (GdL INGV, 2016). The present event and those that preceded it occurred along the spine of the Apennine Mountain range on normal faults and had rake angles ranging from -80 to -100. Each of these events produced substantial damage to local towns and villages; the present event most strongly affected Arquata del Tronto, Accumoli, Amatrice, and Pescara del Tronto. In total there were 299 fatalities, generally from collapses of unreinforced masonry dwellings, and several hundred persons were injured (www.ilgiornale.it).

In the days following the event, the severity of its effects became apparent through media reports. Given the significance of the effects, the quality of the ground motion recording networks in Italy, and the strong ties between the Italian and US earthquake research communities, the decision was made to mobilize engineering reconnaissance activities so as to gather perishable data. This report is principally concerned with reconnaissance undertake by the NSF-funded Geotechnical Extreme Events Reconnaissance (GEER) association, with co-funding from the B. John Garrick Institute for the Risk Sciences at UCLA and the NSF I/UCRC Center for Unmanned Aircraft Systems (C-UAS) at BYU.

The US-based GEER team was mobilized to the earthquake area two weeks after the mainshock. The US team worked in close collaboration with Italian researchers organized under the auspices of the Italian Geotechnical Society, the Italian Center for Seismic Microzonation and its Applications, the Consortium ReLUIS, Centre of Competence of Department of Civil Protection, the Institute of Environmental Geology and Geoengineering (IGAG) of National Research Council, and the DIsaster RECovery Team of Politecnico di Torino. Additional smaller teams from Greece and UK Universities joined the Italy-US GEER main team in successive periods. The objective of the field reconnaissance activities was to collect and document perishable data that is essential to advance knowledge of earthquake effects, which ultimately leads to improved procedures for characterization and mitigation of seismic risk.

The GEER team was multi-disciplinary, with expertise in geology, seismology, geomatics, geotechnical engineering, and structural engineering. GEER coordinated its reconnaissance activities with those of the Earthquake Engineering Research Institute (EERI), whose activities were focused on emergency response and recovery, in combination with documenting the effectiveness of public policies related to seismic retrofit. As such, the task of documenting structural damage patterns was taken up by GEER.

This report covers reconnaissance following the event sequence that began on 24 August 2016, which was followed by a few aftershocks in the subsequent days. We do not address here reconnaissance of subsequent, apparently triggered events that began in late October 2016, including M 5.9 and 6.6 earthquakes. These will be the subject of later reports.

1.2 Overview of Reconnaissance Activities

The approach followed by the GEER team was to combine traditional reconnaissance activities of on-ground recording and mapping of field conditions, with advanced imaging and damage detection routines enabled by state-of-the-art geomatics technology. This combination of reconnaissance techniques provides opportunities for innovative future study.

GEER reconnaissance occurred in three phases, with the first comprising the largest team, and subsequent phases being focused on mapping of structural damage pattern in villages of interest. Phase 1 took place principally from 5-9 September, 2016. Aside from early coordination meetings, the Phase 1 team (comprised of approximately 30 researchers) worked in teams of approximately 3-4 so as to cover as much of the affected region as possible. Activities undertaken by the Phase 1 team included mapping of surface fault rupture, locating and mapping landslides, mapping damage patterns within villages (with the objective of characterizing variable levels of site response including topographic and possible valley effects), and bridge inspections. A tool found to be very useful in some of these activities was three-dimensional imaging from UAVs (Unmanned Aerial Vehicles). Use of the UAV required obtaining permission from the Department of Civil Protection (DPC), and was used in landslide areas and for imaging of structural damage patterns.

Several aspects of the reconnaissance activities benefitted from geo-spatial resources available to the team prior to field mobilization. These included damage proxy maps based on Interferometric Synthetic Aperture RADAR (InSAR) data (http://www.jpl.nasa.gov/spaceimages/details.php?id=PIA20897, last accessed October 25, 2016), provided by Advanced Rapid Imaging and Analysis (ARIA) project team (http://aria.jpl.nasa.gov/ last accessed October 25, 2016) and high-resolution orthophotos provided the Copernicus EMS Rapid Mapping service (http://emergency.copernicus.eu/, last accessed October 25, 2016). These images were overlayed on Google Earth maps, and provided insights into where deformations or damage may have occurred, which was useful in planning of reconnaissance activities.

The Phase 2 team mobilized from 9-13 September 2016 and focused on damage pattern mapping in Amatrice, Accumoli, Arquata del Tronto, and surrounding villages. The Phase 3 team mobilized from 3-6 October 2016 and undertook similar activities, but in different villages (e.g. Norcia and Castelluccio among others). Finally, on 19 October 2016, Francesca Bozzoni from the GEER team, along with representatives of the French Association of Earthquake Engineering (AFPS), visited several dam sites in the epicentral region, to which access had previously been denied.

Following this introduction, Chapter 2 describes the tectonic setting and regional geology, including discussions of major past earthquakes in the region. Also covered in Chapter 2 is mapping of the surface fault rupture mapped jointly by INGV, GEER, and others (i.e. EMERGEO working group, 2016; and INQUA collaborative multi-organizational team, 2016). Chapter 3

describes strong ground motions, which were well recorded. We present the available data, describe the processing that was undertaken, and show how the data compare to predictions from selected ground motion models, including some with Italy-specific regional factors. Chapter 4 presents the earthquake-induced landslides, including the landslide types that were observed, how the seismic landslide activity compares to non-seismic landslides observed historically in the region, and the use of UAV technology in these activities.

Chapter 5 is concerned with the performance of building structures in the villages and hamlets within the strongly shaken area. We present typical construction practices and damage quantification protocols, describe mapping activities that document field performance at varying levels of resolution, describe the damage patterns and statistics revealed by the data from work to date, and illustrate the effectiveness of retrofit activities that had been undertaken in several villages. Chapter 6 documents the performance of bridge structures, including the poor performance of several masonry bridge structures. Chapter 7 addresses the performance of other infrastructure such as retaining walls, dams and pipelines. In the last chapter, significant case histories that can serve as subjects for future research are identified and discussed.

2 Regional Faults and Seismic Source

Fabrizio Galadini, Emanuela Falcucci, Stefano Gori, Robert E. Kayen, Paolo Zimmaro, Jonathan P. Stewart

2.1 Geological Framework

The Apennine belt represents the "spine" of the Italian peninsula and results from the complex interaction between the Africa and Europe plates, and the Adria microplate. The formation of the central portion of the chain started in the Oligocene, when a compressive front began to "squash" and displace Mesozoic and Cenozoic marine carbonate sequences (e.g. Patacca et al., 2008). The front superposed different tectonic units and advanced progressively towards the east and north-east through thrust-and-fold systems that become progressively younger to the east. Migration of the thrust front occurred as a result of successive deformation events, which are expressed as different foredeep and thrust-top basins that are nestled in between the fronts (e.g. Cosentino et al., 2010).

Since the Pliocene, when the compressive deformation was deforming the present Adriatic domain, the inner sectors of the central Apennines began to be affected by tectonic extension, related to the formation and spreading of the Tyrrhenian back-arc basin (Cavinato and De Celles, 1999). The extensional tectonics nucleated a series of NW-SE trending, i.e. chain-parallel, normal fault systems, that displaced the compressive structures and migrated east-northeastwards (e.g. Carminati and Doglioni, 2012). The migration of the compression-extension tectonic pair occurred contemporaneously with chain uplift, which amounted to about 1000 m over the Quaternary (e.g. D'Agostino et al., 2001). Extension and uplift in the central Apennine are defined to be somehow connected to one another (e.g. Galadini et al., 2003).

Evidence of ongoing extension of the central Apennine chain is provided by:

1) Seismicity, with minor-to-major earthquakes on NW-SE trending extensional ruptures, including the **M** 6.3 6 April 2009 L'Aquila earthquake (Chiarabba et al., 2009) and the recent seismic sequence from 24 August to 30 October 2016 (Tinti et al., 2016; Gruppo di Lavoro INGV sul terremoto di Visso, 2016; http://cnt.rm.ingv.it/event/8863681);
2) Geodetic data, with GPS time series testifying to 3 mm/yr NE-SW trending extension (D'Agostino et al., 2011; Devoti et al., 2011);
3) Borehole breakout data, showing minimum horizontal stress oriented perpendicular to the belt (Montone and Mariucci, 2016); and
4) Geological data indicating activity of normal faults and fault systems during the Quaternary (e.g. Galadini and Galli, 2000; Boncio et al., 2004a; Roberts and Michetti, 2004), as well as paleoseismological investigations demonstrating activity of central Apennine major normal faults during historical times, nucleating M 6.5-7 seismic events. Notable among these events are the 1703 seismic sequence, with two major shocks in the

Norcia (14 January) (Galli et al., 2005) and the L'Aquila (2 February) (Moro et al., 2002) sectors and a 1915 event in the Fucino basin (Galadini and Galli, 1999).

The following sections describe regional faults in the epicentral region (2.2), the seismic source for the 24 August 2016 event (2.3), and surface faulting observed during INGV and GEER reconnaissance (2.4).

2.2 Regionally Active Faults and Seismogenic Characteristics

The following sub-sections describe active faults in region that produced the 24 August 2016 earthquake. Each sub-section describes geological data (mainly based on criteria from Falcucci et al., 2016) and reviews historical seismicity, which collectively provide the basis for inferences of current activity. Data on the past earthquakes and the damage distribution have been derived from Rovida et al. (2016).

Two faults among those presented below (namely the Montagna dei Fiori-Monti Gemelli and Leonessa faults) are considered inactive in the sense than they are likely unable to generate earthquakes of sufficient size to produce primary surface rupture (i.e., **M**>6.0±0.2; Falcucci et al., 2016). The discussion about inactivity is relevant for three reasons: *i*) They are normal faults with a trend consistent with the current tectonic regime; *ii*) They are characterized by geomorphologic features that could be incorrectly associated with current activity; and *iii*) Activity has been hypothesised for one of them (Leonessa) in the available literature.

Finally, we discuss an unsolved seismogenic issue, related to the earthquake that struck in 1950 along the Gran Sasso chain (**M** 5.7).

2.2.1 Mt. Vettore Fault

Geological evidence of recent activity

The Mt. Vettore normal fault strikes NNW-SSE to NW-SE and dips WSW to SW, and can be detected for a length of about 27 km (Figure 2.1). It is characterized by a distinct fault scarp carved in the SW carbonate slopes of Sibillini Mts. (Figure 2.2).

Only one intermontane basin can be associated to this fault, i.e. the Castelluccio Plain, close to the southernmost fault section. The basin is bordered by some of the fault splays located in the piedmont area of Mt. Vettore. However, its origin cannot be entirely related to tectonic activity, since geomorphologic traces of karstic processes that contributed to the plain evolution are widespread.

The most impressive fault scarp (fault line scarp at places) is represented by the "Cordone del Vettore" (Figs. 2.2a, 2.2b), located at about 2,000 m a.s.l. in the uppermost portion of the slope (Calamita and Pizzi, 1992; Coltorti and Farabollini, 1995; Cello et al., 1997; Pizzi et al., 2002; Pizzi and Galadini, 2009). Along the bedrock scarp, the exposed fault plane displaces the carbonate rocks, which are overlain by a thin and discontinuous cover of debris on the hanging wall.

A less prominent bedrock fault scarp occurs at lower elevation along the same slope of Mt. Vettore (white arrow in Figs. 2.2a and 2.2b). The fault plane places the carbonate bedrock into contact with slope deposits of Late Pleistocene-Holocene age (Coltorti and Farabollini, 1995).

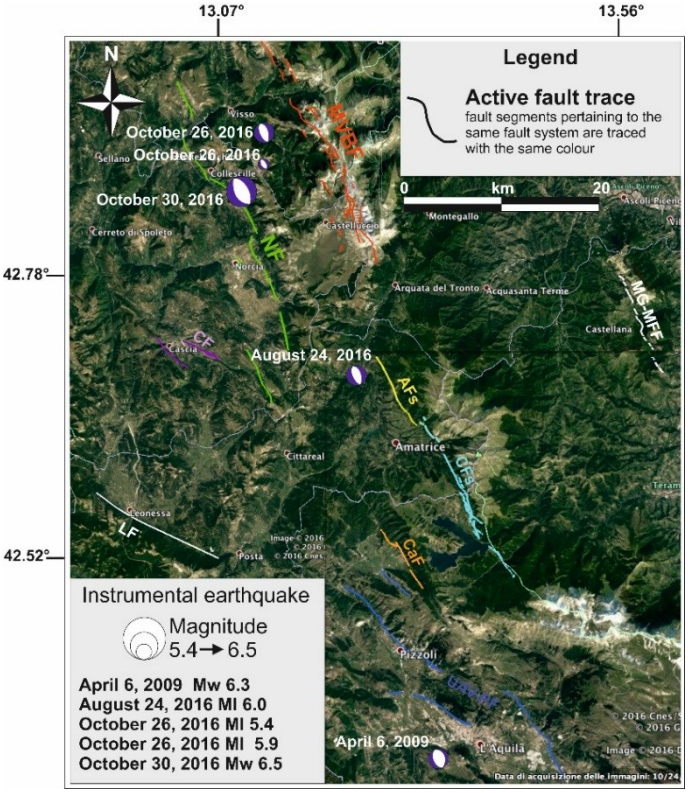

Figure 2.1. Map showing active fault systems discussed in this chapter and locations of large seismic events in the region since 2009. Faults: Mt.Vettore-Bove fault, MVBF; Norcia fault, NF; Cascia fault, CF; Amatrice fault segment, AFs; Campotosto fault segment, CFs; Capitignano fault, CaF; Upper Aterno Valley-Paganica fault ststem, UAV-PF; Leonessa fault,LF; Monti Gemelli-Montagna dei Fiori fault, MGMFF.

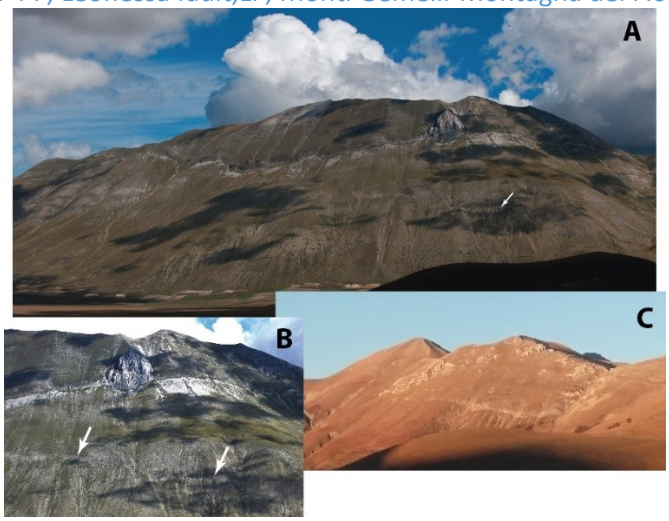

Figure 2.2. a, b) Mt. Vettore fault: bedrock fault scarps along the SW slope; the uppermost scarp is known as "Cordone del Vettore"; the white arrows indicate the bedrock scarp located in the middle sector of the slope; c) bedrock fault scarp along the western slope of Palazzo Borghese, between Mt. Porche and Mt. Argentella, NW of Mt. Vettore.

Based on the available geomorphologic evidence, the fault has been considered active by several authors (e.g. Calamita and Pizzi, 1992; Cello et al., 1997; Galadini and Galli, 2000; Boncio et al., 2004a). Further evidence of recent fault activity is provided by the displacement of a wide alluvial fan filling the northern sector of the Castelluccio basin. The displacement is due to the motion of minor fault sections, parallel to the aforementioned main splays on the slopes (Galadini and Galli, 2003). The alluvial fan is comprised of several depositional units dated between 23,000 and 3,200 BP. The motion of these secondary faults, paleoseismologically investigated in 1999 (Figure 2.3), and the related scarp formation can be attributed to a time span ranging between the Late Pleistocene-Holocene and 3,800-3,200 years BP, resulting in a slip rate between 0.36 and 0.62 mm/yr. Surface faulting (vertical offset up to about 20 cm) along the splay trenched in 1999 has been observed after the earthquake that occurred on 30 Oct 2016 (**M**6.5), as shown in Figure 2.3c).

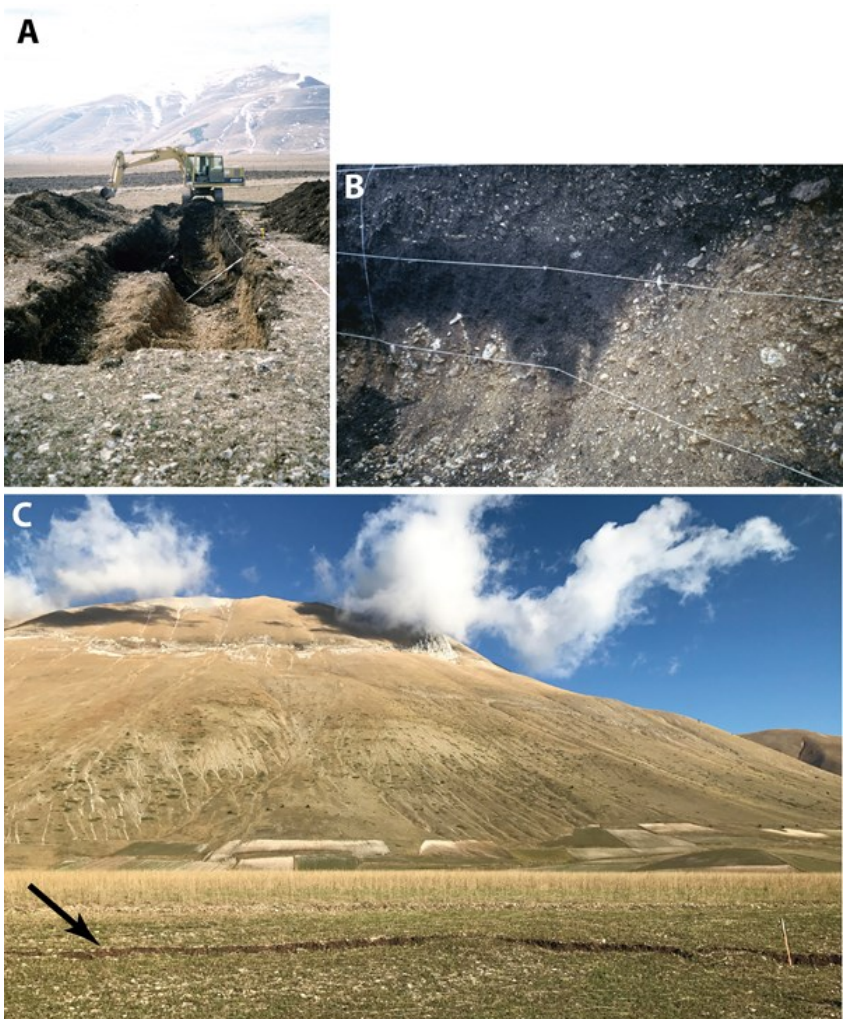

Figure 2.3. Castelluccio plain: a) view of one of the paleoseismological trenches excavated in 1999 by Galadini and Galli (2003); b) NW trench wall: the fault places Late Pleistocene-Holocene gravels in contact with Holocene paleosol and colluvium; c) 10-20 cm surface displacement caused by the 30 October 2016 earthquake (**M** 6.5) along the scarp trenched in 1999.

Associated seismicity

As described in the previous sub-section, the last fault activation is traced to the beginning of the first millennium B.C. based on paleoseismic data (Galadini and Galli, 2003; Galli et al., 2008). However, no historical earthquake can be associated with this fault, and for this reason, the fault has been defined as active but "silent", meaning that the elapsed time since the last significant event is many centuries/some millennia (larger than 2,500 years) (Galadini and Galli, 2003). Therefore, the 2016 earthquakes (August 24, October 26 and 30, **M** 6.1, 5.9 and 6.5, respectively) nucleated along an active fault whose elapsed time since last activation was long (likely larger than 2,500 years).

Seismogenic interpretation

Although historical seismic events cannot be attributed to the Mt. Vettore fault, evidence of recent activity (collected about 16 years ago), combined with interpretations of the fault geometry, have led to the interpretation that it represents the superficial expression of a seismogenic source potentially responsible for strong earthquakes (Galadini and Galli, 2000). Indeed, the geologic and geomorphologic characteristics of the Mt. Vettore fault are similar to those of other well known active faults in the central Apennines. For this reason, the 2016 earthquake sequence is not surprising in terms of the seismogenic characteristics of the Apennines.

Based on the fault geometry as expressed at the surface, the Mt. Vettore fault was proposed as a NW-SE trending seismogenic source by Galadini and Galli (2000, 2003). The proposed source has a superficial expression 27 km in length, which is consistent with an expected maximum magnitude of ~6.7 (Galadini and Galli, 2003; Falcucci et al., 2016).

The fault was not included as an individual seismogenic source in the database DISS (DISS Working Group, 2015). Rather, the area of Mt. Vettore is included as a "debated source" (ITDS002), which means a potential seismogenic source proposed in the literature but not considered reliable enough to be included in the database.

Other source models for this portion of Italy include the Mt. Vettore fault within a map of seismogenic boxes (Boncio et al., 2004a) and as an individual source (Akinci et al., 2009). These source models are not used in current national models for PSHA.

2.2.2 Norcia Fault

Geological evidence of recent activity

The Norcia normal fault is 31 km long (between the villages of Cittareale to the south and Preci to the north), and strikes NNW-SSE and dips WSW, (Figure 2.1). It includes four main segments that are visible in the field along carbonate fault scarps on slopes bordering intermontane depressions (Calamita et al., 1982; 1995; Brozzetti and Lavecchia, 1994; Galadini and Galli, 2000; Pizzi et al., 2002) (Figure 2.4).

The Preci, Campi and Norcia Quaternary basins are associated with the northernmost fault segments (Galadini and Galli, 2000). No basin is associated to the southernmost segment, between the villages of Castel Santa Maria and Cittareale (Blumetti et al., 1990), which displays geomorhpologic evidence of deep seated gravitational deformations (Galadini, 2006).

Figure 2.4. Norcia fault: a) southernmost fault section in the area of Cittareale (Le Piatenette); the arrow indicates the bedrock fault scarp; b) bedrock fault scarp close to Castel Santa Maria; the remains of the Madonna della Neve church, destroyed by the 1979 earthquake, are visible; c) building and the remains of a building close to the emergence of the fault at Castel Santa Maria; d) panoramic view of the NE slope of the Campi basin, north of Norcia, about 15 years ago; sunlight is shining on the slope sector where the fault is emerging, above the village of Campi.

The clearest evidence of Quaternary activity has been found in the Norcia basin, a rectangular depression in plan view, about 10 km long and 3 km wide. Similar to other Apennine intermontane depressions, the tectonic evolution of the Norcia basin has been driven by normal faulting along the east margin of the basin (Calamita and Pizzi, 1992; Calamita et al., 1995; 1999 and 2000; Pizzi et al., 2002; Figure 2.1). The available literature indicates that the western margin of the basin is also a normal fault, in this case with faint geomorphologic evidence of recent activity (Blumetti, 1995; Cello et al., 1998). That fault probably represents the antithetic splay of the main fault emerging along the eastern slope. Considering this structural framework, the Norcia basin probably evolved during the Quaternary as a graben.

The recent (also Holocene) activity of the fault has been described in geomorphologic studies (e.g., Blumetti, 1995). It has been responsible for the displacement of the Patino alluvial fan

deposits (Middle Pleistocene) (Fubelli, 2004) and of slope debris attributed to the Late Pleistocene (Blumetti, 1995). A minimum slip rate of 0.2 mm/yr has been estimated based on topographic offset on a scarp dated at 0.1 Ma and carved into alluvial gravels dated to 0.23 Ma.

Recent displacements have also been related to minor fault sections within Norcia (Galli et al., 2005) (Figure 2.5). Paleoseismological investigations identified slip from the 1703 (14 January) earthquake and events between 6^{th}-5^{th} century BC and 3^{rd}-1^{st} BC (99 BC?). As a result, the recurrence interval for large **M** events can be estimated as 1,700-1,900 years (Galli et al., 2005).

Figure 2.5. Norcia fault: emergence of active fault splays in the settled area of Norcia: a, b) vault and walls of a cellar displaced by a fault which activated during the earthquake of 1979; c) panoramic view of the of the trenches excavated by Galli et al. (2005) in the suburbs of Norcia: the fault places Middle Pleistocene alluvial gravels in contact with colluvial units ranging in age from the Upper Pleistocene (i.e. the lowermost unit with the orange matrix in the hanging wall) to the 18th century AD.

Geomorphologic investigations suggest a total fault displacement between 600 and 900 m over the last 1.1-1.2 Ma (Pizzi e Scisciani, 2000; Pizzi et al., 2002). This estimate is close to that of

Gori et al. (2007) based on displacement subsequent to the formation of the so called “top paleolandscape” (i.e. a flat and erosional landscape of Pliocene age carved into the marine substratum) present in the eastern sector of the basin. Uncertainty about the age of this landscape leads to an uncertain slip rate in the range of 0.25-1.15 mm/yr (Gori et al., 2007).

Evidence of Quaternary activity was also found along the southernmost segment of the Norcia fault, in the area of Mt. Alvagnano (Blumetti, 1995). A bedrock fault scarp is evident along the western slope of this relief and close to the village of Castel Santa Maria (Figs. 2.4b, 2.4c). In this case, however, motion has been conditioned also by deep gravitational deformations (Galadini, 2006). A carbonate fault scarp was also detected in the southernmost sector of this segment, close to Cittareale (Figure 2.4a).

Furthermore, east of the Norcia basin, the Cascia depression is bordered by faults striking NW-SE to N-S, with a total length of about 10 km and exhibiting evidence of Quaternary activity (Calamita et al., 1982; Cello et al., 1997; Fubelli, 2004). In particular, the most recent study presents evidence of displacement affecting Middle Pleistocene lacustrine and alluvial deposits and Late Pleistocene slope deposits.

Associated seismicity

1 December 1328 (**M** 6.5): The damage distribution suggests that this earthquake mainly struck the northernmost sector of the area bordered by the Norcia fault. This may result from the activation of the northernmost sections of this fault (e.g. Galadini et al., 1999). Strong damage has been reported for Preci (10 MCS), close to the macroseismic epicentre, and Norcia (9-10 MCS). Although these near-field effects were severe, it is possible that the magnitude estimate of 6.5 is biased high based on the following considerations: (1) we have no reports of damage in the far-field (beyond the epicentral region) and (2) other large-**M** events originating in the central Apennines in the middle ages have produced notable far-field damage, which makes this event an outlier in this regard.

6 November 1599 (**M** 6.1): Although Norcia suffered damage due to this earthquake (I 8 MCS), the highest intensities (2 localities with I 9 MCS and 6 localities with I 8 MCS) are located about 10 km west of the Norcia plain, in the Cascia area. This is another Apennine sector of the Umbria region, having a Quaternary fault considered as active (Fubelli, 2004). The intensity distribution is consistent with the activation of the Cascia fault (Galadini et al., 1999).

14 January 1703 (**M** 6.9): This earthquake struck the region located on the hanging wall of the Norcia fault system, between Cittareale (I 11 MCS) to the south and Preci (I 8 MCS) to the north. For this reason, it has been suggested that this event activated the entire Norcia fault (Galadini et al., 1999). The impact of this earthquake is demonstrated by reported intensities for multiple villages: 2 localities with I 11 MCS, 3 with I 10-11 MCS, 36 localities with I 10 MCS. Norcia is among the latter and evidence of the 1703 damage and subsequent changes in building construction practices are still visible in the old town centre. The 1703 earthquake produced damage in Amatrice that was assigned an intensity of I 9 MCS.

12 May 1730 (**M** 6.0): The highest intensity datapoints (I 9 MCS) are located in the Norcia plain and surrounding hills and slopes (11 localities with I 9 MCS of the whole 13 with this intensity). This suggests that only the Norcia section of the fault system activated in 1730. Amatrice had damage estimated with I 7-8 MCS.

22 August 1859 (**M** 5.7): Damage occurred in a well defined sector of the Norcia area, specifically in the Campi plain, a few kilometres north of the main town. For this reason, the event has been proposed to have activated the Campi section of the fault (Galadini et al., 1999). The damage from this earthquake is less significant than that from seismic events described previously. It is represented by 5 datapoints reporting a maximum intensity of I 8-9 MCS. Nonetheless, a significant amount of rebuilding in Norcia followed this event. No data about damage at Amatrice is available.

19 September 1979 (**M** 5.8): This event is smaller than those reported above, but it has a key role in the local seismic history because it triggered retrofitting of buildings in the old town centres with modern criteria. These retrofits have been credited with limiting the damage suffered in the Norcia area during the 24 August 2016 mainshock. The effects of the 1979 earthquake are represented by 5 intensity datapoints with I 8-9 MCS and 25 localities with I 8 MCS, mainly located south of Norcia. For this reason, the origin of the earthquake has been attributed to the Cittareale-Mt. Alvagnano section of the Norcia fault. Amatrice experienced damage estimated as I 6-7 MCS.

Seismogenic interpretation

As described above, four historical earthquakes (1328, 1730, 1859, 1979) are attributed to the Norcia fault system based on damage distributions (Galadini et al., 1999). The **M** 6.9 1703 event, which produced damage across the entire Norcia sector, suggests synchronous activation of multiple fault segments. This is also supported by paleoseismological investigations, which find evidence of previous surface ruptures with displacements consistent with the reported magnitude (Galli et al., 2005). The same investigations indicate that a pre-1703 event occurred during the Roman age, possibly 99 BC (i.e. it may coincide with an earthquake known from historical sources).

On the whole, we have evidence of “mixed” seismogenic behaviour, in which single fault sections cause earthquakes with **M** ≤ 6.5 (note that 6.5 is the magnitude attributed to the 1328 event, magnitude possibly overestimated as noted above) combined with multi-segment ruptures causing earthquakes with magnitudes up to 7 (Galadini et al., 1999).

We hypothesise a single seismogenic source between Cittareale (south) and Preci (north), striking NNW-SSE, dip direction WSW, length at surface of 31 km, and maximum magnitude 6.9-7. Its recurrence interval is on the order of 1,700 years (as derived from paleoseismological investigations; Galli et al., 2005). Akinci et al. (2009) present a similar view. By contrast, Boncio et al. (2004a) define two different sources: *i*) the three northernmost segments of the Norcia fault and *ii*) another source linking the Cascia and the Cittareale-Mt. Alvagnano segments. No

single seismogenic sources are defined in DISS Working Group (2015); the Norcia area is included in a "composite seismogenic source." As defined by the DISS Working Group, a composite source consists of a simplified representation of fault geometry encompassing what is now understood to include multiple individual segments. The composite source into which the Norcia region faults are encompassed is ITCS028, with a maximum magnitude of 6.5, and a slip rate of 0.1-1.0 mm/year.

2.2.3 Leonessa Fault

Geological evidence of recent activity

The formation of the Leonessa intermontane basin, about 20 km NNE of Rieti, is generally related to the activity of a normal fault, striking WNW-ESE and dipping NNE, and about 20 km long (Figure 2.1). This fault defines the SSW basin margin, along the northern slope of Mt. Tilia, and is visible as a discontinuous bedrock scarp (Michetti and Serva, 1990; Fubelli et al., 2009). Other portions of the fault are not visible due to cover (seal) from two superimposed orders of alluvial fans attributed to the Upper Pleistocene (Fubelli et al., 2009) (Figure 2.6), as well as by the top depositional surface of an Early Pleistocene (beginning of the Middle Pleistocene) alluvial fan. This setting suggests that the Leonessa fault was possibly active during the Late Pliocene-lower Early Pleistocene and its activity ended or strongly reduced during the Late Quaternary. This kinematic history, described by Fubelli et al. (2009), differs from that defined by other authors (Michetti and Serva, 1990; Cello et al., 1997; Roberts e Michetti, 2004; Walker et al., 2010) who proposed activity based on morphologic surveys at the only two sites where the fault plane is exposed. We believe, however, that fault exposure did not result from tectonic slip but from morphogenic processes involving erosion and landsliding (Fubelli et al., 2009).

Associated seismicity

No historical earthquake are associated with this fault.

Seismogenic interpretation

Considering geological and geomorphological evidence of inactivity, together with the absence of seismicity, we consider that this fault does not correspond to the superficial expression of a seismogenic source potentially responsible for surface faulting earthquakes (i.e. M>6.0±0.2; Falcucci et al., 2016).

A seismogenic source in the area of Leonessa is not reported in Boncio et al. (2004a) nor Akinci et al. (2009). This sector is included in the southernmost portion of the long "composite seismogenic source" ITCS037 in DISS Working Group (2015).

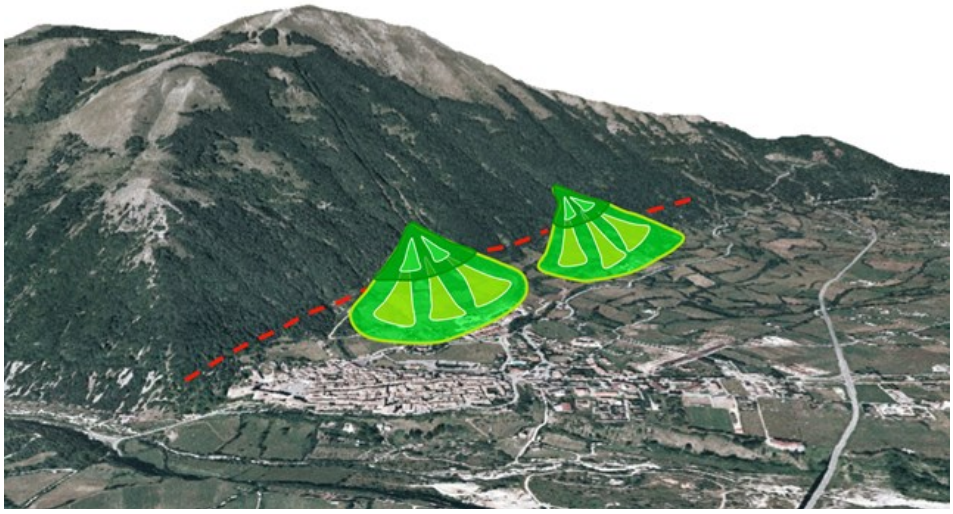

Figure 2.6. Google view of the Leonessa plain and of the NE slope of Mt. Tilia. The fault bordering the plain is sealed by alluvial fans attributed to the Upper Pleistocene.

2.2.4 Laga Mts. Fault

Geological evidence of recent activity

The western slope of the Laga Mts. has a normal fault, about 26 km long, striking NW-SE and bordering two geomorphologic domains: the Amatrice basin to the north and the Campotosto plateau to the south (Figure 2.1). Both areas contain Quaternary deposits (Cacciuni et al., 1995).

Although located along the same fault, the two areas have different geomorphologic characteristics (Galadini e Messina, 2001; Boncio et al., 2004b). The Amatrice area is similar to numerous other basins of the central Apennines, having experienced lacustrine and alluvial deposition during the Quaternary (Cacciuni et al., 1995). In contrast, the Campotosto plateau lacks the characteristics of an intermontane basin, containing only Late Quaternary alluvial and debris deposits typical of piedmont areas (e.g. Galadini and Messina, 2001).

Differently from most of the central Apennine Quaternary faults, the Laga Mts. fault structure only affects the arenaceous and clayey successions of the Laga flysch. Therefore, due to lithology, scarps resulting from recent tectonics and related geological evidence of fault slip can be detected at only few sites along the fault (Figure 2.7).

Two fault segments have been defined as tectonically active in the Quaternary, located in the Amatrice basin and to the Campotosto plateau (Galadini and Messina, 2001). Quaternary activity in the Amatrice sector can be related to the formation of the related intermontane basin from extension, likely with processes similar to those of the other Apennine depressions. The oldest sediments and related landforms are displaced and tilted (Cacciuni et al., 1995).The top of the Early Pleistocene units is only displaced by 20-30 m (Galadini and Messina, 2001), suggesting that tectonic activity decreased during the Quaternary and perhaps the fault has become inactive (or is having reduced slip) in the Late Quaternary (Galadini and Messina, 2001).

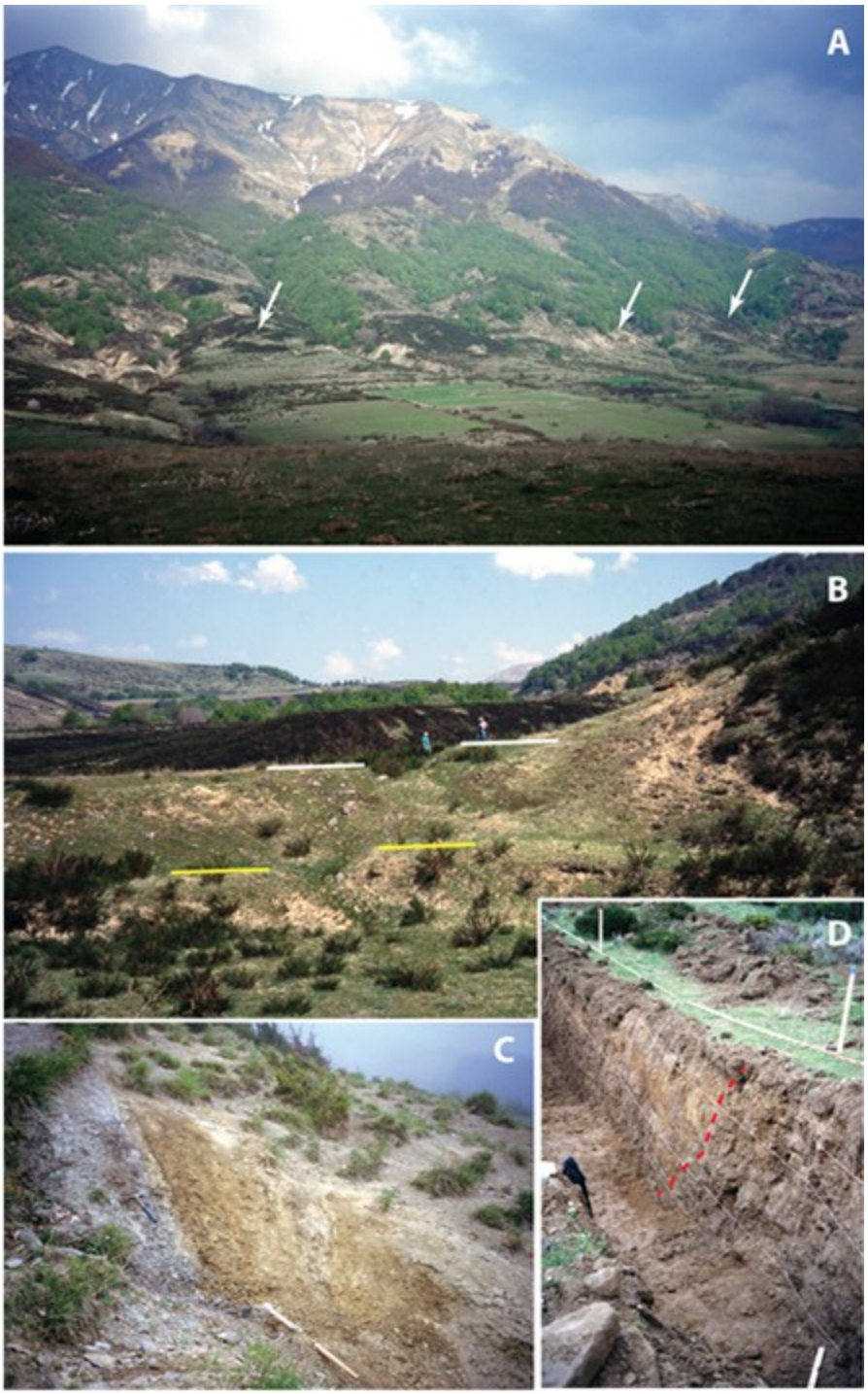

Figure 2.7. a) Panoramic view of the Laga fault in the Campotosto plateau; the arrows indicate places where fault scarps in the arenaceous bedrock have been detected; b) Holocene terraces displaced by the Laga fault in the Campotosto plateau; c) fault plane placing the clayey-arenaceous Laga flysch in contact with colluvium probably deposited during the Upper Pleistocene; d) panoramic view of the trench excavated in 1998 across the Laga fault in the Campotosto plateau by Galadini and Galli (2003); the fault places the areanaceous bedrock of the Laga flysch in contact with colluvial units of Holocene age.

Alluvial and lacustrine deposits not older than the Late Pleistocene are present along the southern fault section (Campotosto plateau), in the piedmont area of the Laga Mts. These deposits overlie the Miocene flysch. This kind of deposition also occurred during the Holocene (Galadini and Galli, 2003). Late Quaternary deposits in the Campotosto area are displaced by the Laga Mountains fault. A vertical displacement larger than 20 m affects an alluvial terrace formed during the upper Late Pleistocene and displacement of alluvial deposits of age 8,000 years BP has been observed (Galadini and Galli, 2003; Figure 2.7d).

Along the Vomano valley, south of the Campotosto plateau, a succession of relict paleo-landsurfaces was identified on the hanging wall of the Laga fault. The absence of similar landforms in the footwall was interpreted as the result of tectonic lowering of the hanging wall and relative minor uplift of the footwall (Galadini and Messina, 2001). This type of terracing up to an elevation close to the present valley bottom suggests the persistence of recent (late Quaternary) tectonic processes (Galadini and Messina, 2001).

In summary, late Quaternary tectonic activity on the two segments of the Laga fault can be summarized as follows: *i*) the northern segment (Amatrice basin) exhibits no evidence of late Quaternary surface slip, and *ii*) the southern segment (Campotosto plateau and Vomano valley) shows evidence of surface activity during the Late Pleistocene and the Holocene. Possibly, the different ages of fault slip indicate a sort of along-fault migration of the activity during the Quaternary, from north to south (Galadini and Messina, 2001).

Associated seismicity

7 October 1639 (**M** 6.2): Historical knowledge about the earthquake sequence that began on 1639 (October 7) is mainly related to a single written source, drawn at Rome, far from the epicentral area, by a writer who gathered oral reports about the coseismic effects. Based on this sparse information, the intensity distribution related to the highest damage has been estimated as intensity I 10 MCS at one location and intensity I 9-10 MCS at 12 locations. Damage at Amatrice was listed with I 9MCS. Most of the coseismic effects occurred in the Amatrice basin; little information is available about damage in surrounding areas.

Considering the significant impact the earthquake had in the Amatrice area and the magnitude attributed to the 1639 mainshock, the 24 August 2016 earthquake has been compared at first to the 1639 event. However, because the damage from the 1639 event was mostly localized in Amatrice and many historical buildings within the city did not suffered damage, it may be that the magnitude of the 1639 event is overestimated. Compounding the problem is the excessive emphasis on historical damage descriptions from a single source (Castelli et al., 2002). We note that the 1639 event produced no strong damage in Norcia and surrounding areas, whereas the 24 August 2016 event caused significant damage north of the Amatrice basin.

Seismogenic interpretation

Geological data suggest two segments along the Laga fault related to the Amatrice basin to the north and the Campotosto plateau and the Vomano valley to the south. These segments appear

to have differing tectonic activity and seismotectonics. Historical seismicity can only be related solely to the 1639 event that struck Amatrice, with little damage to the surrounding areas, which is consistent with the activation of the northern segment. The magnitude attributed to the earthquake (6.2) results from cumulative damage from the seismic sequence and possibly from an exaggeration in the description of the damage by the single historical source, resulting in an overestimation of the actual 1639 earthquake magnitude.

This view is consistent with the characteristics of the northern Laga Mts. fault, whose superficial features do not suggest the repetition of significant surface faulting events during the late Quaternary, i.e. the activation of the northern Laga Mts. fault during the recent geological past does not seem to have been related to high magnitude earthquakes.

For this reason, a seismogenic source can be hypothesised in the Amatrice area, striking NW-SE, with a superficial expression of about 8 km and potentially responsible for earthquakes up to **M** 5.9.

While the southern segment (Campotosto plateau and Vomano valley) provides no evidence of historical activation, geomorphologic and paleoseismological evidence indicates Holocene activity (Figure 2.7). This suggests that the southern segment should be considered as a seismogenic source that strikes NW-SE, is 18 km in length at the surface, and is capable of producing earthquakes up to about **M** 6.5.

Different interpretations are provided by Boncio et al. (2004b) and Akinci et al. (2009). Boncio et al. (2004b) consider the Laga fault as the expression of a single, unsegmented structure (Mt. Gorzano), comprising the Campotosto and the Amatrice sections. Akinci et al. (2009) consider only the Campotosto segment as a source capable of producing strong earthquakes. Indeed, the 1639 earthquakes were considered to have smaller magnitudes than those reported in the seismic catalogues. For this reason, these events are attributed to background seismicity and no individual source is defined in the Amatrice area by Akinci et al. (2009). Also the recent seismicity seems consistent with the definition of two different fault sections, since earthquakes related to the 2009 sequence were mainly associated to the Campotosto sector, while the 24 August 2016 events are limited to the Amatrice basin.

Although the DISS database (DISS Working Group, 2015) reports a fault in the Laga Mountains area (within the debated seismogenic source ITDS073), single seismogenic sources are not defined. However, this area is partly included in composite source ITCS028.

2.2.5 Montagna dei Fiori-Monti Gemelli Fault

Geological evidence of recent activity

The relief of Monti Gemelli is associated with a NW-SE trending anticline related to an ancient thrust active between the Late Messinian and the Lower Pliocene. Topographic relief on the SW slope is affected by a NW-SE trending and SW dipping normal fault 15 km in length. Probably the

normal fault was active during Miocene pre- thrusting and thrusting phases (Scisciani et al., 2002; Storti et al., 2016).

Geomorphologic evidence of the normal fault consists of a scarp affecting the entire slope and having variable heights (up to 50 m). The fault plane is exposed discontinuously along the scarp, mainly due to landsliding and erosional processes in the hanging wall (Fubelli et al., 2009; Figure 2.8). Moreover, the fault is sealed by ancient paleo-landsurfaces attributed to the Late Pliocene-Early Pleistocene and by slope-derived breccias not younger than the lower Middle Pleistocene (Fubelli et al., 2009; Figure 2.8). The current interpretation is that despite the presence of a sporadically exposed fault scarp, the preponderance of evidence suggests that the Monti Gemelli fault is inactive.

Associated seismicity

Strong historical earthquakes cannot be associated to this fault. Minor events of low magnitude sometimes occur in the area bordered by the Monti Gemelli fault to the east. However, these events are characterized by hypocenters at depth in the order of 10-20 km and their relationship with the fault is unclear.

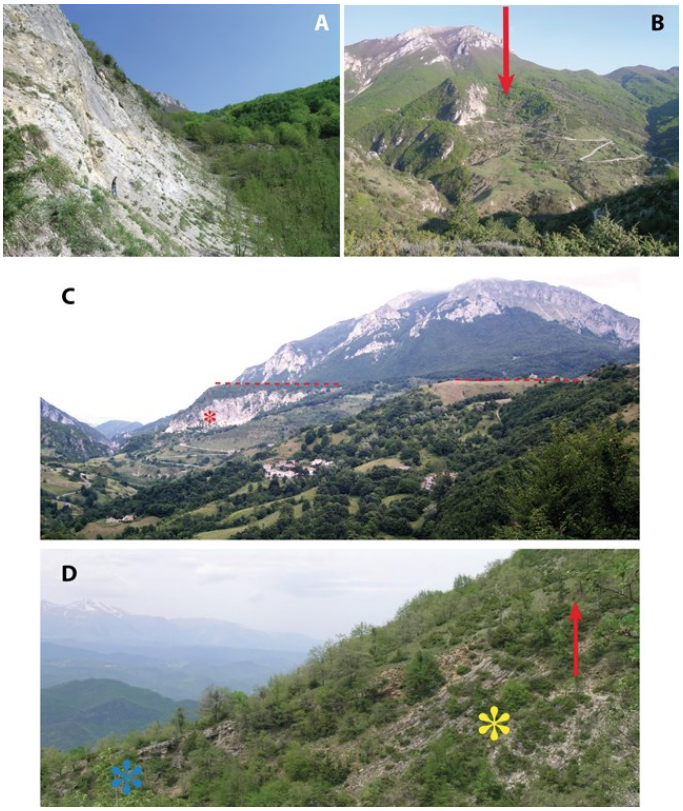

Figure 2.8. The Montagna dei Fiori-Monti Gemelli fault: a, b) bedrock fault scarp exposed by landsliding (red arrow); c) Upper Pliocene-Early Pleistocene paleo-land surfaces (strath terraces) carved into the marine substratum (carbonate bedrock on the left, red asterisk; marly-arenaceous substratum on the right) and located at the same elevation across the fault; d) Pleistocene slope-derived breccias (blue asterisk; the red arrow defines the uppermost limit of the outcrop) sealing the fault (yellow asterisk).

2.2.6 Upper Aterno Valley and Paganica Faults

Geological evidence of recent activity

Quaternary evolution of the upper Aterno valley north of L'Aquila has involved activity of four NW-SE normal fault segments. From the north (Figure 2.1), these segments are: the Capitignano and San Giovanni faults, bounding the Montereale basin and 8 and 4 km in length, respectively (Blumetti, 1995; Cacciuni et al., 1995; Galadini and Galli, 2000; Galadini and Messina, 2001; Civico et al., 2016); the Mt. Marine fault, bordering the Arischia basin, 14 km long (Blumetti, 1995; Bagnaia et al., 1996; Basili et al., 1999; Galadini e Galli, 2000; Messina et al., 2003, 2009); the Pettino fault, bordering the L'Aquila basin and adjacent to L'Aquila city, 9 km long (Bagnaia et al., 1996; Blumetti et al., 1996; Galadini and Galli, 2000; Messina et al., 2003, 2009).

The NW portion of the northernmost segment (Capitignano fault, Figure 2.1) places the clayey-arenaceous Laga flysch in contact with Quaternary deposits related to different orders of alluvial fans (Cacciuni et al., 1995; Chiarini et al., 2014). Tectonic tilting has been identified in the oldest outcropping deposits, attributed to the Middle Pleistocene (Civico et al., 2016). The fault-generated mountain front east of Capitignano is the geomorphologic evidence suggesting recent fault activity (Blumetti, 1995; Civico et al., 2016). This relationship is fostered by the carving of this slope into the erodible arenaceous lithology of the Laga flysch.

A 10 km portion of the SE section of the fault can be detected into the Miocene carbonate substratum but does not provide clear evidence of recent tectonic activity. Evidence of lack of recent activity is provided by Plio-Quaternary relict paleo-landsurfaces in this area at the same elevation on the hanging wall and foot wall sides of the fault (Chiarini et al., 2014). In summary, only the NW portion of the Capitignano fault appears to be recently active (Galadini and Messina, 2001; Chiarini et al., 2014).

The San Giovanni fault presents evidence of Quaternary activity along a scarp south of the Montereale basin (Figure 2.1), where Early Pleistocene slope derived breccias are tilted (Galadini and Messina, 2001; Civico et al., 2016) and Late Pleistocene deposits are displaced (Chiarini et al., 2014). Towards the NW, the fault does not displace deposits of the Montereale basin nor the flat and wide paleolandscape carved into the Laga flysch north of the basin (Galadini and Messina, 2001).

The surface expressions of southern segments (Mt. Marine, Pettino) are characterized by carbonate fault scarps (Figure 2.9). The fault planes place the marine substratum in contact with layered slope deposits that date to the Late Pleistocene. In some cases, slope deposits are displaced by the main faults and by minor shear surfaces close to the main fault (Figure 2.10d). These deposits have been radiocarbon dated at 31,710±760 yr BP and 23,330±300 yr BP (Galadini and Galli, 2000), confirming a previous chronological attribution by Blumetti (1995). Moreover, an alluvial terrace is vertically displaced by 15-20 m close to the NW tip of the Pettino fault (Galadini and Galli, 2000). Accordingly, a vertical slip rate has been estimated in the order of 0.47-0.86 mm/yr (Galadini and Galli, 2000).

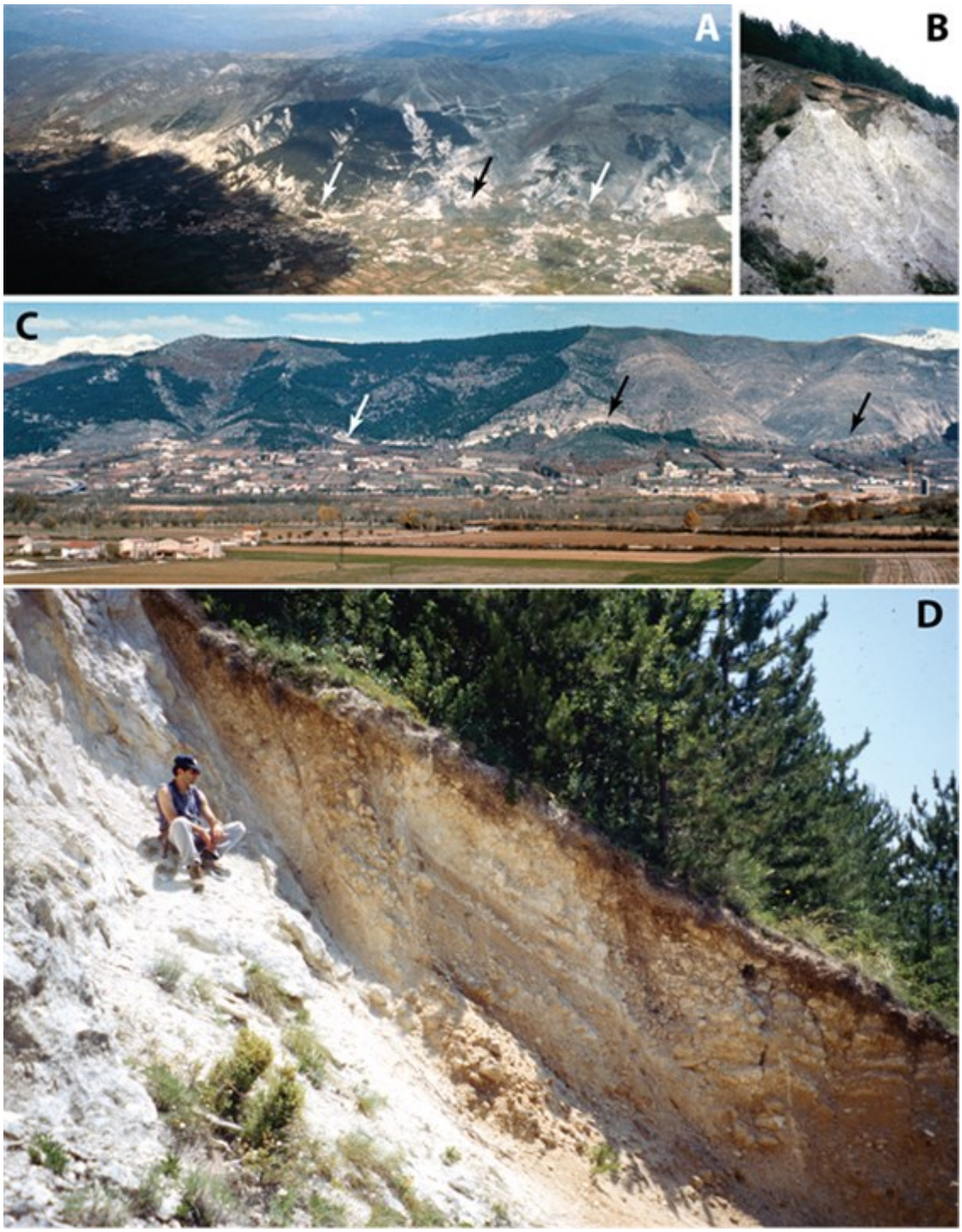

Figure 2.9. a) Mt. Marine fault: the arrows indicate the surface expression of the fault and the thick brecciated area corresponding to the bedrock fault scarp; b) Mt. Marine fault: Upper Pleistocene slope deposits displaced and suspended in the footwall; c) Pettino fault: the arrows indicate the bedrock fault; the panoramic view of more than 30 years ago is preceding the widespread modern building of L'Aquila along this slope; d) Pettino fault: the main fault plane places the carbonate bedrock in contact with Upper Pleistocene slope deposits affected by numerous shear planes.

Along the Mt. Marine fault, the aforementioned slope deposits are present both on the hanging wall and foot wall (Figure 2.9c). Topographic profiles across the scarp suggest vertical displacement of 8-10 m and a slip rate of 0.25-0.43 mm/yr (Galadini and Galli, 2000). The total length of the fault is about 14 km, but clear evidence of recent activity is confined to the SE sector, for a length of about 9 km. Here, the fault has generated the Arischia basin and Holocene and historical activity (i.e. activation during the 1703 earthquake; **M** 6.7) is evident from paleoseismological investigations (Moro et al., 2002; Galli et al., 2011). The NW portion of this fault, instead, has successions of Plio-Quaternary relict paleolandsurfaces across the fault, indicating lack of significant vertical displacements (Basili et al., 1999).

The surface expression of the Paganica fault is located ESE of L'Aquila (Figure 2.1). A wide depression between the villages of Tempera, Paganica, Bazzano and Onna is associated with the recent activity of the fault (Galli et al., 2010; Figure 2.10). Different fault splays have displaced an alluvial succession, in which the oldest units (Middle Pleistocene) are exposed at the NE basin margin while more recent units are stacked in the lowest basin sector.

Figure 2.10. a) Panoramic view of the Paganica-Bazzano plain; the white asterisks indicate the gentle slope where the Paganica fault has been detected; b) wall of one the trenches excavated by Moro et al. (2013) across the Paganica fault: the fault places a Pleistocene colluvium (red unit in the footwall) in contact with Upper Pleistocene and Holocene colluvial units in the hanging wall; c) surface faulting observed along the Paganica fault after 6 April 2009 earthquake.

The Paganica fault generated the 2009 earthquake (**M** 6.3). Surface faulting was observed along the fault after this event (Falcucci et al., 2009; Boncio et al., 2010; Emergeo Working Group, 2010; Galli et al., 2010; Lavecchia et al. 2010; Vittori et al. 2011; Gori et al., 2012; Figure 2.10c). Paleo-seismological analyses indicate past activation during events larger than that of 2009 (Figure 2.10b), based on larger slip. In particular, slip from the 2 February 1703 event has been suggested (Galli et al., 2011; Moro et al., 2013), although similar evidence was not found by Cinti et al. (2011). However, the data of Cinti et al. (2011) does not exclude activation of the Paganica fault during an event subsequent to the 1461 earthquake (maybe in 1703). This means that the Paganica fault probably activated together with Mt. Marine to cause the 1703 earthquake.

Associated seismicity

27 November 1461 (**M** 6.5): This earthquake is considered a seismogenic twin of the 2009 L'Aquila earthquake (Tertulliani et al., 2009). It strongly damaged the same area as in 2009, with the largest intensities in villages south of L'Aquila (Sant'Eusanio Forconese, Poggio Picenze, Onna, Castelnuovo; I 10 MCS in 1461) that were destroyed in 2009.

2 February 1703 (**M** 6.7): This is the strongest historical earthquake recorded in the L'Aquila area, completing the sequence begun at Norcia on 14 January of the same year. Interpretation of damage in terms of intensities MCS is complicated by possible damage to villages of the L'Aquila region by the Norcia earthquake. However, numerous written sources has permitted to attribute the intensity I 10 MCS in 8 localities. Four villages with 10 MCS (Arischia, Pizzoli, Colle, Barete) are located in the upper Aterno valley, along one of the emerging sections of the causative fault. Evidence of post-event rebuilding in L'Aquila (I 9 MCS) is provided by heavy insertion of the baroque style, numerous inscriptions recalling the damage and the reconstruction, and applications of strengthening members such as tie beams.

6 October 1762 (**M** 5.5): This earthquake struck the same territory damaged in 1461 (and 2009), with significant damage at Castelnuovo (I 9 MCS) and Poggio Picenze (I 8 MCS). It is considered smaller than those events, which effectively prevents the possibility of finding geological traces of its occurrence along the faults south of L'Aquila. Possibly, the earthquake did not originate on the Paganica fault but on a still unidentified source to the south, although the 1762 event is attributed to the Paganica fault by Lavecchia et al. (2012).

6 April 2009 (**M** 6.3): This earthquake caused destruction and fatalities in L'Aquila and numerous villages in the Aterno valley. The macroseismic epicenter is located about 10 km SE of the instrumental epicenter, which is west of L'Aquila (Ameri et al., 2011). Most of the damage occurred on a NW-SE trending belt, about 20 km long (Galli et al., 2009). The maximum intensity (I 9-10 MCS) occurred at Castelnuovo and Onna. Collapses and/or severe damage to a significant percentage of buildings (about 50%) occurred at San Gregorio, Sant'Eusanio Forconese, Tempera and Villa Sant'Angelo (I 9 MCS). Collapse and severe damage rates <50% occurred in the old town centre of L'Aquila, Poggio di Roio and Poggio Picenze (I 8-9 MCS). Collapse and severe damage rates < 30% occurred in 21 localities (I between 7-8 and 8 MCS). Lower damage has been attributed to 32 villages with I between 6-7 and 7 MCS.

Seismogenic interpretation

The seismogenic behaviour of the fault segments described above remains an open issue. Paleoseismological and historical data suggest that Mt. Marine fault activated during the 1703 earthquake (Feb. 2) (Moro et al., 2002; Galli et al., 2011), while the Paganica fault may have also ruptured during this event based on further paleoseismological studies (Galli et al., 2011; Moro et al., 2013). The Paganica fault also generated the 2009 earthquake (e.g. Gori et al., 2012 and references therein) and probably the 1461 event.

The northernmost of these segments, i.e. the Capitignano fault, may have generated one of the 1703 events (Jan. 16). Although this event has been reported in the available catalogues (e.g. with **M** 6.0 in Guidoboni et al., 2007), the related damage and associated energy is still a matter of debate. Moreover, paleoseismological data on the Capitignano fault are unavailable, nor do historical written sources provide evidence of coseismic activation.

Our hypothesis is that at least the northernmost (Capitignano) and southernmost (Paganica) faults are capable of activating as single sources, producing earthquakes of moderate magnitude and related significant damage (1461, 16 Jan 1703, 2009). This interpretation is similar to that proposed by Lavecchia et al. (2012).

Since the Paganica fault may have caused the stronger earthquake of 2 Feb 1703 (together with Mt. Marine fault and, possibly, Pettino fault), we hypothesise that it may exhibit “mixed” seismogenic behavior whereby it may also activate together with other fault segments of the upper Aterno valley to generate stronger earthquakes (e.g., 1703). This “mixed” behaviour seems to be similar to that of the Norcia fault.

By merging available historical/paleoseismological information, single segment ruptures up to **M** 6.7 on the Mt. Marine, Pettino and Paganica faults can be postulated, as well as smaller within-segment earthquakes. The Capitignano fault segment can similarly rupture with earthquakes up to **M** 6.0±0.2. The seismogenic behaviour of the San Giovanni fault is unclear, i.e. we do not know if it is part of the main source above mentioned or it is related to the Capitignano fault. Ongoing paleoseismological investigations (by F. Cinti and colleagues) will probably shed light on this issue. For the Mt. Marine, Pettino and Paganica segments, we postulate a recurrence time of ~850-1,200 years for earthquakes with **M** 6.7 and of ~300 years for earthquakes with **M** 6.0-6.2, based on the paleoseismological and historical data.

The DISS database includes the Capitignano and San Giovanni faults in composite source ITCS028, while two different seismogenic sources have been defined in the L’Aquila area, one including Mt. Marine and Pettino faults (ITIS015), the other in the area of the Paganica fault (ITIS131) (DISS Working Group, 2015).

Three different sources, i.e. Montereale (corresponding to the Capitignano fault), Pizzoli-Mt. Pettino (corresponding to Mt. Marine and Pettino faults) and Aquilano (corresponding to the Paganica fault) have been defined by Boncio et al. (2004a).

The definition of two seismogenic sources for the L'Aquila area can also be found in Akinci et al. (2009) and two seismogenic sources, related to the Capitignano and Paganica faults have been defined by Lavecchia et al. (2012).

2.2.7 An Open Issue: Seismogenic Source of the 5 September 1950 earthquake (M 5.7)

This earthquake was responsible for damage over a large area between Leonessa (I 7 MCS) to the west and the periadriatic region to the east, Arquata del Tronto (I 6-7 MCS) to the north, and the L'Aquila region to the south.

The maximum intensity I 8 MCS was assigned to 14 localities. Among them, Accumoli, Arafranco Pinaco and Capricchia (close to Amatrice), Mascioni and Poggio Cancelli (close to Campotosto), San Giovanni and Marana (close to Montereale). Amatrice suffered damage that was assigned as I 7 MCS.

The damage distribution suggests a trend in the E-W direction. However, this may have resulted simply from where villages are located in the piedmont sectors of the E-W trending Gran Sasso chain.

Modelling of the seismogenic fault based on the damage distribution suggests an E-W striking source (strike 91,5±18, length 10,7 km, width 7,4 km), located below the Laga Mountains, which cannot be related to known tectonic structures of the region (Tertulliani et al., 2006). An E-W source is also reported in DISS Working Group (2015). It may be a blind fault, perhaps associated with geologic structure deeper than that of the Apennine normal faults described previously.

2.3 Seismic Source

2.3.1 Moment Tensors

The mainshock occurred on the 24 August, 2016 at 01:36:32 (UTC) and was recorded by Italian National Seismic Network (Rete Sismica Nazionale, RSN; www.gm.ingv.it/index.php/rete-sismica-nazionale/, last accessed 21 November, 2016) owned by the Italian Institute of Geophysics and Vulcanology (Istituto Nazionale di Geofisica e Vulcanologia, INGV). Table 2.1 shows parameters and locations of the mainshock, two main aftershocks recorded within a week (**M**5.3, 24 August, 2016; and **M**4.8, 26 August, 2016), and two events in late October that will be the subject of a subsequent report. The information in Table 2.1 are provided by INGV (http://cnt.rm.ingv.it, last accessed 21 November, 2016).

Table 2.1. Summary of the parameters of the mainshock (bold), two aftershocks, and late October events.

Date	Hour (UTC)	Latitude (N)	Longitude (E)	Depth (km)	**M**
08/24/2016	**01:36:32**	**42.7**	**13.23**	**8**	**6.1**
08/24/2016	02:33:28	42.79	13.15	8	5.3
08/26/2016	04:28:25	42.6	13.29	9	4.8
10/26/2016	19:18:05	42.92	13.13	8	5.9
10/30/2016	06:40:17	42.84	13.11	5	6.5

The focal mechanism shows that the 24 August 2016 mainshock event occurred along a normal fault trending NW-SE (strike 156 deg) with dip SW equal to 50 deg. The strike of the fault from the moment tensor is generally consistent with the orientation of the Mt. Vettore fault to the north and the Laga Mountain fault to the south. Figure 2.11 shows epicenter locations for the five events included in Table 2.1.

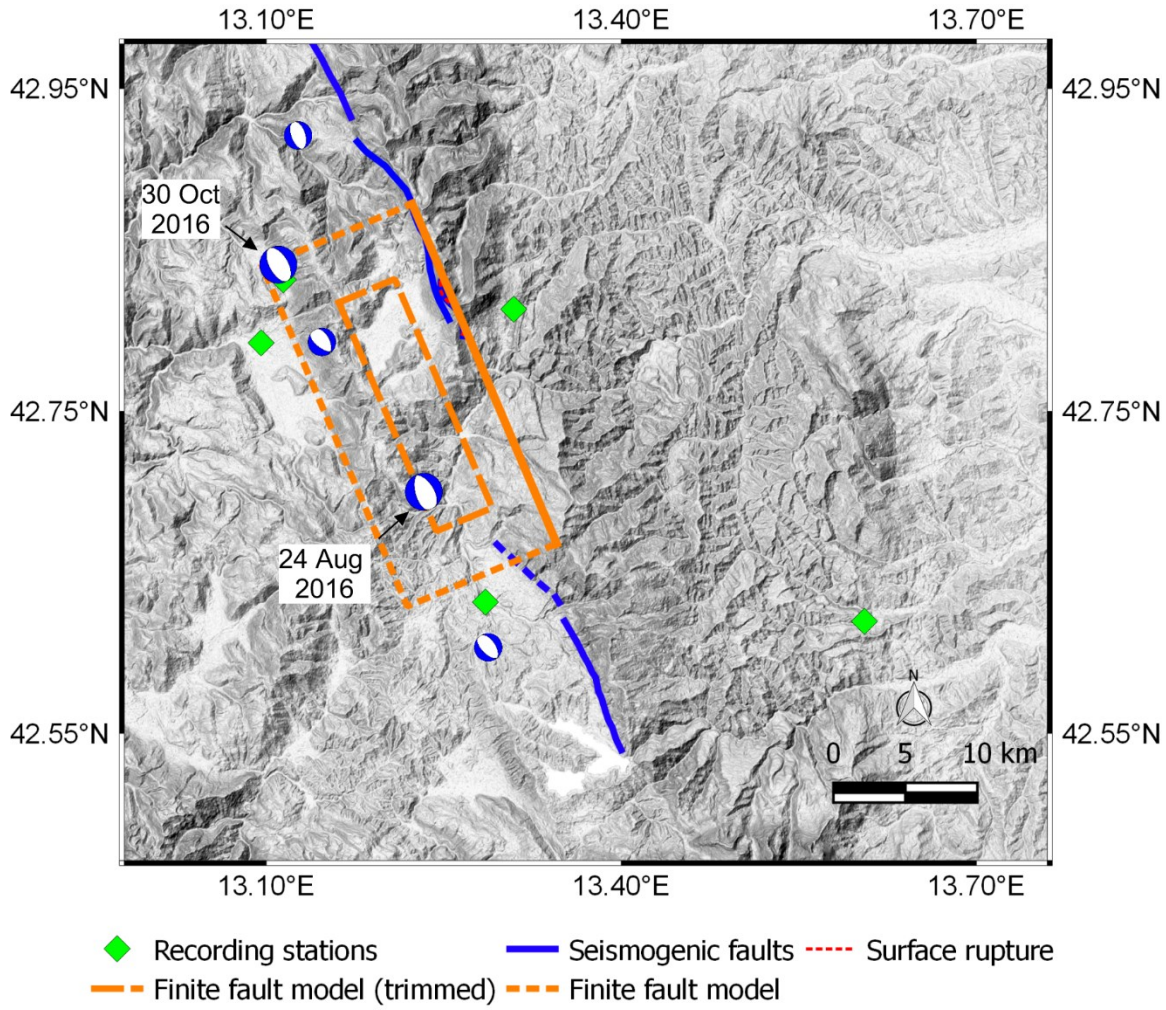

Figure 2.11. Map of epicenter of 24 August 2016 **M**6.1 event, two subsequent aftershocks, and apparently triggered events in late October 2016. Finite fault model adopted in section 2.3.3 shown for reference purposes.

2.3.2 Aftershock pattern

Locations of aftershocks from the 24 August 2016 event over a five-day period are shown in Figure 2.12. The aftershock locations shown in Figure 2.12 were taken from the RSN. The aftershock distribution is aligned along the NW-SE trending faults of the area, but fall in two main patches. The first patch is on the northern portion of the fault between the mainshock hypocenter and the 24 August 2016 **M**4.8 aftershock shown in Figure 2.12. The second patch is

south of the mainshock rupture surface, roughly centered around the 26 August 2016 **M**5.3 aftershock.

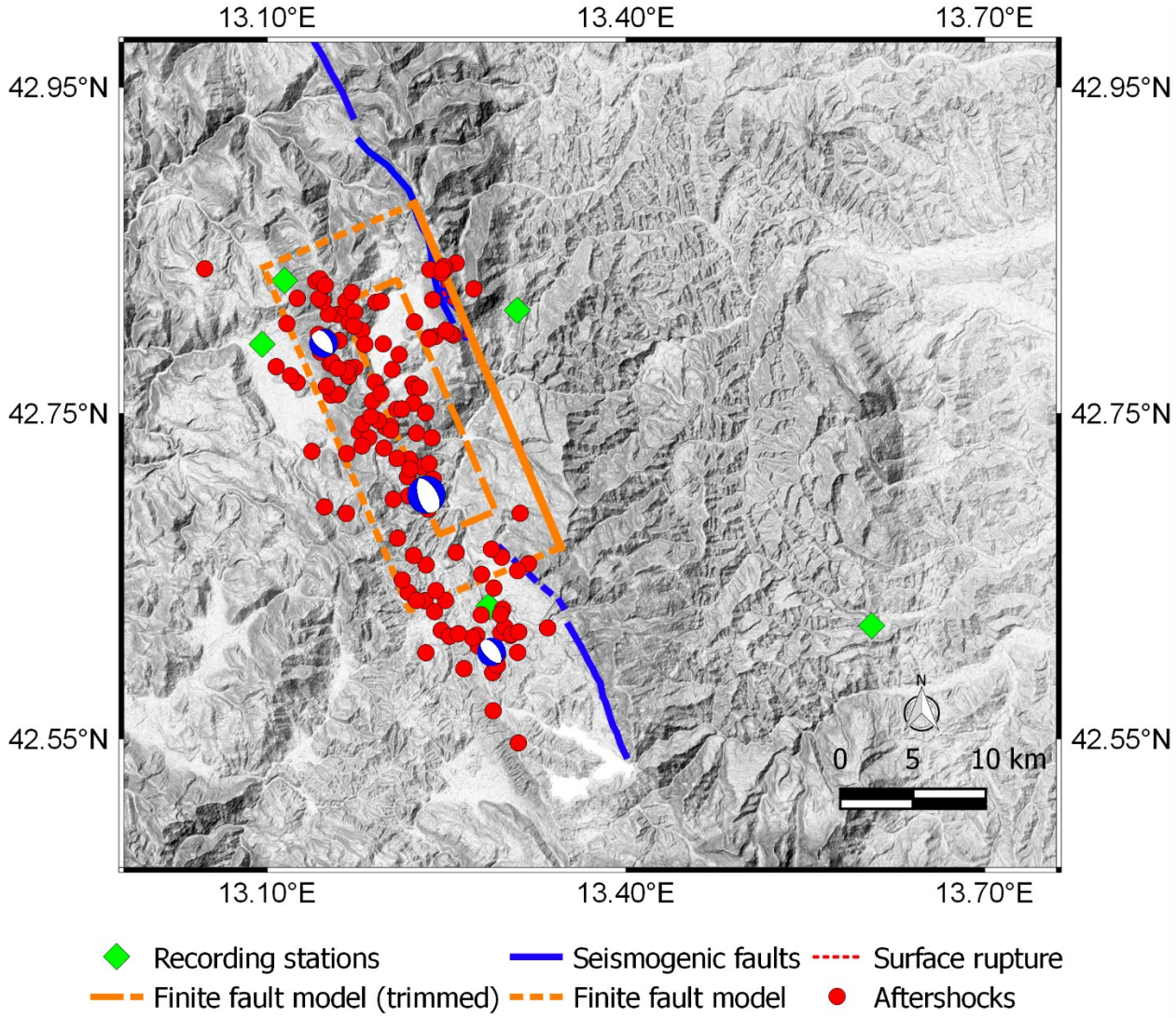

Figure 2.12. Map showing the 24 August 2016 mainshock and aftershocks within a five-day time window. Finite fault model adopted in section 2.3.3 shown for reference purposes.

2.3.3 Crustal Deformations from GPS and Remote Sensing

GPS-based measurements can be used to evaluate co-seismic displacements from large earthquake events. These results, along with the analysis of recorded ground time-series, can be used to assess the spatial distribution of permanent ground displacements. Figure 2.13 shows horizontal and vertical co-seismic displacements (red and blue arrows respectively), derived using GPS data (INGV working group, 2016). The horizontal displacement estimated at the Amatrice (AMAT) GPS station in the NW direction is larger than 2.5 cm. The estimated coseismic subsidence is equal to 1.5 cm. This vertical displacement is consistent with the value obtained analyzing the recorded time-series (Figure 3.7, Section 3.3). The GPS stations NRCI (Norcia), and LNSS (Leonessa), show horizontal displacements of about 2.3-2.4 cm in the SW direction. The

coseismic displacements in the NE direction, evaluated at the ASCC and ASC1 (Ascoli Piceno) stations, are smaller, with an average value of 1.4 cm.

Earthquake-related permanent ground deformations, can be also effectively estimated using synthetic aperture radar (SAR) images. SAR-based techniques are further described in Chapter 4 of the report. Figure 2.14 shows the coseismic displacements along the line-of-sight (LOS) direction, evaluated by the Advanced Rapid Imaging and Analysis (ARIA) project, using data from the Japanese satellite ALOS-2 (JAXA). These results can be compared to those obtained by a joint research effort performed by several Italian agencies (IREA-CNR and INGV working group, 2016). Figure 2.15 shows main results of this study. The data used to perform this analysis has been taken from the following satellites: (1) ALOS-2, (2) Sentinel-1 (Copernicus project), and (3) COSMO-SkyMed (Italian Spatial Agency). Both SAR-based studies show consistent results in terms of ground displacement patterns and magnitude of the deformations.

For the Amatrice and Norcia areas, time-series analysis, GPS, and SAR data show consistent results. The total displacement in both, horizontal and vertical direction is focused on a relatively narrow area. Two distinct deformation areas can be recognized. This results seem to be consistent with a two-plane model (presented in Section 2.3.4). The deformation patches follow a roughly SE-NW alignment with a linear shape along the strike of the surface projection of the causative faults of this events. The alignment is consistent with the location of the Mt. Vettore and Laga Mt. fault systems.

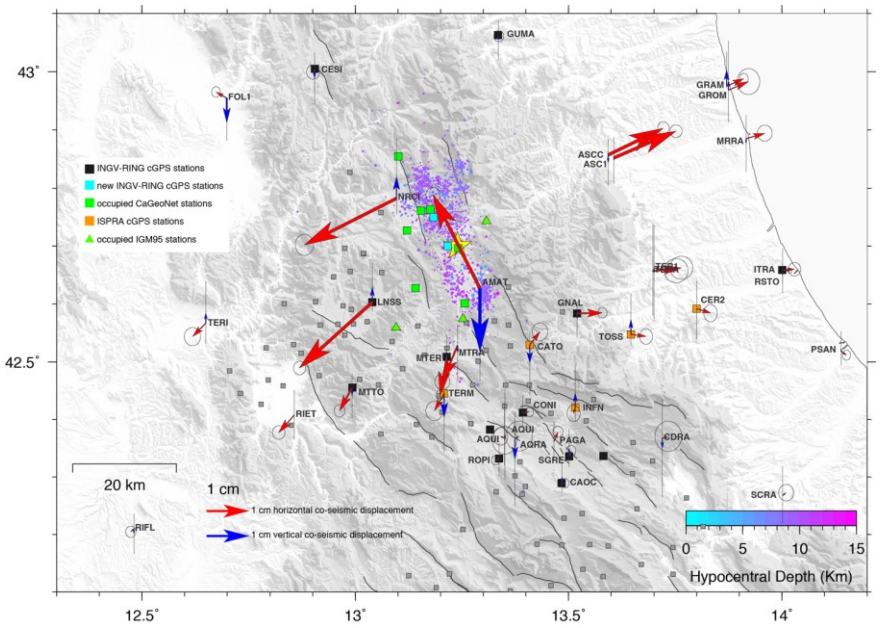

Figure 2.13. GPS-based co-seismic displacement field in the epicentral area. Red arrows represent horizontal displacements, blue arrows represent vertical displacements (from INGV working group, 2016).

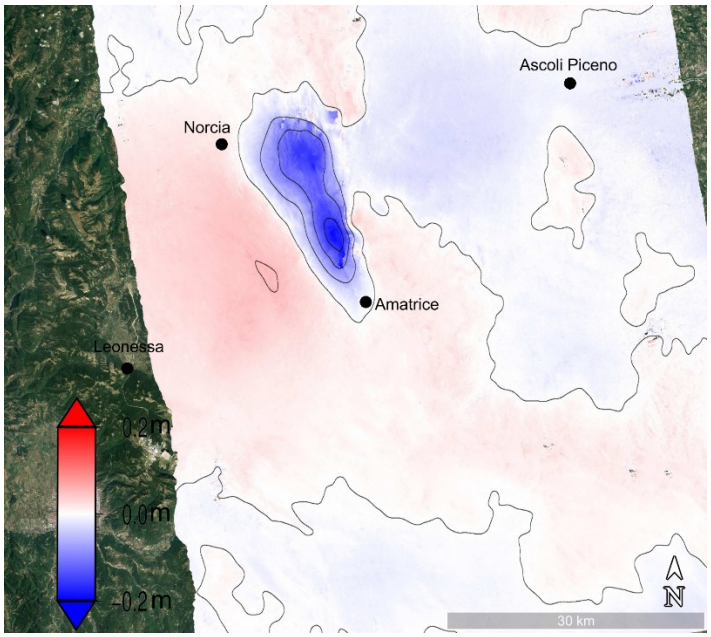

Figure 2.14. SAR-based LOS displacements in the epicentral area (source kmz file available at http://aria-share.jpl.nasa.gov/events/20160824-Italy_EQ/interferogram/, last accessed 21 November 2016).

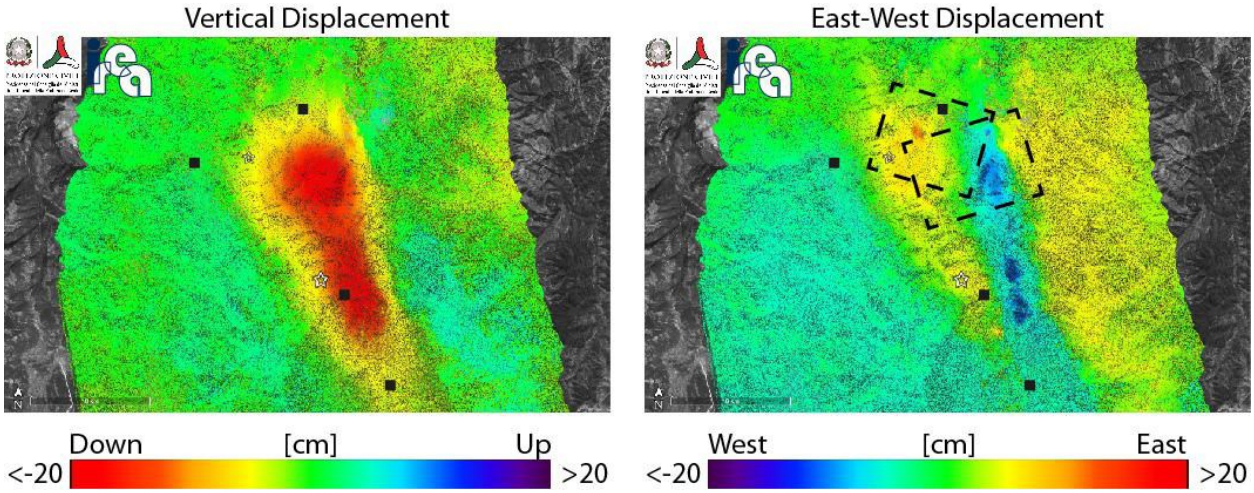

Figure 2.15. SAR-based vertical and horizontal displacements in the epicentral area (from IREA-CNR and INGV working group, 2016, DOI: 10.5281/zenodo.61682).

2.3.4 Finite Fault Model

Several alternative finite fault models are available for the 24 August 2016 event. IREA-CNR & INGV working group (2016) presents two alternative models. One consists of two planes (Figure 2.16a), roughly associated with the Mt. Vettore fault and the Laga Moutain fault, having different dip angles and lengths. The second is single-plane (Figure 2.16b). These models are based on crustal displacements inferred from synthetic aperture radar (SAR), and global positioning system (GPS) data.

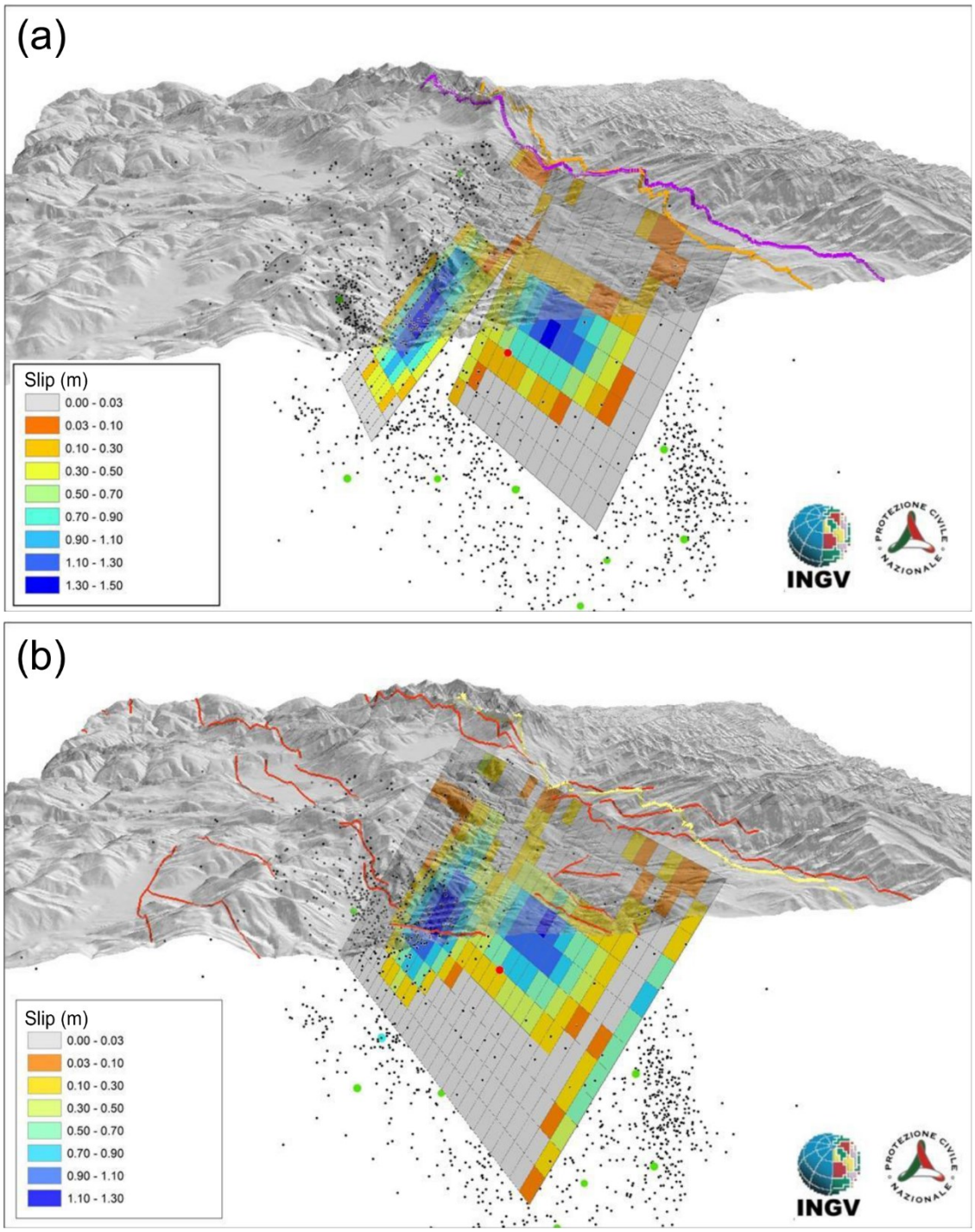

Figure 2.16. (a) Two-plane finite fault model; (b) Single-plane finite fault model. Adapted from IREA-CNR & INGV working group (2016).

The only archival publication of a finite fault model was produced by Tinti et al. (2016). This model constrains the geographic limits of the ruptured fault based on geodetic data, but the slip distribution on the fault is inverted based on recorded ground motions. We adopt the Tinti et al. (2016) model, which is trimmed in accordance with typical NGA practice (Ancheta et al., 2014,

see Figures 2.11 and 2.12) to identify the portion of the finite fault model most responsible for strong ground motions. Figure 2.17 shows a heterogeneous slip distribution, with two distinct patches of relatively large slip. Although the authors show a single-plane solution, they speculate that a two-plane solution may be preferred and developed in the future. A slip model that combines data from ground motion recordings and permanent displacements (e.g. from GPS sensors and/or InSAR) within the inversion has not yet been produced to our knowledge.

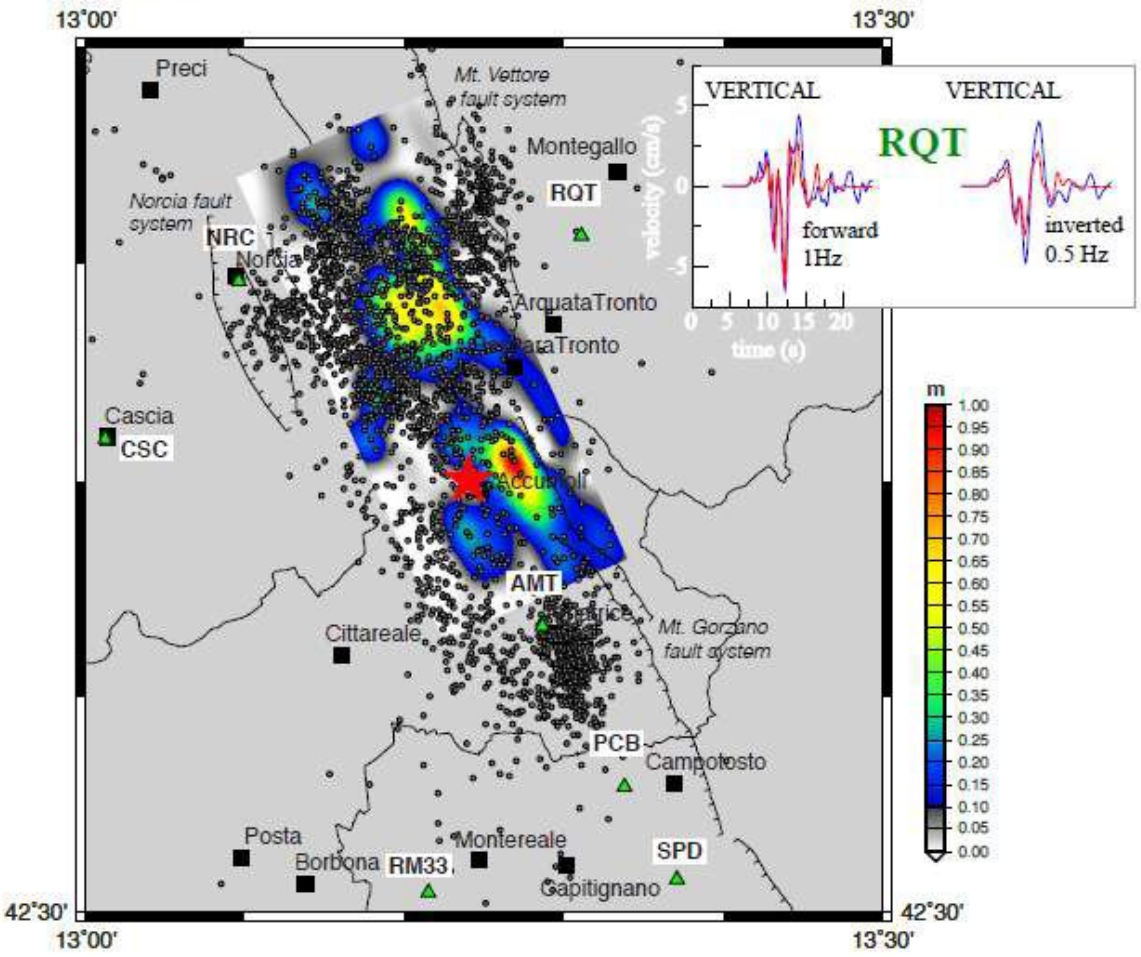

Figure 2.17. Single-plane finite fault model proposed by Tinti et al. (2016), along with slip distribution, recording station locations, 24 August 2016 mainshock and aftershocks.

The attributes of the trimmed finite fault model used for distance and related calculation are summarized in Table 2.2

Table 2.2. Attributes of the trimmed finite fault model.

Attribute	Value
Upper-left corner1	Coordinates: 13.2084E, 42.8321N; depth: 5km
Strike (deg)	156
Along strike length (km)	17
Dip (deg)	50
Downdip width (km)	6.5

[1] Defined as given by Aki and Richards (2002); location is based on perspective of observer looking towards footwall from hanging wall.

2.4 Surface Rupture on Mt. Vettore Fault

The surface expression of the Mt Vettore fault is clearly visible on the southern ridge and Western flank of Mt. Vettore. In this southern and western part of Mt Vettore, the fault trends approximately 330°, and then trends nearly northward on the north side of the mountain. The 24 August 2016 earthquake rupture resulted in clearly observable normal-mechanism displacements on the southern and western slopes. These visible movements represent a fraction of the total overall length of fault surfaces experiencing high slip (17 km), as identified in the previous section. Galadini and Galli (2003) mapped a complex zone of three normal fault splays on the western slope of Mt. Vettore. Two western normal-faults are lower in elevation, one skirting the basin edge of Piano Grande (the basin of the Castelluccio plane), and the other being between the base of the ridge and the upper (eastern) fault. The eastern upper normal fault runs along the southern and western upper flank of a subsidiary peak of Mt. Vettore called Mt. Redentore. This fault trace is clearly visible from the Castelluccio plane. A study by Pierantoni et al. (2013) mapped potentially three faults in this zone, with an oblique normal fault between the western basin-edge fault and eastern upper slope fault.

Figure 2.18 shows the locations of the three faults as described above, along with locations (and amounts) of measured displacements (EMERGEO, 2016). The displacement amounts ranged from null to approximately 35 cm in both the down-dip direction and in horizontal opening of cracks. These displacements were measured by INGV staff.

The GEER team also gathered data on coseismic surface faulting of the Mt. Vettore fault by walking the trace of the fault from the road crossing at SP477 (43.797151N, 13.266943E) over the southern ridge and onto the western flank. Poor weather in rain, wind, and fog prevented a thorough survey of the fault trace by the US team members, but a detailed study was accomplished by INGV geologists and GEER team members Emanuela Falcucci and Stefano Gori, who produced much of the data shown in Figure 2.18.

We report the measurements from the partial survey of September 6. The observed normal down-to-the-west displacements recorded at ten sites affect colluvium and soil near to or adjacent to the bedrock fault plane. We walked the first 1.5 km of the fault rupture above the road until we entered a dense fog bank and turned around. The overall range of displacement measurements was from 0 to 25 cm with an average of 12 cm. These numbers are consistent with longer surveys by the INQUA and INGV teams. Where the fault plane was observed, the average measured strike was 158° with values ranging from 146° to 174°. The average fault dip was 46°, with a range of 36° to 62°. The measurement of 36° was potentially from an out of place block associated with the fault but detached. If we reject that value, then the average dip slope would be 51.5°.

Detailed measurements for the fault trace were recorded on the smartphone app 'Theodolite' and are presented in order of site below in Figures 2.19. Each subsequent site is higher in elevation, and the latitude, longitude, picture orientation, elevation, and fault offset are annotated on the picture.

The characteristics of the surface rupture, the overall subsurface rupture, and the earthquake magnitude indicate that the 24 August 2016 event fit within the normal bounds of predicted earthquake behavior with somewhat negative residuals with respect to the mean response predicted by Wells and Coppersmith, 1994 (WC94, hereafter).

The first comparison of the Italian earthquake data with WC94 is a plot of the ratio of the average surface to maximum surface displacement versus magnitude. WC94 data (WC94, Figure 5) has considerable scatter and indicate a weak correlation between magnitude and the surface rupture ratio. Nevertheless, the Italian earthquake data plots below the center of the cluster ratio values and lies on the low magnitude side of the cluster, consistent with the data from other similar earthquakes (Figure 2.20).

Comparisons between the average and maximum displacements plotted against magnitude (Figures 2.21 and 2.22) show that the maximum displacement data are somewhat lower than the mean regression line predicted by WC94, falling approximately on the lower bound of the 95% confidence limits. Average displacement data, for the 24 August 2016 event, are near the mean line for normal fault mechanism.

Another interesting result is the relationship between magnitude and surface fault rupture length in Figure 2.23. The 24 August 2016 event surface fault rupture length is higher than that predicted by WC94 for **M**6.1. The corresponding relationship for subsurface rupture length is shown in Figure 2.24 and shows the data as being near the mean line.

In summary, the surface rupture of the Mt. Vettore fault extended for nearly 5 km, had a maximum slip of 35 cm an average slip of about 12 cm. The measured slip characteristics are typical, if somewhat below the mean, for a **M** 6.1 event, as provided by WC94. The rupture length characteristics are also consistent with expectation. .

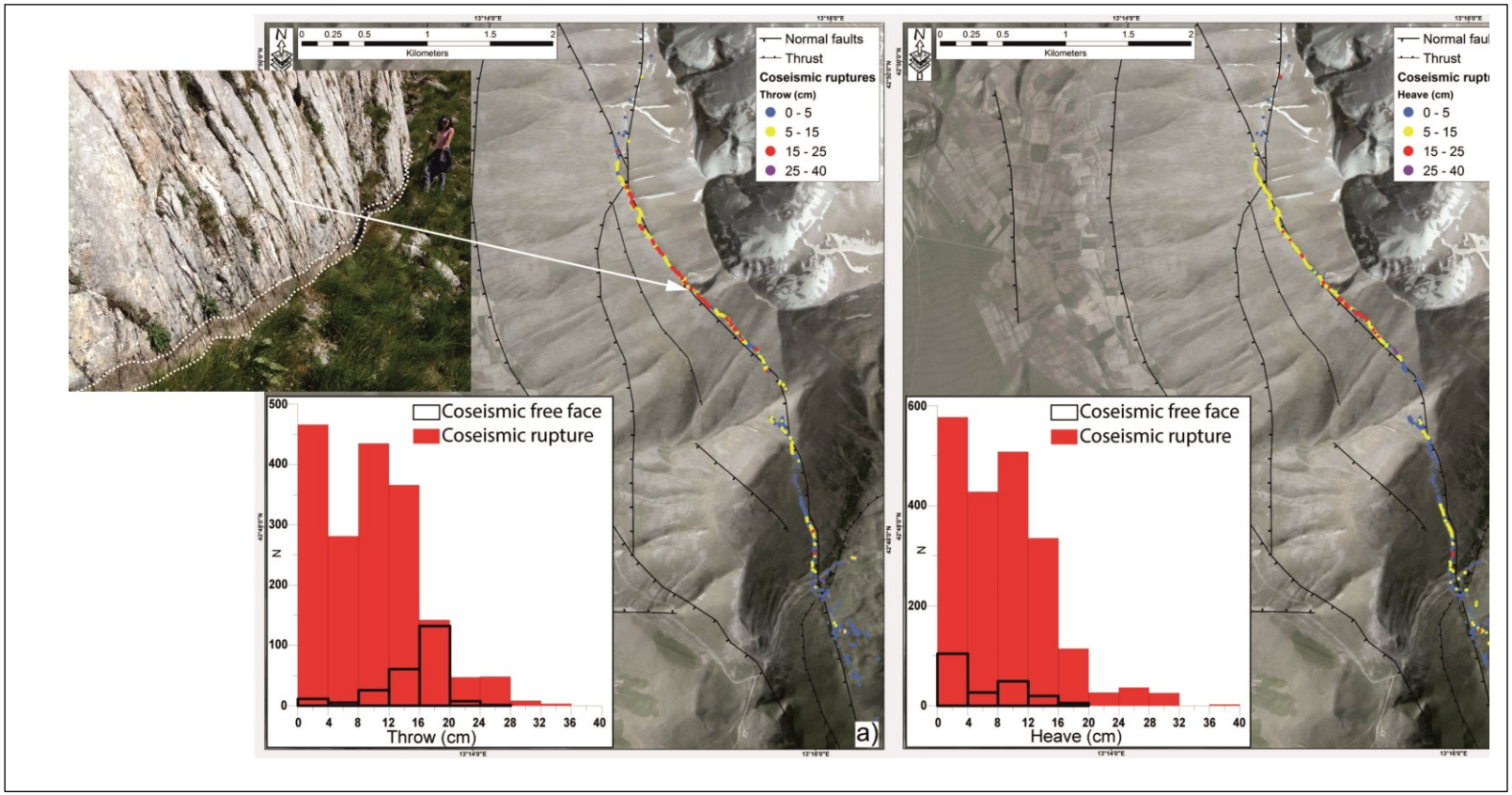

Figure 2.18. Relief map showing amounts of displacement down-dip and horizontally (from crack opening), and histograms of measured displacements (EMERGEO, 2016) along the Mt. Vettore fault splays. Free-face at the base of the fault plane, white dotted lines in inset.

Figure 2.19a. The Mt. Vettore Fault as seen from the south near SP477 during our initial visit to the site on September 5 guided by Dr. Fabrizio Galadini.

Figure 2.19b. Mt. Vettore fault: Damaged asphalt on SP477 at the fault crossing with less than 10cm of normal displacement down toward the west. Displacement are masked by bridging of the asphalt surface (Latitude and Longitude are annotated on the image).

Figure 2.19c. Mt. Vettore fault Site 1 at a WGS84 ellipsoid elevation of 1502 m. The normal fault displacement at this site was 10 cm down toward the west (Latitude and Longitude are annotated on the image).

Figure 2.19d. t. Vettore fault Site 2 at a WGS84 ellipsoid elevation of 1507m. The normal fault displacement at this site was 8 cm down toward the west (Latitude and Longitude are annotated on the image).

Figure 2.19e. Mt. Vettore fault Site 3 at a WGS84 ellipsoid elevation of 1518 m. The normal fault displacement at this site was 5 cm down toward the west (Latitude and Longitude are annotated on the image).

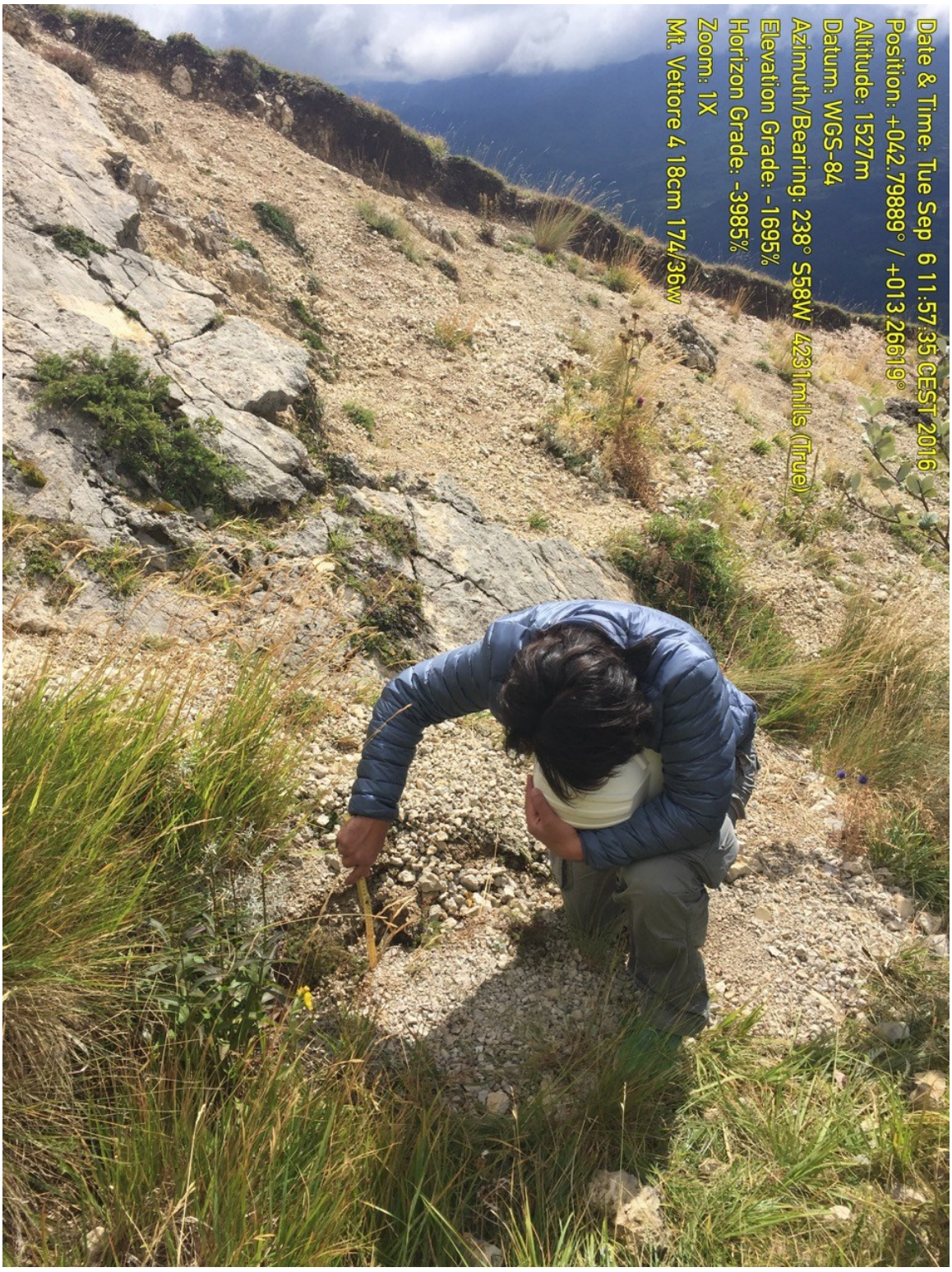

Figure 2.19f. Mt. Vettore fault Site 4 at a WGS84 ellipsoid elevation of 1527 m. The normal fault displacement at this site was 18 cm down toward the west, with a strike was 174° and dip of 36°west (Latitude and Longitude are annotated on the image).

Figure 2.19g. Mt. Vettore fault Site 5 at a WGS84 ellipsoid elevation of 1561 m. The normal fault displacement at this site was 3 cm down toward the west (Latitude and Longitude are annotated on the image).

Figure 2.19h. Mt. Vettore fault Site 6 at a WGS84 ellipsoid elevation of 1527 m. The normal fault displacement at this site was 22 cm down toward the west (Latitude and Longitude are annotated on the image).

Figure 2.19i. Mt. Vettore fault Site 7 at a WGS84 ellipsoid elevation of 1594 m. The normal fault displacement at this site was 25 cm down toward the west. (Latitude and Longitude are annotated on the image).

Figure 2.19j. Mt. Vettore fault Site 7 at a WGS84 ellipsoid elevation of 1527 m. The normal fault displacement at this site was 25 cm down toward the west. The strike of the bedrock fault was 146°, dipping 62° (Latitude and Longitude are annotated on the image).

Figure 2.19k. Mt. Vettore fault Site 8 at a WGS84 ellipsoid elevation of 1628 m. The normal fault displacement at this site was 9 cm down toward the west (Latitude and Longitude are annotated on the image).

Figure 2.19l. Mt. Vettore fault Site 9 at a WGS84 ellipsoid elevation of 1643 m. The normal fault displacement at this site was 18 cm down toward the west (Latitude and Longitude are annotated on the image).

Figure 2.19m. Mt. Vettore fault Site 10 at a WGS84 ellipsoid elevation of 1643m.ch2. The normal fault displacement at this site was 13 cm down toward the west (Latitude and Longitude are annotated on the image).

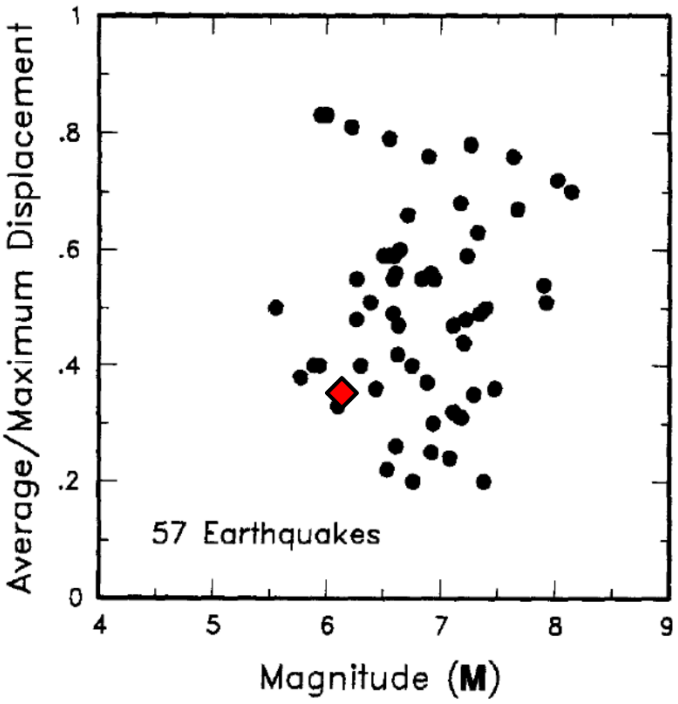

Figure 2.20. The ratio of average to maximum displacement plotted against magnitude for the 24 Aug 2016 **M**6.1 event presented on the data set of WC94.

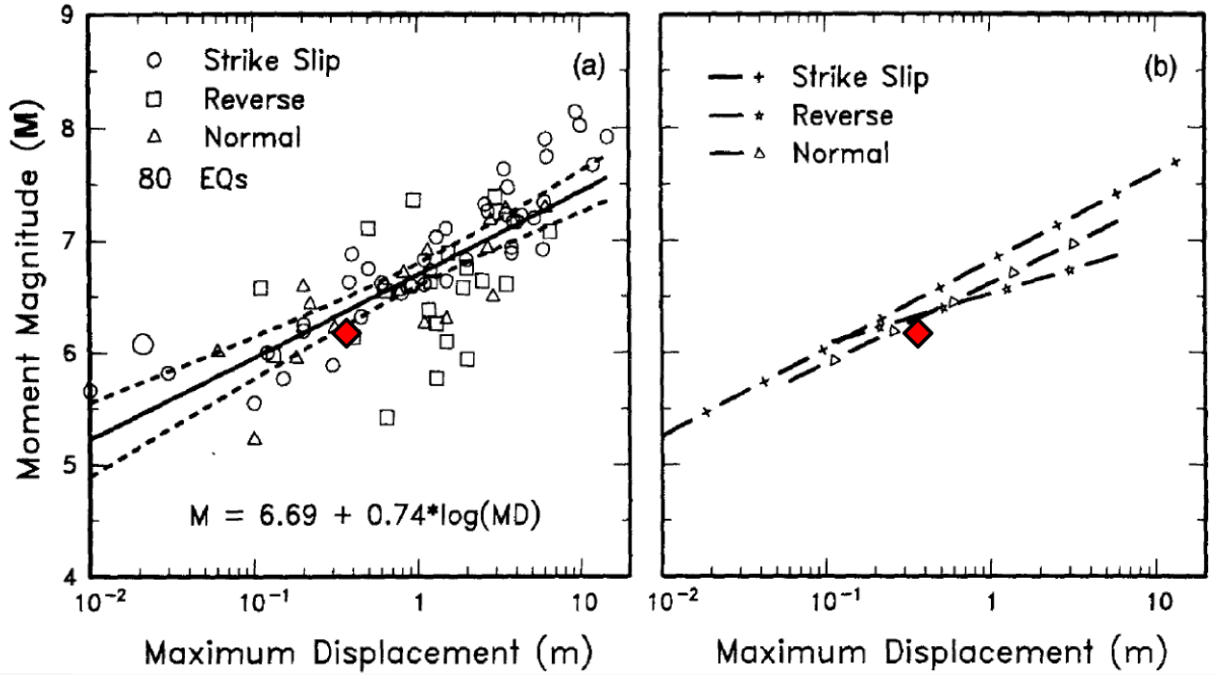

Figure 2.21. The maximum surface fault displacement magnitude for the 24 Aug 2016 **M**6.1 event relative to the data set and regression fit from WC94

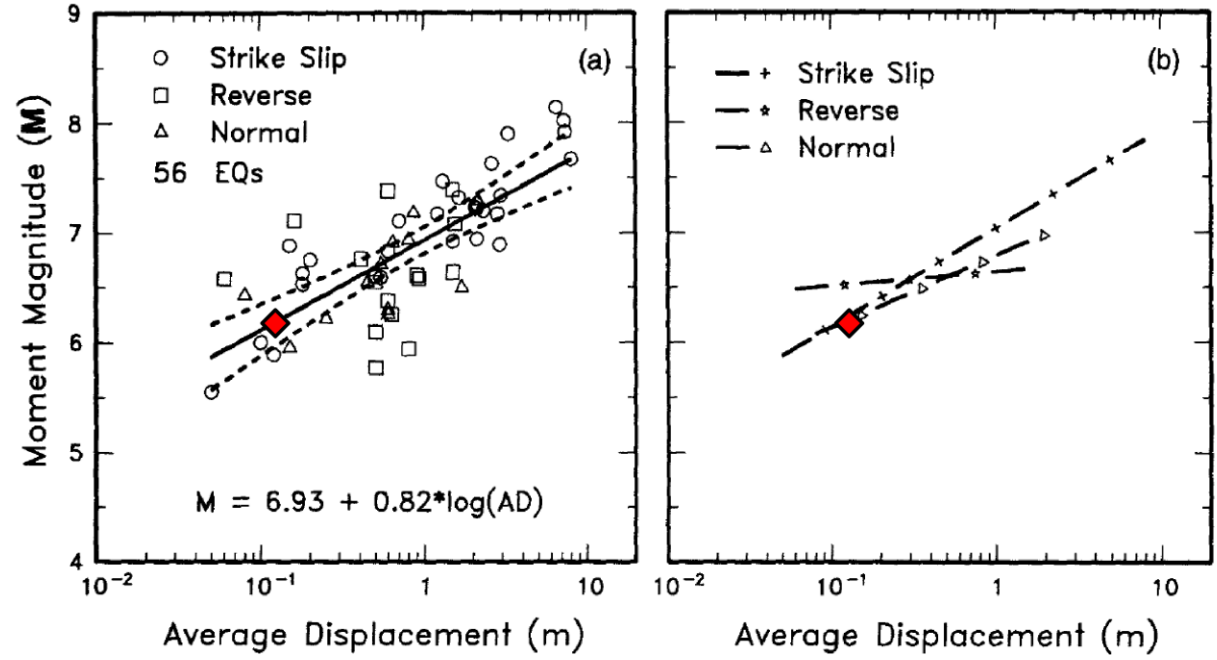

Figure 2.22. The average surface fault displacement magnitude for the 24 Aug 2016 **M**6.1 event relative to the data set and regression fit from WC94

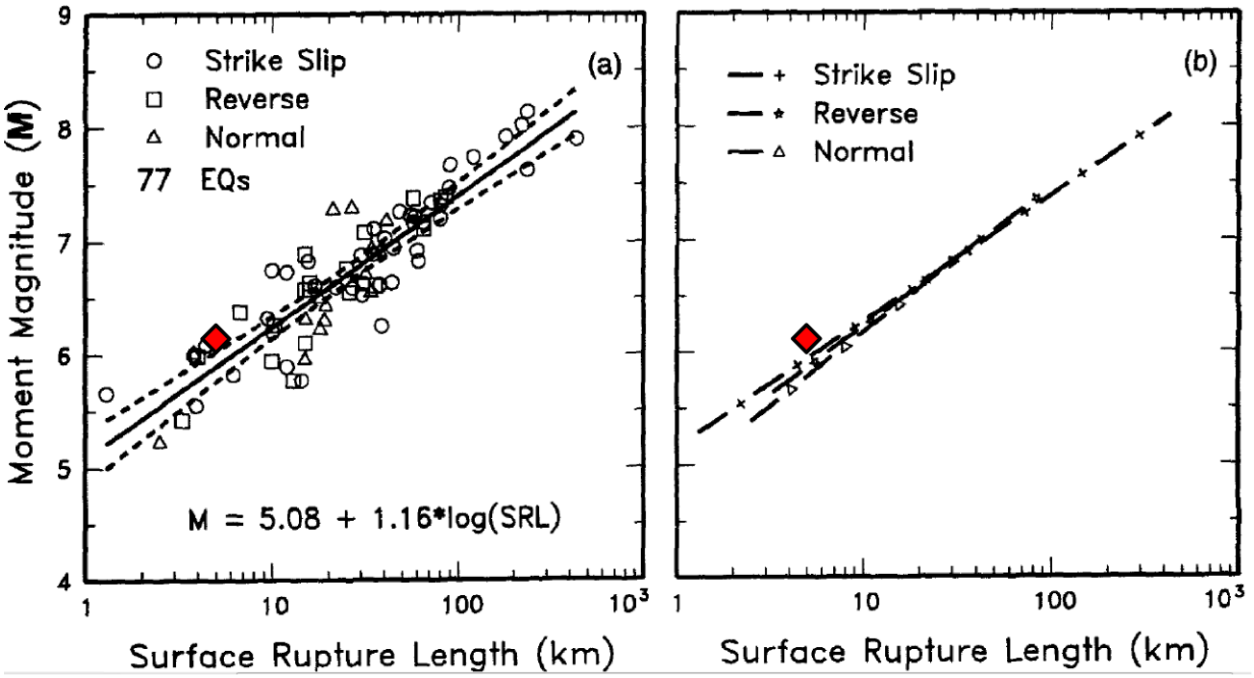

Figure 2.23. The surface fault rupture length plotted vs magnitude for the 24 Aug 2016 **M**6.1 event relative to the data set and regression fit from WC94.

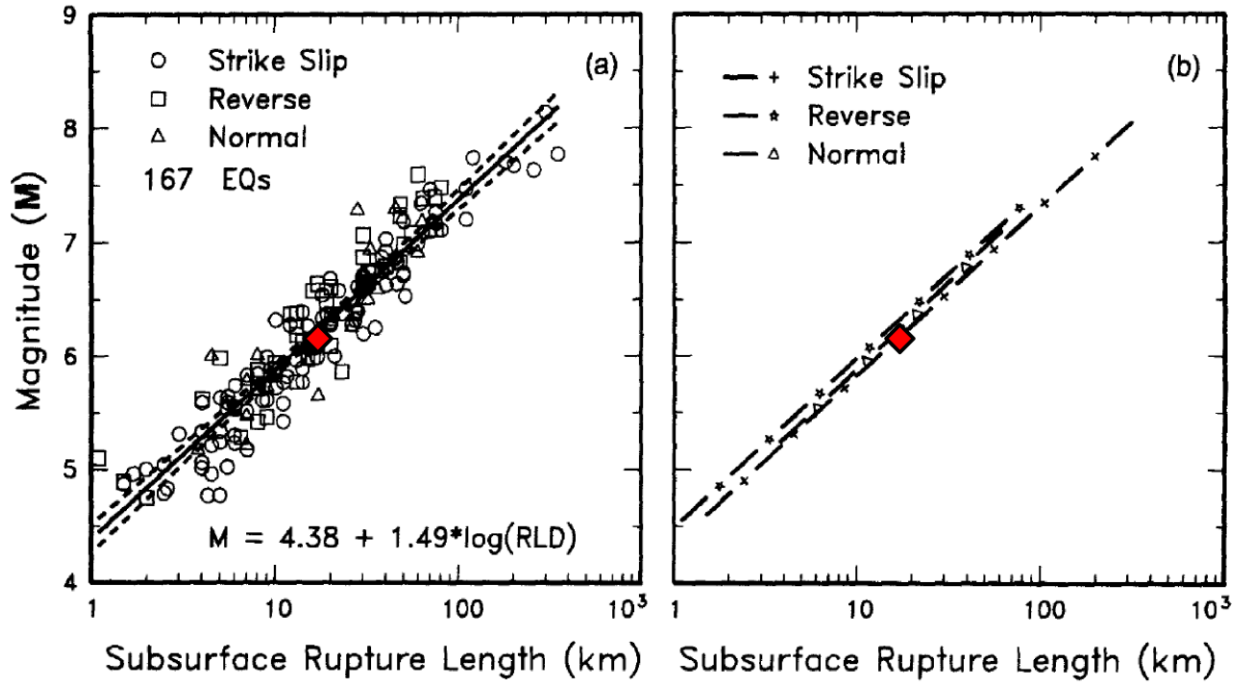

Figure 2.24. The subsurface (overall) rupture length plotted vs magnitude for the 24 Aug 2016 **M**6.1 event relative to the data set and regression fit from WC94.

3.0 Ground Motions

Principal authors: Giuseppe Scasserra, Paolo Zimmaro, Tadahiro Kishida, Jonathan P. Stewart

Contributing authors: Massimina Castiglia, Tony Fierro, Luciano Mignelli, Filippo Santucci de Magistris, Giuseppe Tropeano

3.1 Available Recordings and Site Conditions

According to the ESM database (ESM working group, 2015; http://esm.mi.ingv.it, last accessed October 14, 2016), the mainshock of the 24 August 2016 M6.1 Central Italy earthquake and the two main aftershocks (M5.3 and M4.8; Section 2.3) were recorded by 249, 185 and 145 strong-motion instruments, respectively. Some accelerograms are still flagged as "bad quality" or "restricted" in the latest version of the published database. As a result, fewer recordings are actually available for ground motion characterization purposes.

The ground motion data set considered in this report was downloaded during the first week of September, in order to provide timely input to the field reconnaissance team regarding ground motions. We recognize that subsequent releases of the online ESM database might contain additional usable data. Thus, we anticipate that further refinement of our dataset will be performed subsequently. The selected dataset contains recordings from 205 stations. Each of these stations has recorded at least one of the three considered events. Stations recording all three events number 189. About 60% of the instruments are part of the Italian Accelerometric Network (Rete Accelerometrica Nazionale, RAN; ran.protezionecivile.it/, last accessed 21 November, 2016), owned by the Italian Civil Protection Department (Dipartimento della Protezione Civile, DPC), while almost 37% are part of the Italian National Seismic Network (Rete Sismica Nazionale, RSN; www.gm.ingv.it/index.php/rete-sismica-nazionale/, last accessed 21 November, 2016) owned by the Italian Institute of Geophysics and Vulcanology (Istituto Nazionale di Geofisica e Vulcanologia, INGV). Remaining stations are owned and operated by the following other public institutions: (1) University of Basilicata (UNIBAS network), (2) MedNet Data Center (MNDC, Mediterranean Very Broadband Seismographic Network), (3) National Institute of Oceanography and Experimental Geophysics (Istituto Nazionale di Oceanografia e Geofisica Sperimentale, OGS – North-East Italy Seismic Network), and (4) AlpArray initiative.

Figure 3.1a shows the locations of the cited instruments, while Figure 3.1b shows a close-up view of stations in the epicentral area. Table S1 (available in the electronic supplement to this report) provides metadata for the 205 stations related to site condition and instrument housing. Table S2, shows attributes of the 452 three-component recordings (two horizontal and one vertical) used in this study. All instruments of the dataset are digital. RAN comprises stations located inside the former Italian National Electric Company (Ente nazionale per l'Energia elettrica, ENEL) transformer cabins, generally equipped with Syscom MS2007 instruments (Table S1/Housing: Structure related Free-field) and free-field stations mostly equipped with Kinemetrics sensors (Etna, K2, Makalu, FBA23 or Episensor). General characteristics of the

instruments are: 3-channel sensors, a full scale range of 1g/2g, and 18-24 bit resolution. The instruments of INGV (RSN) are generally Kinemetrics Episensor FBA-ES-T; the unit consists of three Episensor force balance accelerometer modules mounted orthogonally in one small package, with full-scale recording ranges of ± 1g to ± 2g (ESM working group, 2015).

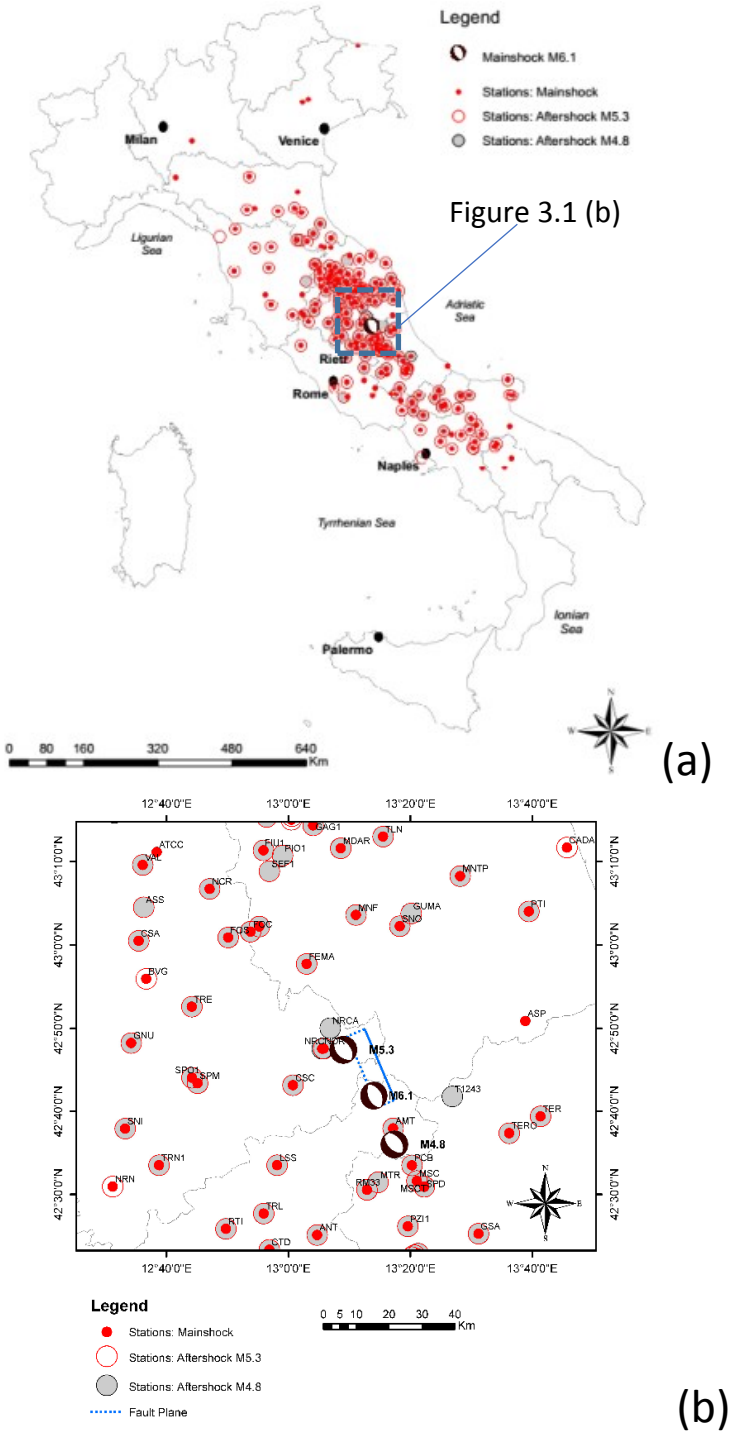

Figure 3.1. (a) Locations of instruments that recorded M6.1, M5.3 and M4.8 Aug 2016 events; (b) detail view of instruments in the epicentral area and which events they recorded.

The GEER team inspected two recording station sites: (1) AMT in the town of Amatrice (Figure 3.2a; Lat: 42.632460 – Long: 13.286176), and (2) NRC in the town of Norcia (Figure 3.2b; Lat: 42.792543 – Long: 13.096475). Both stations are part of the RAN network, owned and operated by the Italian department of civil protection. AMT is a free-field station with a digital sensor protected by a fiberglass box, while the accelerometers at NRT are installed inside an ENEL electric transformer cabin. The AMT and NRC stations recorded the highest acceleration values during the M6.1 mainshock (0.43g and 0.36g, respectively) but the level of damage in Amatrice and Norcia was quite different as discussed in Chapter 5. As shown in Figure 3.2, we did not find ground failure features or earthquake-induced damage traces at these locations.

(a) (b)

Figure 3.2. (a) AMT station; (b) NRC station.

Table S1 lists attributes of the 205 digital accelerometer stations, including location, surface geology, V_{S30} and instrument housing type. For many stations, descriptions of the surface geology are available from station monographies available on the ESM website (ESM working group, 2015). This information is typically based on small-scale maps (1:100.000).

We identify surface geology using local, larger-scale maps (from 1:10.000 to 1:25.000 scale) when available, as for Umbria, Lazio, Marche, Toscana and Emilia regions. In other cases, we used available documentation from ad-hoc site-specific microzonation studies or technical papers (i.e: for Molise region). Site-specific information sources are listed in Table S1. Once this information had been compiled, the evaluation of the VS30 was then performed using the following protocols (Scasserra et al. 2009):

- Data Source Type A: On-site measurements of velocity using established geophysical techniques (downhole, cross-hole, surface wave methods, etc.). Table S1 lists 33 such stations with measured data taken from ESM website

station monographies (ESM working group, 2015). We anticipate additional stations will be characterized in the future, including an activity in this regard by T. Pelekis of the GEER team (results not yet available).

- Type B: Velocity measurements available at nearby sites having the same surface geology as the subject station. Table S1 lists 7 such stations.
- Type C: Velocity estimated based on general correlation relationships between mean shear wave velocity and surface geology (149 stations).
- Type D: VS30 estimated as the average value of the subsoil category indicated in the ESM database following the Italian Code NTC08. For categories A (V_{S30} > 800 m/s), B (360 m/s <V_{S30} < 800 m/s) and C (180 m/s < V_{S30} < 360 m/s), we take V_{S30} as 800, 540 and 270 m/s, respectively. This method is used for 16 stations without geophysical data or surface geologic descriptions.

Table S1 shows data source type (A–D), local geology as inferred from the smallest-scale map currently available, closest-related geologic category of Scasserra et al. (2009), and the corresponding V_{S30} value (as measured or estimated, depending on the data source type).

For Type C, Scasserra et al. (2009) developed relationships between surface geology and V_{S30} for a number of surface geologic categories relevant to the subject regions: Quaternary alluvium categories segregated by sediment depth and material texture (Qal,thin; Qal,deep; Qal,coarse), older Quaternary alluvium (Qoa), Quaternary to Tertiary alluvial deposits (QT), Tertiary sandstone formations (Tss), Pleistocene to Pliocene conglomerate (Pc), and Mesozoic limestone and volcanic rocks (Ml and Mv, respectively). For the Quaternary categories, Scasserra et al. (2009) confirmed the applicability of the relations proposed by Wills and Clahan (2006), whereas for the older bedrock units, new correlation relationships were developed. Figure 3.3 shows data source type for each of the 205 digital stations that produced recordings.

Temporary instruments were deployed after the August 24 main event (INGV working group, 2016). Table 3.1 shows agency/agencies managing the stations, numbers of instruments, and deployment start dates. All of the instruments in Table 2.1 had been deployed as of 2 October 2016 and remain so as of this writing (November 2016). The stations installed under the Center for Seismic Microzonation (CentroMS) project (last four rows of Table 3.1, also shown in Figure 3.4) are managed as follows:

- 23 INGV stations: mostly Reftek-130 24bit, accelerometer Kinemetrics Episensor and velocimeter Le5s;
- 4 CNR stations: Reftek 130 S+5s;
- 10 OGS stations: Reftek130 or Titanxt, Episensor or TXT-3, LE-3Dlite.

3.2 Data Processing

3.2.1 PEER Procedure

In the ESM database, both raw unprocessed, and processed accelerograms are available. We downloaded raw unprocessed ground motion data, which was then processed using standard Pacific Earthquake Engineering Research (PEER) center procedures (Ancheta et al., 2014). For modern digital records such as those from this earthquake sequence, NGA processing consists of applying high-pass acausal Butterworth filters in the frequency domain. Corner frequencies are selected on a component-specific basis by visual inspecting the Fourier amplitude spectra and then testing the influence of alternate corner frequencies on displacement time series. The lowest corner frequency producing displacement time series having reasonable appearance is selected. Baseline correction is also used, in combination with the filter, when filtering alone does not remove non-physical trends in the displacement time series.

3.2.2 Data Quality Issues

Two potentially important recording stations in the near-field did not record properly. The NRCA station, located in the town of Norcia, did not record the mainshock nor the **M**5.3 aftershock**.** This results from a sudden power outage during the earthquake and lack of auxiliary power. NRCA recorded the **M**4.8 aftershock. The RQT station, in Arquata del Tronto, recorded all three events. One of the components (NS) appears to be unusable (signal is essentially zero). RQT is of special interest because it is the only instrument located on the footwall in the near-field area.

Table 3.1. Summary of the temporary stations deployed in the epicentral area after 24 August 2016.

Agency	# Instruments	Deployment start date	Reference	Notes
Italian DPC	10	24-26 August	INGV (2016)	
SISMIKO (INGV)	18	24-28 August	SISMIKO (2016); Moretti et al. (2016)	
EMERSITO (INGV)	22	26-31 August	EMERSITO (2016)	
British Geological Survey	24	-	BGS Seismology1	
Center for Seismic Microzonation	9	-	CentroMS2	EMERSITO stations moved to Amatrice
Center for Seismic Microzonation	14	-	CentroMS2	
Consiglio Nazionale per le Ricerche (CNR)	4	19-27 September	CentroMS2	
OGS	10	29 September-2 October	CentroMS2	

[1] URL: https://mobile.twitter.com/BGSseismology/status/773991277989863424, last accessed, 21 November, 2016

[2] URL: https://www.centromicrozonazionesismica.it, last accessed 21 November, 2016

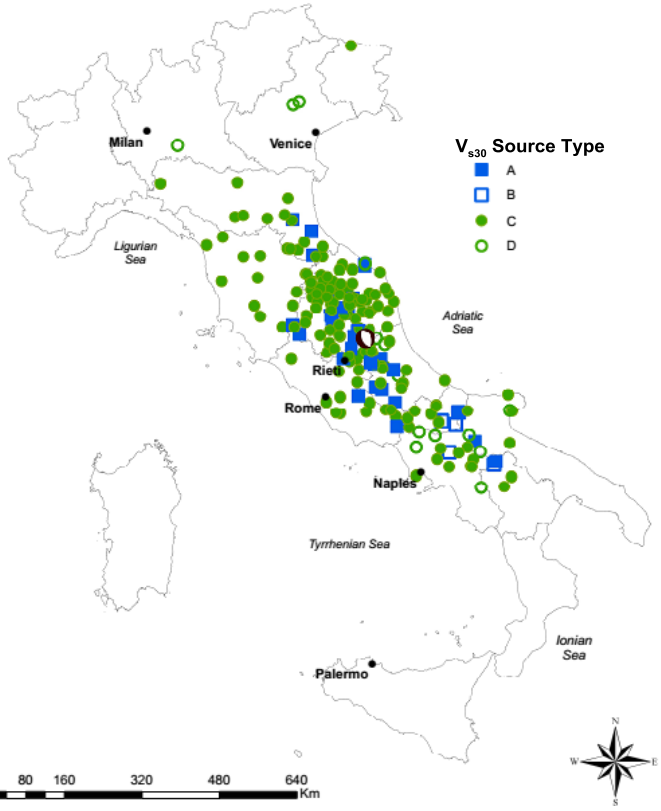

Figure 3.3: Location of consdiered stations distinguished by data source used for V_{S30} estimations

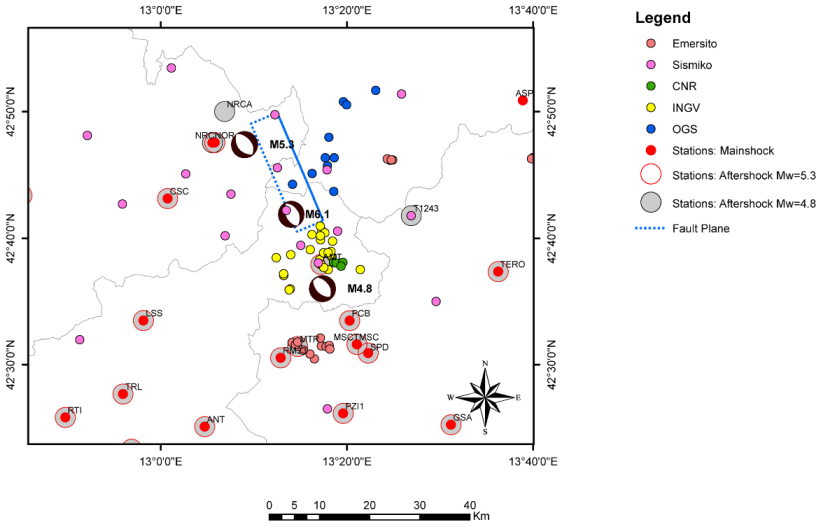

Figure 3.4. Locations of temporary stations installed after the 24 August 2016 event.

3.3 Near Source Ground Motions

Figure 3.5 shows 5% damped pseudo-acceleration response spectra (PSA) from three stations in close proximity to the mainshock rupture plane (AMT, NRC and NOR). The corrected ground motions have been rotated into fault normal (FN) and fault parallel (FP) orientations. The AMT

ground motion shows evidence of polarization in the FN direction at short oscillator periods (< 1.0 sec), while the NRC and NOR motions show higher amplitudes in the FN direction at long periods (> 1.0 sec).

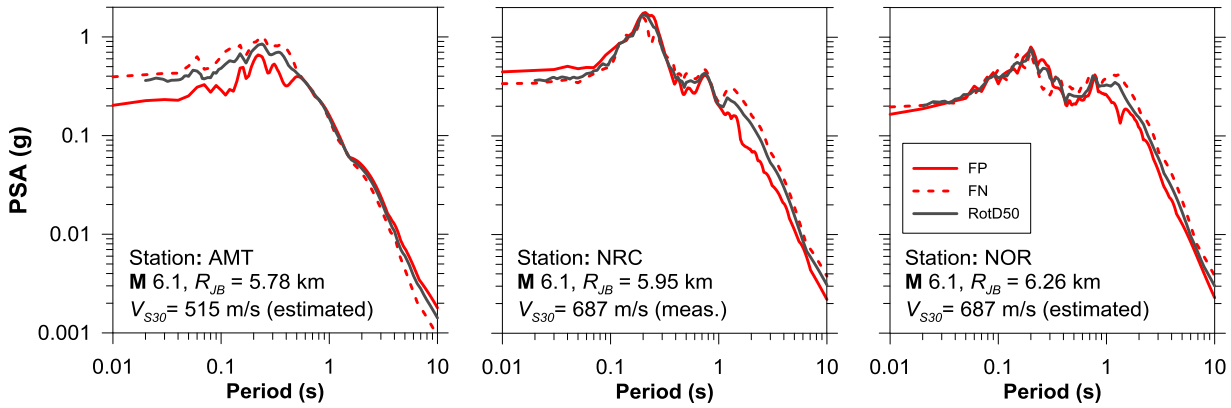

Figure 3.5. Mainshock pseudo acceleration response spectra (5% damping) for Amatrice (AMT) and Norcia (NRC, NOR) sites from the M6.1 mainshock.

Given the location of the hypocenter with respect to the fault plane, rupture directivity effects from this event would be expected in the area east (particularly north-east) of the finite fault model. This region has no recordings other than RQT, the data from which has not yet been considered. Stations AMT, NRC, and NOR are in backward or neutral directivity regions. As a result, we do not expect polarization of the ground motion in the fault-normal direction nor the presence of appreciable pulse-like characteristics. The spectra in Figure 3.5 demonstrate a lack of FN polarization, consistent with expectation. Pulse-like characteristics were checked for the NRC and NOR records using the Baker (2007) pulse identification procedure, as shown in Figure 3.6. Our interpretation is that the pulse effects are weak, which is consistent with expectation.

Earthquake-related static ground displacements, resulting from fault rupture (typically referred to as fling-step effects) can be present in near-source recordings, especially on the hanging wall. We have no recordings on the hanging wall of the trimmed fault model (Figure 2.11), but the NRC stations is close. Nonetheless, the AMT, NRC, and NOR recordings have been reprocessed using a procedure developed to preserve static (permanent or tectonic) displacements (Gregor et al., 2002). Figure 3.7 shows the vertical component of the AMT station recording, for which a small (3 cm) static displacement is identified. The other two components of this recording, and all the components of the NRC and NOR recordings, show static displacements that were judged not to be significant (R. Darragh, 2016; personal communication). This lack of fling-step is consistent with expectation. In contrast, the 2009 L'Aquila earthquake had several hanging wall records and much larger static displacements (Stewart et al. 2012).

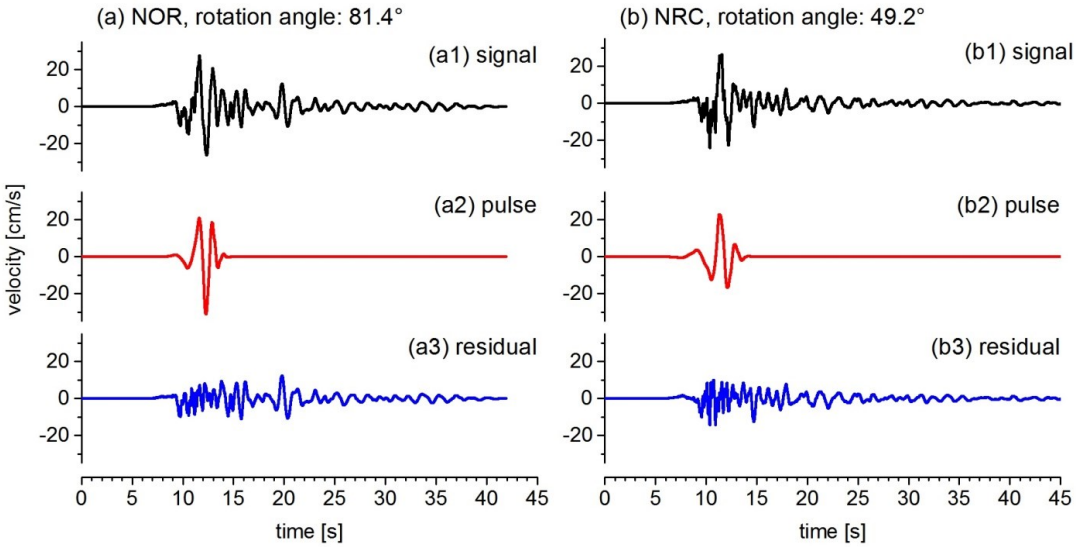

Figure 3.6. Original ground motion, extracted pulse, and residual ground motion for main shock recorded at the NOR (a) and NRC (b) stations.

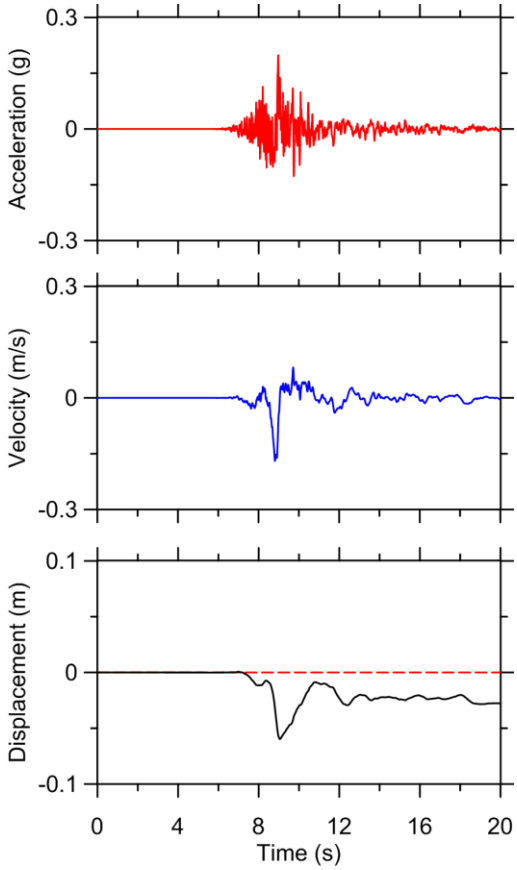

Figure 3.7. Vertical component of acceleration, velocity, and displacement time-series recorded at the AMT stations, processed using the Gregor et al. (2002) procedure.

3.4 Comparison to Ground Motion Models

Ground motion models (GMMs) are used for prediction of the expected level of shaking conditional on magnitude, source-to-site distance, and site condition. In this section, we compare GMM predictions to observed data. The aim of the comparison is to provide a means by which to assess main features of the recorded data (e.g. attenuation with distance, near-source ground motions), rather than attempt to validate predictive models against data.

In recent years, many studies focused on the selection of suitable GMMs to use in global (Stewart et al., 2015), regional (Delavaud et al, 2012), or site specific applications in Italy (Zimmaro and Stewart, 2015). While local models can reflect local geologic and tectonic conditions, which may differ from those represented by global models, the limited database size used to develop local models may be inadequate to constrain GMMs for conditions often critical for application (large magnitudes and small distances). Global models are more effective for such conditions, because they are typically based on much larger databases, but may contain bias with respect to local effects.

One approach to reduce the bias of global models is to introduce regional adjustment factors, as in the NGA West-2 project (Bozorgnia et al., 2014). Those factors relate to anelastic attenuation and/or site effects, applicable to California, Turkey, Taiwan, Japan and Italy.

Here we compare recorded data with the following GMMs: (1) an Italy-specific model by Bindi et al. (2011; hereafter B11), (2) the average of four NGA West-2 GMMs, without regional adjustments (Abrahamson et al., 2014; Boore et al., 2014; Campbell and Bozorgnia, 2014; and Chiou and Youngs, 2014; hereafter NGA2), and (3) the average of three NGA West-2 models containing regional adjustments applicable to Italy (Boore et al., 2014; Campbell and Bozorgnia, 2014; and Chiou and Youngs, 2014; hereafter NGA2-I).

The selected GMMs, use different distance metrics. The B11 and Boore et al. (2014) models use closest distance to the horizontal projection of the rupture plane, or Joyner and Boore distance (R_{JB}). The Abrahamson et al. (2014), Campbell and Bozorgnia (2014), and Chiou and Youngs (2014) models use the closest distance to the rupture plane (R_{RUP}) as the primary distance metric. Figure 3.8 illustrates the various distance metrics for a dipping fault. We calculate distances R_{JB} and R_{RUP} using the trimmed finite-fault model described in Section 2.3.

Figure 3.9 shows the distance-dependence of RotD50 horizontal peak horizontal acceleration (PHA) and peak horizontal velocity (PHV) for all three events. Recorded data are divided into three categories: (1) rock ($V_{S30}\geq$800 m/s), (2) stiff soil (360$\leq V_{S30}<$800 m/s), and (3) soft soil ($V_{S30}<$360 m/s). Also shown in Figure 3.9 are median predictions from the B11 model, the average of the four NGA2 models, and the average of the NGA2-I models. The model predictions have been calculated using a constant V_{S30}=580 m/s. This V_{S30} value falls into subsoil class B of the Italian building code (Norme Tecniche per le Costruzioni, 2008; NTC08) and is considered to be a typical value for the region.

While Figure 3.9 shows that all models fit the data reasonably well, the relatively fast attenuation of the mainshock data beyond R_{JB}=100 km is only captured by the NGA2-I models (with regional adjustment for Italy). This feature is characteristic of Italian data, and it has been observed in previous studies (e.g., Scasserra et al., 2009). These fast attenuation features are observed in the aftershock data as well, although none of the considered models appear to be unbiased for aftershock data beyond about 80-100 km. At short distances (i.e. 1-10 km), data are sparse, but there are differences between models. In particular, B11 has a wider flat-attenuation region at close distance, likely due to a larger 'fictitious depth term' in the function.

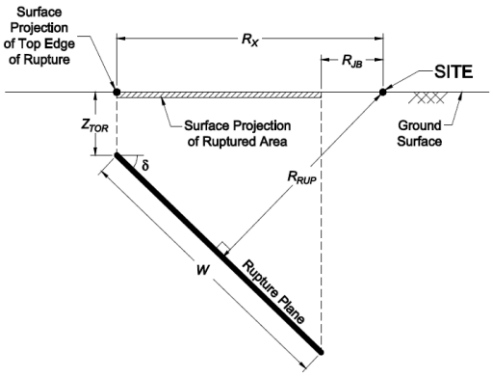

Figure3.8. Scheme of an earthquake source and distance measures using a vertical cross-section through a fault rupture plane (from Kaklamanos et al., 2011).

To more accurately evaluate the performance of multiple GMMs relative to the data, we calculate residuals for each data point considering the appropriate source-to-site distance and site condition as follows:

$$R_i = \ln(IM_i)_{rec} - \ln(IM_i)_{GMM} \quad (1)$$

where $(IM_i)_{rec}$ is the value of ground motion intensity measure from recording *i* and $(IM_i)_{GMM}$ is the value of that same IM from ground motion models. For the NGA West-2 models, $(IM_i)_{GMM}$ corresponds to the average of all four GMMs (*NGA2*) or to the average of the three with regional adjustment (*NGA2-I*), while for B11, the median prediction is used.

We show residuals for two intensity measures: (1) PHA (Figure 3.10), and (2) PHV (Figure 3.11), for the **M**6.1 mainshock and the **M**5.3 and **M**4.8 aftershocks. All data are compared in each plot with binned means of the residuals, along with their standard deviations, using five intervals for each log-cycle (due to paucity of data, a unique bin is assumed for R_{JB} between 0-10 km).

The results for PHA in Figure 3.10 suggest good consistency between the models and mainshock data for distances up to 100 km, while only the NGA2-I models provide nearly flat residuals trends at greater distances. The non-zero residuals of B11 for large distances may result from sparse data (especially from old events) for distances greater than 100 km in their data set.

The mean misfit of the models relative to the data is similar to an event term as evaluated from mixed effects analysis. Figure 3.12 shows these approximate period-dependent event terms (mean residual for each event and IM) for the three considered earthquake events. Also shown

are plus/minus one between-event standard deviations from the Boore et al. (2014) GMM. For short periods (PGA to 0.5s), the Central Italy event terms are negative, whereas they are nearly zero for greater periods. This trend is consistent with what was observed for the 2009 L'Aquila event ground motions (Stewart et al., 2012).

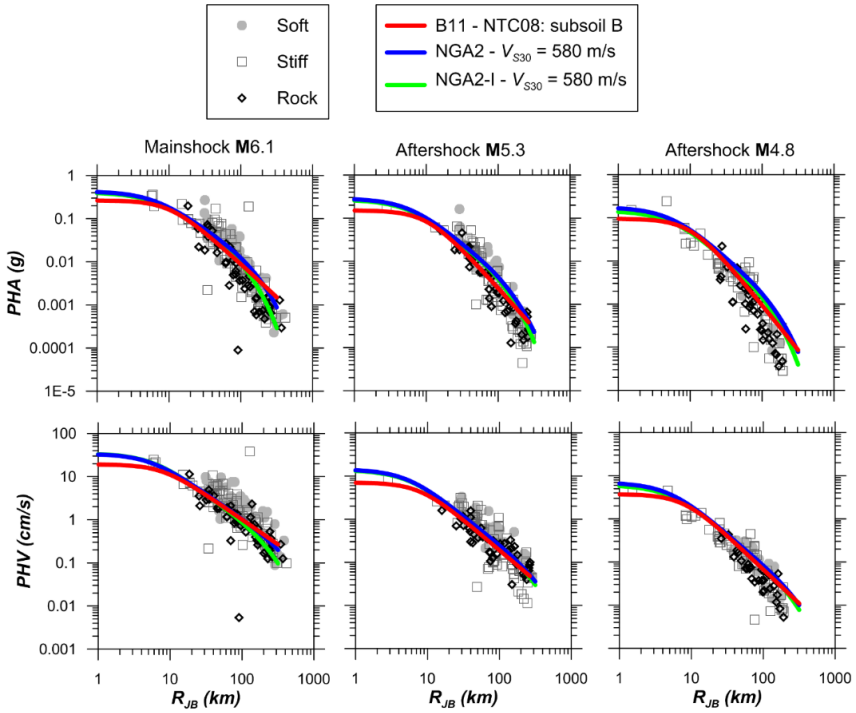

Figure 3.9. Variation of PHA and PHV with R_{jb} for rock (NTC08: A), stiff (NTC08: B), soft soil (NTC08: C, D, E).

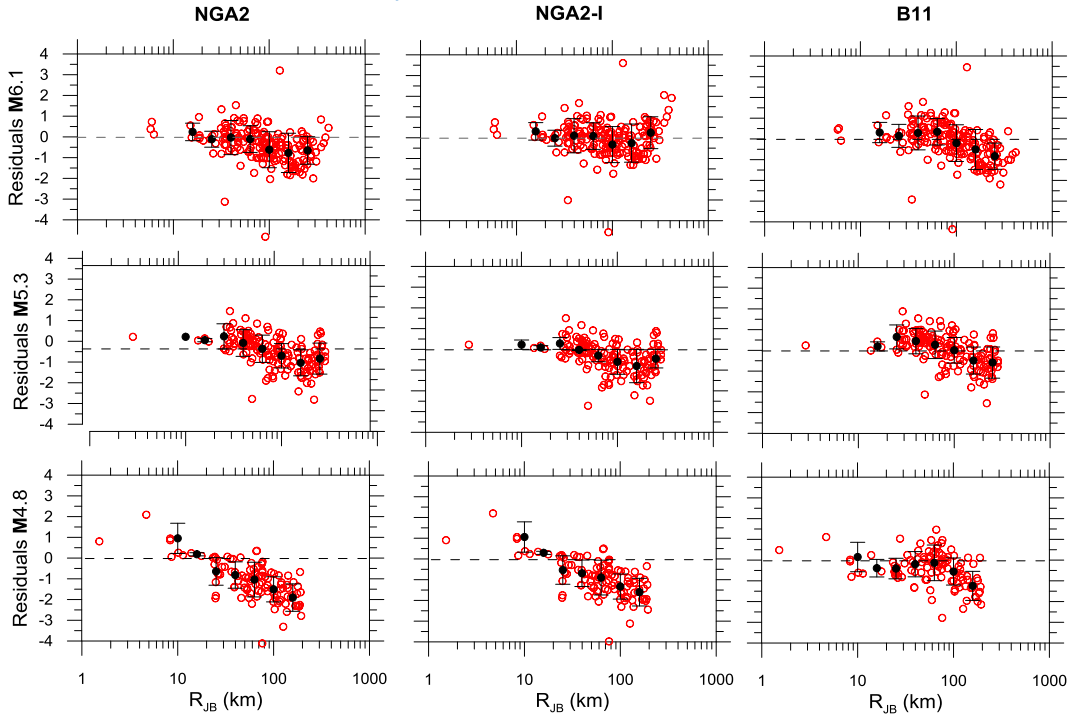

Figure 3.10. Residuals of PHA from recorded ground motions relative to predictions of the NGA2, NGA2-I andB11. Binned means shown with +/- one standard deviation.

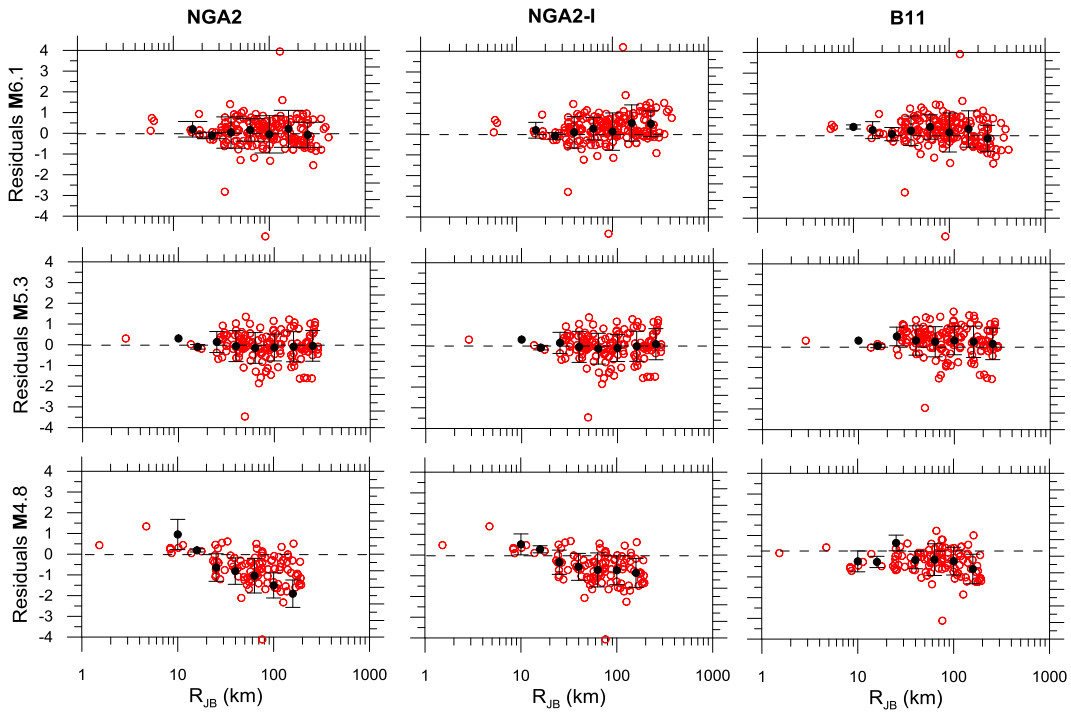

Figure 3.11. Residuals of PHV from recorded ground motions relative to predictions of the NGA2, NGA2-I andB11. Binned means shown with +/- one standard deviation.

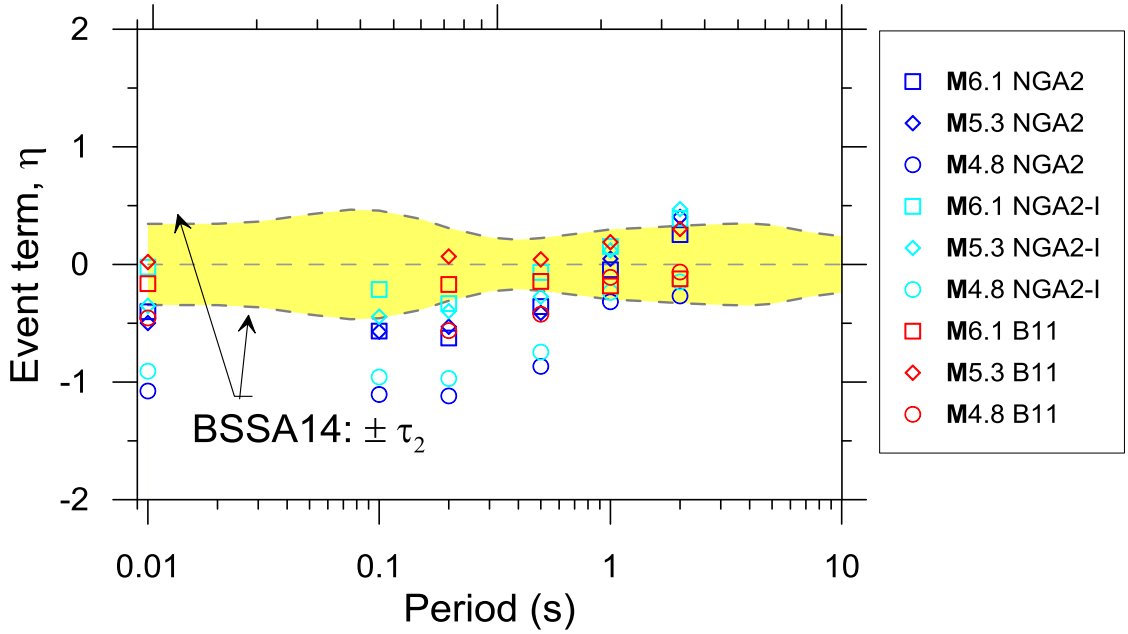

Figure 3.12. Event terms for PGA and PSA oscillator periods of 0.1-2.0 sec for the three sets of models and three events. For context, the +/- one between-event standard deviation for M ≥ 5.5 (τ2) is shown from the Boore et al (2014) model.

4. Landslides and Rockfalls

Principal authors: Kevin Franke, Paolo Tommasi, Paolo Zimmaro

Contributing authors: Filiberto Chiabrando, Vincenzo Di Pietra, Nives Grasso, Robert E. Kayen, Brandon Reimschiissel, Giuseppe Scasserra, Francesco Silvestri

4.1 Landslide Reconnaissance Approach

Our general approach was to first identify locations of possible landslides from resources available to us prior to field deployment. We targeted reconnaissance sites on this basis and performed detailed imaging analysis for several critical, and research-useful, case histories.

4.1.1 Initial Reports of Field Reconnaissance

Two initial reports describing observed landslides were released to the public prior to the arrival of the GEER team: one report by the Italian Institute for Environmental protection (ISPRA), and another report by the Research Center for Prediction, Prevention and Monitoring of Geological Risks of Sapienza University (CERI). The latter report was provided in the form of a kmz file downloadable at the CERI website (CERI 2016). Placemarks in the file link to photographs of observed slope instability phenomena. A brief caption explaining type of "damage" is also linked to the placemarks. A third initial report was released by the National Institute for Geophysics and Volcanology (INGV 2016), but provided little information pertaining to landslides. Observations described in these reports were made on 25-26 August 2016. The CERI list includes almost all observations made by ISPRA. Figure 4.1 shows locations of landslides in the near-source region mapped by ISPRA and CERI.

The ISPRA (2016) report, which refers to a smaller investigation area extending across the paths joining the most damaged Inhabited centers (Amatrice, Accumoli and Arquata del Tronto), includes 13 surface effects. Those effects include rockfalls, damages to road asphalt, the major Pescara del Tronto landslide and the retaining structure failure at Accumoli.

The original landslide list from CERI includes about 140 instability phenomena, most (but not all) of which involved the effects of landslides and other instability phenomena on road structures. The investigated area is large, spanning 20 km to the north of the 24 August 2016 M_w 5.6 aftershock to 30 km south of the 24 August 2016 M_w 6.0 mainshock (southernmost event). Most of the CERI observations consist of rock falls from road cuts or natural slopes above roads. A few cases of movements occurring on slopes below roads are also reported. The major landslide observed below Pescara del Tronto is reported. Some of the rockfalls reported by CERI were small, involving blocks of few tens of cm^3. Some of the reported instabilities could be antecedent to the earthquake (e.g. a slump in the fill-slope of the road SR 260 to Amatrice). A check is currently being conducted in the framework of the PARSIFAL project, which was started simultaneously with other seismic microzoning projects of the area.

The INGV report only describes which types of landslides were observed, particularly rockfalls and slumps of small-to-medium size. The former are located especially on steep slopes in coarse-grained or fill materials. An interesting observation concerns the southeastern part of the earthquake area (near Ortolano) where there are evidences of reactivated slope movements (dating back to the 2009 earthquake), but no apparent signs of new movements.

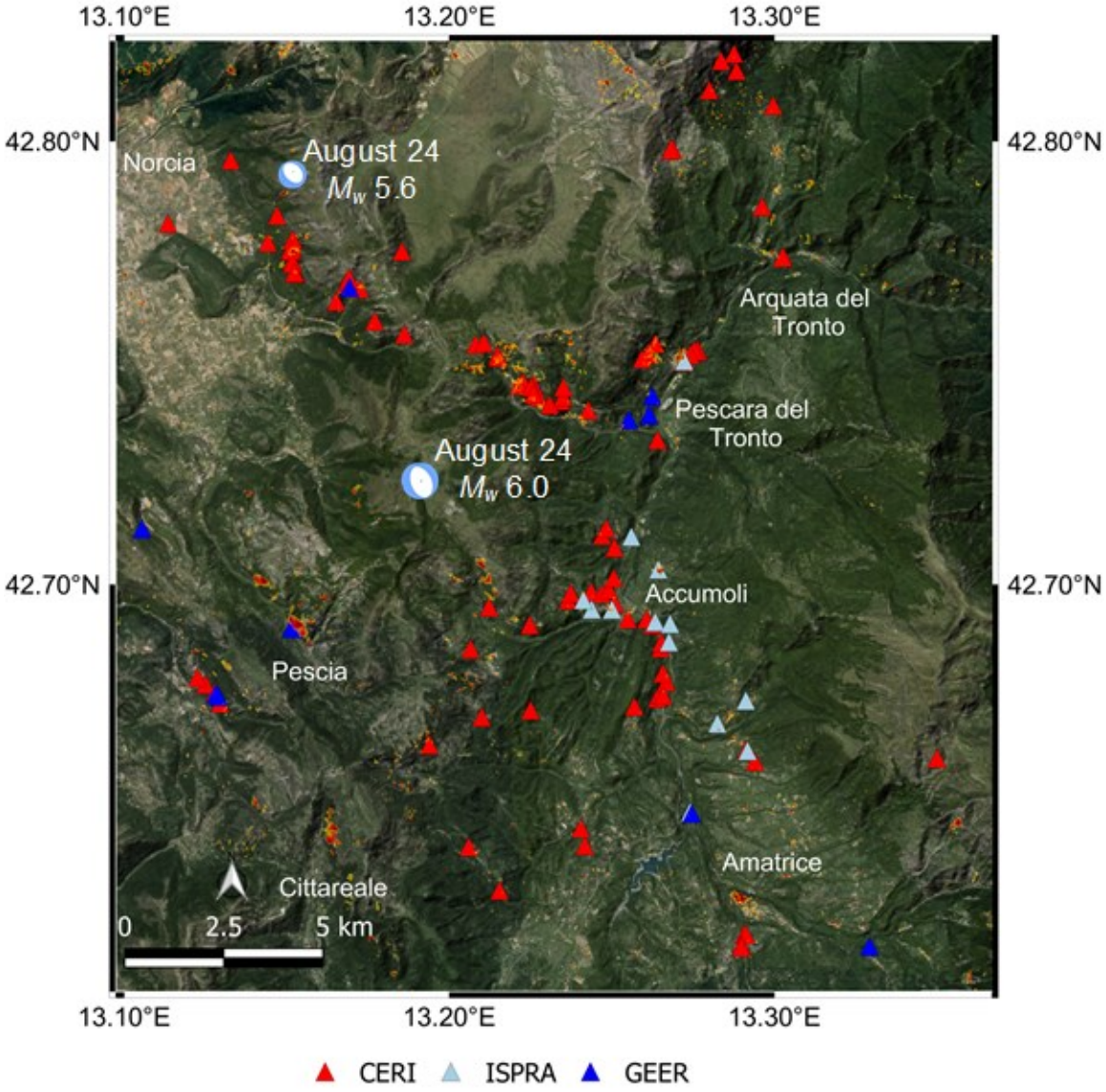

Figure 4.1. Mapped rockfalls and landslides from ISPRA (red circles), CERI (blue circles), and GEER (this study; white circles), along with the damage proxy map of the area produced by the ARIA project (Google earth kmz files used to produce this figure are available at: http://aria-share.jpl.nasa.gov//events/20160824-Italy_EQ/DPM/, last accessed 19 October, 2016).

4.1.2 NASA JPL ARIA Damage Proxy Maps

Several currently available geodetic methods use synthetic aperture radar (SAR) images to generate digital elevation models (DEM) for monitoring ground and structural deformations. These techniques are usually based on differences in the phase of waves returning to a moving

platform (e.g. aircrafts or satellites). In recent years, SAR-based techniques have been used to identify deformation phenomena such as (1) earthquake-related surface deformations and ruptures (e.g. Jo et al., 2010; Fielding et al., 2014), (2) volcanic eruptions (e.g. Jung et al., 2011; Lee et al., 2013), (3) subsidence (e.g. Choi et al., 2011; Zhang et al., 2012), and (4) massive landslides (e.g. Ausilio and Zimmaro, 2016). Such techniques can be also used for producing rapid post-disaster deformation maps. This is one of the goals of the Advanced Rapid Imaging and Analysis (ARIA) project (http://aria.jpl.nasa.gov/, last accessed October 19, 2016). In recent years, the ARIA project team has released damage proxy maps (DPMs), following main earthquake events, globally. The DPMs are produced by comparing interferometric SAR coherence maps from before and after an extreme event (e.g. Fielding et al., 2005; Yun et al., 2011).

The effectiveness of the DPMs has been recently tested for the rapid evaluation of earthquake-induced landslides and rockfalls after the 2015 **M**7.8 Gorkha Earthquake. In particular, Yun et al. (2015) show that the extent of several observed earthquake-related instability phenomena in the Himalayas were well captured by the DPMs. We used DPMs produced after the 2016 **M**6 Central Italy earthquake (http://www.jpl.nasa.gov/spaceimages/details.php?id=PIA20897, last accessed 19 October, 2016) to identify possible landslide and rockfall locations, as shown in **Figure 4.1**.

4.1.3 GEER Preliminary Site Selection Process

Given the initial reports from CERI, ISPRA, and INGV, as well as the JPL-ARIA DPM, dozens of confirmed and potential slope deformations had been identified before the arrival of the GEER team to central Italy. Because the duration of the GEER reconnaissance mission was just a few days, a strategy had to be implemented to efficiently reconnoiter as many of the significant landslides as possible. Priorities were established based on:

1) Size of the landslide
2) Impact to infrastructure
3) Accessibility
4) Potential for future site characterization

We note that the ARIA DPM indicated significantly more potential slope deformation sites than the GEER team could possibly visit during the reconnaissance. Given the priorities listed above, GEER team members relied heavily upon satellite imagery, the ARIA DPM, and the previously identified landslides/rockfalls from the available initial reports to select a handful of potential landslide sites to reconnoiter. These sites were:

(1) Mountain slope north of Cittareale (42.6422 N 13.1634 E; Figure 4.2)
(2) Mountain slope north of Pescia (42.6909 N 13.1533 E; Figure 4.2)
(3) Eastern slope below the town of Accumoli (42.6941 N 13.2500 E; Figure 4.3)
(4) The town of Pescara del Tronto (42.7510 N 13.2701 E; Figure 4.4)

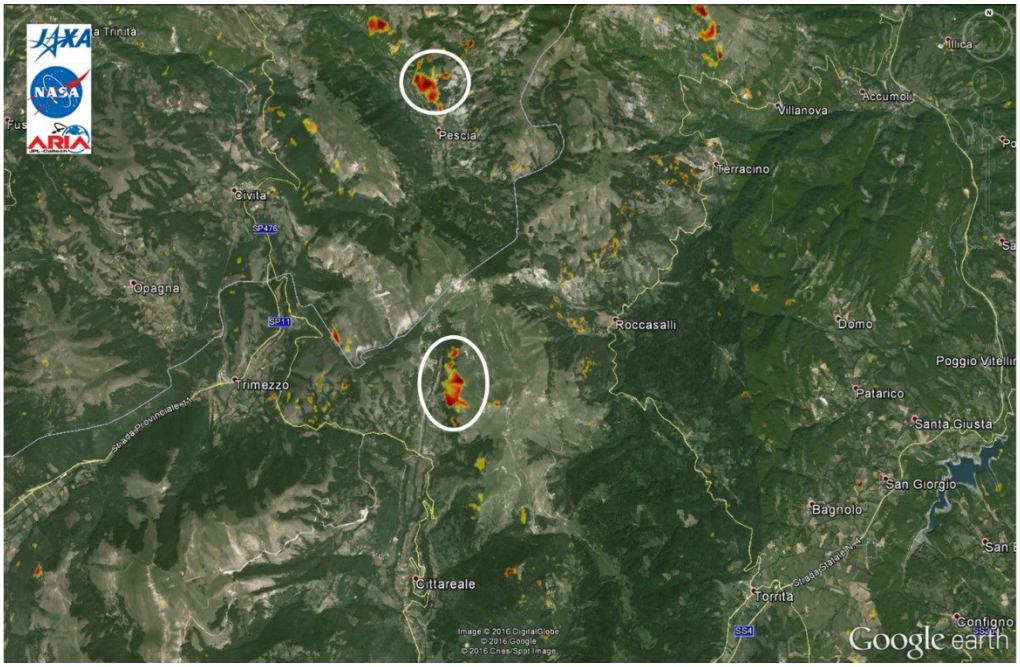

Figure 4.2. Targeted landslide areas for reconnaissance north of Cittareale and Pescia (image courtesy of Google, DigitalGlobe, Cnes/Spot Image, and NASA JPL).

Figure 4.3. Targeted landslide area for reconnaissance east of the town of Accumoli (image courtesy of Google, Cnes/Spot Image, and NASA JPL).

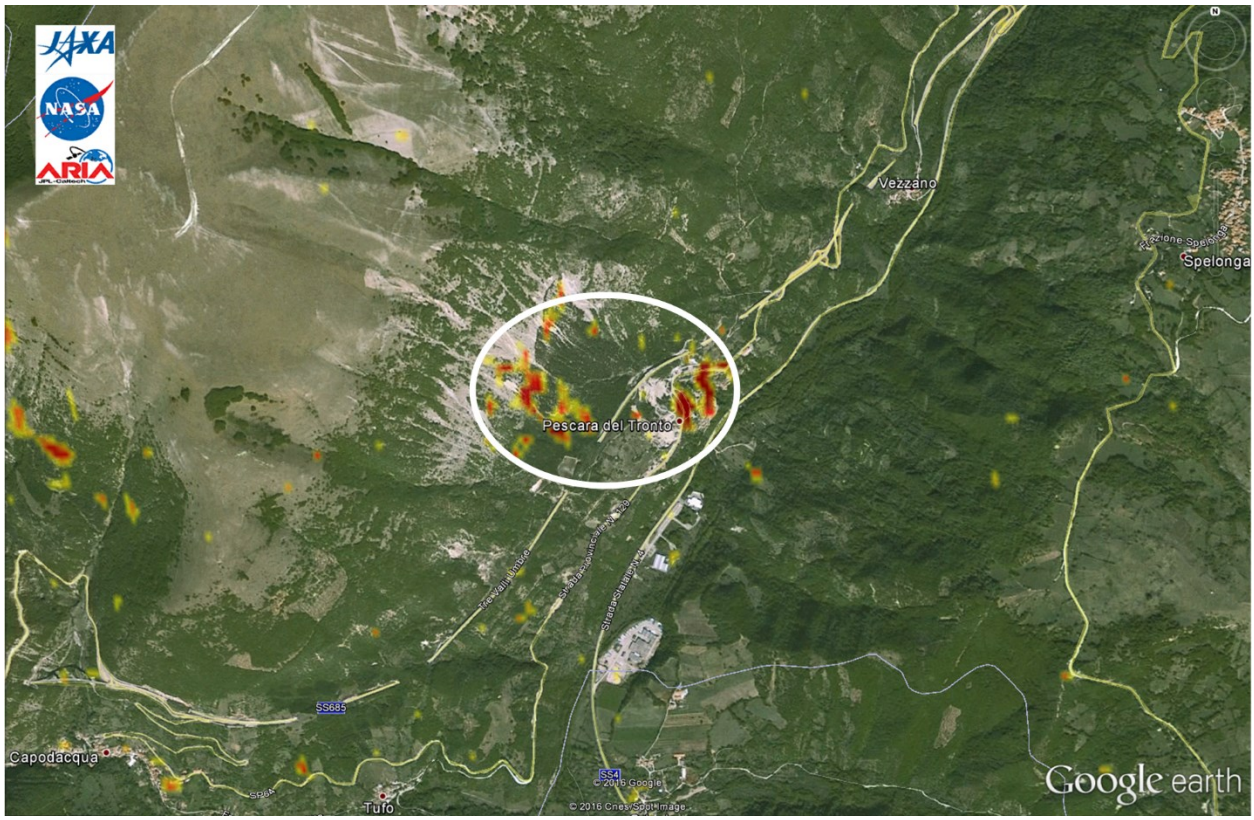

Figure 4.4. Targeted landslide area for reconnaissance near the town of Pescara del Tronto (image courtesy of Google, Cnes/Spot Image, and NASA JPL).

4.2 Regional Risk for Landslides and Rockfalls

4.2.1 Landslide Types and Lithology

The slope instabilities observed on engineered and natural slopes can be grouped into:

i) Rock failures on steep cuts or cliffs generating rockfalls;
ii) Small slumps or slides on road fill-slopes, steep soil slopes or gully banks;
iii) Deformations linked to failure/displacement of retaining structures

Rock Failures

Rock failures observed after the Central Italy earthquake involve Miocene flysch units and the Carbonatic units of the Umbria-Marche Succession. Flysch units (*Laga formation*) consist of alternating sandstone and marls layers, where sandstone is always the prevailing component. The flysch, similar to many other turbidite formations, presents variations in sandstone/marl ratio and layer thickness due to the distance from the source area in the depositional basin. Discontinuity spacing further varies depending on the distance from fault zones. Weathering of marl layers, though limited to extremely shallow depth, occurs soon after marls are exposed from highway cuts and excavations. This weathering is sufficient to undercut overlying sandstone slabs, which can break free when exposed to strong ground motions (Figure 4.5).

Figure 4.5. Rockfall involving sandstone slabs overlying marl layers (after CERI 2016).

In the Central Italy event, strong ground motions triggered larger rock failures only where the flysch was regularly fractured and/or block interlocking was insufficient to keep the rocks in place due to relatively low confining stresses. Observed failures in the flysch most commonly occurred along highway cut slopes. Different mechanisms of rock failure were detected both by GEER and CERI investigators: detachment of sandstone slabs overlying marl layers (Figure 4.5), wedge sliding (Figure 4.6), or planar sliding along bedding joints and toppling.

Observed carbonate units were generally comprised of limestone (*Calcare Massiccio formation*) and bedded limestone (*Maiolica formation*). Rock falls involving the *Calcare Massiccio* formation generally had large blocks (up to 4 cubic meters) and long runout distances. Rock falls involving the *Maiolica formation* generally had much smaller rock fragments and limited runout distances. Failures involved both natural cliffs and cut slopes, with intensely fractured limestone (Figure 4.7) in most cases.

Observed rock failures from the Central Italy earthquake also involved also weak rocks as breccias, moderately-cemented travertines and slightly cemented coarse debris.

Figure 4.6. Free-face wedge sliding that is governed by bedding joint attitude.

Figure 4.7. Failure in intensely fractured (i.e., sugar-cube) limestones (cataclasite).

Landslides in Soil Slopes

Relatively few unstable soil slopes were observed following the Central Italy earthquake. Those landslides that were observed were generally located along fill-slopes next to roads, in loose debris, and on slopes carved in the colluvial/weathering cover of the parent *Laga* flysch formation. In the latter case, the prevalence of the sandstone component in the formation limited the clay fraction and, hence, the thickness of the degradation cover.

Documented landslides in soil following the Central Italy earthquake were generally classified as slump failures or very shallow transitional deformations. No such landslides were observed in the colluvial/weathering blanket of the flysch bedrock on open slopes, but were instead observed along gully banks (see Figure 4.25) and adjacent to some small bridge abutments. Most of the observed landslides in soil appeared to be re-activations of older slides. However, none of these landslides were notably large or resulted in significant displacements.

Displacements Due to Retaining Wall Failure

Many of the observed landslides from the Central Italy earthquake appeared to coincide with the failure of an adjacent retaining wall. Soil failures behind the walls ranged from insignificant cracks (<2 cm in width) behind the wall, to significant cracking and slumping (i.e., vertical deformations up to 50 cm in magnitude; see Figure 4.43), to large scale vertical deformations accompanying complete structural collapse of the wall (see Figure 4.31).

With soil displacements that accompany retaining wall failures, it is not always immediately clear whether the soil deformation caused the failure of the retaining wall (global failure below the wall), or whether the failure of the retaining wall caused the soil deformation (local failure behind the wall). To determine the causative mechanism, engineers must evaluate the mode of retaining wall failure and the depth/geometry of the shear plane in the soil. Based on initial observations following the Central Italy earthquake, most of the soil displacements appear to be caused by failure of the retaining wall due to the limited extent of the soil displacements, suggesting that the deformations correspond to a local slope failure behind the wall.

4.2.2 Existing Mapped Regional Landslide Hazard

Data on landslide susceptibility and risk as derived from pre-earthquake studies are reported in two databases: the Inventory of landslide phenomena in Italy (IFFI) and the Plans for Landslide and Flood Risk Management (PAI), which are both prepared at the basin scale. The earthquake area extends over two basins – Tiber River and Tronto River. For the Tiber River basin, risk level is associated with landslide types (http://www.abtevere.it/node/133?q=node/134). This basin includes the eastern part of the affected area. For the Tronto River Basin (western part of the damaged area), risk maps do not include landslide types (http://www.autoritabacinotronto.it/Cartografia%20on%20line.htm).

The map in Figure 4.8 combines IFFI and PAI pre-earthquake landslide areas, as well as the earthquake effects as recorded by the JPL-ARIA DPM.

With the exception of a few field case observations, the observed landslides and rockfalls following the Central Italy earthquake are necessarily at a scale that is much smaller than that considered by IFFI and PAI databases. Observed instabilities are usually associated with road cuts or road embankment failures, which are highly localized features.

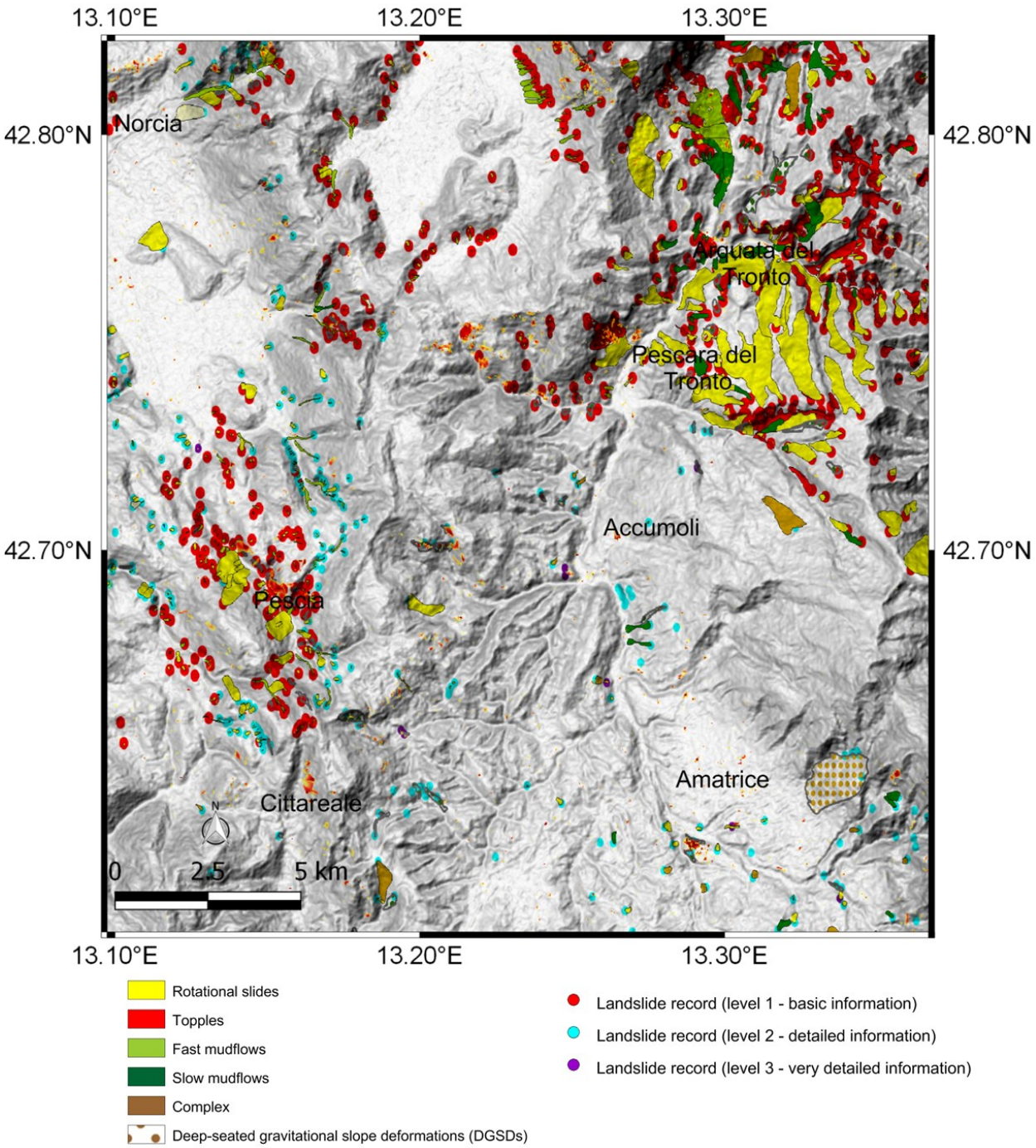

Figure 4.8. Italian landslide inventory (Inventario dei Fenomeni Franosi in Italia, IFFI project, ISPRA - Dipartimento Difesa del Suolo-Servizio Geologico d'Italia, available at: http://www.progettoiffi.isprambiente.it, last accessed October 24, 2016), along with the damage proxy map (DPM) of the area produced by the ARIA project (Google earth kmz files used to produce this layer are available at http://aria-share.jpl.nasa.gov//events/20160824-Italy_EQ/DPM/, last accessed 24 October 2016). In the DPM colored scale, yellow to red pixels indicate increasingly more significant potential damage.

4.3 Use of Unmanned Aerial Vehicles and Terrestrial Photogrammetry for Landslide Reconnaissance

Recognizing that many of the proposed landslide reconnaissance sites would involve rugged and/or steep terrain, heavy vegetation, and/or limited site access, GEER researchers elected to use UAVs to digitally image several of the more significant landslide events in Central Italy. Researchers from the Politecnico di Torino Geomatics group and Brigham Young University subsequently used multiple small UAVs to collect digital high-resolution imagery from the slope north of Pescia, the slope north of Cittareale, Accumoli, Pescara del Tronto, and the rockfall area along a stretch of Highway SP 477. The researchers from Politecnico also performed GNSS measurements of several marker and natural points at the towns of Accumoli and Pescara del Tronto for Structure for Motion (SfM) computer vision post-processing and georeferencing of the acquired UAV data.

4.3.1 The UAV Platforms

The eBee

Select flights over the towns of Accumoli and Pescara del Tronto were performed with an eBee™ small UAV platform, manufactured by Sensefly, and equipped with a digital camera Canon Power Shot S110™, which offers a 1/1.7" Canon CMOS sensor, 12 MP images, and a focal length of 5.2 mm.

The eBee, shown in Figure 4.9, is a lightweight fixed-wing UAV. It weighs approximately 0.6 kg and can carry a maximum payload of 125 grams. The maximum flight duration is approximately 40 minutes, wherein it can image up to 8 square kilometers of ground. The UAV navigates itself using an autopilot and pre-programmed GPS waypoints. The platform is extremely manageable and is very useful for rapid map realization in emergency case (Boccardo et al., 2015; Baiocchi & Pesaresi, 2015)

Figure 4.9. The eBee™ small UAV by Sensefly.

The eBee system is certified by ENAC as EBM-1539 and it is also approved as inoffensive by the Italian Department of Civil Protection. The autopilot is managed by the dedicated mission planning software, called *eMotion*, that allows to plan photogrammetric missions specifying the

area, the flight height, the images overlap (in both the directions) and the expected final result in terms of precision.

The Phantom 4

Flights over portions of Accumoli, Pescara del Tronto, the slope north of Pescia, and the slope north of Cittareale were performed using a Phantom 4™ quadrotor small UAV, manufactured by DJI Technologies. The Phantom 4 is equipped with a 4K video camera that has a 1/2.3" CMOS sensor, 94-degree field of view, 12.4 MP images, and a focal length of infinity. The Phantom 4 system weighs 1.38 kg, has a maximum flight time of 28 minutes, and offer the ability to hover and/or collect imagery from vertical faces. An image of the Phantom 4 is presented in Figure 4.10.

Figure 4.10. The Phantom 4™ small UAV by DJI Technologies.

The TRex 800e

Flights over the rockfall on Highway SP 477 were performed with a TRex 800e™ small UAV, manufactured by Align. The TRex 800e flown in Central Italy is modified and optimized for photogrammetric remote sensing. The helicopter platform weighs 4.1 kg and incorporates a blade that is 1.74 meters in diameter. Due to its size, the TRex 800e can carry a sensor payload of approximately 9 kg. It uses two parallel 6-cell 22.2 volt 8,000 mAh batteries. The TRex 800e used in Italy has a 3-axis Align nose gimbal placed upon it, which houses a Nikon D750™ DSLR camera with 24 MP image resolution, 35.9x24.0 CMOS image sensor, and 35 mm fixed focal length lens. The average flight duration of the TRex 800e is relatively short at 12 minutes per battery pair. An image of the modified TRex 800e used in Italy is shown in Figure 4.11.

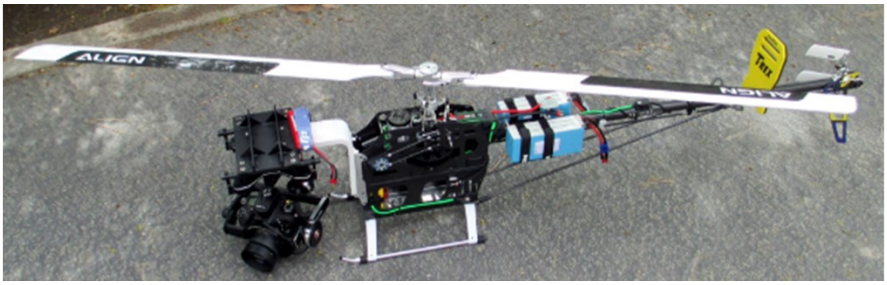

Figure 4.11. Customized TRex 800e™ small UAV by Align.

4.3.2 Flight Paths

High accuracy photogrammetric results require a substantial overlap between the digital images. Most SfM software programs recommend an image overlap of 70-80%. Therefore, the flight path plan to acquire the digital images must be carefully designed, taking into account the following:

1) The terrain that is going to be imaged (i.e., vertical or flat);
2) Ground Sampling Distance (GSD): the GSD defined by the project specifications will define the altitude at which the images have to be taken;
3) Overlap: the overlap will depend on the type of terrain that is mapped and will determine the rate at which the images have to be taken.

The GSD is the distance between pixel centers measured on the ground, and it depends on the camera characteristics and on the objective of the survey and on the level of detail required. The larger the GSD value, the lower the spatial resolution of the image is and the fewer details are visible. The GSD is related to the flight altitude. The higher the altitude of the UAV, the larger the GSD value. Even when flying at a constant height, the images of a project may not have the same GSD. This is due to the terrain elevation differences and the angle of the camera while shooting.

Two flight path approaches were taken with the UAVs used in this reconnaissance mission. The eBee UAV was used to develop nadir images of Accumoli and Pescara del Tronto for the development of ortho-rectified images (i.e., orthophotos). The Phantom 4 and TRex 800e UAVs were used to capture closer skewed images of the sites of interest for the development of 3D computer vision models. Flights with the eBee UAV where planned using the *eMotion* software. According to the morphology of the area of interest the planning was performed considering the terrain shape. Flights with the Phantom 4 and the TRex 800e were performed manually with an experienced UAV operator. Imagery from the UAV was transmitted to the operator in real time, and he ensured significant image overlap while maneuvering the UAV to capture the skewed imagery from objects of interest. This approach was also used successfully to model liquefaction sites following the 2014 Iquique earthquake (Franke et al. 2017).

4.3.3 Acquisition of Ground Control Points (GCPs)

To georeference the digital imagery from Pescara del Tronto and Accumoli, it was necessary to place numerous Ground Control Points (GCPs) throughout the target sites. The GCPs used for this mission were comprised of both hand-placed artificial markers (Figure 4.12a) and recognizable surface objects or features (Figure 4.12b).

The position of the GCPs (23 total for Pescara del Tronto and 20 total for Accumoli) were surveyed using the GNSS Geomax Zenith 35™ (www.geomax.com). The instruments was used as rover in Real Time Kinematic (RTK) configuration survey using for receiving the correction the Leica ItalPos GNSS permanent networks (http://it.smartnet-eu.com/italpos_146.htm). The rover connects to the network RTK server via a one-way or two-way communication link (e.g.

radio modem, GSM or Internet). In the case of the realized survey the connection was realized using the GSM. Once the rover receives the RTK data it computes its position using the appropriate algorithm. Which algorithm the rover uses and how the distance dependent errors are minimized depends on the network RTK method being used. With this technique, it is possible to measure the points directly in the correct reference system (UTM WGS 84 Fuse 33 N cartographic system in this case) with an accuracy of about 2 cm.

Images showing the GCP layout in Pescara del Tronto and Accumoli are shown in Figure 4.13 and Figure 4.14, respectively.

Figure 4.12. Artificial GCP marker (a), and natural GCP marker (b).

Figure 4.13. Position of the GCPs in Pescara del Tronto (red indicated artificial marker, green indicates natural marker).

Figure 4.14. Position of the GCPs in Accumoli (red indicates artificial marker, green indicates natural marker).

4.4 GEER Landslide Reconnaissance Observations

4.4.1 General Observations Regarding the Applied Reconnaissance Approach

Several general observations can be made regarding the landslide reconnaissance approach that the GEER team used during this mission:

1) The JPL-ARIA DPM and mapped landslide/rockfall locations from CERI and ISPRA were useful tools for initial planning of potential landslide locations to be investigated.
2) Unfortunately, we did not observe a strong correlation between the locations of many landslides/rockfalls and the "hot zones" on JPL-ARIA DPM. A few of the significant landslides we observed, including the landslide on the eastern slope below Pescara del Tronto, did not appear as hot zones on the DPM ("false negatives"). Similarly, several of the noted CERI rockfalls and landslides also did not appear as hot zones on the DPM. Conversely, a few of the larger hot zones on the DPM (e.g., the mountain north of Cittareale) did not show any signs of slope distress or deformation ("false positives").
3) The DPM did, however, appear to detect most of the significant vertical ground deformations, including structural collapses.
4) The UAVs proved to be a valuable tool for observing and documenting the landslide and rockfall events from the Central Italy earthquake. Because access to the region was restricted by the military and local fire departments, we were generally allowed only

limited ground access to observe sites of interest. Using UAVs, even the largest sites (e.g., the town of Pescara del Tronto) were imaged in less than two hours. The UAVs allowed us to see areas that were not accessible due to safety concerns, rugged terrain, and/or heavy vegetation.

5) Pre-reconnaissance efforts to gain authorization for the UAVs was (and always is) challenging. Every country has laws regarding non-hobby UAV flights, and the GEER team worked in close coordination with local government authorities and researchers to obtain necessary authorizations. In addition, transportation of 22-cell batteries for the operation of larger UAVs is challenging due to airline restrictions.
6) Overall, the approach to reconnoitering landslides during this GEER mission was successful, and is recommended for future GEER missions where similar resources (e.g., initial landslide reports, JPL-ARIA DPMs) are present.

4.4.2 Rockfall and Landslide Observations

Rockfalls and landslides caused by the Central Italy Earthquake were limited spatially and in volume despite the steep morphology of the region and the significant seasonal rainfall that had occurred in the week prior to the August 24 event. Figure 4.15 presents the mapped rockfall locations from CERI in the region. The GEER reconnaissance team observed remarkably few areas of significant rockfalls and landslides while driving through the area. A large number of very small rockfalls and gravel debris were observed along roadways throughout the earthquake zone. These sites were noted by GEER team members, but were not documented in detail due to their frequency and relative insignificance.

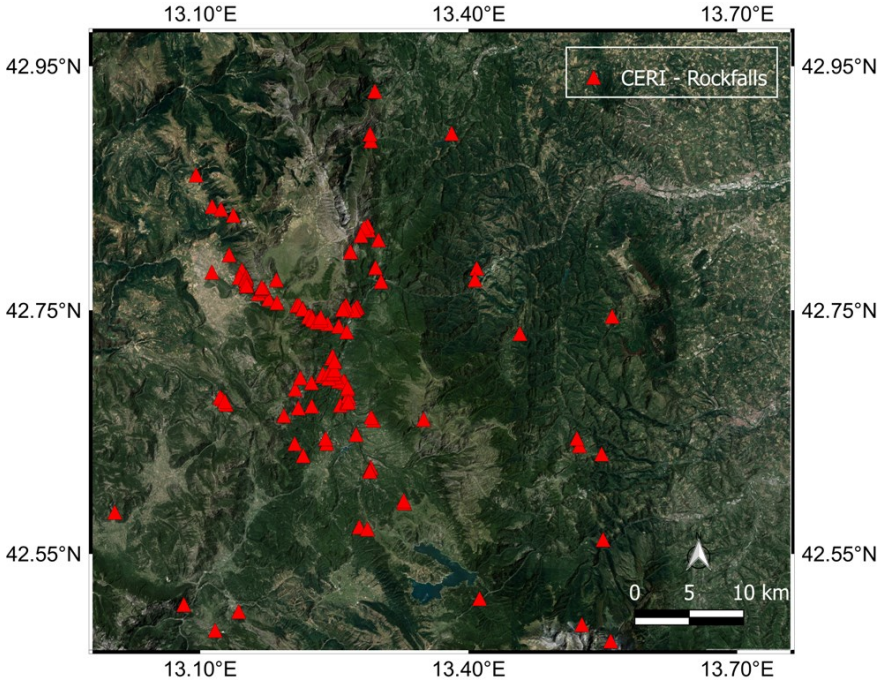

Figure 4.15. CERI catalog of rockfalls for the central Italian region affected by the 24 August 2016 **M**6.1 earthquake.

During the GEER team visit, many road closures were in place, primarily for damage in towns and cities. Some road closures were due to rockfalls. The team was able to map in detail rockfalls occurring near highways SS4, SP11, SP64 and SP477, and in the town of Pescara del Tronto.

Several minor rockfalls and slope failures in the flysch formation were observed along SR260 between Lake Scandarello and Amatrice, highway SS4 below Arquata del Tronto and SP129 between Capodacqua and Arquata del Tronto. Failures and rockfalls in the travertine deposits were observed below Pescara del Tronto (discussed in Section 4.4.5) as well as near Acquasanta Terme. Rockfall and failures in calcareous breccia deposits were observed along the SP11 road between Cittareale and Norcia (Figure 4.16). Existing ruptures in breccia deposits were not mobilized during the Central Italy earthquake and did not result in any noticeable deformations (**Error! Reference source not found.**17).

Rockfalls and failures in massive and layered limestones were observed along the SP477 and south of Norcia (local road Savelli Pescia). The latter are described in detail in Section 4.4.4.

Figure 4.16. Failure in calcareous breccia along the SP11 road between Cittareale and Norcia.

An area of intense rockfall was observed along state provincial route SP64 (Tufo–Castelliccio) and SP477 (Castelluccio-Norcia), along with a 12 km zone of steep terrain and switchback roads. Almost all of the rockfall occurred when isolated blocks of limestone detached from outcropping bedrock above the highway. Many of these blocks came to rest on the shoulder or pavement of the road, whereas other blocks maintained enough velocity to cross the road and continue descent downslope. An example of isolated blocks on Highway

SP477 can be seen in Figure 4.17 and Figure 4.18. An online UAV-based 3D surface model of the rockfall area along Highway SP477 can be accessed from the GEER event webpage. An image of the 3D model developed for the SP477 rockfall is presented in Figure 4.19.

Slope protection in the form of rock bolts, tiebacks, retaining walls, and rockfall nets and fences were deployed in the epicentral region, and seemed to be effective at protecting roads and structures below. Figure 4.20 shows an example of falling debris caught behind rock-nets on the road to Plano Grande and Casteluccio. These successful applications of rock-net protection allowed roads to remain functional after the earthquake and provided critical access to the severely damaged town of Castelluccio immediately after the earthquake.

Figure 4.17. Large block of breccia (a) before the earthquake (image courtesy of Google 2016), (b) after the earthquake, and (c) example of rock fall below the Plano Grande on SP477. A large 2-m block of limestone crossed the road came to rest on the downslope side of the roadbed below a prominent outcrop of limestone (42.76729 N 13.16983 E).

Figure 4.18. Example of rock fall below the Plano Grande on SP477. Blocks a large as 3 to 4 m across came to rest on the flat roadbed below a prominent outcrop of limestone (42.76729 N 13.16983 E).

Figure 4.19. 3D model image of the SP 477 rockfall. Visible rocks and debris on the road are circled in yellow (42.7661 N 13.1669 E).

Figure 4.20. Rock-net protection with captured debris from the earthquake, including minor small debris in the foreground and a large ~0.5-m block in the background (42.78392 N 13.18333 E).

4.4.3 Observations from the Slope North of Cittareale

The Phantom 4 UAV was used to investigate possible slope failures along the mountain slope north of Cittareale. The UAV was flown directly over the hot zone indicated on the DPM, but no deformation of the ground could be identified. It is not clear to our team why the DPM would indicate significant movements of the ground over that area, but we did not see any deformations. As a result, no further digital imagery was captured and the team proceeded to the next site of interest near Pescia.

4.4.4 Observed Landslide/Rockfall from the Slope North of Pescia

The Phantom 4 UAV was used to investigate mountain slopes high above Via del Passero, just north of the town of Pescia (42.69082 N 13.15368 E). None of the mountain slopes could be seen from the road due to the dense and tall vegetation immediately adjacent to the road. However, the Phantom 4 UAV allowed the GEER team to observe the mountain slopes above the vegetation. The general lack of vegetation and significant amount of eroded debris along the mountainside suggested that this was a pre-existing and active landslide/rockfall area. Lighter discoloration in the limestone rock along the mountainside suggests that some large boulders likely fell due to the earthquake, but could not be located due to the heavy vegetation below. A single flight was performed with the Phantom 4, and the subsequent video still images were processed with SfM computer vision using *ContextCapture* software by Bentley. A screen capture of the resulting 3D model of the rockfall is presented in Figure 4.21. The white circles in Figure 4.21 highlight the areas of lighter discoloration. Bentley *Acute3d Viewer* software was used to capture this image as well as the remainder of the 3D model images presented in this chapter.

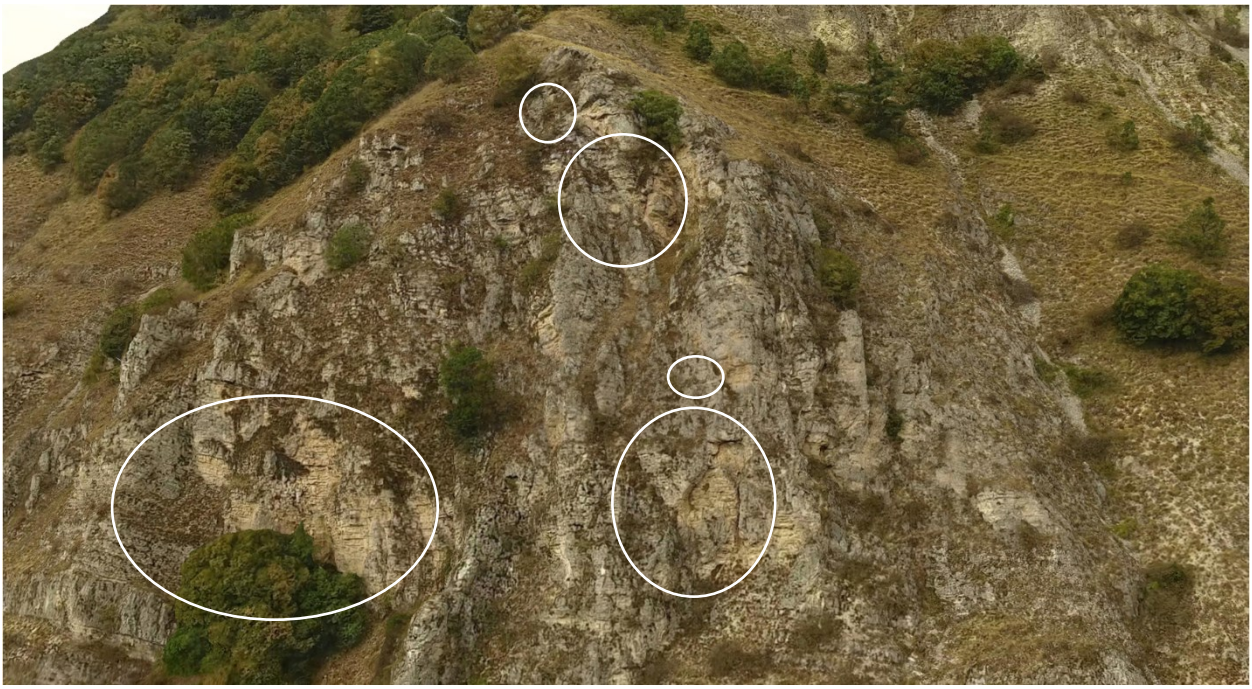

Figure 4.21. 3D surface model of the rockfall north of Pescia (42.6908 N 13.1537 E)

4.4.5 Observed Landslides in Pescara del Tronto

Significant ground and structural deformations were known to have occurred in the town of Pescara del Tronto. At the time of our visit, the town was evacuated and guarded by military and firefighting personnel. We gained authorization from DPC to enter the town for reconnaissance purposes for approximately 2 hours on September 8, 2016. This reconnaissance was performed under close supervision from firefighters. The GEER team used this limited time perform a series of UAV flights to collect aerial imagery over as much of the devastated town as possible. The aerial imagery was subsequently processed with a SfM computer vision algorithm using Bentley *ContextCapture* software and *Pix4D* software (Vallet et al. 2011; Suziedelyte et al 2016*)*. The following discussion and imagery are taken from subsequent post-reconnaissance analysis of these models. The UAV-based 3D model of Pescara del Tronto can be viewed online using a simple web browser by accessing the model link presented on the GEER event webpage. An overview image of the Pescara del Tronto 3D model is presented in Figure 4.22. An orthophoto of Pescara del Tronto developed from *Pix4D* is presented in Figure 4.23.

Figure 4.22. Screenshot of the 3D model of the town of Pescara del Tronto.

Figure 4.23. Orthophoto of Pescara del Tronto.

Investigation of the 3D model of Pescara del Tronto revealed numerous shallow earthquake-induced landslides and retaining wall failures. These landslide locations are summarized on a site vicinity map presented in Figure 4.24. The largest landslide occurred on the east slope below the city (42.75057 N 13.27223 E), directly above Highway SS4 (marked as #1 in Figure 4.24). A modeled image of this landslide is presented in Figure 4.25. At the time of the GEER reconnaissance, this landslide was approximately 75 meters wide by 30 meters high. The landslide itself was quite shallow, with only the upper meter or less of soil sliding downslope. The slope bedrock is formed by the flysch bedrock overlain by a layer of fluvio-lacustrine sediments and a slightly-to-moderately cemented travertine deposit. The landslide damaged and/or undercut retaining wall structures surrounding the city, leaving portions of the overlying city dangerously susceptible to collapse (Figure 4.26). Two large tilted travertine blocks remained exposed along the side slope (Figure 4.27), and it was not immediately clear whether those blocks were stable. Although there was no debris visible along Highway SS4 at the time of the GEER team visit, the road surface was discolored below the landslide, suggesting that the landslide most likely ran out onto the road and obstructed it until cleanup crews could remove the debris. An orthophoto of the landslide developed in *Pix4D* is presented in Figure 4.28.

Figure 4.24. Site vicinity map showing the locations of the identified earthquake-induced landslides in Pescara del Tronto

Figure 4.25. 3D model image of the large landslide below Pescara del Tronto (42.75057 N 13.27223 E).

Figure 4.26. 3D model image of retaining wall damage from landslide below Pescara del Tronto (42.75057 N 13.27223 E).

Figure 4.27. 3D model of two large protruding rock outcrops on the landslide below Pescara del Tronto (42.75057 N 13.27223 E).

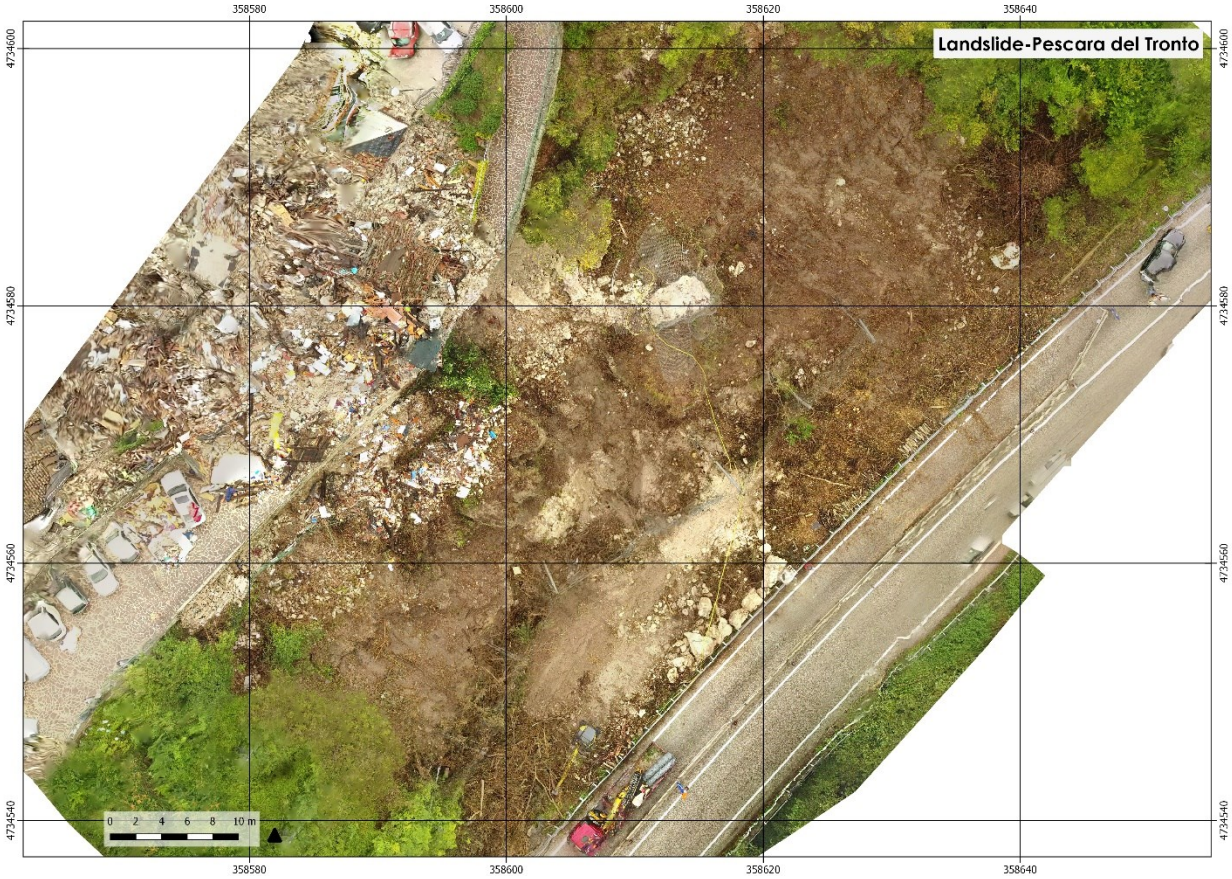

Figure 4.28. Orthophoto of the large landslide below Pescara del Tronto (42.75057 N 13.27223 E)

A second, smaller shallow landslide was located above Highway SS4 (marked as #2 in Figure 4.24), just south of the larger landslide discussed above (42.7501 N 13.2719 E). This landslide was approximately 16 meters wide and occurred on a slope 26 meters high. A model image of this landslide is presented in Figure 4.29.

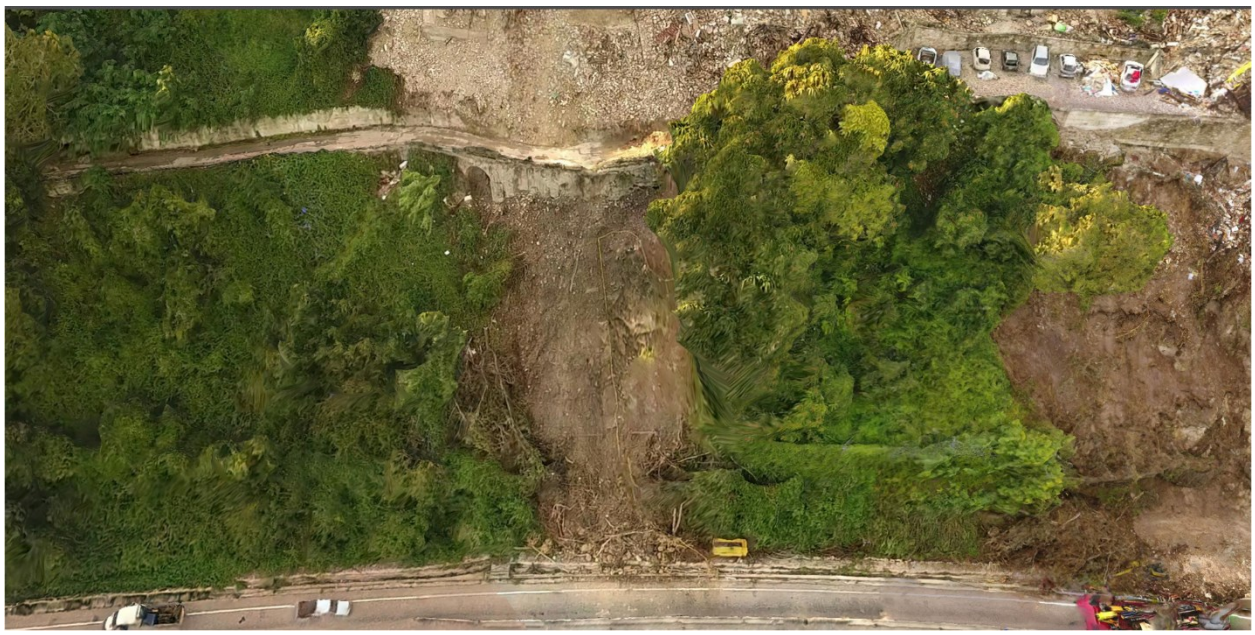

Figure 4.29. 3D model of smaller landslide adjacent to Highway SS4 (42.7501 N 13.2719 E).

A few of the observed slope failures in Pescara del Tronto appear to be related to potential retaining wall failures. For example, a significant slope failure occurred just north of the large landslide described above (marked as #3 in Figure 4.24). The location of this failure is 42.75109 N 13.27208 E. A model image of the slope failure is presented in Figure 4.30. The slope failure occurred adjacent to a vertical, 24 m-high masonry retaining structure that appears to have partially collapsed in the vicinity of the slope failure (Figure 4.31). From poor resolution and vertical angle of the Google Earth imagery, it is impossible to determine the extents of the masonry wall prior to the earthquake. Several possible masonry stones are visible in the debris pile below the slide. Figure 4.31 also shows that the landslide undercut portions of a cobblestone road and parking area. As another example, a similar but smaller retaining wall failure and subsequent landslide occurred just east of the previous slide (marked as #4 in Figure 4.24; 42.75136 N 13.27194 E), and is shown in Figure 4.32. This smaller slide is approximately 5 meters wide by 13 meters high, and appears to have caused the complete collapse of an overlying residential structure on top of the wall. A third portion of the same retaining wall (marked as #5 in Figure 4.24; 42.75166 N 13.27111 E) appears to have collapsed, resulting in another localized landslide that damaged portions of an overlying road. This third landslide was not observed during the actual UAV flights, but was identified later when studying the 3D model of the town. The landslide occurred beneath heavy tree canopy, and only a portion of the slide can be seen from directly above it (Figure 4.33).

Figure 4.30. 3D model of a slope failure in Pescara del Tronto possibly caused by a retaining wall collapse (42.75109 N 13.27208 E).

Figure 4.31. Model image of slope failure and possible retaining wall collapse (42.75109 N 13.27208 E).

Figure 4.32. Model image of a smaller retaining wall failure and subsequent landslide in Pescara del Tronto (42.75136 N 13.27194 E).

Figure 4.33. Model image of a landslide following a corner retaining wall failure in Pescara del Tronto (42.75166 N 13.27111 E).

Another shallow landslide occurred on the northern side of Pescara del Tronto (marked as #6 in Figure 4.24; 42.75171 N 13.27261 E). Low-resolution pre-earthquake satellite imagery from Google Earth suggests that this area was already partially barren of vegetation, perhaps due to an existing localized landslide. However, the aerial imagery from the UAV and resulting

3D model, presented in Figure 4.34, show exposed tree roots (circled in yellow) and scarps that appear to be less than one meter-deep into the hillside. The landslide is approximately 17 meters wide by 20 meters high. Significant amount of structural rubble from collapsed residences is also visible in the landslide debris.

Figure 4.34. Model of shallow landslide below a northern portion of Pescara del Tronto (42.75171 N 13.27261 E).

Another set of interesting landslide features in Pescara del Tronto is located near the gravel pit on the southern upper portion of the town (marked as #7 in Figure 4.24; 42.74985 N 13.26893 E). An overview image of the gravel pit taken from the UAV-based 3D model is presented in Figure 4.35. The gravel pit is approximately 70 meters by 90 meters, and has 2.4V:1H side slopes comprised of slightly cemented cartaclasized limestone blocks interspersed in a gravelly-sandy matrix comprised of angular limestone clasts. A dirt haul road traveling up and along the edge of the slope is located on the south side of the gravel pit. At the time of the GEER reconnaissance, a significant amount of debris was observed on Road SP129, which passes directly adjacent to the gravel pit on the east and south. A landslide had obviously occurred, and had exposed about 15 meters of a 50 cm-diameter pipeline that was shallowly buried beneath the dirt haul road (Figure 4.36). Comparisons with Google Street View images from May 2011 showed that the pipeline had not been exposed prior to the earthquake, as shown in Figure 4.37. Also shown in Figure 4.37 is a tree that appears to have moved 9.3 meters downslope (circled in yellow). On the other side of the slope (inside the gravel pit), a portion of another pipe (…possibly the same pipe) was visible in the Google Street View images in May 2011, but the 3D model suggests that an additional 10 meters of pipeline became exposed from landslides inside the gravel pit following the August 24 earthquake (Figure 4.38). A final view of both exposed pipelines and the failed slopes is presented in Figure 4.39. From this image,

sections of the slope up to 5 meters wide broke loose and slid downslope due to the earthquake.

Figure 4.35. Overview model image of the gravel pit in Pescara del Tronto (42.74985 N 13.26893 E).

Figure 4.36. Model image of landslide near gravel pit and Road SP 129 that exposed a 50 cm-diameter pipeline (42.74950 N 13.26958 E).

Figure 4.37. Both pre-earthquake (a) and post-earthquake (b) images of the slope near the gravel pit where a landslide exposed a pipeline. Pre-earthquake imagery courtesy of Google.

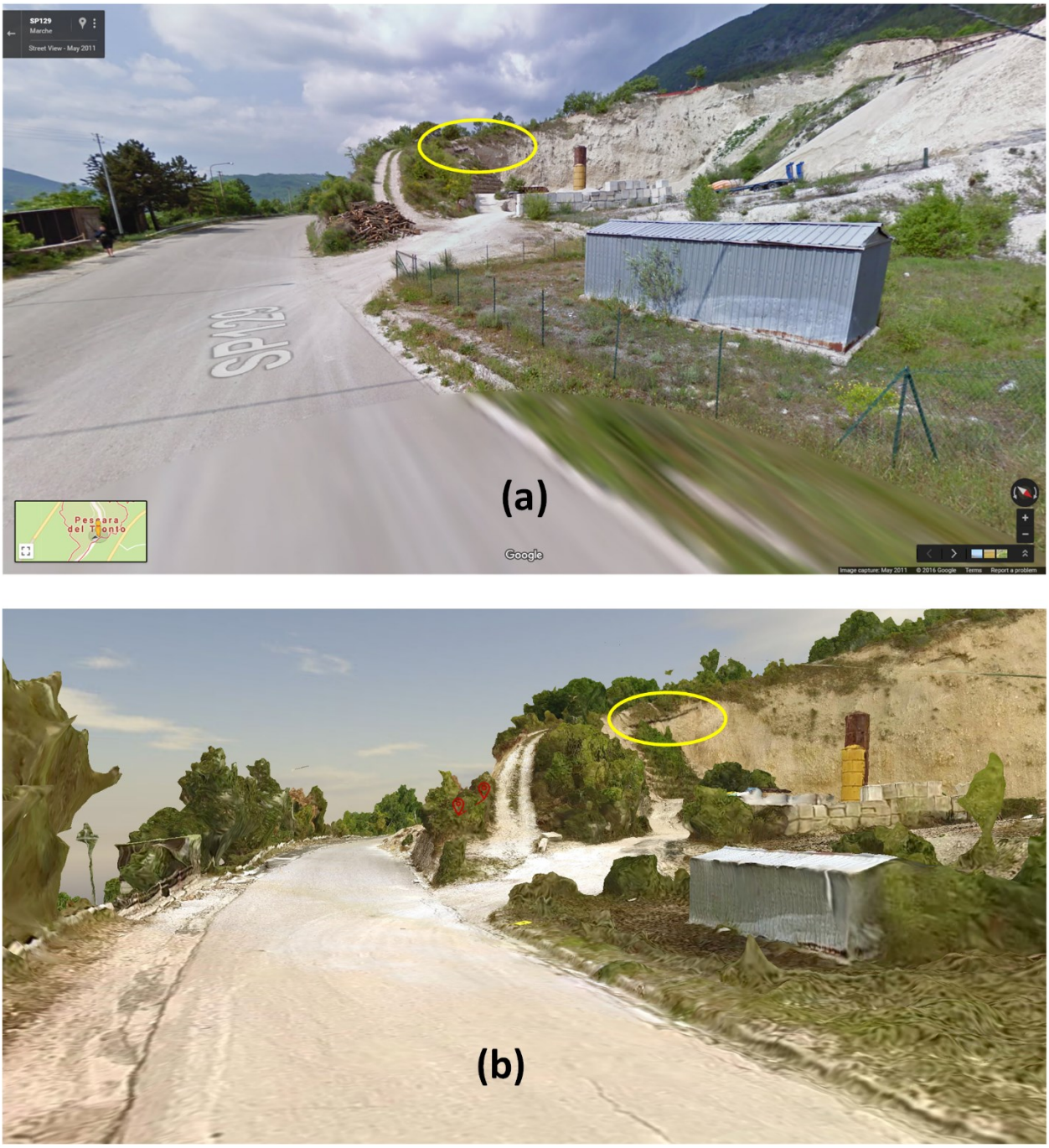

Figure 4.38. Pre-earthquake (a) and post-earthquake (b) images of the haul road slope inside the gravel pit, with exposed pipeline. Pre-earthquake imagery courtesy of Google. From these images, it appears that the earthquake and subsequent landslide into the gravel exposed 10 meters more of the pipeline.

Figure 4.39. Landslides along dirt haul road in Pescara del Tronto, with exposed pipelines. The earthquake caused up portions of the slope up to 5 meters wide to fail, including portions of the dirt haul road itself.

4.4.6 Observed Ground Displacements in Accumoli

Reports from firefighters, military personnel, and the ARIA DPMs suggested that significant deformations had occurred on the eastern slope below the town of Accumoli (42.69409 N 13.25013 E). Following a lengthy authorization process, the GEER team was allowed access to the eastern portion of the town under firefighter escort. Just prior to this, the Politécnico members of the GEER team obtained authorization to place GCPs throughout the town and to fly the eBee UAV over the entire town to develop an orthophoto, which is presented in Figure 4.40. Thus, the Phantom 4 UAV was only authorized to fly over the eastern portion of the town where the suspected landslide had occurred. Figure 4.41 presents an overview of the 3D model that was developed of the eastern portion of Accumoli.

Three distinct instability phenomena were observed in adjacent zones of the south-eastern spur of the village. Significant deformation and cracking was visible in the ground at the eastern portion of Accumoli. These cracks were all originally believed to be caused by landslide, but subsequent analysis of the 3D model revealed that many of the cracks were due to failure of a reinforced concrete retaining wall. Figure 4.42 and Figure 4.43 presents a retaining wall (42.69446 N 13.24980 E) that rotated outwards 3.5 degrees, moving horizontally outwards 57 cm and downslope nearly 18 cm. A soil graben approximately 2.7 meters wide formed behind the rotated wall, causing the soil to settle between 45-50 cm directly behind the wall and to develop cracks up to 46 cm in width. Another failed stone-masonry retaining wall (42.69438 N 13.24995 E) was observed a few meters to the east beneath the road Frazione Fonte del Campo (SP18; shown in Figure 4.44), causing the curb to displace outward horizontally 25 cm and

vertically down 6.8 cm. However, investigation of the UAV aerial imagery and subsequent 3D model revealed a series of cracks in the fillslope below the road Frazione Fonte del Campo (42.69406 N 13.25019 E). The cracks, which are orthogonal to the dip of the slope, range in width from 5 to 14 cm and are shown in Figure 4.45. Subsequent investigation of these cracks by Italian researchers revealed that the cracks were limited only the soft silty-sandy soil located near the surface of the fillslope. No evidence of a larger landslide was observed at the bottom of the slope. Further investigation of the 3D model found that one of the telephone poles founded in the hillside below the identified cracks was tilted approximately 13 degrees from vertical, while the other telephone poles in the hillside appear to be vertical (Figure 4.46). This tilting telephone pole could have been caused by soil deformations in the fillslope on the hillside.

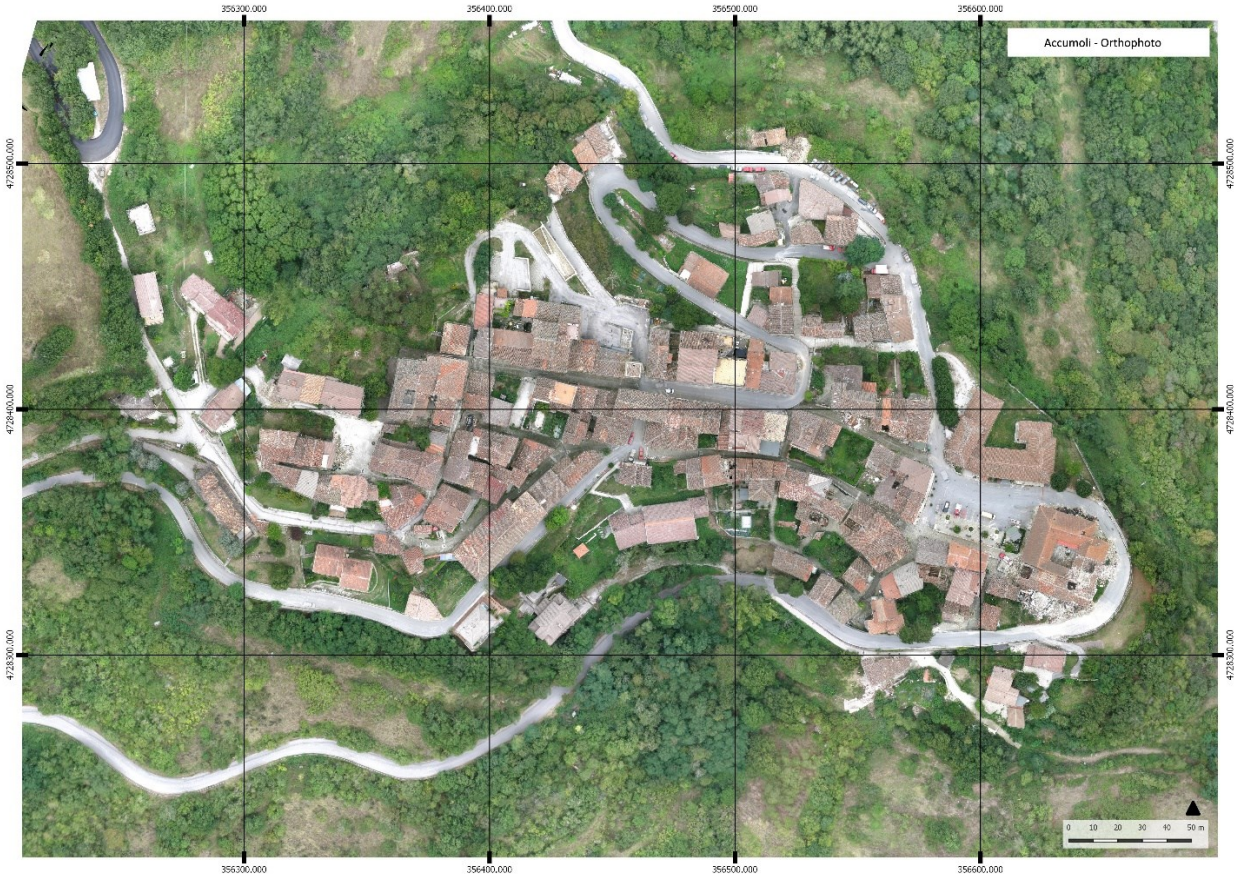

Figure 4.40. Orthophoto of the town of Accumoli (42.96467 N 13.24760 E).

Figure 4.41. 3D Model overview image of the eastern portion of Accumoli

Figure 4.42. Model image of a rotated retaining wall (3.5-degrees) and the subsequent soil graben behind the wall (42.69446 N 13.24980 E).

Figure 4.43. Rotated retaining wall and subsequent graben behind the wall. Soil settlement between 45-50 cm behind the wall, and formed cracks up to 45 cm in width (42.69446 N 13.24980 E).

Figure 4.44. Rotated retaining wall below the road Frazione Fonte del Campo and subsequent cracks up to 25 cm in width (42.69438 N 13.24995 E).

Figure 4.45. Model image of the cracks found in the silty-sandy fillslope located adjacent to the eastern walls of Accumoli. Crack widths range from 5 to 14 cm (42.69406 N 13.25019 E).

Figure 4.46. 3D model image of a rotated telephone pole in the slope below the cracks. The telephone pole is rotated 13 degrees from vertical, while the other telephone poles are approximately vertical.

4.5 Comparison to Historic Data

In this section, we compare epicentral distances within which the landslides and rockfalls were observed from the August 24 central Italy earthquake to those from prior events. As shown in

Figure 4.42, the data are plotted with the abscissa taken as surface wave magnitude, M_S, which is 5.9 for the present event. An historic relation of this sort was prepared by Keefer and Wilson (1989). The pre-2016 data points in Figure 4.47a-b are from a national historical database (Martino et al., 2014), recently updated by Silvestri et al. (2016).

The plots are prepared for landslides with mechanisms falling into Category I (i.e., with significant disruption of the sliding mass, such as rockfalls and topples) and Category II (i.e. rigid body movements, such as rotational or translational landslides). Particular emphasis is given to observations from recent Italian earthquakes (after 1984), which triggered a significant number of landslides (Umbria-Marche, 1997; Pollino, 1998; l'Aquila, 2009). The data points can be compared to the original upper bound relation suggested by Keefer and Wilson (black line) and a more conservative relation (red line) proposed by Silvestri et al. (2006), which takes into account the Italian national database. The data points for the landslides observed in this reconnaissance fall well below both of the proposed relations. Occurrences of additional landslides at larger epicentral distances cannot be excluded, because limited reconnaissance was undertaken in these regions.

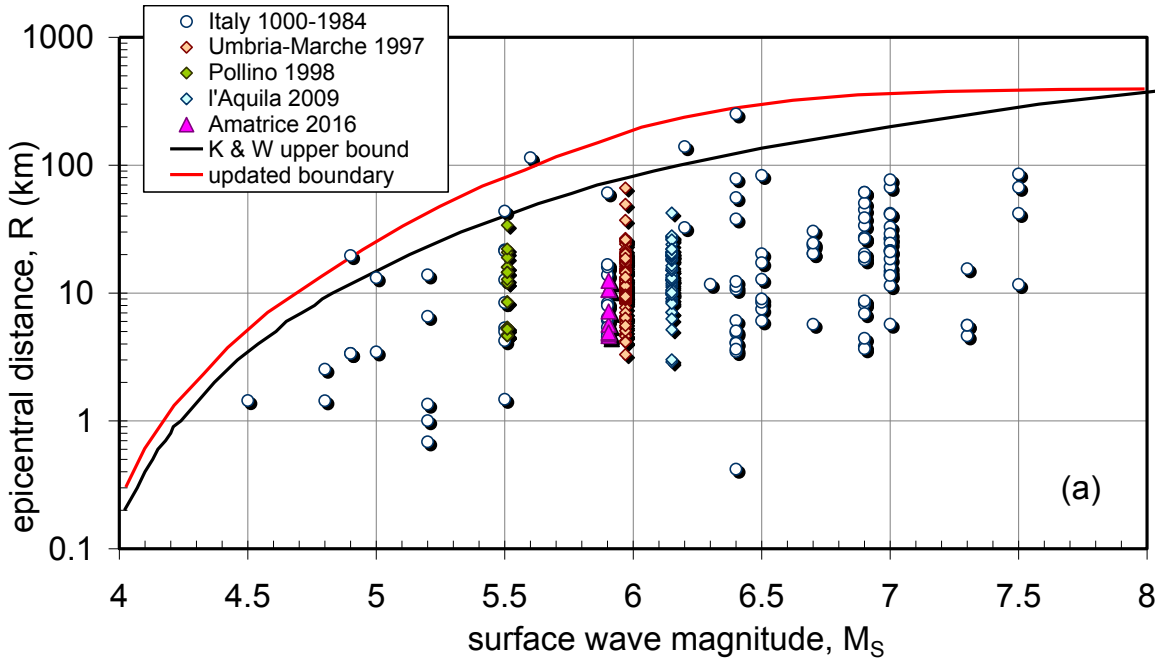

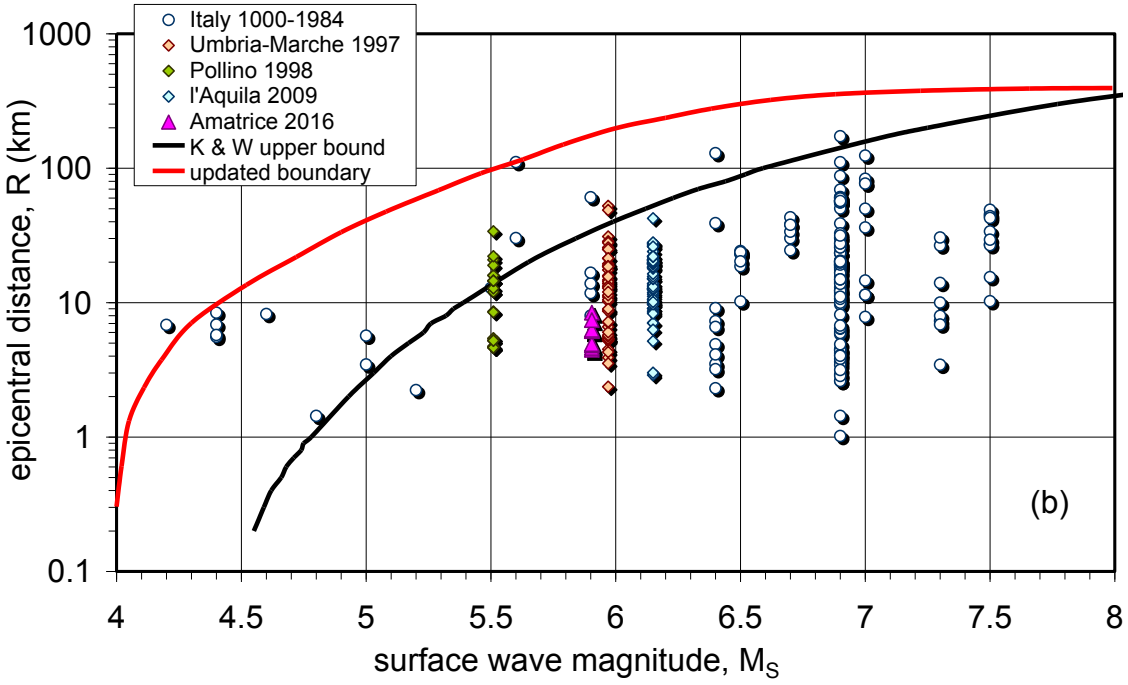

Figure 4.47. Data points showing surface wave magnitude and epicentral distance (km) for (a) Category I (rock falls and topples) and (b) Category II (rigid body landslides) inventoried in Italy together with those surveyed by GEER team after the 24 August 2016 earthquake (labelled as 'Amatrice 2016). The data are compared to upper bound relationships for Category I and II instability mechanisms proposed by Keefer and Wilson (1989) (lower curves) and those updated by Silvestri et al. (2006) (upper curves).

5.0 Performance of Building Structures and Damage Patterns

Principal authors: Shideh Dashti, Sebastiano Foti, Alessandro Pagliaroli, Anastasios Sextos

Contributing authors: Nicholas Alexander, Francesca Bozzoni, Massimina Castiglia, Filiberto Chiabrando, Anna Chiaradonna, Anna d'Onofrio, Raffaele De Risi, Filomena De Silva, Vincenzo Di Pietra, Luigi Di Sarno, Maria Giovanna Durante, Michalis Fragiadakis, Kevin Franke, Silvia Giallini, Nives Grasso, Elpida Katsiveli, Giuseppe Lanzo, Michele Mucciacciaro, George Mylonakis, Augusto Penna, Ioannis Psycharis, Brandon Reimschiissel, Filippo Santucci de Magistris, Stefania Sica, Armando L. Simonelli, Francesco Silvestri, Elisavet Vintzilaiou, Paolo Zimmaro

5.1. Introduction

The GEER team evaluated building damage patterns for villages in the epicentral region together with geological and topographical information, in order to gain insight into: 1) site response and amplification effects; 2) types of structures most vulnerable to earthquake shaking; and 3) types of retrofit most successful in limiting structural damage. In particular, significant attention was paid to the combined influence of geology, topography and structural vulnerability on the observed damage patterns. The reconnaissance approach involved aerial image analysis from Copernicus satellite images, Orthophotos, 3D texture models from drones (detailed in Chapter 4), detailed ground surveys, and general qualitative ground surveys. This section is the result of multi-organizational collaboration among GEER, EERI, Reluis, EUCenter, Center for Microzonation and its applications, Hellenic Association of Earthquake Engineering, and others that are gratefully acknowledged.

This chapter is organized as follows: Section 5.2 reviews types of masonry structures (these are the most commonly encountered structure type in the studied region) and the selected damage classification scheme; Section 5.3 describes result of damage and structure typology mapping in larger villages where detailed structure-by-structure mapping occurred; and Section 5.4 describes results of broader performance assessment where selected structures were inspected, but more detailed structure-by-structure mapping was not undertaken.

5.2. Types of Masonry Structures

The damage classification adopted in this report is based on the visual inspection of buildings. It follows the scheme provided by the Department of Civil Protection (DPC) in Italy for post-earthquake reconnaissance purposes. According to this scheme, as summarized in Table 5.1, the damage scale ranges from D0 (no damage) to D5 (collapse of the structure). The DPC scheme is comprised of four sections:

1. Description of the building: this section is focused on the description of data related to geometrical details (number of floors, height, area), age of building (and renovation), and its use (main purpose, number of units, utilization, occupancy and owner);

2. Type of construction: the classification is based on the structural type (masonry, RC frame, RC walls and steel frames), type of roofing, and regularity of the building;
3. Structure damage: the quantification of the damage is based on its extension and on the main structural components involved (vertical elements, slabs, stairs, roofing, and walls). This section also provides guidance on the overall damage level assignment (D0-D5)
4. Soils and foundations: this section is broadly focused on topographic conditions (crest, steep or smooth slope and level ground), and possible slope instability.

The main advantages of using one synthetic parameter (damage level) for each building are: *(i)* the identification of damaged patterns that, combined with geological information, can suggest the presence of site effects; and *(ii)* evaluation of vulnerability by buildings type.

Table 5.1. Definition of damage categories (adapted from Bray and Stewart 2000)

Damage Level	Description	Marker Color
D0	No damage	
D1	Cracking of non-structural elements, such as dry walls, brick or stucco external cladding	
D2	Major damage to the non-structural elements, such as collapse of a whole masonry infill wall; minor damage to load bearing elements	
D3	Significant damage to load-bearing elements, but no collapse	
D4	Partial structural collapse (individual floor or portion of building)	
D5	Full collapse	

5.3 Village-Specific Observations

This section describes observations from the larger villages, for which we sought to evaluate the spatial distribution of damage patterns. Each subsection below includes the following: a short description of the village; information on local geology; map of the city and damage patterns; types of structures damaged; and locations of geophysical tests, as applicable.

For each of the villages described in this section, GEER and its partners performed detailed structure-by-structure evaluations of damage levels and structural typologies within defined regions. The motivation for this mapping was to assess performance in an unbiased manner; the alternative of anecdotal inspections of particular structures within a region tends to produce an assessment that is biased towards those locations where damage occurred. The data from these detailed inspections is not presented in its entirety in this report, largely because it has not been

distilled yet into a publishable form. This information will be provided electronically in supplements in a later version of the document.

5.3.1. Accumoli

Accumoli is a small village of about 700 inhabitants located in the Rieti province. Apart from the main village, it is constituted by several small hamlets, namely: Collespada, Fonte del Campo, Grisciano, Illica, Libertino, Macchia, Poggio Casoli, Poggio d'Api, San Giovanni, Tino, Terracino, and Villanova.

We report here the results of detailed reconnaissance from the main village. An assessment of damage patterns at a regional scale is given in Section 5.4.2. The site is located near the epicenter of the 24 August 2016 mainshock.

Geological bedrock in the area consists of a turbiditic succession of Messinian age known as Laga Formation (or Laga Flysch), mainly composed of arenaceous and pelithic-arenaceous lithofacies. This formation is locally covered by fluvial deposits, detrital covers made of coarse calcareous/arenaceous debris sometimes in sandy matrix, or quaternary lacustrine sediments. The main village is located along an elongated WNW-ESE ridge at an altitude spanning from 890 to 860 m above sea level (ASL). In particular, most the village is located along a steep slope.

The village was reported to have suffered damages during the 14 January 1703 Valnerina earthquake (**M**=6.9) (Section 2.2). An excerpt of the historical seismicity as reported in the CPTI15 database maintained by INGV is reported in Figure 5.1.

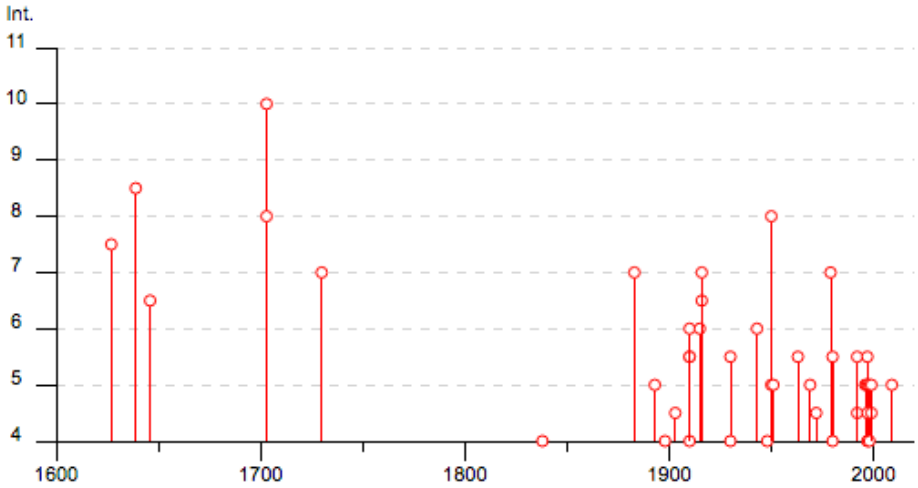

Figure 5.1. Historical seismicity in Accumoli (database CPTI15, Rovida et al., 2016).

The locations of some photographed representative structures within Accumoli are reported in Figure 5.2 on the ortho-image, obtained with a flight of an eBee lightweight fixed-wing UAV (Sections 4.3.1 and 4.4.6). Details (WGS-84 coordinates, damage level of buildings, and other notes) can be found in Table 5.2. Figure 5.3 shows an excerpt of the UAV-based 3D model of the

most damaged portion of Accumoli (easternmost part of the village). The pictures are shown in Figure 5.4. Only the eastern part of the village was accessible during the field survey.

The most severe damage was observed at the easternmost margins of the village, likely associated with the specific ground conditions. The presence of man-made fills is likely in the area, considering the local topography. The damage observed on the earth retaining walls at the eastern edge of the village may indicate possible relative movements associated with instabilities, as discussed further in Section 4.4.6. Damage in other portions of the village is more homogeneous, and local variations are likely associated with different building vulnerabilities.

Figure 5.2. Locations of representative structures inspected in the village (see Table 5.2 for details).

Figure 5.3. Excerpt of the 3D model with the most damaged portion of Accumoli (easternmost part of the village).

Table 5.2. Locations of representative structures (Figure 5.4) with damage descriptions

Picture	DATUM	Location		Damage Level
		Lat.	Long.	
P01	WGS-84	42.695561°	13.248314°	D5
P02	WGS-84	42.695010°	13.248600°	D2
P03	WGS-84	42.694972°	13.248886°	D3
P04	WGS-84	42.694611°	13.249071°	D3
P05	WGS-84	42.694635°	13.248798°	D4
P06	WGS-84	42.694215°	13.248842°	D3
P07	WGS-84	42.694304°	13.249263°	D3
P08	WGS-84	42.694428°	13.249379°	D3
P09	WGS-84	42.694325°	13.249507°	D3
P10	WGS-84	42.694073°	13.249509°	D4
P11	WGS-84	42.694346°	13.249726°	D3
P12	WGS-84	42.693962°	13.249787°	D5

P01

P02

P03

P04

P05

P06

P07

P08

P09

P10

P11

P12

Figure 5.4. Representative pictures taken in Accumoli during the GEER survey (see Table 5.2).

The level of damage increased from D1-D2 to D3-D4 moving downhill facing east. A tentative damage zonation is reported in Figure 5.5. A few cases of full collapse of vulnerable masonry buildings (Damage level D5) were observed along the eastern margin. These are also associated with relevant movements of backfill walls as observed in the 3D model. Damage patterns from the aerial image analysis from the Copernicus project were not well defined, as for other villages.

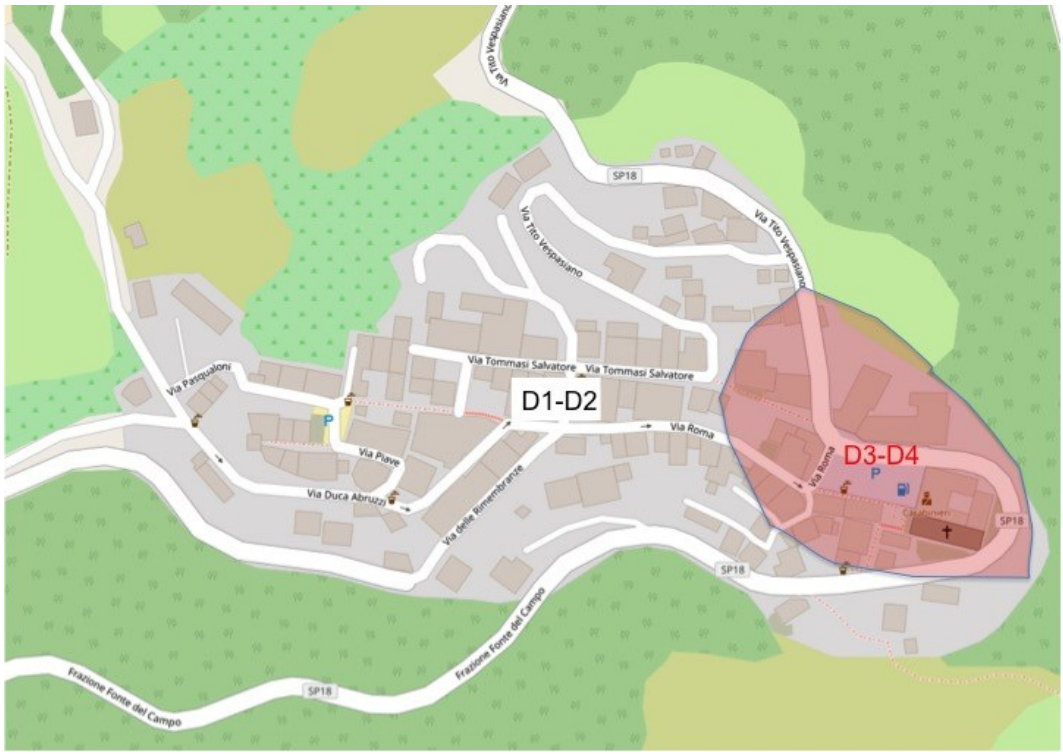

Figure 5.5. Damage zonation within the village of Accumoli.

5.3.2. Amatrice

The territory of Amatrice, including 49 hamlets or, as commonly defined, "villas", covers 174 km^2 of a basin located on the east border of the Lazio region. Archaeological discoveries show a human presence in the area of Amatrice since prehistoric times. Further, ruins of Roman buildings and tombs have been found in this area. Figure 5.6 shows a plan view of the city. The western part of the city has typical medieval arrangement with the main street Corso Umberto I, oriented along the longest dimension of the upland and some minor streets parallel and orthogonal to the principal one. Along the grid of straight streets, there are large and small buildings of relevant artistic value from the 16th, 17th, and 18th centuries. Consistent with their age, in the old center most of the structures were made of masonry, while houses and buildings in the eastern territory were built more recently with reinforced concrete. For the two largest magnitude events, **M**=6.1 and **M**=5.3, Table 5.3. shows fault surface projection distances (R_{JB}) of Amatrice and of the villages Collecreta, Cascello, Moletano, Retrosi, and Voceto.

Table 5.3. Source to site distance for the August 24 mainshock.

	Lat	**Lon**	R_{JB}
	°dec	**°dec**	**km**
Amatrice	42.628	13.292	9.48
Collecreta	42.630	13.324	9.66
Cascello	42.635	13.310	8.79
Moletano	42.627	13.324	9.66
Retrosi	42.623	13.316	10.16
Voceto	42.634	13.324	9.66

The Macroseismic Intensity (I_{MCS}) assessed for the sites varies from VII and VIII, as shown in the map in Figure 5.7 derived from Galli et al. (2016).

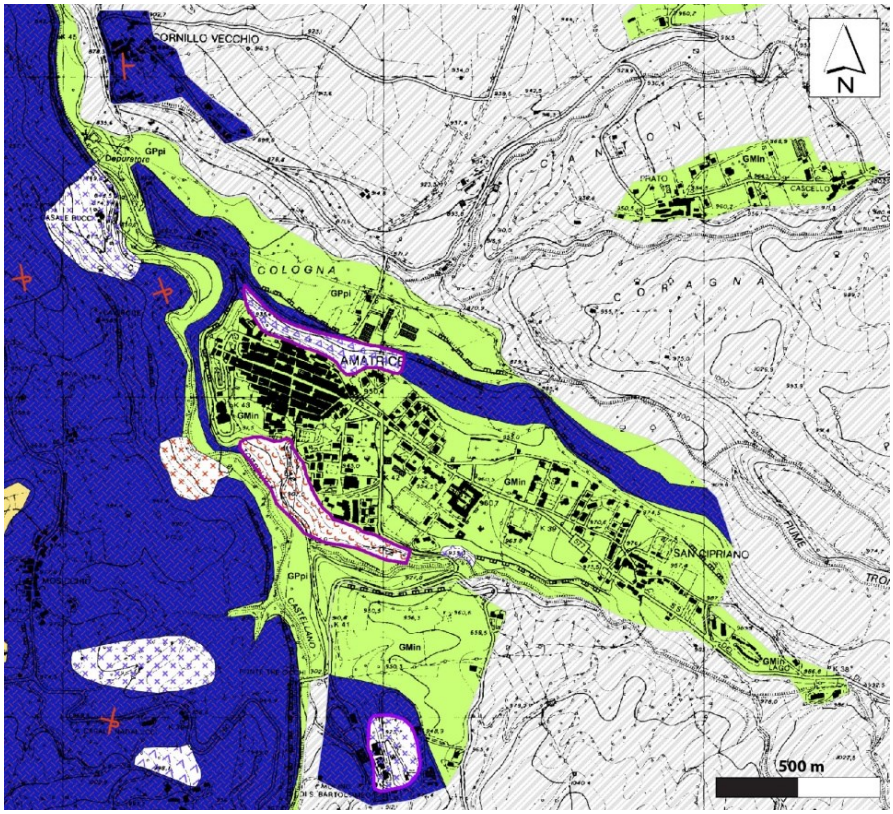

Legend

Covering terrains

- GP, pi — Poorly graded gravels, gravelsand mixtures, little or no fines; Floodplain (Holocene).
- GM, fd — Loamy gravels, poorly graded, gravel sand and silt mixtures; Detrital aquifer (Holocene).
- SM, ec — Silty sands, poorly graded sand–silt mixtures; Colluvial–Eluvial (Holocene).
- GM, in — Loamy gravels, poorly graded, gravel sand and silt mixtures; Intramontane basin (Upper Pleistocene).

Tectonic structural elements

- Direct fault inactive (presumed)
- Inverse fault inactive (presumed)

Surface and buried forms

- Morpholohgic Scarp Edge (>20 m)

Geological and hydrogeological elements

- 30 — Strata
- Overturned strata

Geologic Substrate

- SF — Highly fractured / altered
- ALS — Lithotype alternation, layered

Slope instabilities

- Collapse or orverturn – active
- Slipage – active
- Flow – quiescent
- Flow – quiescent
- Complex – active
- Complex – quiescent

Figure 5.6. Geological map of Amatrice village (Regione Lazio, 2016).

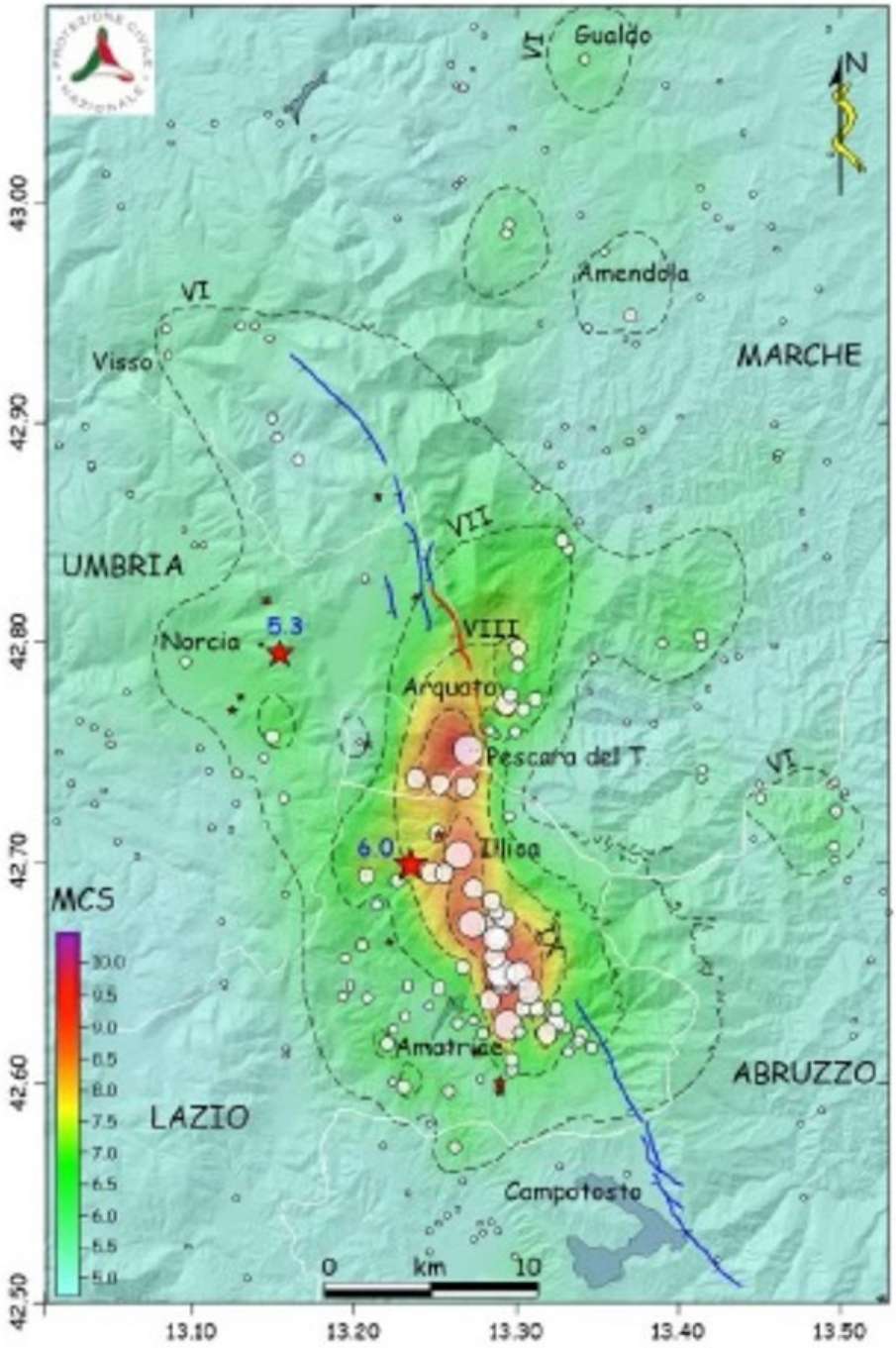

Figure 5.7. Macroseismic Intensity of the sites struck by the earthquake (Galli et al., 2016)

The center of the town is located on top of an upland (900-1000m ASL) above the confluence of Tronto and Castellano rivers. It lies on terraced alluvial soil of lacustrine-fluvial origin (GMin in the legend in Figure 5.6), which overlap the local substrate of Laga Flysch (ALS in Figure 5.6).

Field Survey at the perimeter of the Red Zone

A field survey was first conducted in a suburb of Amatrice, since the historic center (red zone) was initially not accessible (Figure 5.8). Different damage levels have been classified according to the categories reported by Bray and Stewart (2000). The variability of the damage is mainly associated with the different structural typologies. Indeed, all the fully collapsed structures were unreinforced masonry buildings (e.g., pictures P04 and P06 in Figure 5.9, coordinates listed in Table 5.4), while concrete structures suffered damage mostly to non-structural elements. In general, the detected damage can be attributed mainly to the vulnerability of the buildings, and no clear patterns of damage that would be suggestive of site amplification effects were detected. For this region, we did not undertake a detailed structure-by-structure survey, but instead documented the performance of a series of representative structures shown in Figure 5.9 and Table 5.4.

The building surveys conducted in the Amatrice suburb and elsewhere enable (1) detecting variable levels of building performance, including minor damages; and (2) checking of the damage levels assigned by others based on Copernicus satellite surveys (Figure 5.10). As expected, we found that structures with minor damage (D1-D2) were not mapped as such from satellite images. Moreover, the Copernicus satellite survey does not correctly classify the collapse-level damage states observed in some structure, two examples of which are P04 and P05 in Figure 5.9. Picture P04 shows a masonry structure collapsed under a heavy RC roof, which remained intact. In this case, the satellite survey did not recognize the totally collapsed building under the roof and classified the building as moderately damaged. Picture P05 shows a structure with partial collapse (D4), which had been identified as collapsed (D5) by Copernicus.

Major damage was observed in critical buildings, such as police stations (the one of the *Carabinieri* corps, which is a three-story masonry structure strengthened with steel ties, P15 and P16 in Figure 5.9, and the one of the Highway Patrols, P11) and a school that, despite previous interventions, collapsed partially (P17). Also evident are structural members that were individually strengthened (P18). Multi-story reinforced concrete buildings behaved relatively well, mainly exhibiting in-plane shear failure of infill panels (P19) and minor to moderate damage at their beam-column joints (P20).

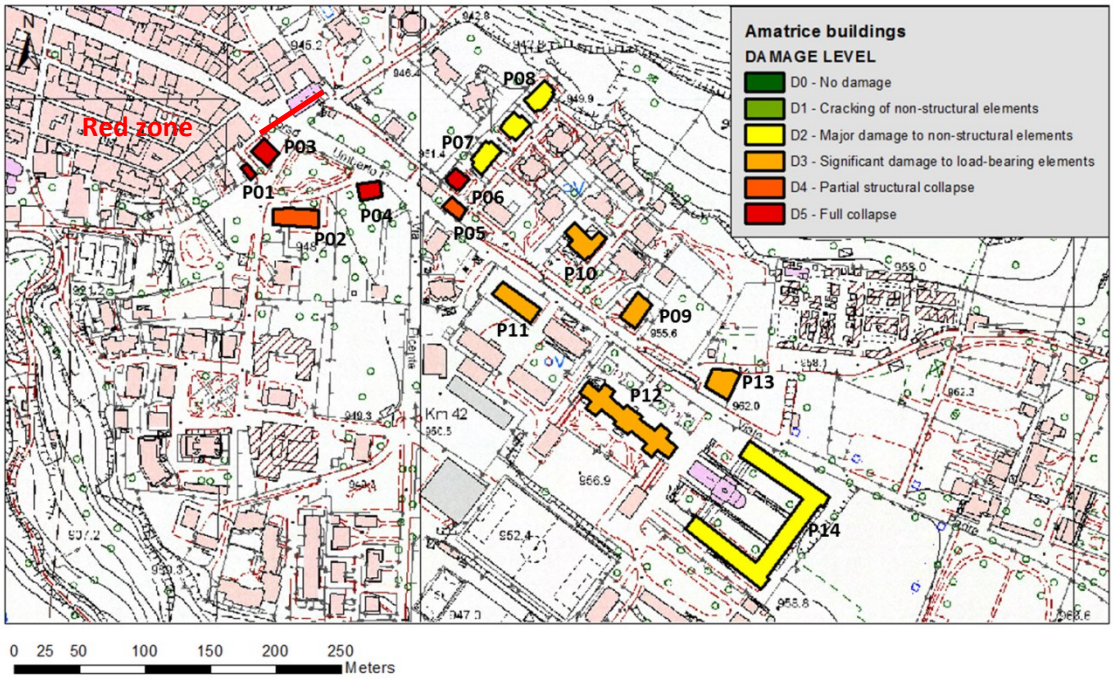

Figure 5.8. Locations of representative structures inspected in the village (see Table 5.4 for details).

Table 5.4. Locations of representative structures (Figure 5.9) with damage descriptions.

Picture	DATUM	longitude	latitude	Damage level	Note
P01	WGS- 84	13.29141	42.62804	D5	
P02	WGS- 84	13.29155	42.62845	D4	
P03	WGS- 84	13.29167	42.62806	D5	
P04	WGS- 84	13.2925	42.62806	D5	
P05	WGS- 84	13.29306	42.62778	D4	
P06	WGS- 84	13.29309	42.62791	D5	
P07	WGS- 84	13.2932	42.62821	D2	
P08	WGS- 84	13.29444	42.62694	D2	
P09	WGS- 84	13.29444	42.62722	D3	
P10	WGS- 84	13.29339	42.62788	D3	
P11	WGS- 84	13.29361	42.62722	D3	Police station
P12	WGS- 84	13.29639	42.62694	D3	
P13	WGS- 84	13.29578	42.62686	D3	
P14	WGS- 84	13.29553	42.62656	D2	
P15	WGS- 84	13.290809	42.62722	D3	Police station
P16	WGS- 84	13.290809	42.62722	D3	Police station
P17	WGS- 84	13.2913634	42.62684	D4	
P18	WGS- 84	13.2913634	42.62684	D3	
P19	WGS- 84	13.2901480	42.62609	D3	
P20	WGS- 84	13.2901480	42.62609	D3	

P01

P02

P03

P04

P05

P06

P07

P08

P09

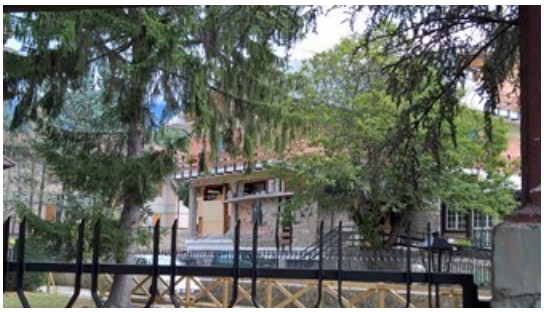

P10

P11

P12

P13

P14

P15

P16

P17

P18

P19

P20

Figure 5.9. Representative pictures taken in Amatrice during the survey (see Table 5.4)

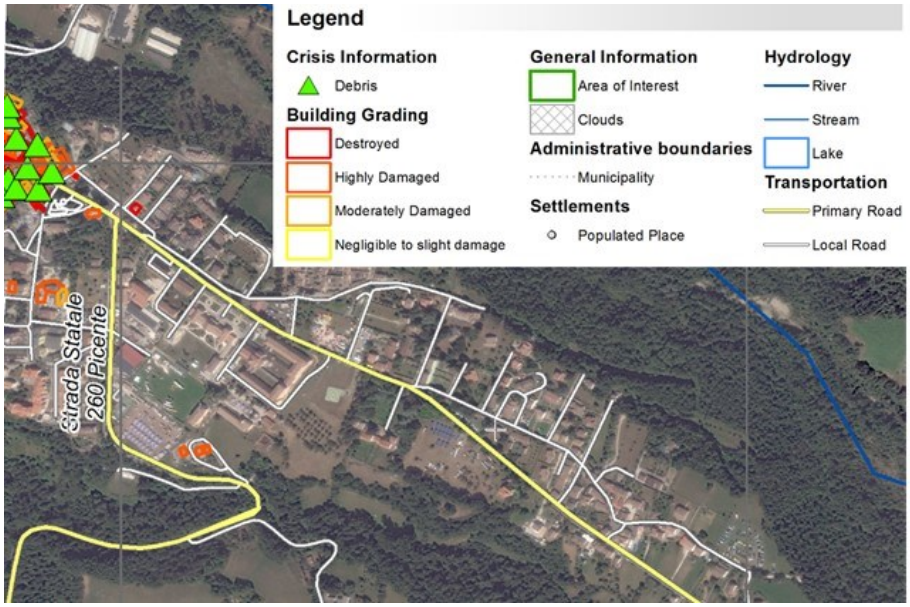

Figure 5.10. Damage pattern from Copernicus post event images for Amatrice suburb.

Field Survey within the Red Zone

During the second phase of the reconnaissance field mission detailed building-by-building inspections were performed within the Amatrice Red Zone (as shown in Figure 5.11 along with a pre-event aerial photo). It is noted that for safety purposes, access to the Red Zone was permitted to specific streets only, e.g., the main Amatrice market street, a number of perpendicular streets, as well as streets around the inner perimeter of the Red Zone. The steps of the detailed visual inspection of Amatrice were also followed in all other areas inspected by the group and are briefly summarized as follows: (a) Initialization of the field mission based on Copernicus aerial imaging, (b) geo-localization of the photoshoots, (c) identification of the structural typologies and translation of the Italian quick inspection sheet as described in the Field Manual for the Post-earthquake damage and short-term counter measures (AeDES form), (d) transformation of the AeDes form into an Access database for archiving and statistical post-processing, (e) completion of hardcopy AeDes forms in the field for reliability purposes, (f) correlation of the damage observed for each building with pre-event Google Street View photos, (g) definition of a quantitative weighting procedure to derive the global building damage at a scale of D0 to D5 based on the local damage identified according to the Italian quick inspection sheet, (h) generation of the spatial distribution of damage in the form of shape and KMZ files.

Figure 5.12 (top photograph) illustrates the extent of structural damage while the distribution of global damage is portrayed in lower figures (it is noted that the building sample is still being processed). Characteristic images of building collapses are shown in Figure 5.13 and Figure 5.14 (P21-P28) while corresponding coordinates are reported in Table 5.5. Of particular interest was the five story R/C building of P29-P30 in Figure 5.14 along the main market street, which exhibited major damage but did not collapse during the **M**6.1 main shock nor subsequent aftershocks. Unfortunately, it subsequently collapsed during the 26 October 2016 **M**6.1 event. A few buildings, recently restored, remained undamaged or suffered only minor damage, two of which are depicted in P31-P32. The same applies to the three-story steel building of P33-P34 (Figure 5.15) that experienced minor damage (i.e., shear failure of the infill panels and only minor buckling to one of its columns). The latter building was located very close to the R/C building of Hotel Roma, the town's main hotel, which collapsed (P35-P36 in Figure 5.15).

Figure 5.11. Overview of Amatrice Red Zone before and after the 24 August event.

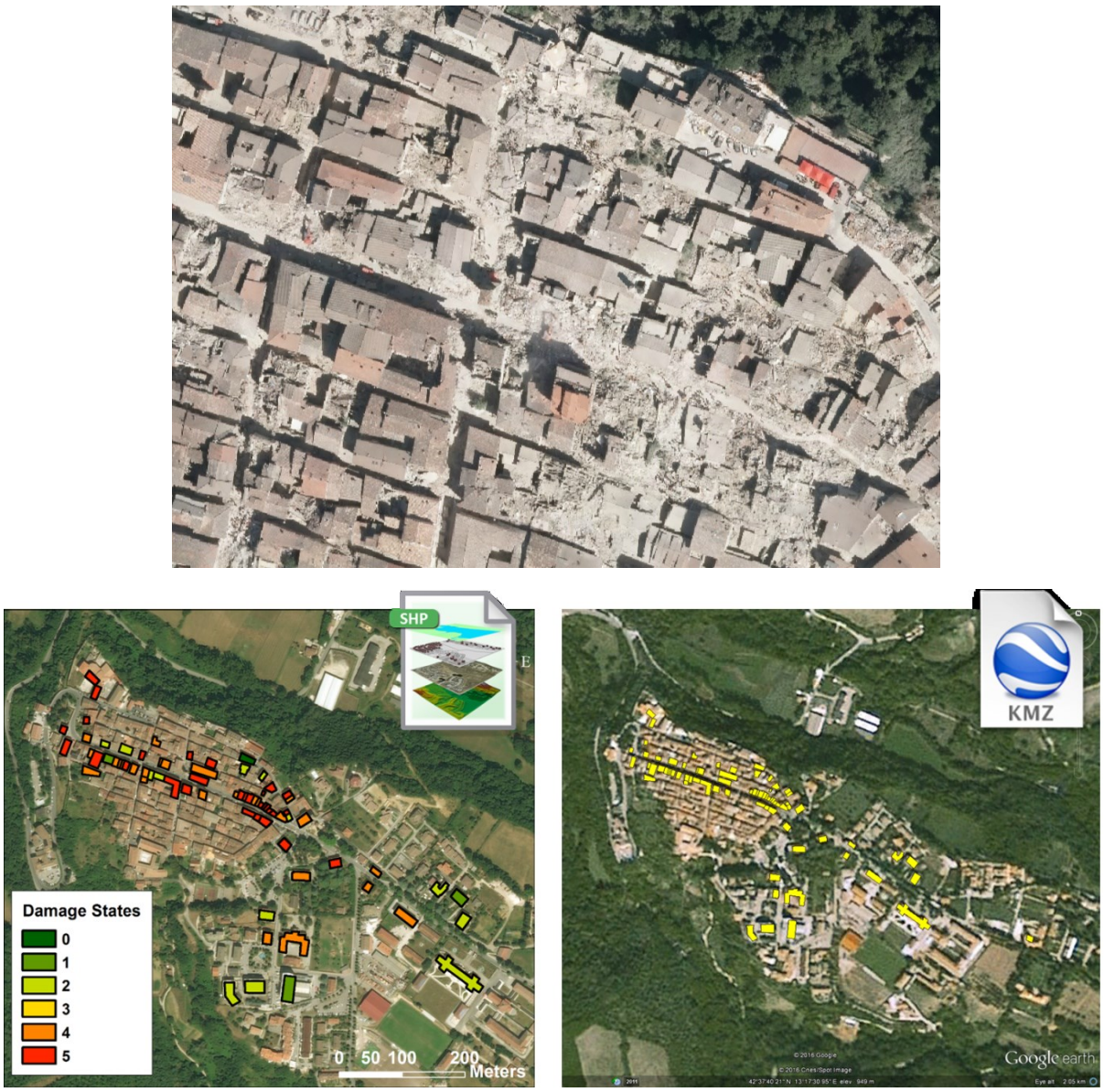

Figure 5.12. Overview of structural damage within the Amatrice Red Zone as seen by aerial image and after visual inspection (note that access to some streets within the Red Zone was not permitted and that additional inspection data are still under post-processing).

Table 5.5. Locations of representative structures (Figures 5.13-5.15) with damage descriptions.

Picture	DATUM	longitude	latitude	Damage level	Note
P21	WGS- 84	13.291061	42.62863	D4	
P22	WGS- 84	13.29059	42.62862	D5	
P23	WGS- 84	13.29043	42.62889	D5	
P24	WGS- 84	13.29016	42.62894	D5	
P25	WGS- 84	13.28724	42.62971	D5	
P26	WGS- 84	13.28732	42.63057	D5	
P27	WGS- 84	13.28937	42.62907	D5	
P28	WGS- 84	13.29051	42.62929	D5	
P29	WGS- 84	13.28952	42.62892	D5	
P30	WGS- 84	13.28952	42.62892	D5	
P31	WGS- 84	13.28840	42.62923	D2	
P32	WGS- 84	13.28801	42.62955	D2	
P33	WGS- 84	13.29037	42.62945	D2	
P34	WGS- 84	13.29037	42.62945	D2	
P35	WGS- 84	13.28799	42.62977	D5	
P36	WGS- 84	13.28799	42.62977	D4	

P21

P22

P23

P24

P25

P26

Figure 5.13. Photos of extensive building collapse within Amatrice Red Zone after the 24 August event.

P27

P28

P29

P30

P31

P32

Figure 5.14. Photos of building collapse (P27, P28) but also mahor (P29 and P30) and minor (P31 and P32) damage along the main market street of Amatrice.

P33

P34

P35

P36

Figure 5.15. Photos of a characteristic steel building with minor-to-moderate damage (DS2, P33-P34) next to Hotel Roma, a collapsed R/C building (P35, P36).

5.3.3. Arquata del Tronto

Arquata del Tronto is a small village of about 1200 inhabitants located in the Ascoli Piceno province. It consists of a large number of small hamlets, namely: Arquata, Borgo, Camartina, Capodacqua, Colle, Faete, Pescara del Tronto, Piedilama, Pretare, Spelonga, Trisungo, and Tufo e Vezzano. This section summarizes the results of the reconnaissance effort in Arquata and the adjacent hamlet of Borgo. These sites are located about 9 km northeast of the 24 August 2016 mainshock epicenter.

The geological bedrock in the area is represented by a turbiditic succession of Messinian age known as Laga Flysch mainly composed of arenaceous and pelithic-arenaceous lithofacies. This formation is locally overlain by fluvial deposits or by detrital covers comprised of coarse calcareous/arenaceous debris sometimes in a sandy matrix or quaternary lacustrine deposits. The main hamlet (Arquata) is located on an elongated WNW-ESE ridge at altitude of about 730 m ASL. In particular, the village is positioned at the SE part of the ridge approximately 100 m above the valley bottom. Most of the village is elongated almost perpendicular to the main axis of the ridge as shown in Figure 5.16. The geological map in the figure was compiled as part of a level 1 Seismic Microzonation (SM) study. The ridge is constituted by Laga Flysch (indicated as stratified bedrock “ALS” in the legend) while eluvial/colluvial gravelly soils (GC,ec) and fluvial gravels and sands (GW,tf) cover the flyschoid bedrock NE and SE of the ridge. The hamlet of Borgo is located only 200-300 m NE of Arquata and lies essentially on gravelly covers. The thickness of the covers is reported to be in the order of 10-30 m.

Gravitational slope instability phenomena involving the previously described debris covers are widespread in the area. A NNW-SSE oriented geological section crossing the Arquata and Borgo hamlets is shown in Figure 5.16. The village was reported to have suffered intensity IX MCS during the 14 January 1703 Valnerina earthquake (**M**=6.9) and VII-VIII MCS during the 12 May 1703 Valnerina earthquake (**M**=6). In the 4 July 1916 Monti Sibillini earthquake (**M**=4.8), intensity VII MCS was reported (Rovida et al. 2016).

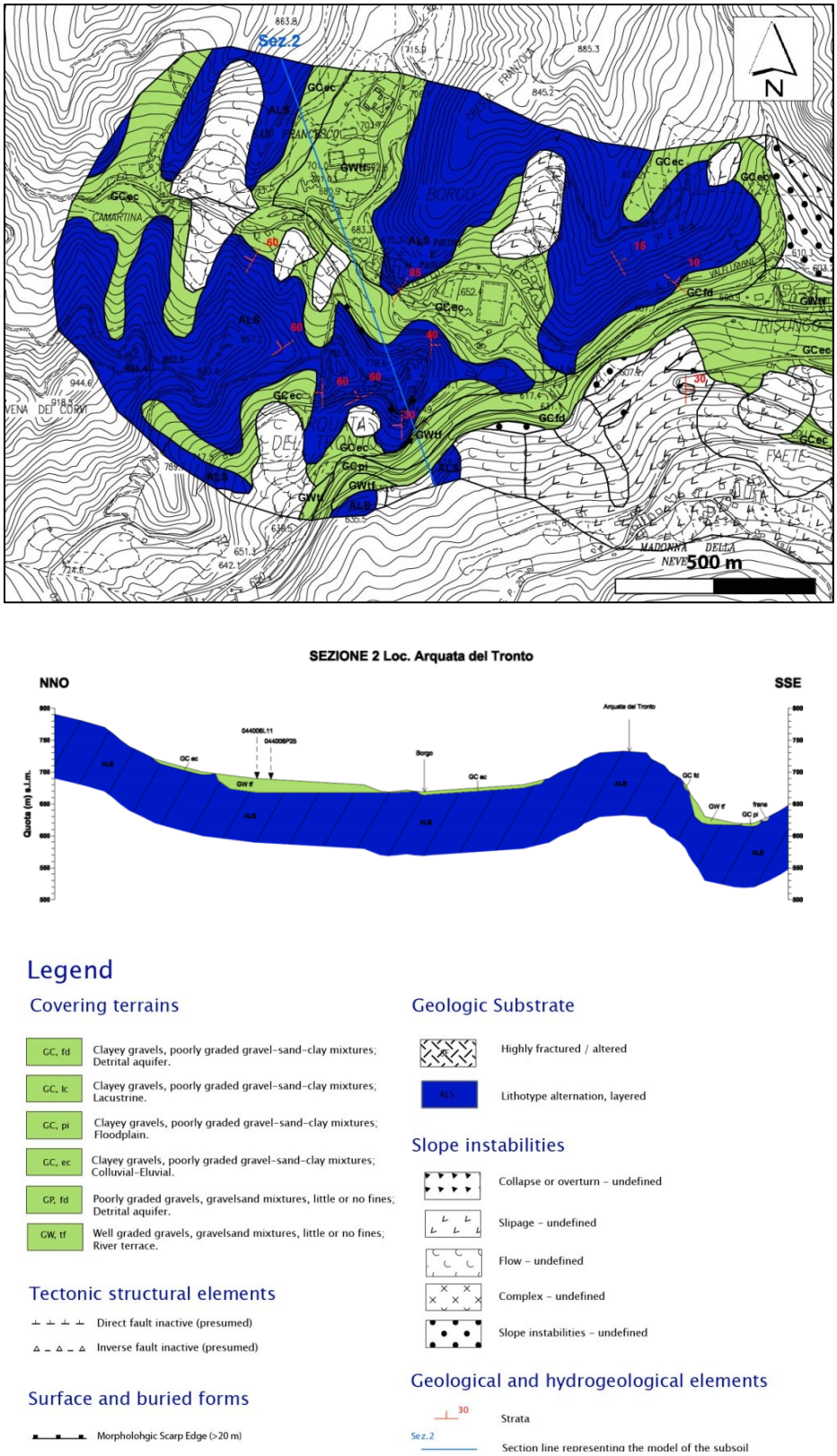

Figure 5.16. Geological map and cross-section of Arquata and Borgo hamlets (Regione Marche, 2014).

Locations of representative structures inspected in Arquata and Borgo by the GEER team are reported in Figure 5.17, while details (WGS-84 coordinates, damage level of buildings, other notes) are given in Table 5.6. The pictures are presented in Figure 5.18. The area around P15 (especially the zone NE of this point) had limited access on the date of the survey. The village consisted mainly of un-reinforced masonry structures, 2-3 stories in height. Very few of the structures were retrofitted with through-going iron bars (for instance P4). Isolated relatively modern reinforced concrete structures were found (see P08) showing negligible or low damage.

Figure 5.17. Locations of representative structures inspected in the village (see Table 5.6 for details).

Table 5.6. Locations of representative structures (Figure 5.18) with damage descriptions

Picture	DATUM	Location		Damage Level	Notes
		Lat.	Long.		
P01.jpg	WGS-84	42.770325°	13.295548°	-	panoramic view of the village
P02.jpg	WGS-84	42.775114°	13.295960°	D1	
P03.jpg	WGS-84	42.774799°	13.295947°	D1	
P04.jpg	WGS-84	42.774552°	13.296814°	D2	
P05.jpg	WGS-84	42.775631°	13.295103°	D2	
P06.jpg	WGS-84	42.776332°	13.293630°	D3	
P07.jpg	WGS-84	42.775636°	13.293699°	D3	
P08.jpg	WGS-84	42.775376°	13.294010°	D0	
P09.jpg	WGS-84	42.772017°	13.296579°	-	collapse of wall, permanent deformations of backfill
P10.jpg	WGS-84	42.772398°	13.296700°	D4	
P11.jpg	WGS-84	42.772787°	13.296941°	D4	
P12.jpg	WGS-84	42.772008°	13.296221°	D5	
P13.jpg	WGS-84	42.772387°	13.296340°	D5	
P14.jpg	WGS-84	42.772761°	13.296606°	D4	
P15.jpg	WGS-84	42.772398°	13.295842°	D2-D3	

P01

P02

P03

P04

P05

P06

P07

P08

P09

P10

P11

P12

P13a

P13b

P14

P15

Figure 5.18. Representative pictures taken in Arquata and Borgo during the survey (see Table 5.6).

The village was significantly damaged by the mainshock. However, the degree of damage to buildings is quite variable in space. A tentative damage zonation is reported in Figure 5.19. The hamlet of Borgo suffered minor damage (mainly cracking of non-structural elements) and no collapses were observed. The level of damage slightly increased form D1-D2 to D2-D3 moving in the NW direction. Arquata, founded on top of the ridge, was highly damaged. Several un-reinforced masonry structures were partially or fully collapsed (P10-P14). A few cases of retaining wall failures along the road leading to the village were observed, which consisted of permanent deformation of the wall as a whole and collapse of the upper part of the wall. Some buildings survived the event but appeared to have approached the point of collapse or severe damage (see P11 for instance). The level of damage decreased away from the edge of the cliff (P15), although this area was not fully accessible on the date of our survey.

During the 1703 earthquake, Arquata had experienced major damage (IX MCS) in the Borgo hamlet (VII-VIII MCS).

Damage patterns evaluated from aerial image analysis of Arquata are presented in Figure 5.20. No information is provided for Borgo. The higher degree of damage in Arquata, located near the top of the ridge, relative to Borgo was captured on average. Again, a decreasing degree of damage was observed away from the edge. The cases of full collapse were generally captured by the aerial image analysis (P13 and P14 were reproduced, while P12 was reported as highly damaged). The degree of damage to highly damaged and partially collapsed buildings was sometimes underestimated and identified as “negligible to slight damage” (e.g., P11).

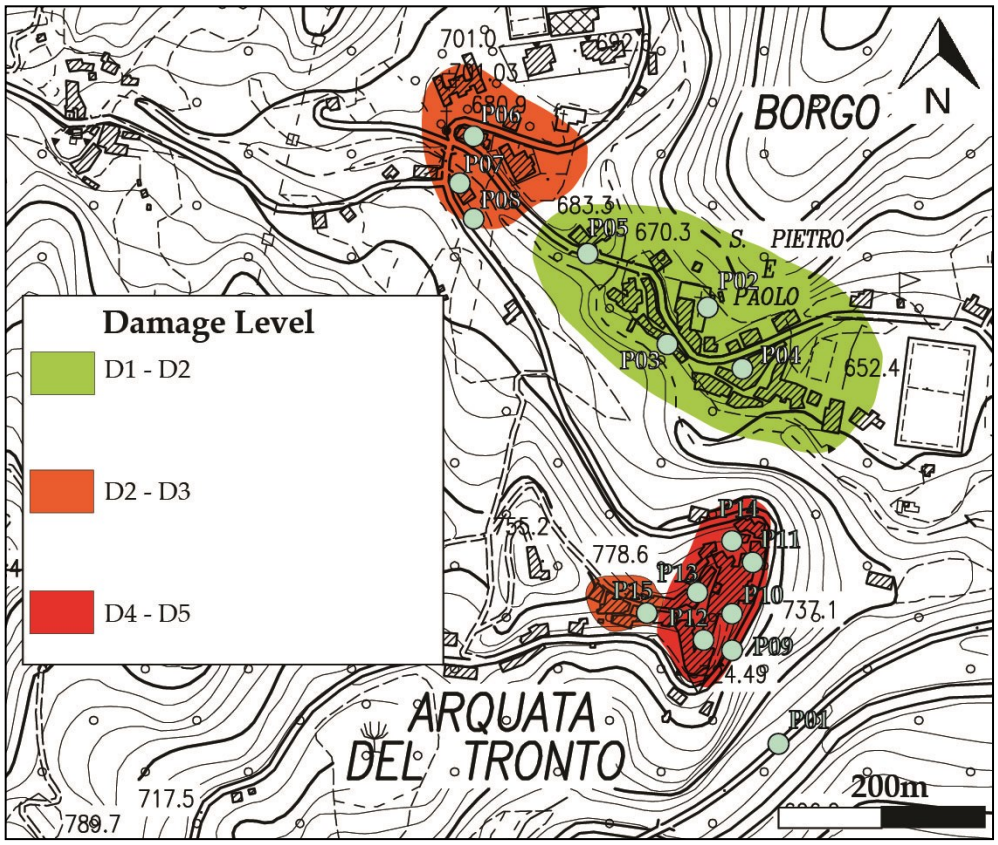

Figure 5.19. Damage zonation within the villages of Arquata and Borgo.

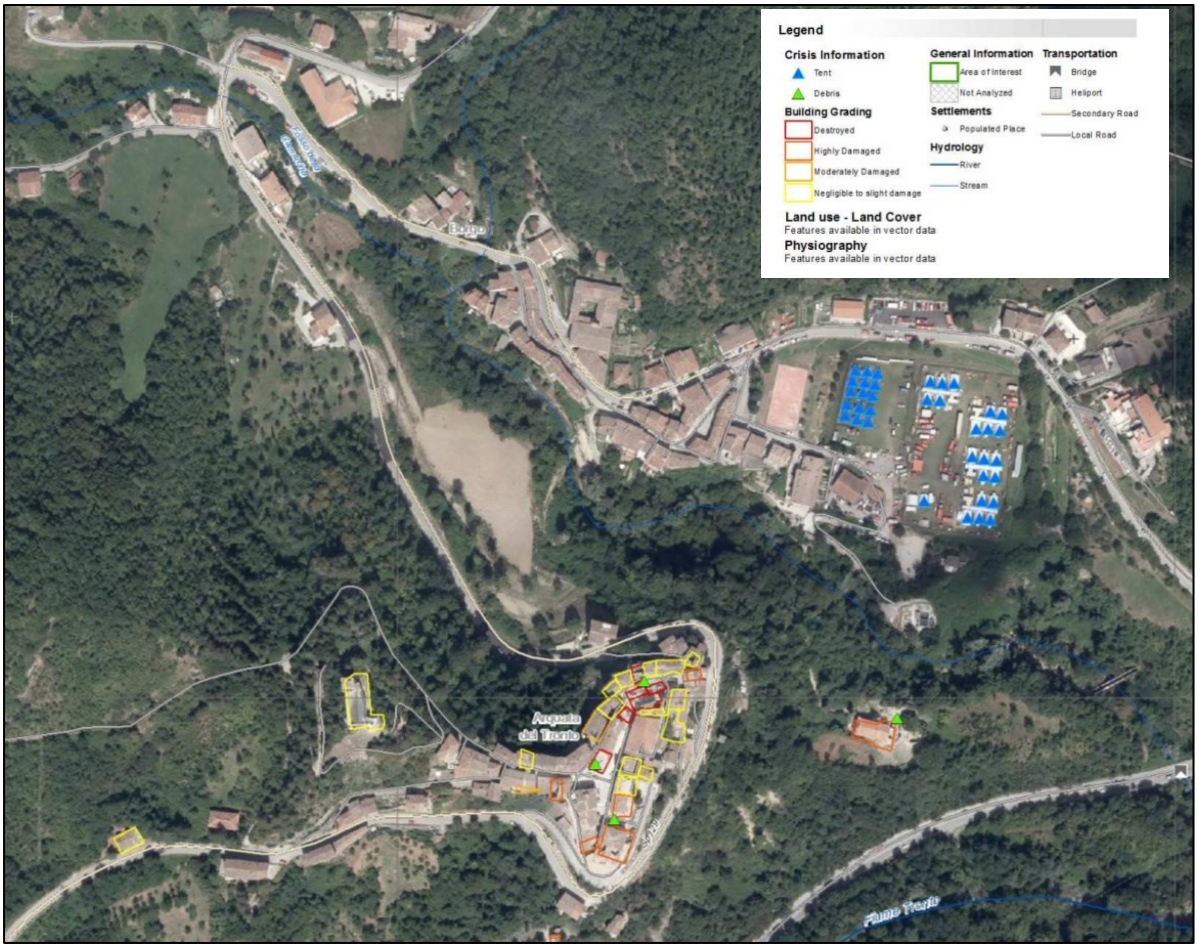

Figure 5.20. Damage pattern from Copernicus post event images (http://emergency.copernicus.eu/mapping/list-of-components/EMSR177/ALL/EMSR177_19ARQUATADELTRONTOAERIAL)

Four noise measurements were carried out during the survey in Borgo and Arquata (see Figure 5.21 for locations). A portable Tromino tomograph was employed and the total duration of each measurement was approximately 15 minutes. Horizontal-to-vertical (H/V) spectral ratios were computed by using the geometrical mean of horizontal components. Moreover, in order to investigate preferential directions of the amplification (i.e., polarization of ground motion), H/V ratios were computed by rotating the horizontal component between 0° and 180° (directional or polar HVSR). Both H/V and polar H/V are reported in Figure 5.22.

Figure 5.21. Locations of representative noise measurements carried out in the village.

No significant H/V peaks can be observed in T1 measurements. A pronounced H/V peak was identified at about 3-4 Hz in T2, indicating possible site effects that may have contributed towards the damage observed in the NW portion of the Borgo hamlet. In this area, an MASW test was carried out in the level 1 seismic microzonation study, which highlighted an impedance contrast between gravelly covers (thickness in the range 12-18 m and Vs=200-300 m/s) and the underlying Flysch bedrock (Vs≈800 m/s). The fundamental frequency of the gravel cover reasonably matches that measured from H/V.

In Arquata, two noise measurements were carried out (T3 and T4) both of which indicate H/V peaks around 3 Hz, with horizontal motion polarized in the NS direction, i.e., roughly perpendicular to the axis of the major ridge. Close to the edge, a second peak at about 10 Hz was observed, again with NS polarization. These results are preliminary and the HVSR technique for complex topographies is far from ideal for the applicability of the method. Similar results for other regions have been obtained previously (Pagliaroli et al. 2015).

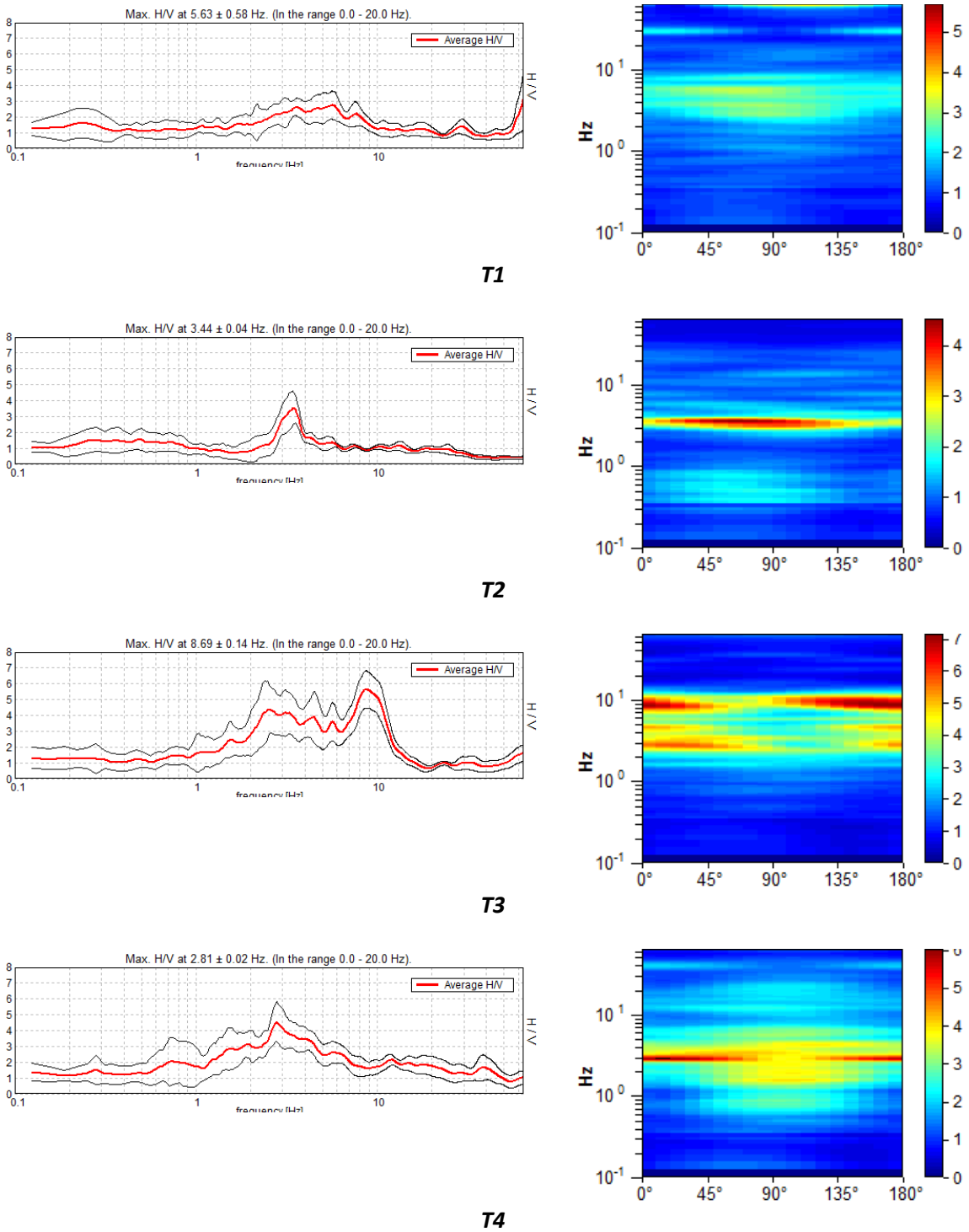

Figure 5.22. Noise measurements results in terms of H/V spectral ratio (on the left column) and H/V polar plots (on the right).

It appears that the major damage in Arquata may be partially related to topographic amplification effects. However, in this area, the buildings were also slightly more vulnerable compared to Borgo: no reinforced masonry structures were identified in the severely damaged area. Iron bar-reinforced buildings were observed only in Borgo, whereas isolated concrete structures and more recently constructed masonry buildings were found in Arquata. The combination of topographic amplification and greater structural vulnerability may explain the significant differences in damage level observed in the two hamlets. Moreover, the non-uniform damage patterns observed in Borgo can be tentatively explained by some stratigraphic amplification effects in the NW portion of the hamlet, roughly supported by geophysical data.

5.3.4. Pescara del Tronto (Arquata del Tronto)

Pescara del Tronto is a small village included in the Comune of Arquata del Tronto. The geological model (Figure 5.23) shows that the geologic bedrock (ALS) in the area (Laga Formation), is bordered on the SE by terraced alluvial deposits of the Tronto River (GW, tf) and from slope debris (GC, ec) and detrital covers (GP, fd).

The geological setting is complex due to convergence of the two mountain ridges – a calcareous ridge of the Sibillini Mountains and a turbiditic ridge of the Laga Mountains, oriented respectively NNE-SSW and NW-SE (Figure 5.24). The welding of these two structures was produced by the great Sibillini thrust that overlaps the calcareous lithotypes above the turbiditic. Toward the mountain, on the calcareous lythotypes of the slope, it is possible to observe a large landslide crown between the heights of 900 and 1150 m ASL. It seems to be generated, given its articulated configuration, by the union of several complex and probably rotational-translational gravitational phenomena, whose evidence (benches, counter-slopes, and high scarps) are still present along its slope. In Figure 5.24, on the bottom part, the extremely complex kinematics of these phenomena is presented: 1) initial rotational-translational slide that overlapped the calcareous plate onto an eluvial-colluvial “bed” made of mainly pebbly-sandy-silty material; 2) activation of slides–flows with shear planes occurring within the eluvial-colluvial coverings and/or in the top levels of the turbidic bedrock; 3) passive transport of the calcareous plate by the above mentioned slide-flow phenomena along a gently dipping slope; and 4) successive phases of valley incision, during the late Pleistocene and the Holocene, which produced erosion processes at the foot of the “plate” and triggered gravitational slumping of the plate itself producing numerous benches and scarps.

Limited information about historical earthquakes is available. The village was reported to have experienced IX MCS during the 14 January 1703 **M**6.9 Valnerina earthquake and damage of VII MCS during the 19 December 1941 **M**5.0 Monti Sibillini earthquake (Rovida et al., 2016).

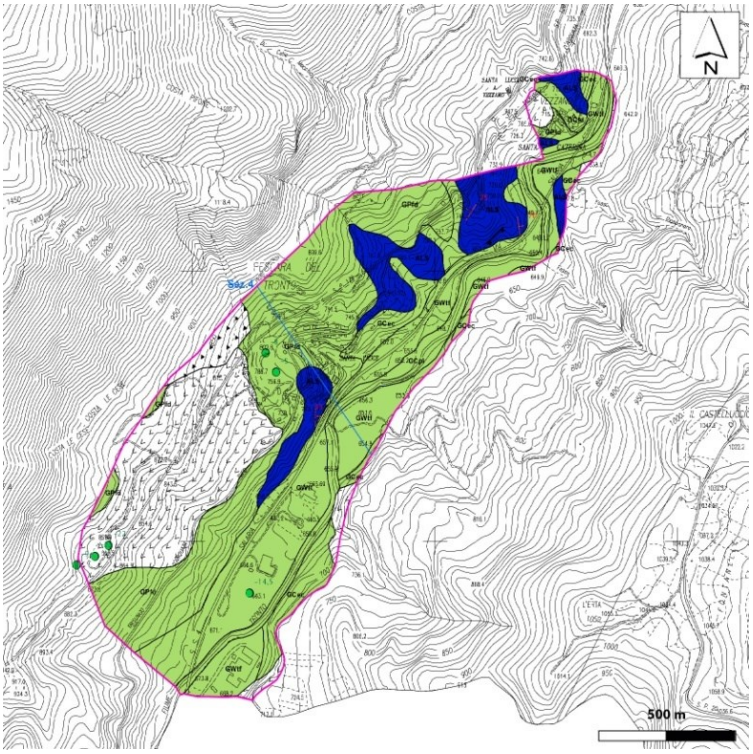

Legend

Covering terrains

- GC, fd — Clayey gravels, poorly graded gravel–sand–clay mixtures; Detrital aquifer.
- GC, lc — Clayey gravels, poorly graded gravel–sand–clay mixtures; Lacustrine.
- GC, pi — Clayey gravels, poorly graded gravel–sand–clay mixtures; Floodplain.
- GC, ec — Clayey gravels, poorly graded gravel–sand–clay mixtures; Colluvial–Eluvial.
- GP, fd — Poorly graded gravels, gravelsand mixtures, little or no fines; Detrital aquifer.
- GW, tf — Well graded gravels, gravelsand mixtures, little or no fines; River terrace.

Tectonic structural elements

- Direct fault inactive (presumed)
- Inverse fault inactive (presumed)

Surface and buried forms

- Morpholohgic Scarp Edge (>20 m)

Geologic Substrate

- Highly fractured / altered
- Lithotype alternation, layered

Slope instabilities

- Collapse or overturn – undefined
- Slipage – undefined
- Flow – undefined
- Complex – undefined
- Slope instabilities – undefined

Geological and hydrogeological elements

- 30 — Strata
- Sez.4 — Section line representing the model of the subsoil
- -12 — Depth (m) of investigation or well that has reached the Geologic Substrate

Figure 5.23. Geological map and cross-section of Pescara del Tronto (Regione Marche, 2014).

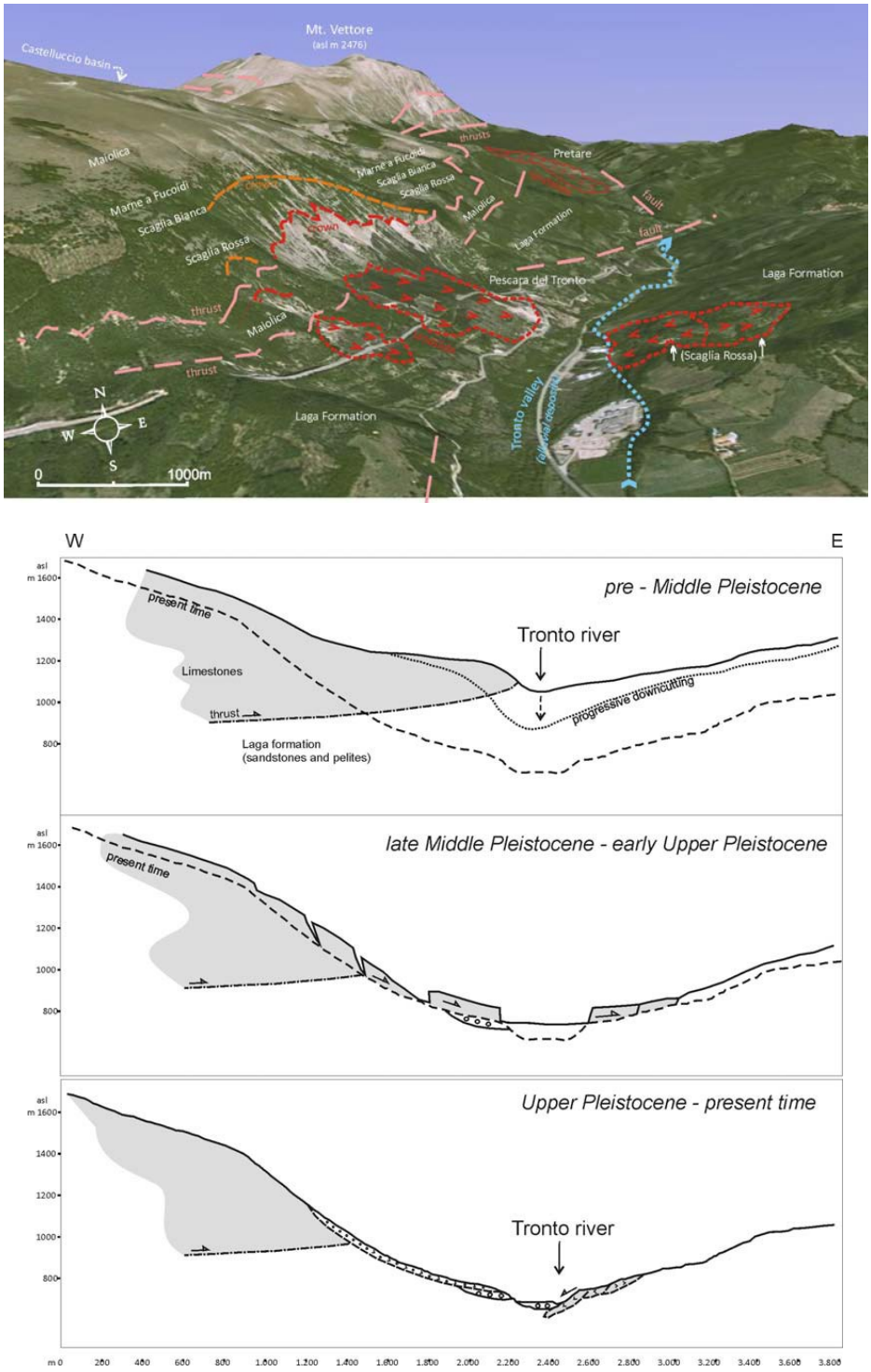

Figure 5.24. Pescara del Tronto: in the upper part geomorphological setting; in the bottom interpretative sketch of the mass movement (Aringoli et al., 2010).

The site is located about 6 km northeast of the 24 August 2016 mainshock epicenter. The locations of some representative structures surveyed in Pescara are reported in Figure 5.25, with details (WGS-84 coordinates, damage level of buildings, other notes) in Table 5.7. The pictures are reported in Figure 5.26. The most damaged area (southern part of the village, see P09 and P13) was not accessible on the date of the survey, although from afar we observed almost total destruction of the southern part of the village and the widespread presence of rubble.

Buildings in the village mainly consisted of un-reinforced masonry structures 2-3 stories in height. Very few of the structures were retrofitted (see for instance P11). Isolated, relatively modern reinforced concrete structures can be found along the road to access to the village and were subjected to relevant damage (P01).

Figure 5.25. Locations of representative structures inspected in the village (see Table 5.7 for details)

Table 5.7. Locations of representative structures with damage descriptions.

Picture	DATUM	Location		Damage Level	Notes
		Lat.	Long.		
P01	WGS-84	42.753147°	13.273536°	D3	
P02	WGS-84	42.752496°	13.271350°	D3	
P03	WGS-84	42.752434°	13.270156°	D2	
P04	WGS-84	42.752046°	13.270447°	D2-D3	*Partial collapse of the roof*
P05	WGS-84	42.752469°	13.272192°	D4	
P06	WGS-84	42.752295°	13.272490°	D5	
P07	WGS-84	42.751717°	13.270616°	-	*collapse of retaining wall (size: 0.25x1x5 m)*
P08	WGS-84	42.751558°	13.271005°	D5	
P09	WGS-84	42.750950°	13.270979°	D4-D5	
P10	WGS-84	42.751137°	13.270225°	D4-D5	
P11	WGS-84	42.751332°	13.271040°	D3	
P12	WGS-84	42.751986°	13.271575°	D4-D5	
P13	WGS-84	42.750423°	13.271891°	D4-D5	

P01

P02

P03

P04

P05

P06

P07

P08

P09

P10

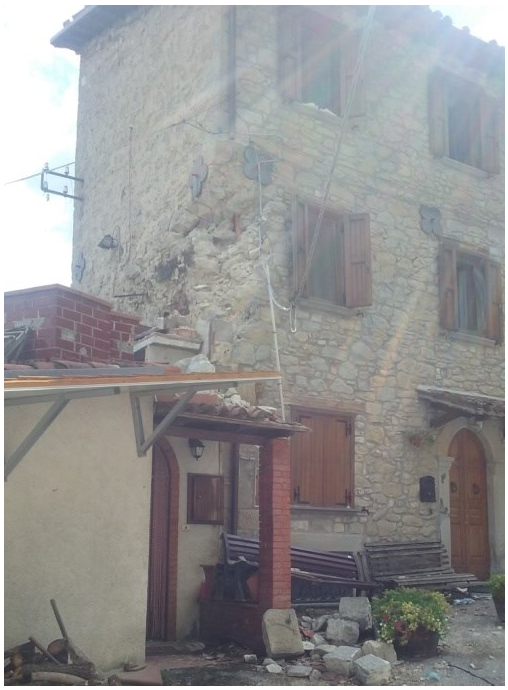

P11

P12

P13

Figure 5.26. Representative pictures taken in Pescara del Tronto during the survey.

The village was extensively damaged by the mainshock, with the degree of damage greater than or equal to D3 in most places. A tentative damage zonation in this area is reported in Figure 5.27. On the road leading to the southern part of the hamlet (P01-P06) the level of damage seemed slightly lower; partial or full collapse (P02, P05 and P06) was observed together with smaller degrees of damage (P03, P04). It should be noted that the only concrete building in the village was subject to significant damage to beam-column nodes (D3 damage, see P1). The southern part of the hamlet was almost completely destroyed, ranging from partial to full collapse (P09-P13). These areas were not accessible to the GEER team, but the patterns can be

identified from the 3D model of the village built from drone flights and reported in Figure 5.28 (further details in Chapter 4).

Damage patterns from aerial image analysis of Pescara are reported in Figure 5.29. The major damage in the southern portion of the village was well captured. As observed for Arquata del Tronto, the buildings with minor damage were not always correctly identified (e.g., P03 not captured by aerial analysis while P04 was identified as highly damaged).

The 3D model clearly showed complex landslides affecting the southern part of the village (see also Section 4.4.5). A photograph taken form Salaria road close to the Tronto river at the southern toe is presented in Figure 5.30. Moreover, tension cracks were observed to be widespread in the hamlet. The subsoil in the area affected by mass movement is quite complex and has not been studied. In addition to the flyschoid bedrock and slope debris deposits, a preliminary geologic survey highlighted in the area the presence of a travertine bank and highly heterogeneous anthropic covers.

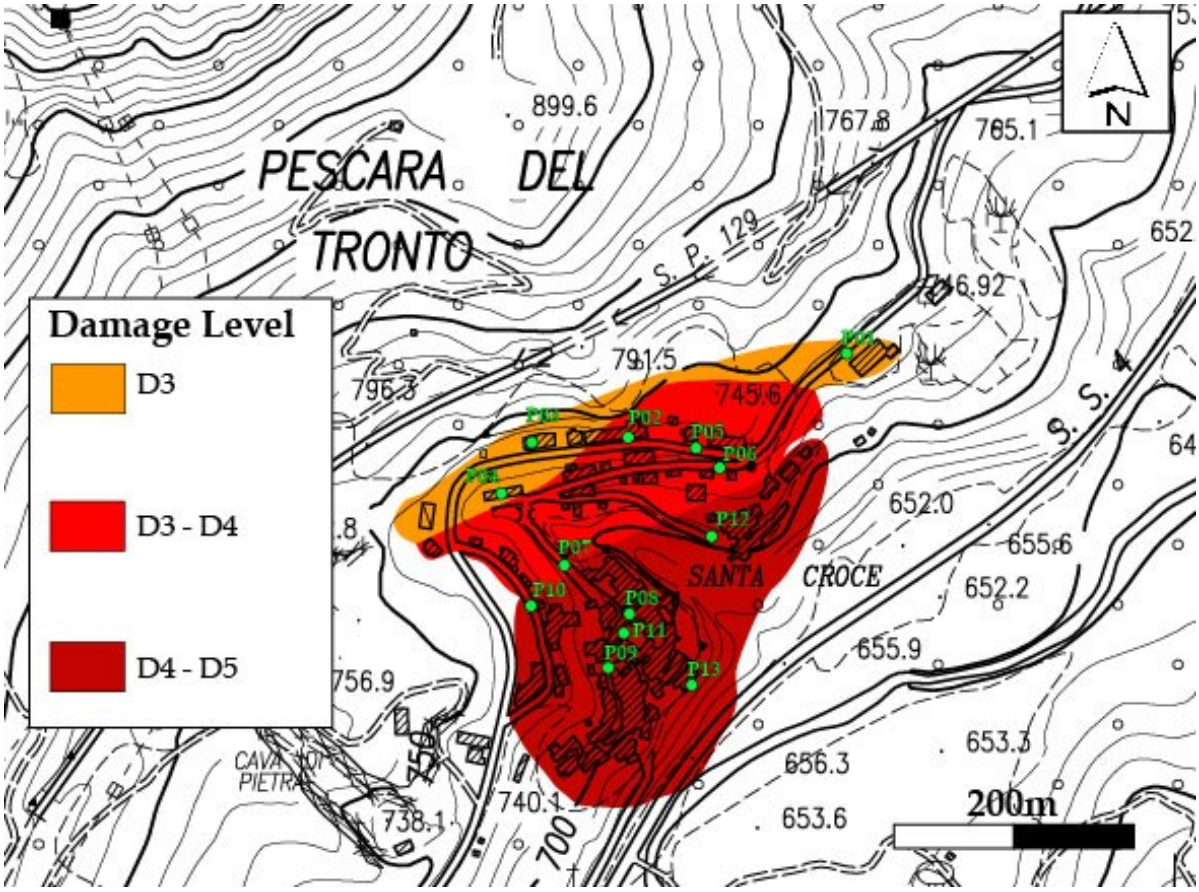

Figure 5.27. Tentative damage zonation within the village of Pescara del Tronto.

Figure 5.28. 3D model from drone flights on the village of Pescara del Tronto.

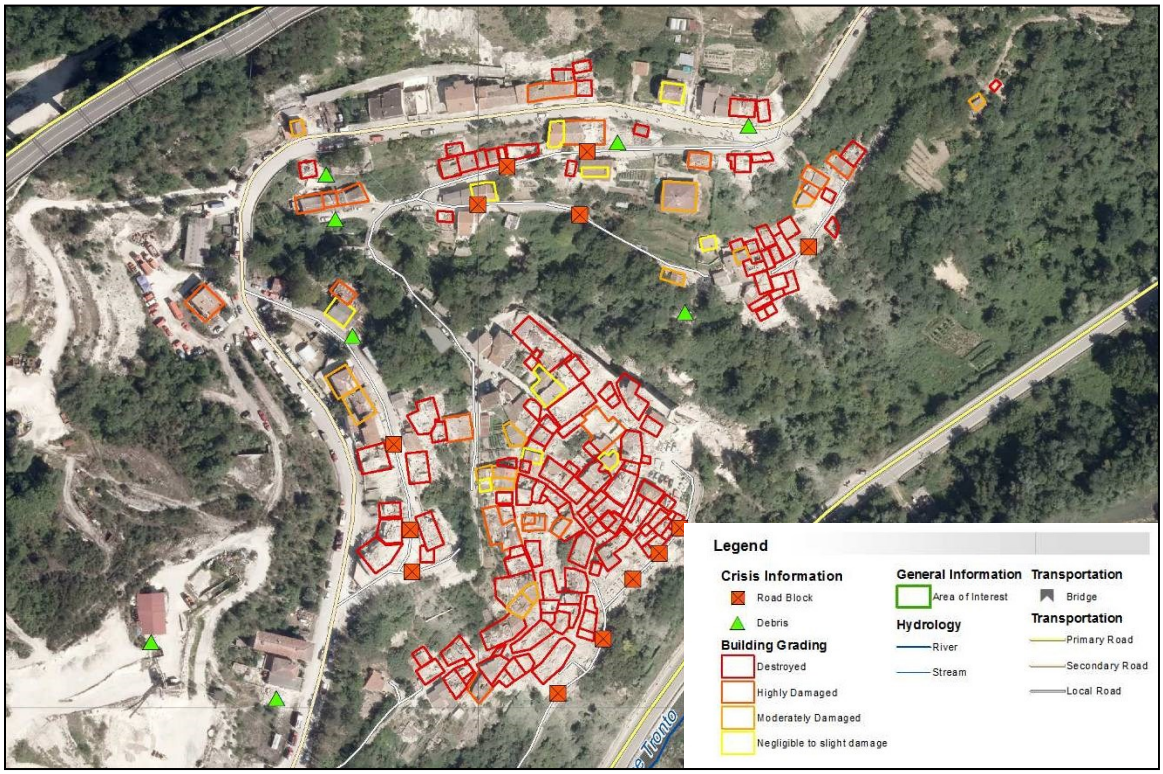

Figure 5.29. Damage pattern from Copernicus post event images (http://emergency.copernicus.eu/mapping/list-of-components/EMSR177/ALL/EMSR177_17PESCARADELTRONTOAERIAL).

In Pescara del Tronto, the GEER team collected 4 noise measurements (Figure 5.31) using a three-component Tromino® tromograph. The methodology used for these measurements is the same as that described for Arquata del Tronto. Both H/V and polar H/V are reported in Figure 5.32. No significant H/V peaks can be observed in the measurements, which suggests a lack of stiffness contrast between slope debris-detrital covers and the underlying Flysch bedrock, at least in the investigated area. However, the complex subsoil in the most damaged southern portion of the village (in which measurements could not be carried out) may differ and be capable of producing stratigraphic and topographic site effects. As noted previously, the major damage in this area was accompanied by significant mass movements and permanent ground deformations to rock and soil deposits.

Figure 5.30. Landslide affecting the southern portion of Pescara del Tronto.

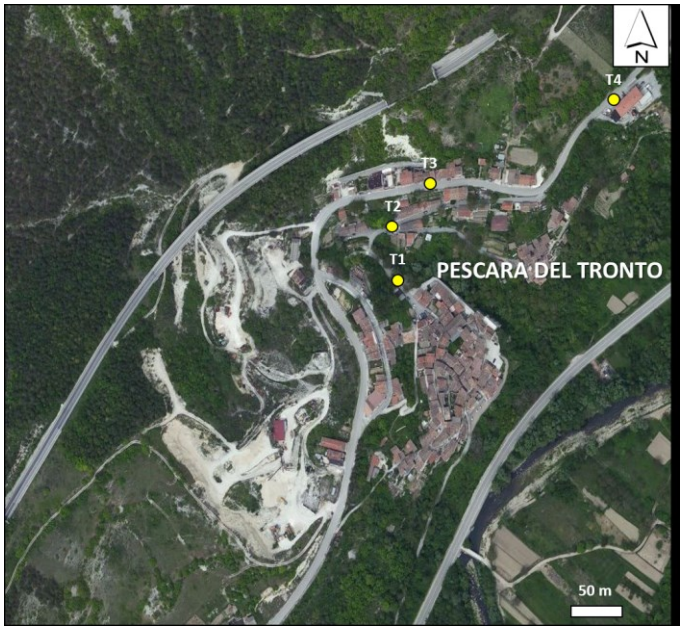

Figure 5.31. Locations of representative noise measurements carried out in the village.

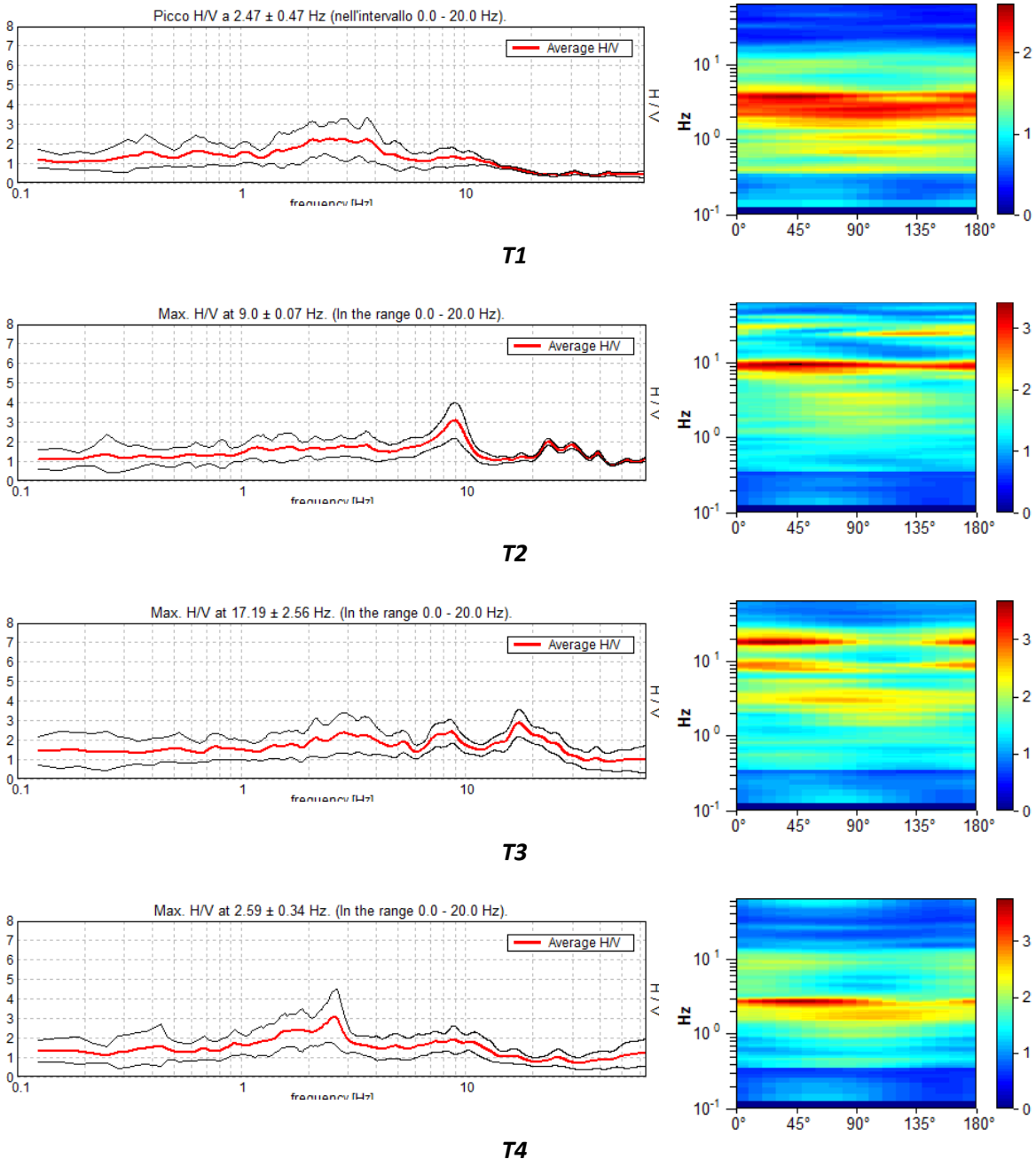

Figure 5.32. Noise measurements results in terms of H/V spectral ratio (on the left column) and H/V polar plots (on the right).

5.4 Overall Damage Patterns

5.4.1 Norcia and Castelluccio

Norcia is a city located near the margin of the trimmed finite fault model (Figure 2.11) that experienced strong shaking (Chapter 3). The damage observed in Norcia was relatively minor and isolated as a result of the subject event sequence, although appreciable damage has been reported from the late October events that will be presented in subsequent reconnaissance reports.

Following the 24 August 2016 earthquake sequence, some cracks were visible, especially inside houses. Few collapses occurred, which were old and non-maintained buildings. Some structures having typically small levels of damage in the center of Norcia are shown in Figure 5.33-5.34. The implementation of appropriate seismic design practices, careful repair of a number of structures, and the successful retrofitting of the buildings in Norcia contributed to the good performance of buildings under the 24 October 2016 event and its aftershocks.

A devastating earthquake that occurred in 1859 led to the development of a new building code at the time. The reconstruction that followed was based on that new code, which established a minimum wall thickness, the use of buttresses, the reduction of the building height, the use of vaults only at the ground floor, and the mandatory presence of good wall-to-wall connections. The increased wall thickness is visible in many structures, while in several buildings, the thickness of the wall varies linearly along the height of the first story and remains constant along the rest of the building's height (Figure 5.34). These measures helped reduce the fatalities and extent of damage during the following earthquakes.

Furthermore, the generally successful response of the buildings in Norcia can undoubtedly be attributed to the successful repair and strengthening interventions that followed the 1979 Norcia and 1997 Umbria and Marche earthquakes. These interventions are not visible from the outside of the buildings, but confining steel rings and cross-ties are visible in many cases. Some typical examples of retrofitting with cross-ties are shown in Figure 5.35. These measures appeared to be quite successful and believed to be the primary reason for limited damage in Norcia.

Figure 5.33. Limited damage was observed in the buildings of Norcia.

(a) (b) (c)

Figure 5.34. Earthquake resistant construction practices in the center of Norcia – linearly varying thickness of the first story.

Figure 5.35. Buildings and towers retrofitted with cross-ties in Norcia.

The available geological maps for Norcia include: (a) The Italian Geological map with resolution 1:100,000 (Figure 5.36a); and (b) the Regional Geological map with resolution 1:10,000 (Figure 5.36b). The available data show that the center of Norcia is underlain by Pleistocene Colluvial, terraced alluvial, fluviolacustrine, and fluvioglacial deposits. During the survey, eight buildings were investigated in detail, as shown in Table 5.8. The location of the surveyed buildings and the graphical representation of their damage state are shown in Figure 5.37.

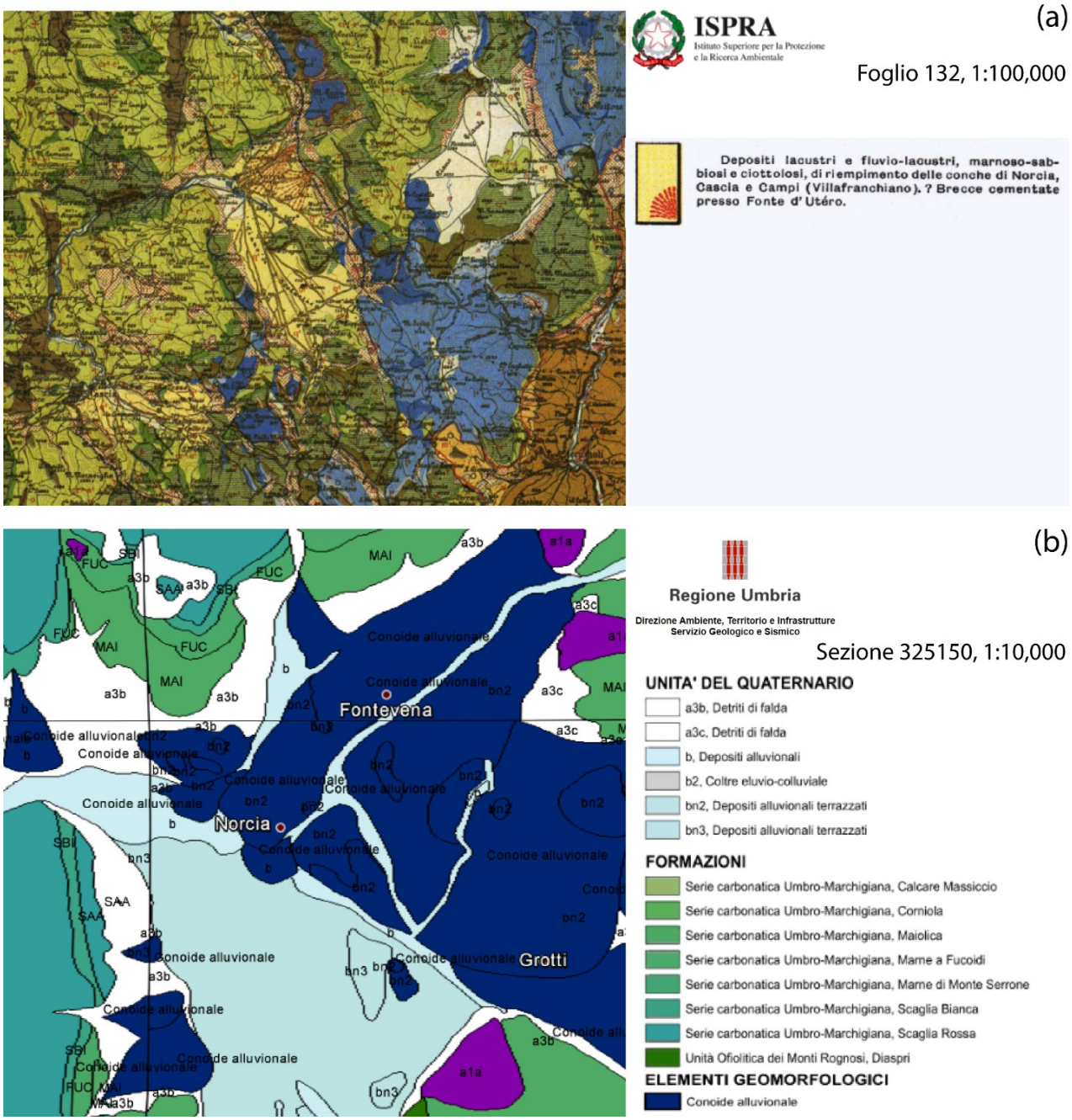

Figure 5.36. Geologic maps available at (a) ISPRA web site(http://193.206.192.231/carta_geologica_italia/tavoletta.php?foglio=132), and (b) Regione Umbria website (http://storicizzati.territorio.regione.umbria.it/Static/GeologiaKmz/GeologiaKmz/Index_kmz.htm).

Table 5.8. Locations of representative structures with damage descriptions.

Picture	DATUM	Location		Damage Level	Notes
		Lat.	Log.		
P01	WGS-84	13.09439	42.79219	DS2	Masonry
P02	WGS-84	13.09432	42.79248	DS2	Masonry
P03	WGS-84	13.09463	42.79255	DS2	Masonry
P04	WGS-84	13.09525	42.79253	DS4	Masonry
P05	WGS-84	13.09511	42.79280	DS2	Masonry
P06	WGS-84	13.09480	42.79321	DS1	Masonry
P07	WGS-84	13.09720	42.78633	DS4	RC
P08	WGS-84	13.09590	42.79328	DS2	Masonry

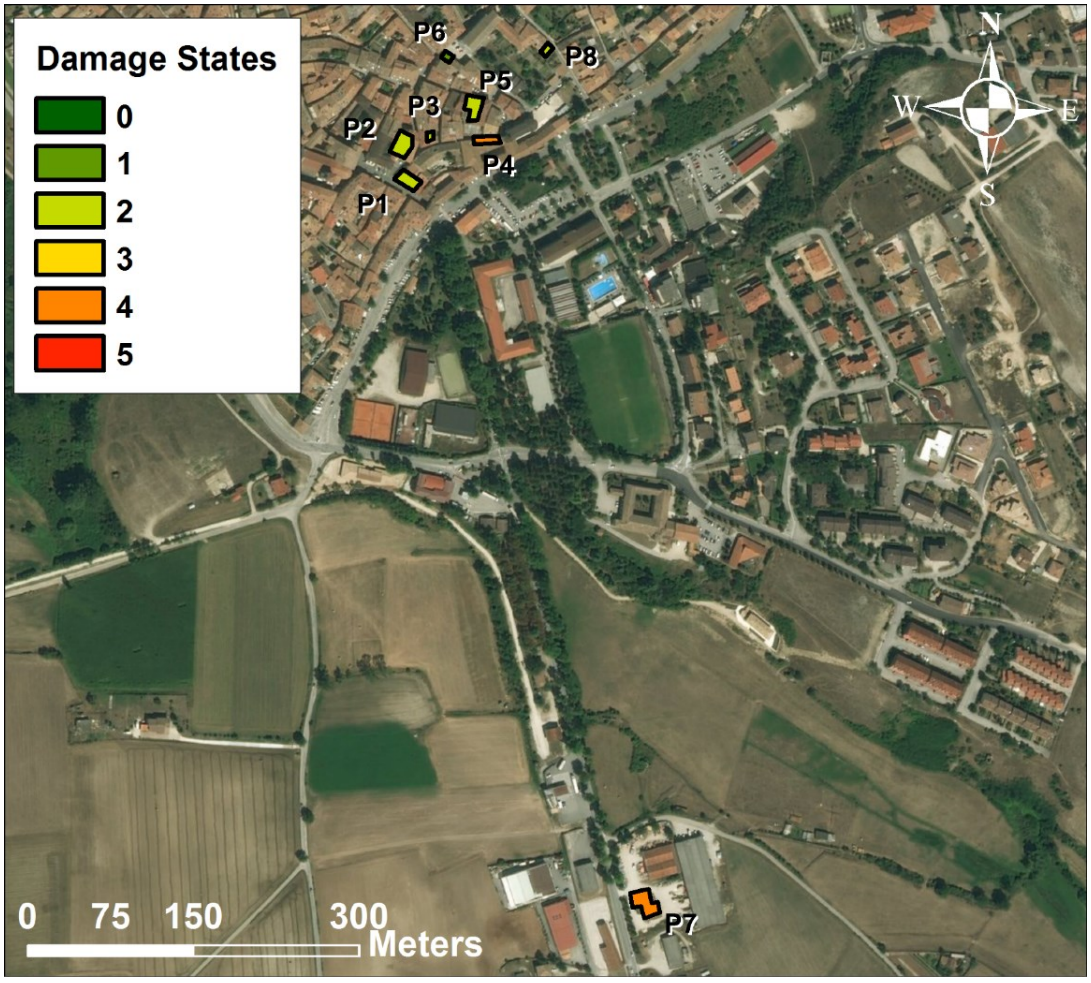

Figure 5.37. Location of surveyed buildings and their damage state.

Castelluccio di Norcia is a small hamlet of population 120 < 100 buildings (Figure 5.38). It belongs to the Norcia Municipality and is located 23km NE of Norcia. This hamlet rises on the crest of a hill (Figure 5.38b) at elevation 1452 m. It is in the center of a Karst plateau known as *Piani di Castelluccio*, one of the largest of the Italian plateaus.

(a) (b)

Figure 5.38. (a) Aerial photo of Castelluccio di Norcia, (b) Panoramic view of the hamlet.

The available geological maps include: (a) the Italian Geological map with resolution 1:100,000 (Figure 5.39); and (b) the Regional Geological map with resolution 1:10,000 (Figure 5.39b). The maps show that Castelluccio's hill is comprised of Limestones, marly limestones, and marls of pelagic facies (Jurassic, Lower Cretaceous). Surficial materials on the plateau are Quaternary alluvial deposits.

Almost the entire portfolio of buildings is of masonry construction, built or renovated within the last century. Given the touristic nature of the location, the village has many accommodation facilities such as small hotels and B&Bs. Such facilities have been recently renovated and therefore shown slight to no earthquake damage.

We documented the performance of five buildings according to the Italian inspection sheet, with the results in Table **5.9**. The location of the surveyed buildings and the graphical representation of their damage state as well as representative photographs of damage are shown in Figure 5.40 and Figure 5.41.

Table 5.9. Locations of representative structures with damage descriptions.

Picture	DATUM	Location		Damage Level	Notes
		Lat.	Log.		
P01	WGS-84	42.829358	13.205331	D4	
P02	WGS-84	42.82886	13.206422	D4	
P03	WGS-84	42.828836	13.206584	D5	
P04	WGS-84	42.82846	13.207108	D4	
P05	WGS-84	42.828289	13.207392	D1	

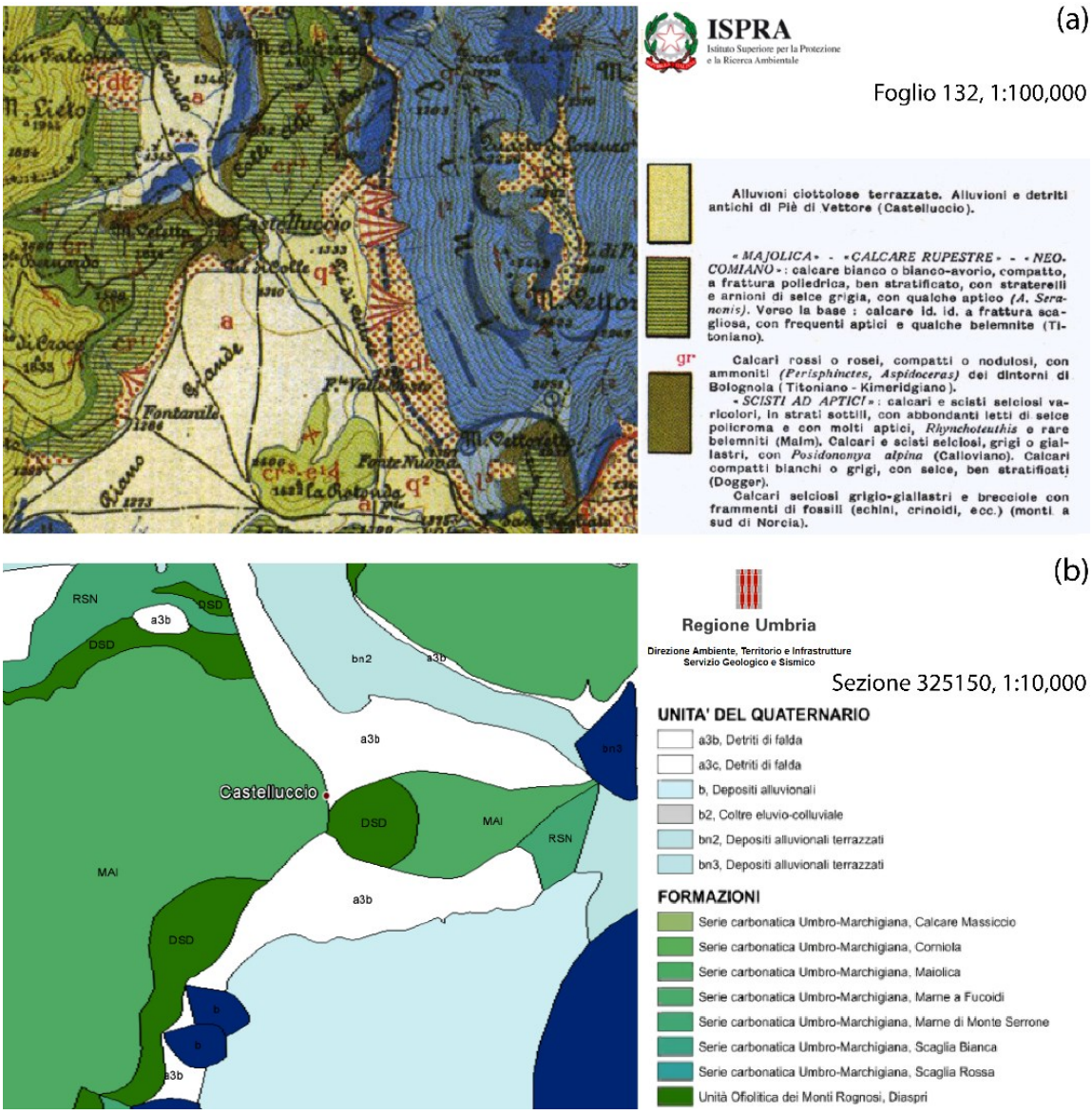

Figure 5.39. Geologic maps available at (a) ISPRA web site (http://193.206.192.231/carta_geologica_italia/tavoletta.php?foglio=132), and (b) Regione Umbria website (http://storicizzati.territorio.regione.umbria.it/Static/GeologiaKmz/GeologiaKmz/Index_kmz.htm).

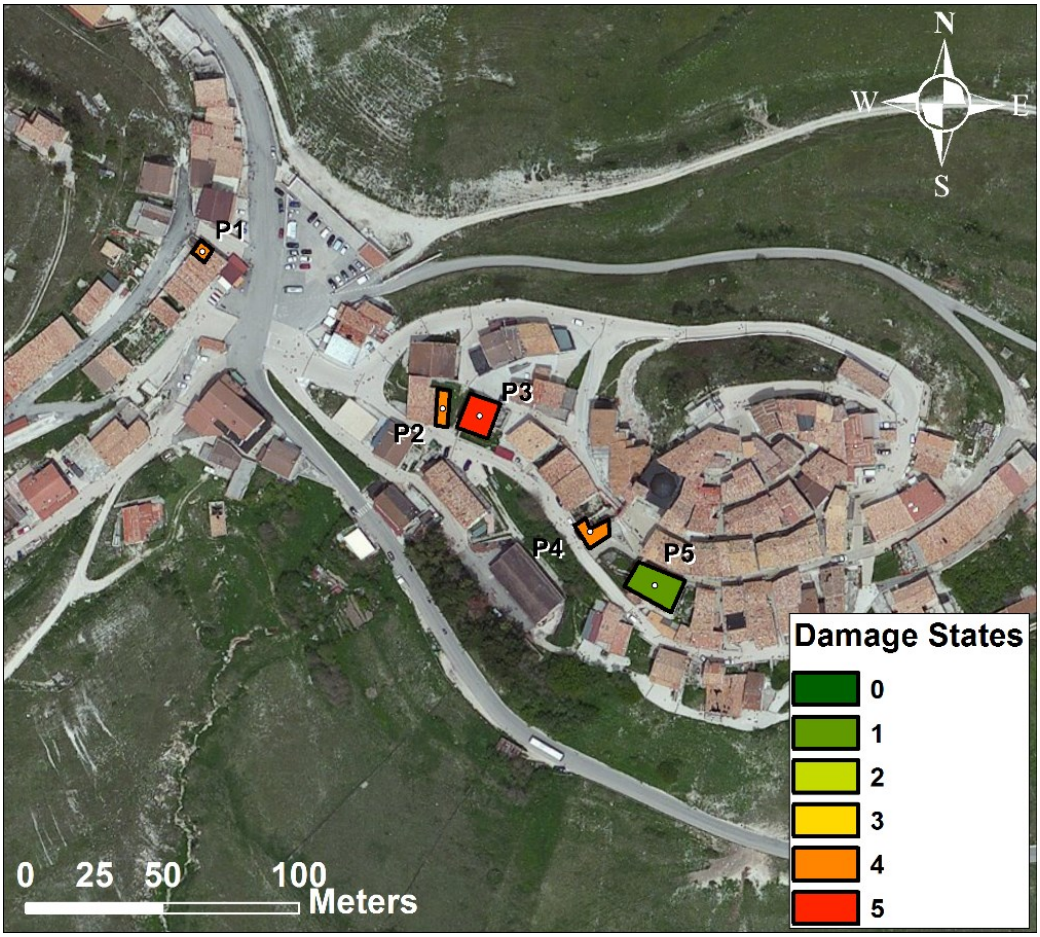

Figure 5.40. Location of surveyed buildings and their damage state.

P01

P02

P03

P04

P05

Figure 5.41. Representative pictures taken in Castelluccio during the survey.

5.4.2 Tufo (Arquata del Tronto)

Tufo is a small hamlet (with only 7 residents) of the Arquata del Tronto village located 5.3 km away in the southwest direction. The geological map of Tufo, available from the Marche region (section 337080) shows that the deposit in this area is mainly uniform (Figure 5.42). From the

visual inspection of the buildings (Figure 5.43 through Figure 5.45 and Table 5.10), it appears that site effects were minor, and only poorly constructed and not retrofitted/unreinforced masonry buildings experienced major damage.

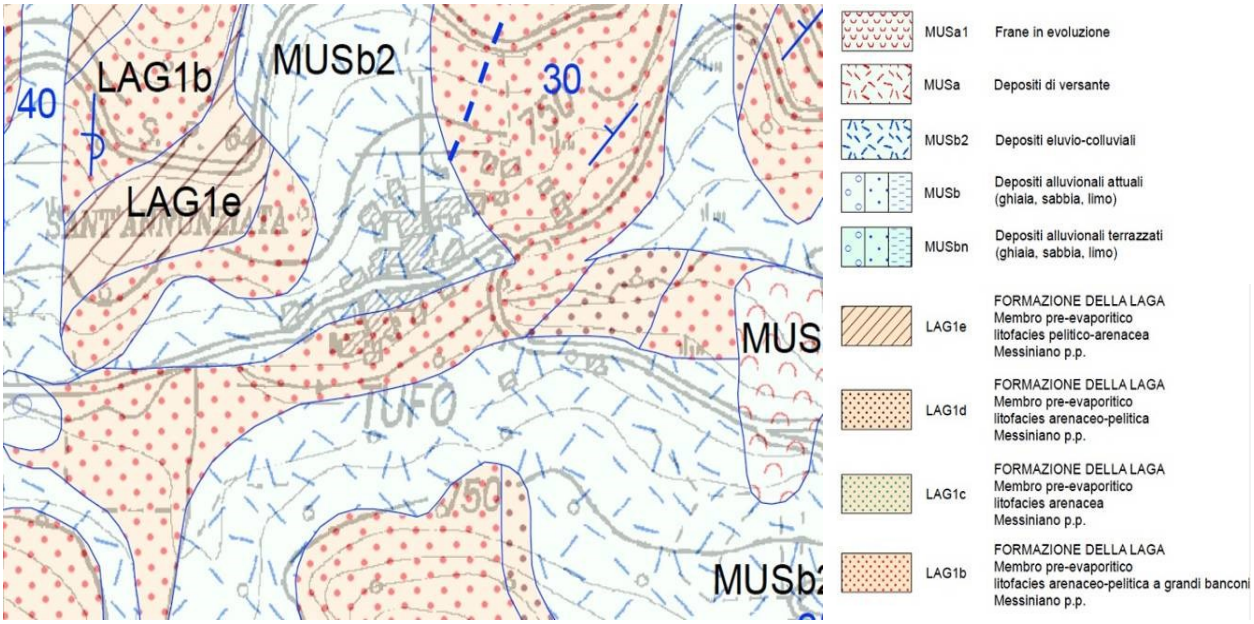

Figure 5.42. Geological map (provided by Marche region (section 337080) http://www.ambiente.marche.it/Territorio/Cartografiaeinformazioniterritoriali/Archiviocartograficoeinformazioniterritoriali/Cartografie/CARTAGEOLOGICAREGIONALE110000.aspx.

Figure 5.43. Locations of representative structures in the hamlet (see Table 5.10 for details).

Table 5.10. Location of representative structures with damage descriptions.

TAG	DATUM	Location		Damage level	Notes
		Lat.	Long.		
P1	WGS-84	42.7353°	13.2532°	D3	Diffused cracks
P2	WGS-84	42.7353°	13.2530°	D5	Collapse of the entire structure
P3	WGS-84	42.7354°	13.2528°	D2	Crack starting from the window corner
P4	WGS-84	42.7351°	13.2519°	D0	No damage
P5	WGS-84	42.7351°	13.2522°	D0	No damage
P6	WGS-84	42.735°	13.2522°	D4	Partial collapse of the structure

P1

P2

P3

P4

P5

P6

Figure 5.44. Representative pictures taken in Tufo during the survey.

The comparison of the observed damage with the patterns obtained from aerial image analyses (provided by the Copernicus Emergency Management Service) shows good agreement in terms of damage levels.

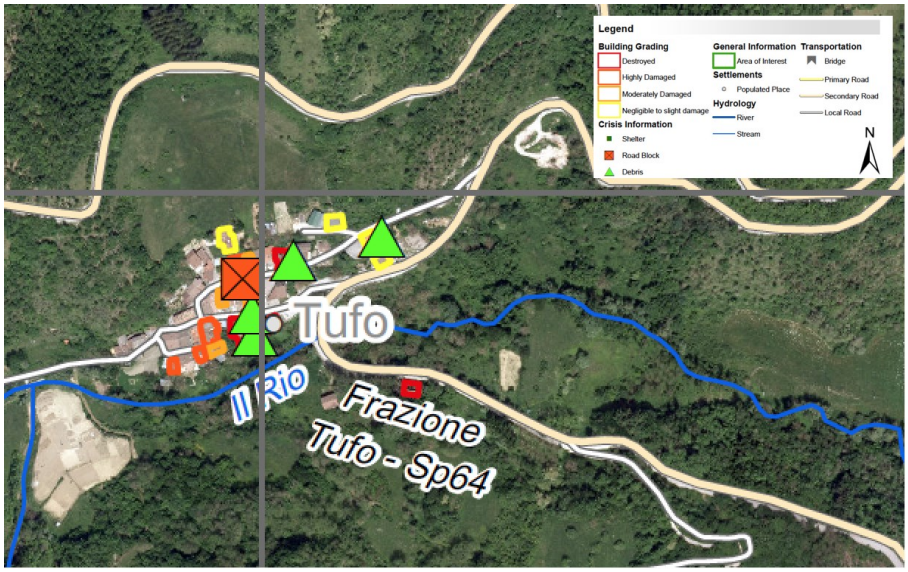

Figure 5.45. Damage pattern from Copernicus post event images (http://emergency.copernicus.eu/mapping/system/files/components/EMSR177_05GRISCIANO_GRADING_OVERVIEW-MONIT02_v1_300dpi.pdf).

5.4.3 Fonte del Campo (Accumoli)

The municipality of Accumoli includes several small hamlets along with the main village for which the effects of the earthquake were described in section 5.3.1. In particular, three distinctive geological environments are identified. On the western side of the Tronto river, outcropping Laga Flysch prevails, whereas on the eastern side is characterized by several alluvial fans composed of

coarse calcareous/arenaceous debris. The lower portion in the vicinity of the river is mainly characterized by recent alluvial deposits.

Located 749 m ASL on flat land, the hamlet of Fonte del Campo belongs to the municipality of Accumoli and is located 630 m away from it. Buildings in the center of the hamlet are primarily masonry, whereas in widespread surrounding areas residential buildings are primarily reinforced concrete. From a geological point of view, most of the structures are located on talus and lacustrine deposits, overlying the the Laga Flysch ("Molasse sandstones" in Figure 5.46). As detailed in the grade 1 microzonation map (Regione Lazio, 2013) (Figure 5.47), two stratigraphic sequences can be detected (Sa7 and Sa8) both characterized by talus or alluvial deposits more than 10 - 15 m thick overlying the Flysch bedrock.

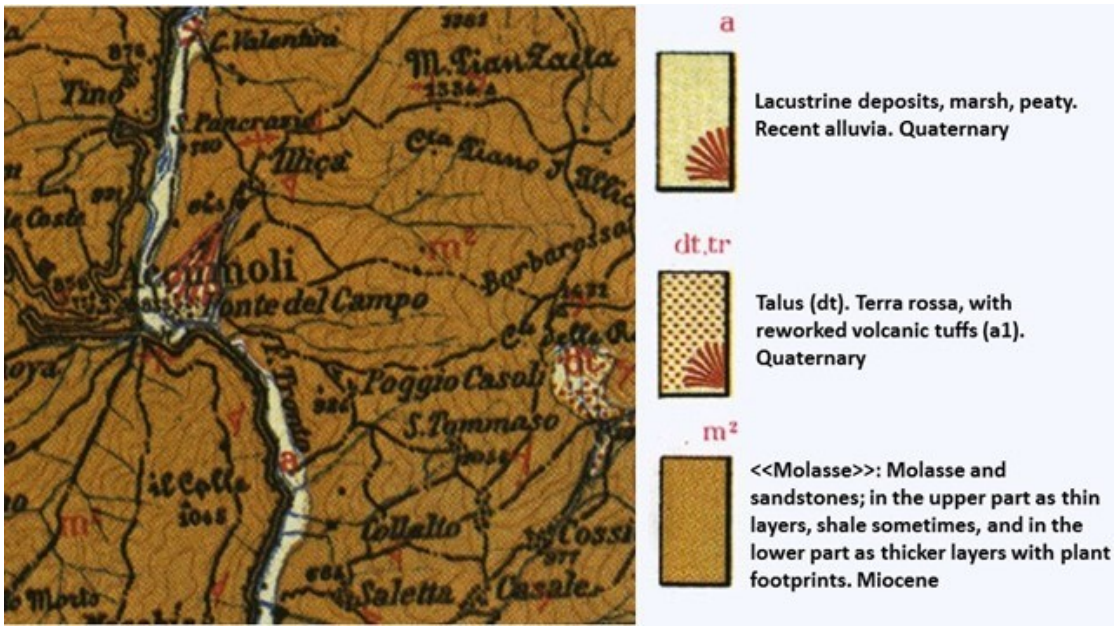

Figure 5.46. Geological map 1: 25000 (Carta Geologica d'Italia – f. 132 – from ISPRA, 2016).

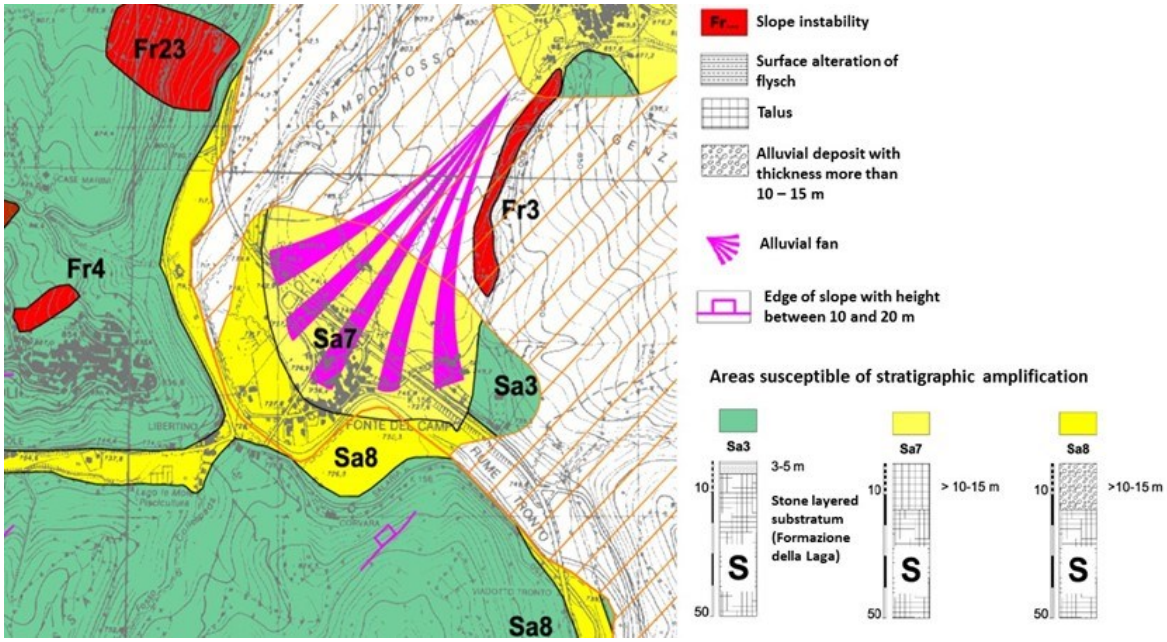

Figure 5.47. Fonte del Campo: grade 1 seismic zonation 1: 10000 (Regione Lazio, 2013).

As reported in Figure 5.48 to Figure 5.51 and Table 5.11, masonry buildings were the most highly damaged structures in the area. Two zones have been drawn based on the distribution of the damage: the most ancient part of the village characterized by damage levels D4-D5, and the more recently built surrounding zones characterized by a damage levels not exceeding D3. The same damage pattern was reported on the Copernicus map (Figure 5.51).

Figure 5.48. Locations of representative structures inspected in the hamlet (see Table 5.11 for details)

Table 5.11. Locations of representative structures with damage descriptions.

Picture	DATUM	longitude	latitude	Damage level	Note
P01.jpg	WGS- 84	13.255	42.69528	D3	
P02.jpg	WGS- 84	13.255	42.69417	D4	View of several buildings
P03.jpg	WGS- 84	13.255	42.69528	D3	View of several buildings
P04.jpg	WGS- 84	13.255	42.69528	D3	
P05.jpg				D3	Downloaded from http://www.fontedelcampo.it/foto/foto-terremoto/
P06.jpg				D5	Downloaded from http://www.fontedelcampo.it/foto/foto-terremoto/
P07.jpg				D3	Downloaded from http://www.fontedelcampo.it/foto/foto-terremoto/

P01

P02

P03

P04

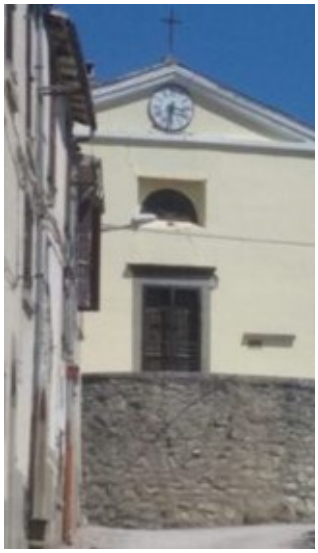

P05

P07

P06

Figure 5.49. Representative pictures taken in Fonte del Campo during the survey.

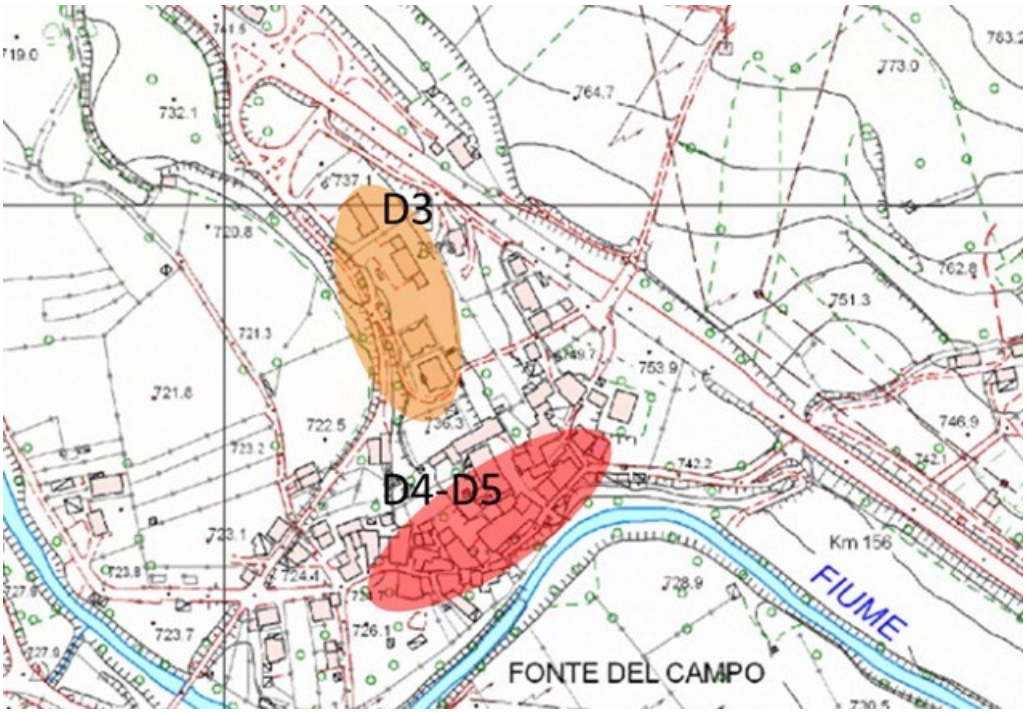

Figure 5.50. Damage zonation within the village.

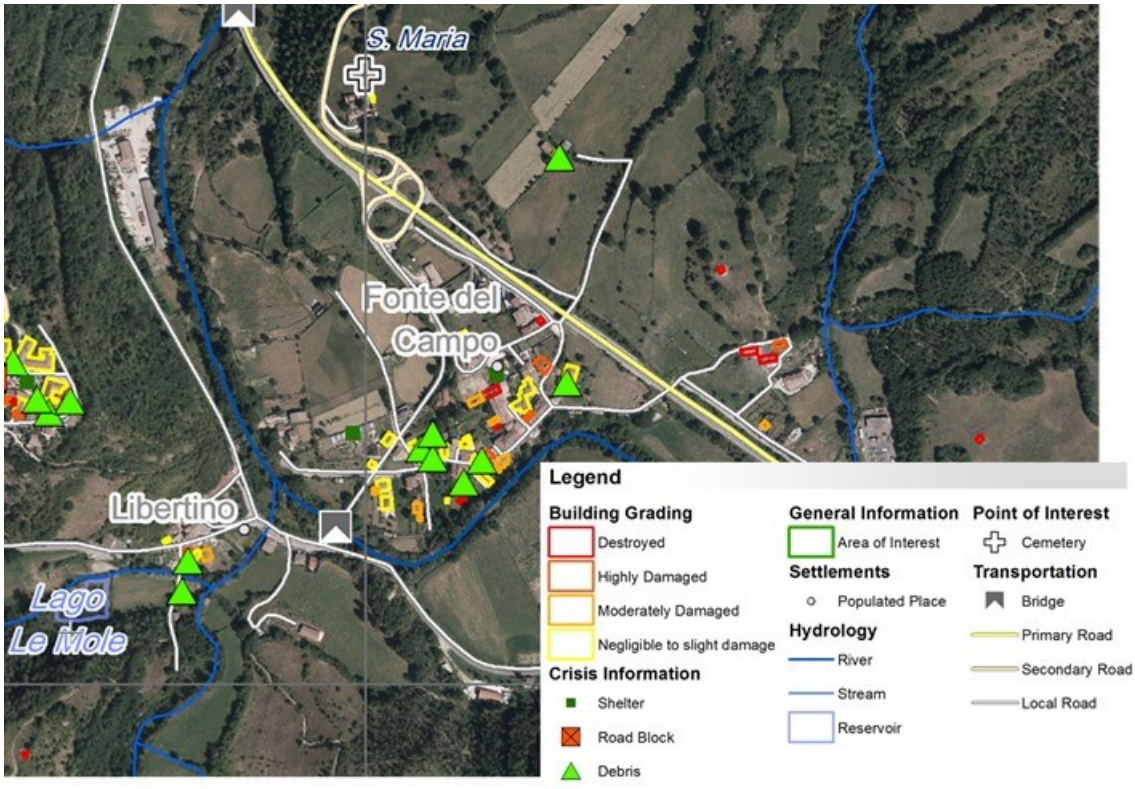

Figure 5.51. Damage pattern from Copernicus post event images.

5.4.4 Amatrice (surrounding hamlets)

The territory of Amatrice covers 174.43 km^2 of a basin located near the east border of the Lazio region. Approximately 2,660 people live in the territory of Amatrice (Table 5.12), including its 49 hamlets or, as commonly defined, “villas”. The GEER field survey covered 11 of the 49 hamlets in Amatrice (e.g., Figure 5.52 and Figure 5.53). The hamlets located east of Amatrice are on Pleistocene terraced alluvia and alluvial fans, whereas the remaining hamlets are directly on the Laga formation.

The detailed description of the geology reported in the excerpts of the Grade 1 seismic microzonation map of Amatrice (Figure 5.54) confirms that all the hamlets along the west side of the Tronto river (Poggio Vitellino, S. Giusta and Mosicchio) are located directly on the Laga (2099 - SFALS) formation, classified as seismic bedrock. East of the Tronto river, most of the hamlets (Saletta, San Lorenzo e Flaviano, Sommati, Voceto, Cascello and Collecreta) are mapped as having alluvial deposits, except for Casale and Cornillo Vecchio, which are located directly on the Laga bedrock.

Figure 5.52. Amatrice: Center and surrounding villages analyzed in this section.

Table 5.12. Demographic data of Amatrice and its hamlets (data from ISTAT 2011, http://dati.istat.it).

Hamlet Name	Inhabitants	Hamlet Name	Inhabitants
Amatrice center	1044	Nommisci	56
Arafranca-Pinaco	59	Pasciano	19
Bagnolo	44	Patarico	61
Capricchia	19	Petrana	11
Casale	22	Poggio Vitellino	32
Casali di Sopra	16	Ponte a Tre Occhi	44
Casali di Sotto	12	Prato	21
Cascello	16	Preta	19
Collalto	16	Retrosi	29
Collecreta	31	Rio	/
Collegentilesco	18	Roccapassa	22
Collemagrone	19	Rocchetta	36
Collemoresco	28	Saletta	33
Collepagliuca	19	San Benedetto	25
Colli	9	San Capone	24
Configno	39	San Giorgio	33
Cornillo Nuovo	52	San Lorenzo a Pinaco	21
Cornillo Vecchio	36	Sant'Angelo	68
Cossito	19	Santa Giusta	46
Domo	11	Santi Lorenzo e Flaviano	48
Faizzone	44	Scai	114
Ferrazza	8	Sommati	100
Forcelle	13	Torrita	73
Moletano	45	Varoni	17
Mosicchio	27	Voceto	42

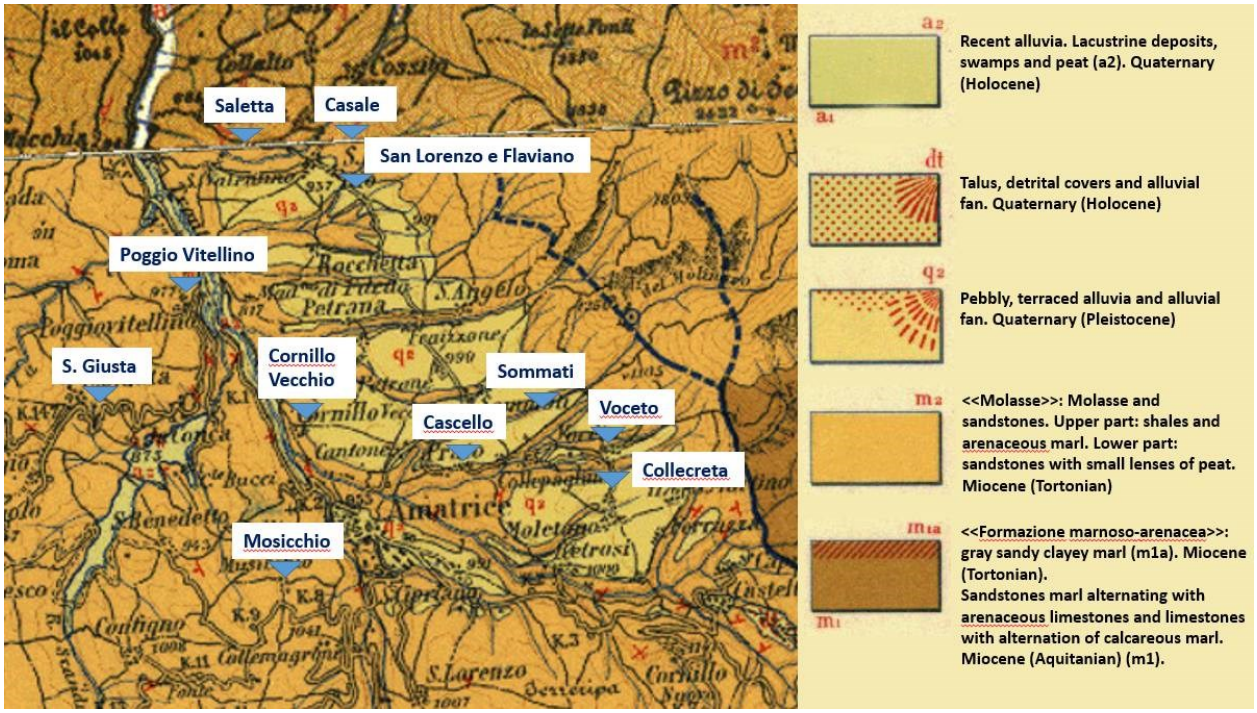

Figure 5.53. Location of the hamlets surrounding Amatrice on the 1: 25000 geological map (Carta Geologica d'Italia – f. 139 – after ISPRA, 2016).

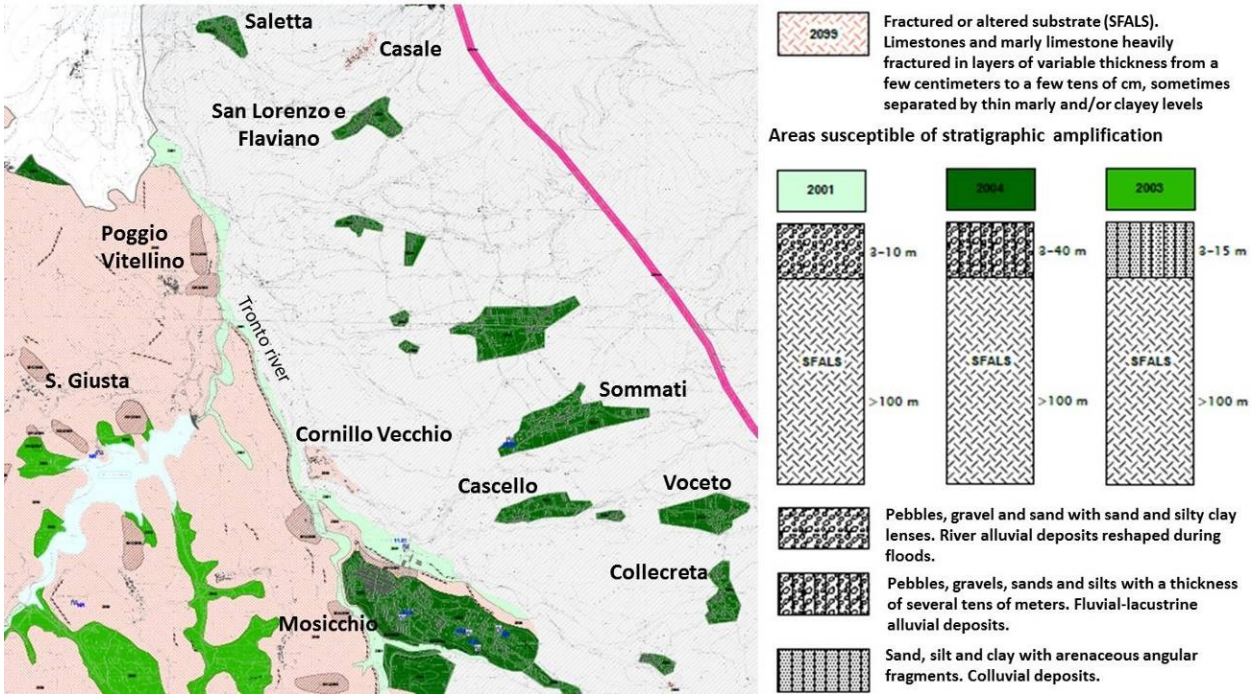

Figure 5.54. Location of the hamlets surrounding Amatrice on the 1:10.000 Grade 1 seismic zonation map (Regione Lazio, 2016).

Cascello (Amatrice)

Cascello is located along the road northeast of Amatrice at approximate elevation 940 m ASL. This hamlet has 16 inhabitants, one of the smallest in the Amatrice municipality. Figure 5.55 and Table 5.13 summarize locations of the most significant damage cases in the area. Figure 5.56 shows the different mechanisms of damage detected during the field survey. Almost all the dwellings were two to three story, old buildings made of arenaceous masonry. Undamaged houses (e.g. P03, P04) were often found near partially collapsed buildings (P02, P05), indicating that local damage variability was mainly attributed to the vulnerability of the structures. The retrofitted structures often had tie rods, which proved more effective when installed at both second and third floors of the structures (e.g. P07, P12), otherwise they could not prevent partial collapse (e.g. P06) or extensive cracking (P08, P09) of the masonry walls. The building damage distribution, including several cases of partial collapse, seemed to be compatible with the macroseismic intensity IMCS=8 (Galli et al., 2016).

Figure 5.55. Location of representative pictures taken at Cascello (see Table 5.13 for details).

Table 5.13. Locations of representative structures with damage descriptions.

Picture	DATUM	longitude	latitude	Damage level	Note
P01.jpg	WGS- 84	13.3084861	42.6349806	D4	Roof and inner walls collapsed
P02.jpg	WGS- 84	13.3101861	42.6350861	D4	Collapsed roof
P03.jpg	WGS- 84	13.3101972	42.6350861	D1	Only few cracks
P04.jpg	WGS- 84	13.3101972	42.635075	D0	Almost undamaged
P05.jpg	WGS- 84	13.3098639	42.6349722	D4	Collapsed roof showing poor masonry brickwork (adjacent to P04)
P06.jpg	WGS- 84	13.3099917	42.6349333	D3	Center - breached wall
P07.jpg	WGS- 84	13.3098361	42.6349333	D1	Effective tie rods
P08.jpg	WGS- 84	13.3098194	42.6349361	D4-D1	Collapsed unreinforced part (left) - Effective tie rods (right)
P09.jpg	WGS- 84	13.3098028	42.6349528	D3-D2	Diagonal cracks (left) – Almost effective tie rods (right)
P10.jpg	WGS- 84	13.3094667	42.6349056	D3	Diagonal cracks at the ground floor
P11.jpg	WGS- 84	13.3102028	42.6351083	D0	Undamaged recent (r.c.?) building
P12.jpg	WGS- 84	13.3098	42.6349	D1	Effective tie rods (installed also at the intermediate floor)

P01

P02

P03

P04

P03-P02-P04 (left to right)

P05

P06

P07

P08

P09

P10

P11

P12

Figure 5.56. Representative pictures taken at Cascello (see Table 5.13 for details)

Voceto (Amatrice)

Voceto is a hamlet with 42 inhabitants, located on the east side of Amatrice at 1067 m ASL, close to a road bend (Figure 5.57), and at the toe of a Pleistocene fan (see Figure 5.53). In Voceto, the damage distribution was mainly related to the vulnerability of the structures (Figure 5.58). Table 5.14 shows locations of the most significant damage cases in the area. Old masonry structures closer to the main road (P10, P12, P13), including a small chapel (P01) and structures around the inner small square (P05, P06) were severely damaged with partially collapsed walls. Retrofitted structures (P07, P08) or more recent buildings (P09), including some reinforced concrete structures, in the village expansion uphill did not suffer significant damage. Overall, the average damage level was approximately D3 for IMCS=7 (Galli et al. 2016)

Figure 5.57. Locations of representative structures inspected in Voceto (see Table 5.14 for details).

Table 5.14. Locations of representative structures with damage descriptions.

Picture	DATUM	longitude	latitude	Damage level	Note
P01	WGS- 84	13.324171	42.634639	D3	Old chapel, façade and absidal walls very deformed and x-cracked
P02	WGS- 84	13.324385	42.634543	D0	Almost undamaged new building in front of the chapel
P03	WGS- 84	13.324870	42.634559	D3	Intensely cracked building with a singular breach at the toe
P04	WGS- 84	13.325142	42.634781	D2 - D3	Small houses unevenly damaged
P05	WGS- 84	13.325969	42.634808	D3	Court house with dominating inter-openings cracks
P06	WGS- 84	13.325967	42.634803	D3-D4	Poor brickwork cracked (left) and breached (right)
P07	WGS- 84	13.325984	42.634731	D0	Undamaged restored building nearby
P08	WGS- 84	13.326309	42.634897	D0 – D1	Undamaged houses, one recently reinforced (see bottom picture, dated 2011) with tie rods with elliptical plates
P09	WGS- 84	13.326246	42.634884	D0	Recent low constructions uphill, almost undamaged
P10	WGS- 84	13.324369	42.634103	D3 - D4	Upper walls often breached
P11	WGS- 84	13.324422	42.633758	D3	Recent brickwork cracked and displaced
P12	WGS- 84	13.324433	42.633853	D3	Bulged and cracked poor masonry wall
P13	WGS- 84	13.324433	42.634000	D2	Partial damage even with tie rods

P01

P02

P03

P04

P05

P06

P07

P08

P09

P10

P11

P12

P13

Figure 5.58. Representative pictures taken at Voceto (see Table 5.14 for details).

Mosicchio (Amatrice)

The hamlet of Mosicchio (42.623488N, 13.279381E) belongs to the municipality of Amatrice and is only 1 km SW of the Amatrice center. It is located at 978 m ASL. Geologic conditions consist of alternating stratified arenaceous rocks interbedded with marls (Turbidite or Flysch). Figure 5.59 shows the geological map produced in the Level 1 Seismic Microzonation study of Amatrice.

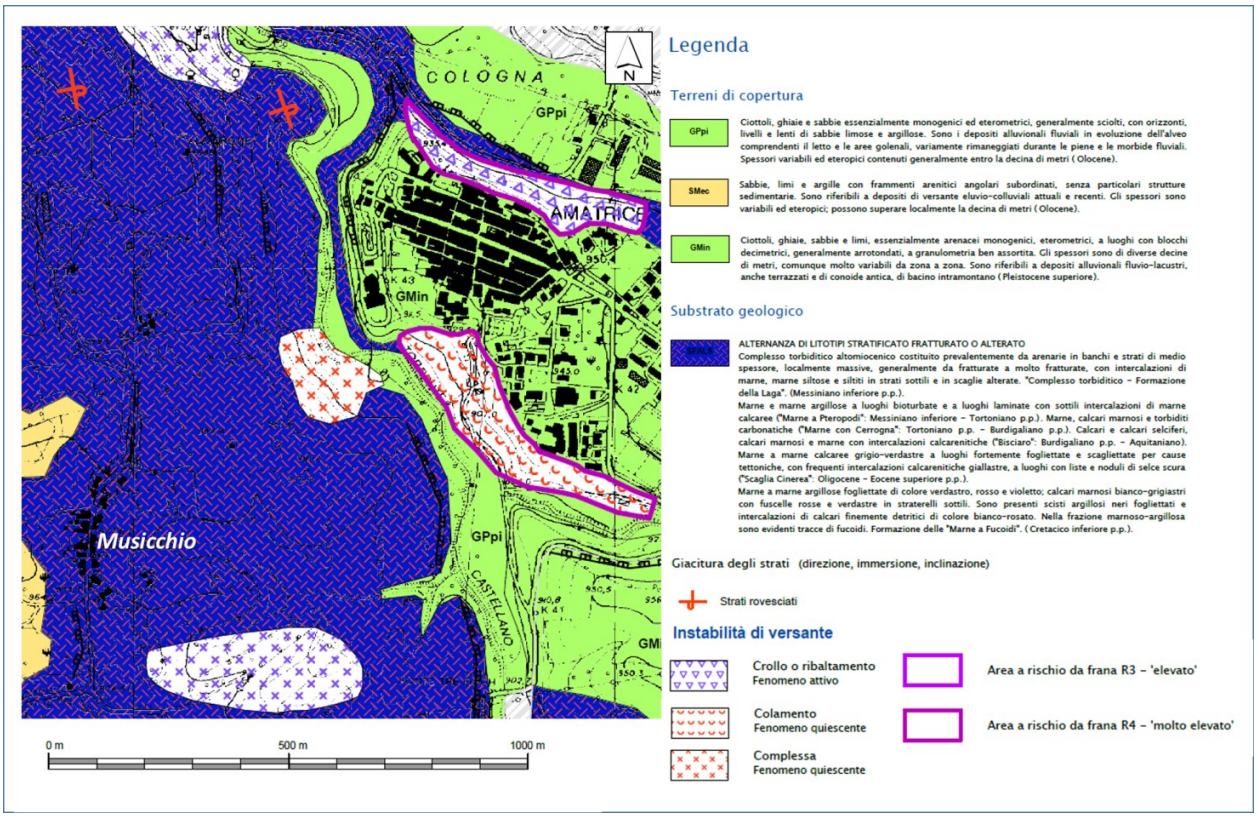

Figure 5.59. Geological map of Mosicchio and Amatrice (Regione Lazio, 2016).

Photos of representative structures inspected in Mosicchio are shown in Figure 5.60, with further details provided in Table 5.15 (WGS-84 coordinates, damage level of buildings, other notes). The hamlet consists mainly of unreinforced masonry structures, 2-3 stories in height. The damage was quite low, on average classified as D2. Only one case of partial collapse (D4) was observed in a poorly constructed, unreinforced masonry building (see P4).

P01

P02

P03

P04

Figure 5.60. Representative pictures taken at Mosicchio (see Table 5.15 for details).

Table 5.15. Locations of representative structures with damage descriptions.

Picture	DATUM	Location		Damage Level	Notes
		Lat.	Long.		
P01	WGS-84	42.622807°	13.279402°	D0-D1	
P02	WGS-84	42.623130°	13.279552°	D1-D2	
P03	WGS-84	42.623654°	13.279299°	D2-D3	
P04	WGS-84	42.623777°	13.279313°	D4	*Partial collapse of the roof*

Noise measurements were obtained during the survey close to buildings shown in picture P01 (Figure 5.60). A portable Tromino tomograph was employed. The methodology used for these measurements is the same as that described in Section 5.3.3. Both H/V and polar H/V are reported in Figure 5.61. No significant H/V peaks can be observed in the measurements, roughly supporting that the village is located on seismic bedrock (Flysch) and often no significant amplification effects are expected. This apparent lack of site effect may have contributed to the low to moderate levels of damage.

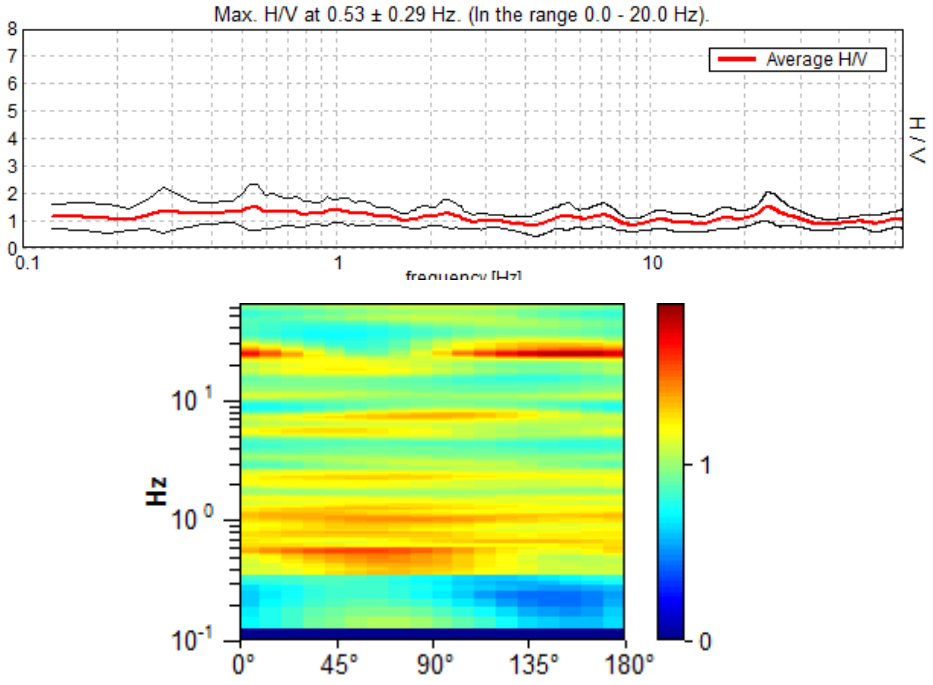

Figure 5.61. Noise measurements results in terms of H/V spectral ratio (on top) and H/V polar plots (on the bottom).

Casale (Amatrice)

The hamlet of Casale (42.670071N, 13.286158E) belongs to the municipality of Amatrice and is about 4.5 km from the Amatrice center. It is at 962 m ASL. It has 22 inhabitants according to the ISTAT census of 2013. It is located above the Amatrice basin, and as shown in Figure 5.62, the geological classification may be classified as alternating stratified arenaceous soils interbedded with marl, constituting the so-called turbiditic complex pertaining to the Laga formation (from the Level 1 Microzonation map of Amatrice).

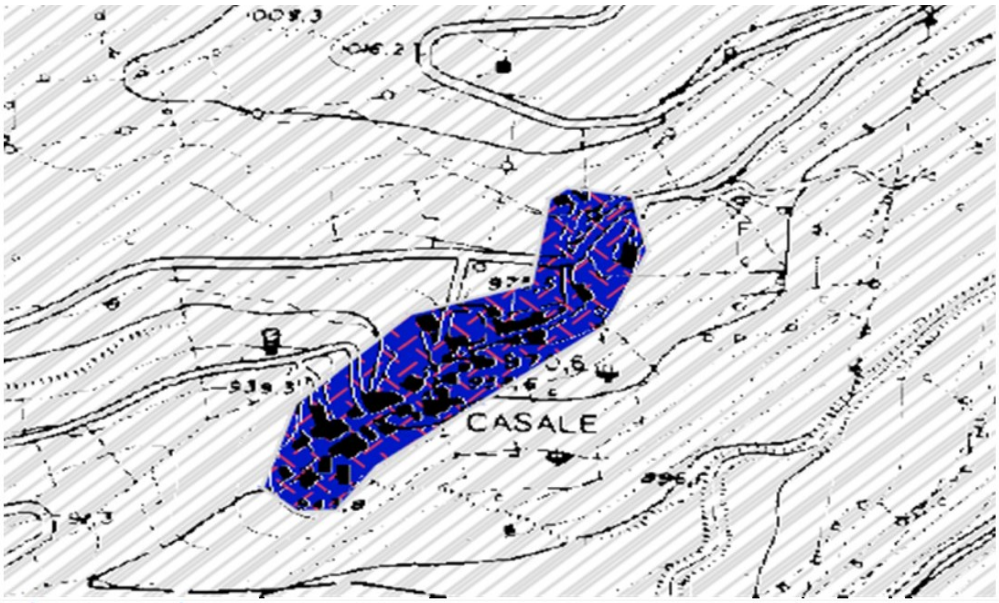

Figure 5.62. Geological map of Casale hamlet retrieved from the Level 1 Microzonation of Amatrice map (Regione Lazio, 2016).

Figure 5.63 and Table 5.16 show locations and details of representative buildings inspected in Casale. Figure 5.64 shows representative structures. There were a significant number of partial (e.g. P03, P05, P07) or total (P01, P02, P08, P11) collapses of masonry buildings in Casale with an average damage level between D4 and D5, which is consistent with local I_{MCS} = 10 (Galli et al. 2016).

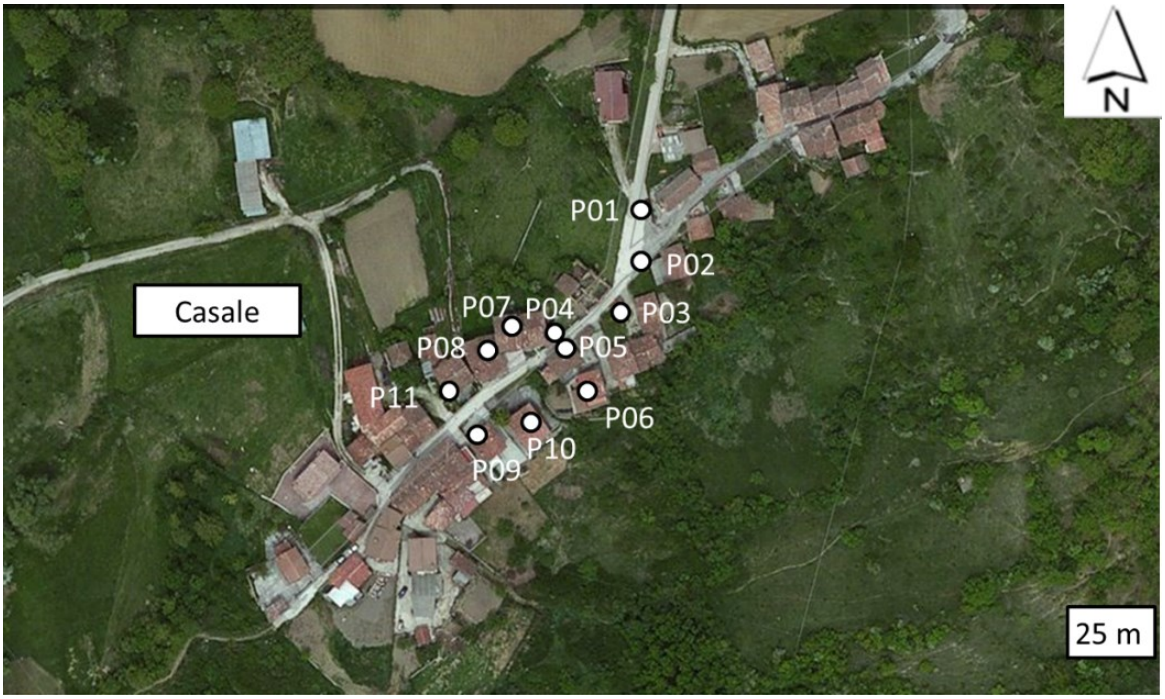

Figure 5.63. Locations of the representative structures inspected in Casale (see Table 5.16 for details).

Table 5.16. Locations of representative structures with damage descriptions.

Picture	DATUM	Location		Damage Level	Notes
		Lat.	Long.		
P01	WBG-84	42.670069	13.286015	D5	
P02	WBG-84	42.669812	13.285955	D5	
P03	WBG-84	42.669689	13.285857	D4	
P04	WBG-84	42.669553	13.285667	D3	
P05	WBG-84	42.669553	13.285667	D4	
P06	WBG-84	42.669596	13.285710	D0	
P07	WBG-84	42.669514	13.285550	D4	
P08	WBG-84	42.669473	13.285491	D5	
P09	WBG-84	42.669293	13.285254	D3	
P10	WBG-84	42.669330	13.285297	D3	
P11	WBG-84	42.669293	13.285254	D5	

P01

P02

P03

P04

P05

P06

P07

P08

P09

P10

P11

Figure 5.64. Representative pictures taken at Casale (see Table 5.16 for details).

Saletta (Amatrice)

The hamlet of Saletta (42.671157N, 13.272289E) is located at 864 m ASL and is approximately 4.8 km from the center of Amatrice. This hamlet has 33 inhabitants according to the ISTAT 2013 census. Figure 5.65 shows the geological classification of the area of Saletta as retrieved from the Level 1 Microzonation map. The upper soil layers in the hamlet are mostly classified as an alternation of silt, sand and gravel, arenaceous, with included blocks of decimetric size. These soils may be ascribed to the fluvial-lacustrine deposit of intra-mountain basin.

The buildings surveyed along the main road (Figure 5.66 and Table 5.17) showed a significant number of partial (e.g. P02, P06, P15 to P17) or total (P01, P03 to P05, P13, P18) collapse of the masonry buildings (Figure 5.67). The hamlet of Saletta had an average damage level between D4 and D5 for a local IMCS = 10 (Galli et al. 2016).

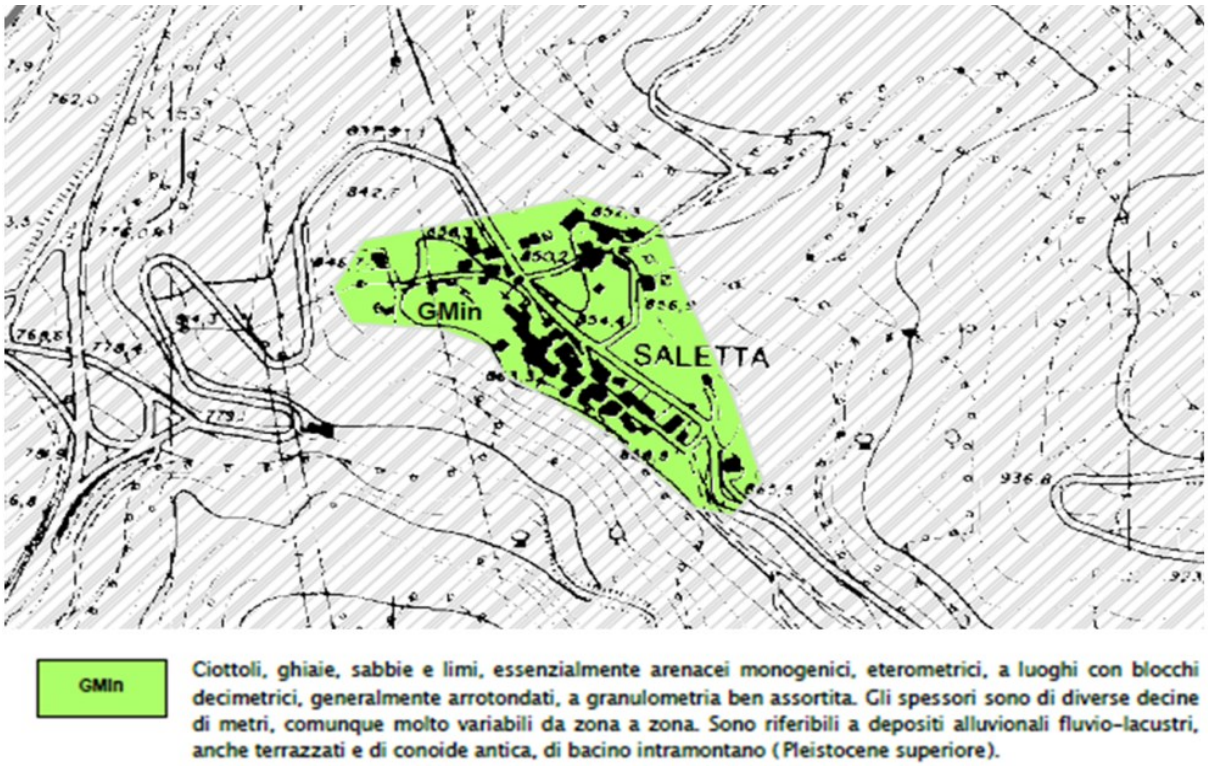

Figure 5.65. Geological setting of Saletta hamlet, retrieved from the Level 1 Microzonation map of Amatrice (Regione Lazio, 2016).

Figure 5.66. Locations of representative structures inspected in Saletta (see Table 5.17 for details).

Table 5.17. Locations of representative structures with damage descriptions.

Picture	DATUM	Location		Damage Level	Notes
		Lat.	Long.		
P01	WBG-84	42.670660	13.273112	D5	
P02	WBG-84	42.670803	13.272817	D4	
P03	WBG-84	42.670873	13.272713	D5	
P04	WBG-84	42.670823	13.272245	D5	
P05	WBG-84	42.670770	13.272265	D5	
P06	WBG-84	42.670791	13.272260	D4	
P07	WBG-84	42.670791	13.272260	D3	
P08	WBG-84	42.670740	13.272282	D3	
P09	WBG-84	42.670740	13.272282	D3	
P10	WBG-84	42.670647	13.272412	D3	
P11	WBG-84	42.670332	13.272980	D3	
P12	WBG-84	42.670332	13.272980	D3	
P13	WBG-84	42.670427	13.272803	D5	
P14	WBG-84	42.670056	13.273478	D3	
P15	WBG-84	42.670137	13.273330	D4	
P16	WBG-84	42.672120	13.272418	D4	
P17	WBG-84	42.672120	13.272418	D4	
P18	WBG-84	42.672005	13.272686	D5	

P01

P02

P03

P04

P05

P06

P07

P08

P09

P10

P11

P12

P13

P14

P15

P16

P17

P18

Figure 5.67. Representative pictures taken at Saletta (see Table 5.17 for details).

Sommati (Amatrice)

The hamlet of Sommati (42.642604N, 13.309713E) is at elevation 975 m ASL and is 2.2 km from the center of Amatrice. Sommati has 100 inhabitants according to the ISTAT 2013 census. Figure 5.68 shows the geological classification of the area, as retrieved from the Level 1 Microzonation map. The upper soils in the hamlet are mainly classified as the GMin formation, i.e. alternation of silt, sand and gravel, mostly arenaceous, including blocks of decimetric size. These soils may be ascribed to fluvial-lacustrine deposit in the intra-mountain basin.

Only a small part of the village was accessible in the days of the reconnaissance, which was surveyed as shown in Figure 5.69 and Table 5.18. The few buildings inspected (Figure 5.70) in some cases were partially or totally collapsed (P02, P03, P07), but most frequently had diffuse cracking (P04, P05, P06). Sommati had an average damage level in the order of D3-D4 with a local IMCS = 9 (Galli et al. 2016).

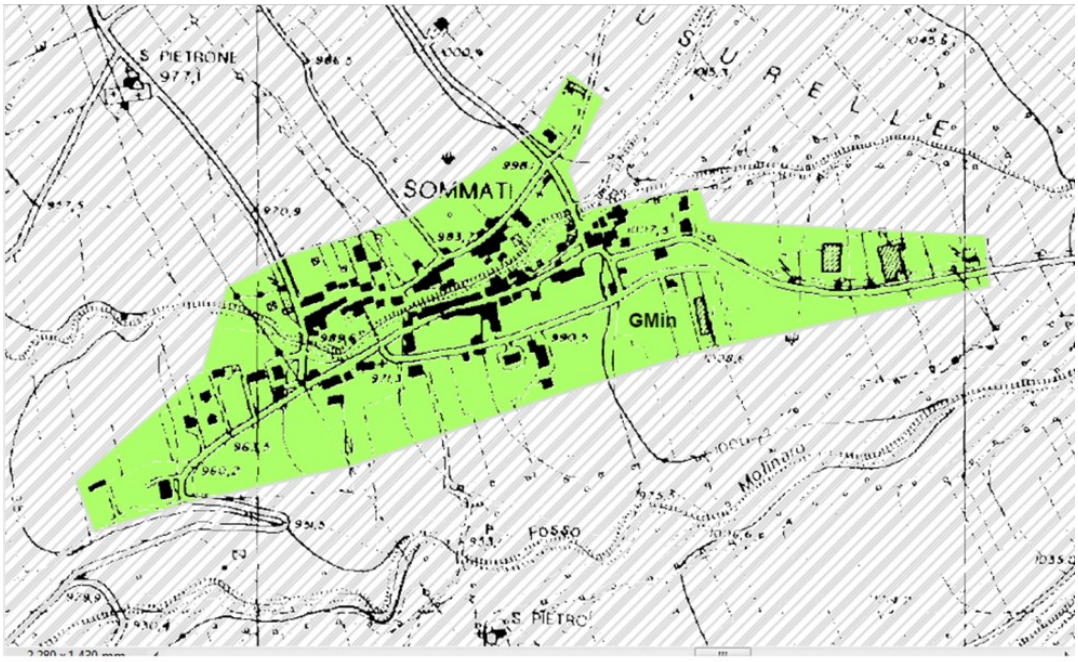

Figure 5.68. Geological map of Sommati hamlet retrieved from the Level 1 Microzonation map of Amatrice (Regione Lazio, 2016).

Figure 5.69. Locations of representative structures inspected in Sommati (see Table 5.18 for details).

Table 5.18. Locations of representative structures with damage descriptions.

Picture	DATUM	Location		Damage Level	Notes
		Lat.	Long.		
P01	WBG-84	42.642058	13.304934	D2	
P02	WBG-84	42.641640	13.305167	D4	
P03	WBG-84	42.641709	13.305461	D5	
P04	WBG-84	42.641251	13.306553	D1-D2	
P05	WBG-84	42.641172	13.306394	D3	
P06	WBG-84	42.641388	13.306857	D3	
P07	WBG-84	42.641438	13.307067	D3-D4	

P01

P02

P03

P04

P05

P06

P07

Figure 5.70. Representative pictures taken at Sommati (see Table 5.18 for details).

Villa San Lorenzo Flaviano (Amatrice)

The hamlet of San Lorenzo e Flaviano (42.665189N, 13.287606E) belongs to the municipality of Amatrice. It is located at 954 m ASL and is about 4 km from the Amatrice center. The hamlet has 48 inhabitants according to the ISTAT 2013 census. Figure 5.71 shows the geological classification of the area of San Lorenzo e Flaviano, as retrieved from the Level 1 Microzonation map. As in Sommati, the upper soil layers in the hamlet are generally classified as the GMin formation. Building inspections were performed through two building clusters along the main road (Table 5.19 and Figure 5.72). We found a significant number of partial (e.g. P02, P06, P07, P09, P10, P15 to P17) or total (P01, P03, P05, P14, P18) collapses of masonry buildings (Figure 5.73). The hamlet had an average damage level between D4 and D5 with a local I_{MCS} = 9-10 (Galli et al. 2016).

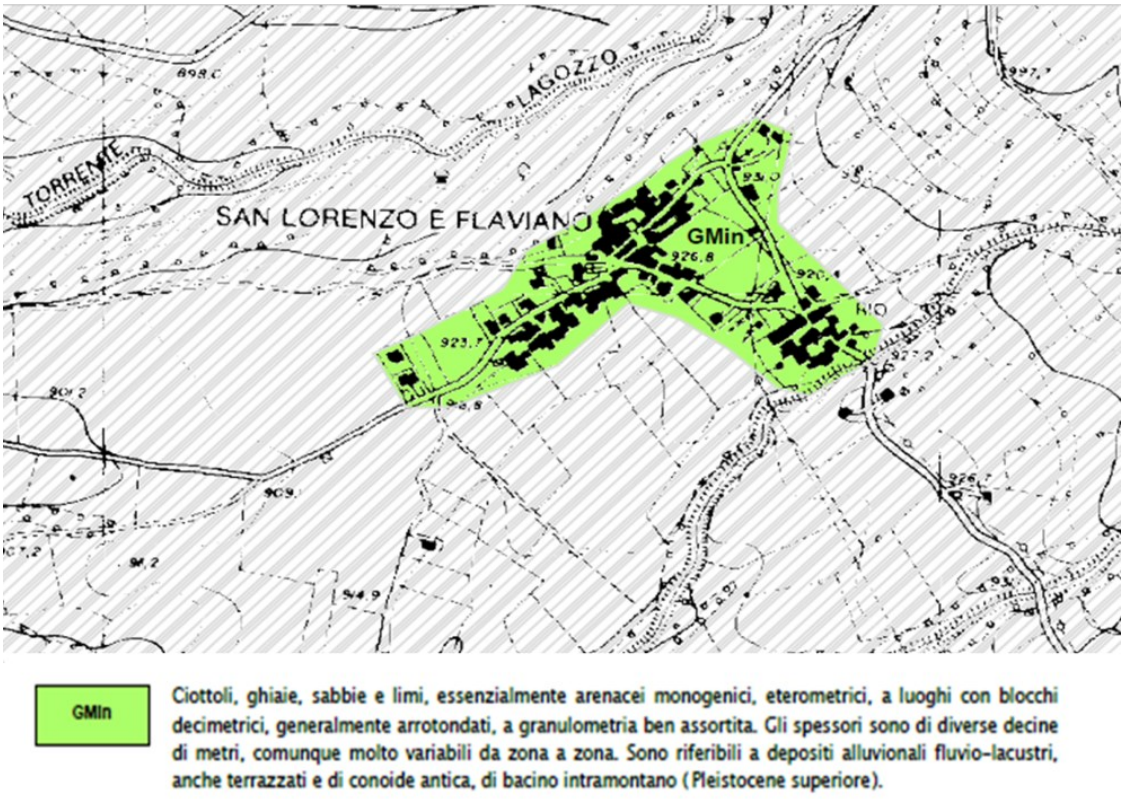

Figure 5.71. Geological map of San Lorenzo e Flaviano hamlet retrieved from the Level 1 Microzonation map of Amatrice (Regione Lazio, 2016).

Figure 5.72. Locations of the representative structures inspected in San Lorenzo e Flaviano (see Table 5.19 for details).

Table 5.19. Location of representative structures with damage descriptions.

Picture	DATUM	Location		Damage Level	*Notes*
		Lat.	Long.		
P01	WBG-84	42.665401	13.288931	D5	
P02	WBG-84	42.664418	13.289463	D4	
P03	WBG-84	42.664803	13.287449	D5	
P04	WBG-84	42.664831	13.287356	D3	
P05	WBG-84	42.664912	13.286910	D5	
P06	WBG-84	42.664897	13.286813	D4	
P07	WBG-84	42.664794	13.286675	D4	
P08	WBG-84	42.664897	13.286813	D3	
P09	WBG-84	42.664738	13.286589	D4	
P10	WBG-84	42.664724	13.286543	D4	
P11	WBG-84	42.664555	13.286144	D3	
P12	WBG-84	42.664167	13.285836	D0	
P13	WBG-84	42.664167	13.285836	D3	
P14	WBG-84	42.664066	13.285641	D5	
P15	WBG-84	42.664259	13.285575	D4	
P16	WBG-84	42.663913	13.289765	D4	
P17	WBG-84	42.664034	13.289765	D4	
P18	WBG-84	42.663913	13.289765	D5	

P01

P02

P03

P04

P05

P06

P07

P08

P09

P10

P11

P12

P13

P14

P15

P16

P17

P18

Figure 5.73. Representative pictures taken at San Lorenzo e Flaviano (see Table 5.19 for details).

Collecreta (Amatrice)

Collecreta is a hamlet located east of Amatrice at 1065 m ASL. It has 31 inhabitants (Table 5.20). The hamlet lies along the slope of a Pleistocene alluvial fan. The geomorphology of this site appears smoother than those of the surrounding hamlets, such as Cascello, Voceto and Sommati. Interviews with the (few) inhabitants who were present at the time of the reconnaissance revealed that the toponym (literally, 'clay hill') derives from the presence of shallow layers of likely soft clay. An overview of the hamlet showing the inspected structures is shown in Figure 5.74. Rather surprisingly, both old masonry and recent concrete buildings experienced little to no damage (Figure 5.75). The average damage level in the village of Collecreta is approximately D0. This hamlet was not listed among the villages with a local macroseismic intensity greater than 5 by Galli et al. (2016).

Figure 5.74. Locations of the representative structures inspected in Collecreta (Table 5.20 for details).

Table 5.20. Location of representative structures with damage descriptions.

Picture	DATUM	longitude	latitude	Damage level	Note
P01	WGS- 84	13.324494	42.630019	D0	Traditional buildings facing the small square, all undamaged
P02	WGS- 84	13.324644	42.629939	D1	Only slight cracking visible
P03	WGS- 84	13.324978	42.629897	D1	Maybe the most 'damaged' building
P04	WGS- 84	13.323975	42.630127	D0	New houses close to the main road, totally undamaged
P05	WGS- 84	13.323884	42.629816	D0	
P06	WGS- 84	13.323549	42.630106	D0	

P01

P02

P03

P04

P05

P06

Figure 5.75. Representative pictures taken at Collecreta (see Table 5.20 for details).

5.4.5 Montegallo

Montegallo is a municipality in the province of Ascoli Piceno located in the Marche Apennines, 30 km from Ascoli Piceno and 190 km from Rome. The area of Montegallo (Figure 5.76) extends approximately 50 km^2 from the toe of the eastern slope of Mount Vettore, the highest mountain of the chain of Sibillini Mountains. It includes 23 small hamlets, the locations of which are shown in Figure 5.76, that is: Abetito, Astorara, Balzetto, Balzo (county town), Bisignano, Casale, Castro, Colle, Collefratte, Colleluce, Collicello, Corbara, Fonditore, Forca, Inteprete, Migliarelli, Piano, Pistrino, Propezzano, Rigo, Santa Maria in Lapide, Uscerno and Vallorsara. The altitude changes significantly from the built areas of Uscerno located at the elevation of 494 m ASL to the highest peak of Colleluce at 1023 m ASL.

Figure 5.77 illustrates the geology of the area, as retrieved from the geological map of Regione Marche (1:10000). The geological bedrock of the area is a turbiditic succession of Messinian age known as Laga Flysch mainly composed of arenaceous and arenaceous-pelitic lithofacies. Figure 5.78 and Figure 5.79 show excerpts from the geological map. In these areas, the bedrock is locally covered by eluvial-colluvial deposits (MUSb2 in Figure 5.77) consisting of silty sand and mixtures of silt and sand as well as alluvial terraced deposits (MUSbn in Figure 5.77). Landslides are also common in the area (MUSa1 in Figure 5.77). Figure 5.80 presents the macroseismic intensity map produced by Galli et al. (2016) for a few hamlets in the Montegallo region.

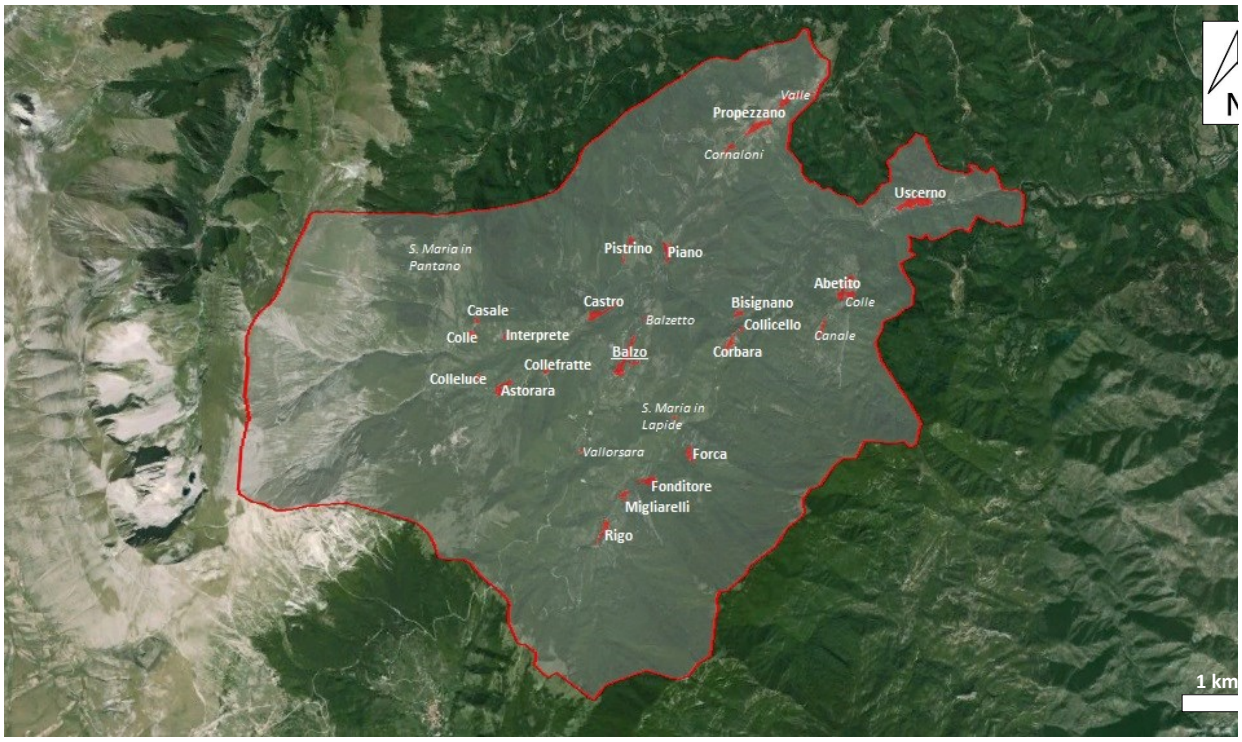

Figure 5.76. Map showing the location of main hamlets constituting Montegallo municipality.

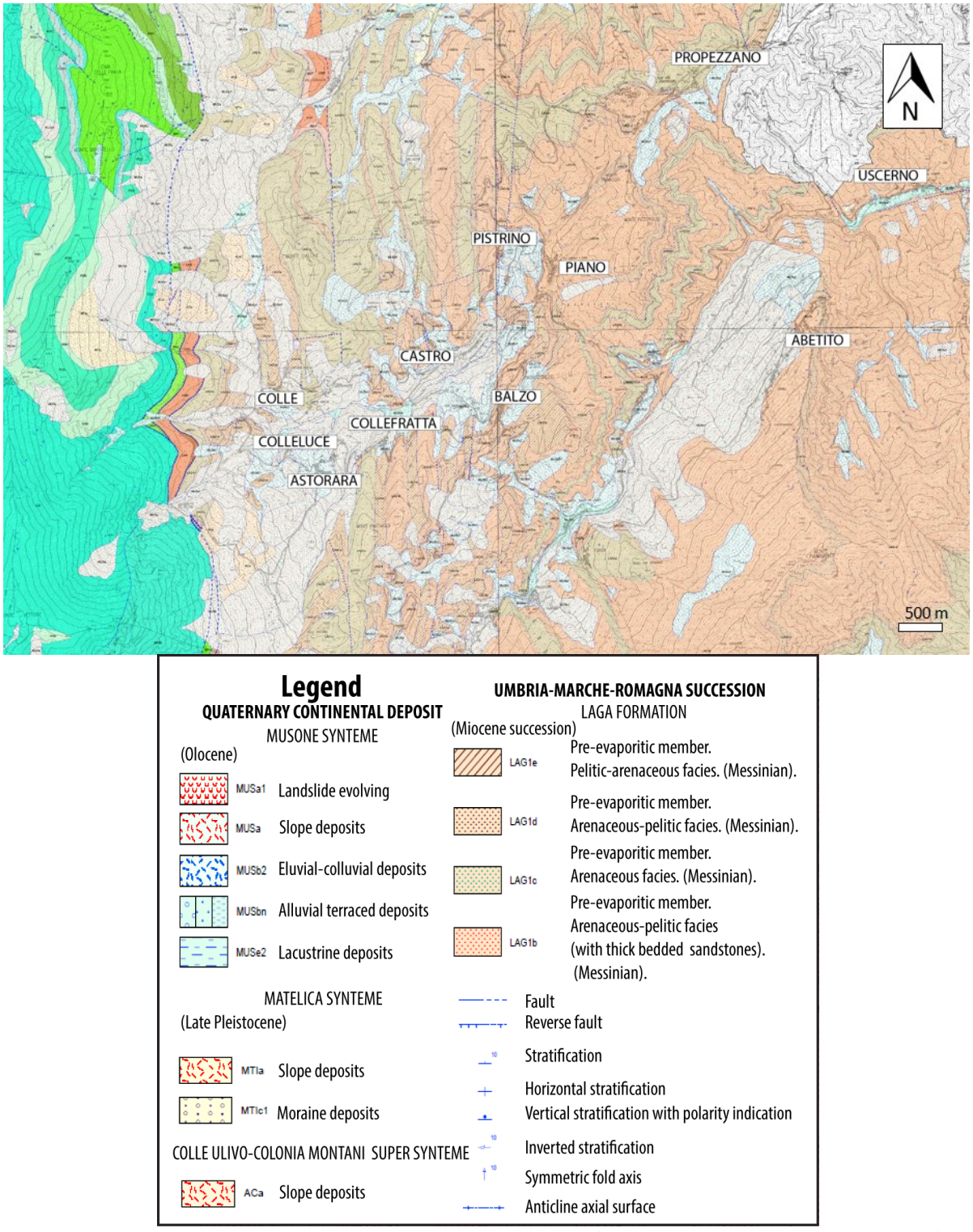

Figure 5.77. Geological large scale map including all districts of Montegallo municipality. Excerpt from geological map of Regione Marche (1:10000).

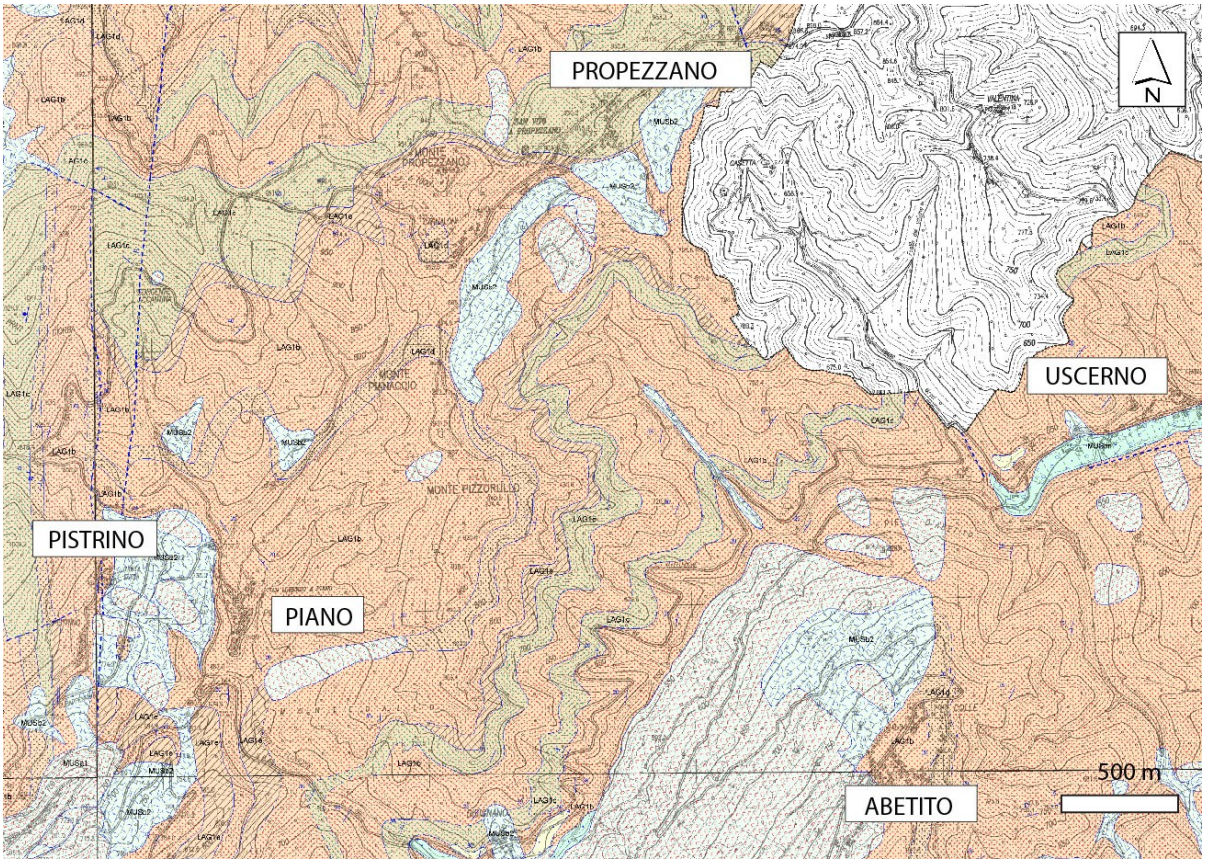

Figure 5.78. Excerpt from geological map of Regione Marche (1:10000). In the figure the position of Abetito, Piano, Pistrino, Propezzano and Uscerno hamlets is shown.

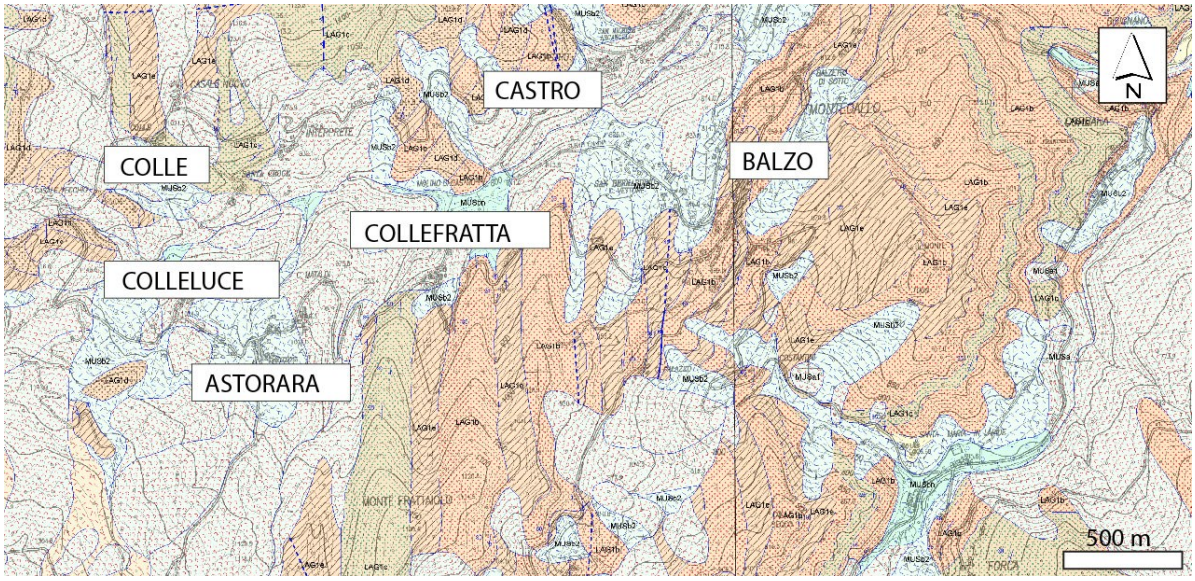

Figure 5.79. Eexcerpt from geological map of Regione Marche (1:10000). In the figure the position of Astorara, Balzo, Castro, Colle, Collefratta and Colleluce hamlets is shown.

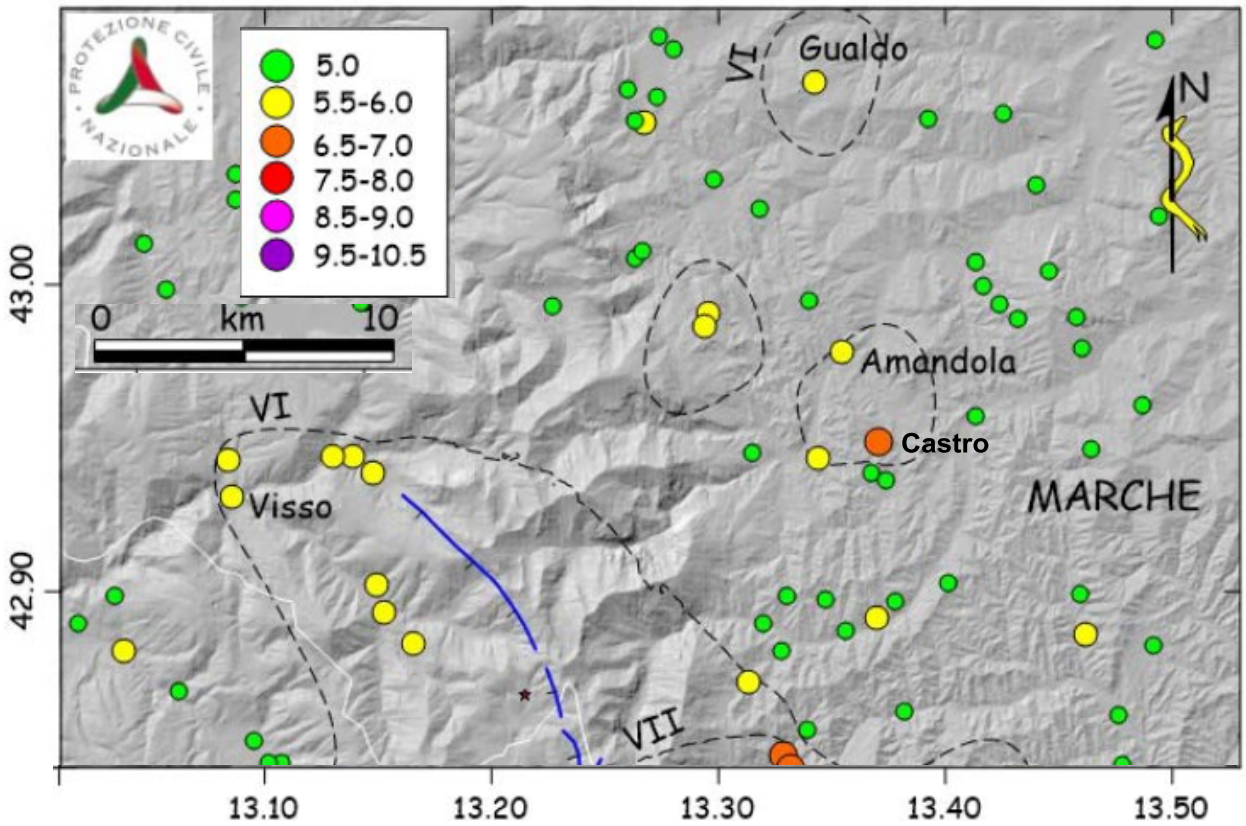

Figure 5.80. Macroseismic intensity map north of the epicentral area not visible in the figure (modified from Galli et al., 2016).

Among the 23 hamlets, 9 were investigated by the reconnaissance team. Table 5.21 presents, for each hamlet, a general description of the geological and morphological features, the latter being subdivided into three categories (ridge, slope and toe) according to the schematic representation in Figure 5.81. Table 5.21 reports also an average damage level for each hamlet, inferred from the behavior of some representative structures there listed. More detailed information on the damage to the representative structures (Figure 5.82) in each hamlet is given in Table 5.21. In the following paragraphs, a brief description of a few hamlets is presented.

Balzo is the main district of the municipality of Montegallo and also the county town. It is located at an elevation of 870 m ASL. The hamlet was built on a ridge made of the Laga Flysch Formation. Unfortunately, no photos are available for this village. However, a local I_{MCS} = 6.5 was attributed to this hamlet by Galli et al. (2016).

Castro is located at an elevation of 827 m ASL, 2 km north of the county town of Balzo. This hamlet is built on a ridge constituted by the Laga Flysch Formation in arenaceous-pelitic facies. According to Galli et al. (2016), a local I_{MCS} = 7.0 was attributed to this village, which is the maximum macroseismic intensity in the Montegallo districts. The more vulnerable 1-2 story masonry buildings showed moderate to severe damage (P17-P18) to partial collapse (e.g. P15-

P16). The village had an average damage level between D3 and D4. More recently constructed buildings did not suffer noticeable damage.

Collefratte is located at an elevation of 899 m ASL, 2 km northwest of Balzo. From the geomorphological point of view it is similar to Castro, i.e., it is located on a ridge made of calcareous eluvial-colluvial deposits resting on the pelitic-arenaceous formation. About 30% of the 1-2 story masonry buildings showed significant cracking (P19-P20); in one case falling of a chimney was observed. The average damage level attributed to this village is D2-D3.

Astorara is a small hamlet located at elevation of 1008 m ASL, 3 km from Balzo. It is built on the Laga Flysch Formation, locally covered by eluvial colluvial deposits that in this area never exceed 2-10 m in thickness (from Seismic Microzonation Level 1-Regione Marche, Montegallo municipality, Regione Marche, 2015). The 1-2 story masonry buildings (P14) as well as the masonry monumental buildings behaved adequately, apparently suffering no damage. One such example, as evidenced in picture P13, is the *Santa Liberata* Chuch, dated presumably to the XVI-XVII century. The hamlet had an average damage level of D0-D1.

Pistrino is a very small hamlet located at an elevation of 813 m ASL, 4 km from Balzo. The hamelt was developed on a mild slope and built on eluvial-colluvial deposits consisting of silty sand-mixtures (from Seismic Microzonation Level 1) resting on the Laga Formation. The lower part of the hamlet had some damage to 1-2 story masonry structures (P04-P06). On the other hand, no observable damage was observed in the upper part only 0.5 km away (P07-P09). An example of a heritage masonry buildings is the *Santa Lucia* Church, which dates to approximately the XV century (construction date is unknown), which apparently had no observable damage (P07). Further, a more recent reinforced concrete building with a first soft-story (“pilotis”) (Picture P08) suffered no damage. The upper part of the village had a damage level of D0-D1, while the lower part experienced a higher damage level of D2-D3. The different damage levels observed in the two adjacent areas points to the possibility of local site effects in the lower part of Pistrino.

Importantly, the ancient church of *Santa Maria in Pantano* located in the northwestern side of the Montegallo area suffered significant damage, with the partial collapse of the tower and fall of the sixteenth century bell. Partial collapse also occurred on the church sidewalls.

In summary, the Montegallo area is the farthest from the epicenter of the mainshock (about 18 km) among those surveyed and is composed of many districts, the most important being Balzo and Castro. One or two-story masonry buildings are the most prevalent in the area, although reinforced-concrete buildings are also present. Throughout the villages, different damage levels were observed. In some villages, the historical masonry buildings suffered almost no damage (for instance Piano, Astorara, and upper part of Pistrino), whereas others experienced moderate levels of damage (Collefratte, Colleluce, lower part of Pistrino) or severe damage (e.g. Castro). Considering the distance from the epicenter, site effects are expected to have contributed significantly to the different levels of damage observed in the area.

Table 5.21. Main geologic and geomorphologic features of the surveyed Montegallo's districts and estimated average damage level.

#	Hamlet	Geological setting	Active landslides	Topograhic features (see Fig. 5.81)	Structures (see Table 5.22)	Average damage level
1	Astorara	Laga Flysch, pelitic-arenaceous facies**	no	slope	P13-P14	D0-D1
2	Balzo	Laga Flysch, pelitic-arenaceous facies	no	ridge	-	-
3	Castro	Laga Flysch, pelitic-arenaceous facies	yes	ridge	P15-P18	D3-D4
4	Colle	Laga Flysch, arenaceous facies	no*	slope	P01- P03	D2-D3
5	Collefratte	eluvial-colluvial deposits	yes	ridge	P19-P20	D2-D3
6	Colleluce	eluvial-colluvial deposits	yes	slope	P21-P22	D1-D2
7	Piano	Laga Flysch, pelitic-arenaceous facies	no	toe	P10-P11	D0-D1
8a	Pistrino (lower part)	eluvial-colluvial deposits**	yes	slope	P04-P06	D2-D3
8b	Pistrino (upper part)	eluvial-colluvial deposits**	yes	slope	P07-P09	D0-D1
9	Propezzano	Laga Flysch, arenaceous facies	no	ridge	P12	-

*Landslide observed during the survey

**Information taken from Seismic Microzonation Level 1-Regione Marche, Montegallo municipality (Regione Marche, 2015)

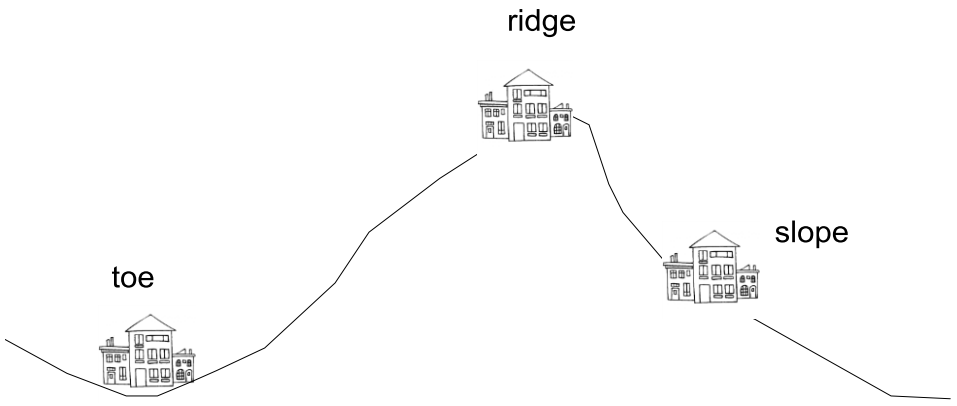

Figure 5.81. Schematic representation of the morphological categories identified from the surveyed hamlets within the Montegallo municipality.

Table 5.22. Location of representative pictures with estimation of average damage level.

Picture	Hamlet	DATUM	Position		Damage Level
			Lat.	Long.	
P01	Colle	WBG-84	42.843548°	13.307100°	D2-D3
P02	Colle	WBG-84	42.843584°	13.306980°	D2-D3
P03	Colle	WBG-84	42.843645°	13.307208°	D2-D3
P04	Pistrino	WBG-84	42.853423°	13.331786°	D2
P05	Pistrino	WBG-84	42.853335°	13.331713°	D2
P06	Pistrino	WBG-84	42.853186°	13.331661°	D2
P07	Pistrino	WBG-84	42.855579°	13.332642°	D0-D1
P08	Pistrino	WBG-84	42.855579°	13.332649°	D0-D1
P09	Pistrino	WBG-84	42.855579°	13.332649°	D0-D1
P10	Piano	WBG-84	42.854116°	13.339129°	D0
P11	Piano	WBG-84	42.853984°	13.339126°	D1
P12	Propezzano	WBG-84	42.860406°	13.378996°	D1-D2
P13	Astorara	WBG-84	42.837436°	13.31119°	D0-D1
P14	Astorara	WBG-84	42.838135°	13.307323°	D0-D1
P15	Castro	WBG-84	42.846221°	13.325959°	D4
P16	Castro	WBG-84	42.846416°	13.326965°	D4
P17	Castro	WBG-84	42.846416°	13.326965°	D3
P18	Castro	WBG-84	42.846416°	13.326965°	D3
P19	Collefratte	WBG-84	42.839388°	13.319004°	D3
P20	Collefratte	WBG-84	42.839388°	13.319004°	D3
P21	Colleluce	WBG-84	42.838439°	13.308071°	D1-D2
P22	Colleluce	WBG-84	42.838439°	13.308071°	D1-D2

P01 (Colle)

P02 (Colle)

P03 (Colle)

P04 (Pistrino lower part)

P05 (Pistrino lower part)

P06 (Pistrino lower part)

P07 (Pistrino upper part)

P08 (Pistrino upper part)


P09 (Pistrino upper part)

P10 (Piano)

P11 (Piano)

P12 (Propezzano)

P13 (Astorara)

P14 (Astorara)

P15 (Castro)

P16 (Castro)

P17 (Castro)

P18 (Castro)

P19 (Collefratte)

P20 (Collefratte)

P21 (Colleluce)

P22 (Colleluce)

Figure 5.82. Representative pictures in Montegallo (location listed in Table 5.22).

5.4.6 Other villages far from the epicentral area

Montereale

The Montereale municipality is located in the high Aterno valley (L'Aquila territory) and is inhabited by approximately 2,600 permanent residents. The main village is sitting along the crest of a hill and was destroyed by the 1703 Valnerina Earthquake (**M**6.9) (Rovida et al., 2016) and rebuilt thereafter. The local geology is reported in Figure 5.83, showing that the site is on an outcrop of the Laga formation ("Molasse" in the geologic map of Figure 5.83).

Montereale was damaged by the 2009 L'Aquila Earthquake. In particular, some buildings around the main square are still temporarily supported, and it is not easy to identify the incremental damage caused by the 24 August 2016 event. The village was visited by the GEER team and information collected through interviewing local inhabitants. A few buildings were identified with additional minor exterior damage, such as falling debris from the facade or from the roof. Local residents reported additional damage to the interior of houses, which we did not confirm. The overall level of damage to this village is D0-D1.

Some representative structures are shown in Figure 5.84 together with the corresponding coordinates. In particular, P01 shows damage from the 2009 Earthquake, whereas P02 shows an example of limited external damage as observed after the 2016 event. A temporary accelerometer network was placed by INGV in Montereale and Capitignano soon after the 24 August 2016 Earthquake to monitor aftershocks (Table 3.1, Figure 3.4).

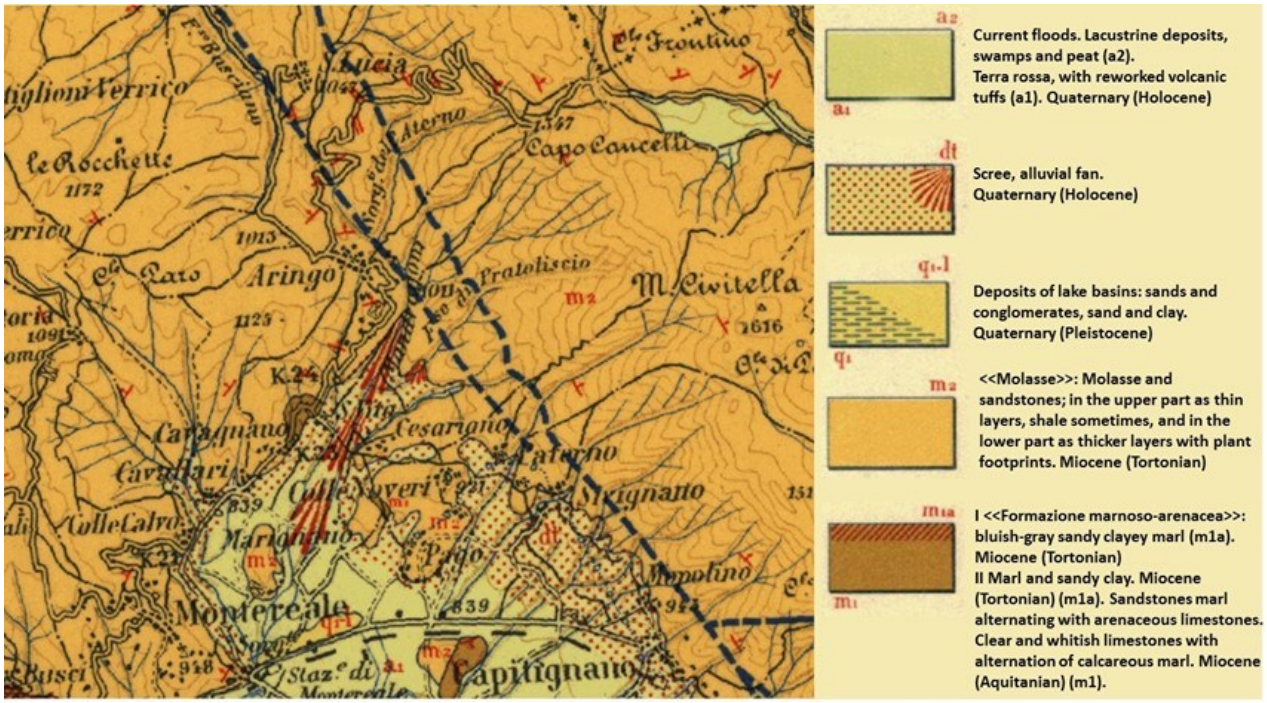

Figure 5.83. Geological map 1: 25000 (Carta Geologica d'Italia – f. 139- from ISPRA, 2016).

P01
42° 31' 22" N; 13° 14' 45" E

P02
42° 31' 24" N; 13° 14' 47" E

Figure 5.84. Representative structures in Montereale.

Capitignano

Capitignano is a village of approximately 700 inhabitants located in the vicinity of Montereale, but with different geologic conditions: recent (quaternary) deposits (Figure 5.83). Montereale was damaged heavily during the L'Aquila Earthquake in 2009 and several buildings were retrofitted or were under restoration at the time of the 24 August 2016 event. The village was visited by the GEER team, and some information was collected through interviewing local residents. Some retrofitted buildings were reported to have behaved well during the 24 August 2016 event, whereas others suffered some level of damage with cracks visible on the outside (e.g. P01 in Figure 5.85). Some buildings that were already damaged after the 2009 Earthquake suffered additional significant damage during the 2016 Earthquake (e.g., P02 in Figure 5.85). The overall level of damage in this area may be classified as D0-D1. A temporary accelerometer network was placed by INGV in Montereale and Capitignano soon after the 24 August 2016 event to monitor aftershocks (Table 3.1, Figure 3.4).

P01

P02

Figure 5.85. Representative pictures of damage in Capitignano.

Aringo (Montereale)

Aringo is a hamlet of the Montereale municipality, in the territory of l'Aquila. Located 984 m ASL on a flat land, the town is placed near the Gran Sasso National Park, surrounded by the mountains of the Aterno Valley. According to the Chronicles, inhabitants settled in the territory during the Roman period, but most of the current buildings were built in the 20th century. Most of the buildings in this hamlet are made of brick. Before the earthquake, approximately 50 people lived in Aringo. The village is located directly on the Laga formation (Figure 5.86). No damage was detected from the field survey (Figure 5.87 and Table 5.23), in line with observations from Copernicus satellite image analysis.

Figure 5.86. Location of representative picture taken in the village of Aringo (see Table 5.23 for details).

Table 5.23. Location of representative pictures with description of reported damage.

Picture	DATUM	longitude	latitude	Damage level
P01	WGS- 84	13.26763	42.55525	D0
P02	WGS- 84	13.26752	42.55489	D0
P03	WGS- 84	13.26760	42.55502	D0

P01

P02

P03

Figure 5.87. Representative structures in Aringo (Montereale).

Santa Lucia (Montereale)

Santa Lucia is a hamlet of the Montereale municipality, in the territory of l'Aquila. It is located approximately 1050 m ASL at a distance of about 5.5 km from the main village of Montereale. Most of the buildings are residential masonry structures. Before the earthquake, only a few people (less than 10) were residing in Santa Lucia, with many homes used only during the summer season.

This hamlet is located at about 14 km from the epicenter of the 24 August 2016 event. Compared to the nearby hamlet di Aringo, it suffered much greater damage, possibly because of higher building vulnerability. The locations of representative structures inspected during the GEER survey are reported in Figure 5.88. Details (WGS-84 coordinates, damage level of buildings, other notes) can be found in Table 5.24, while the pictures are shown in Figure 5.89.

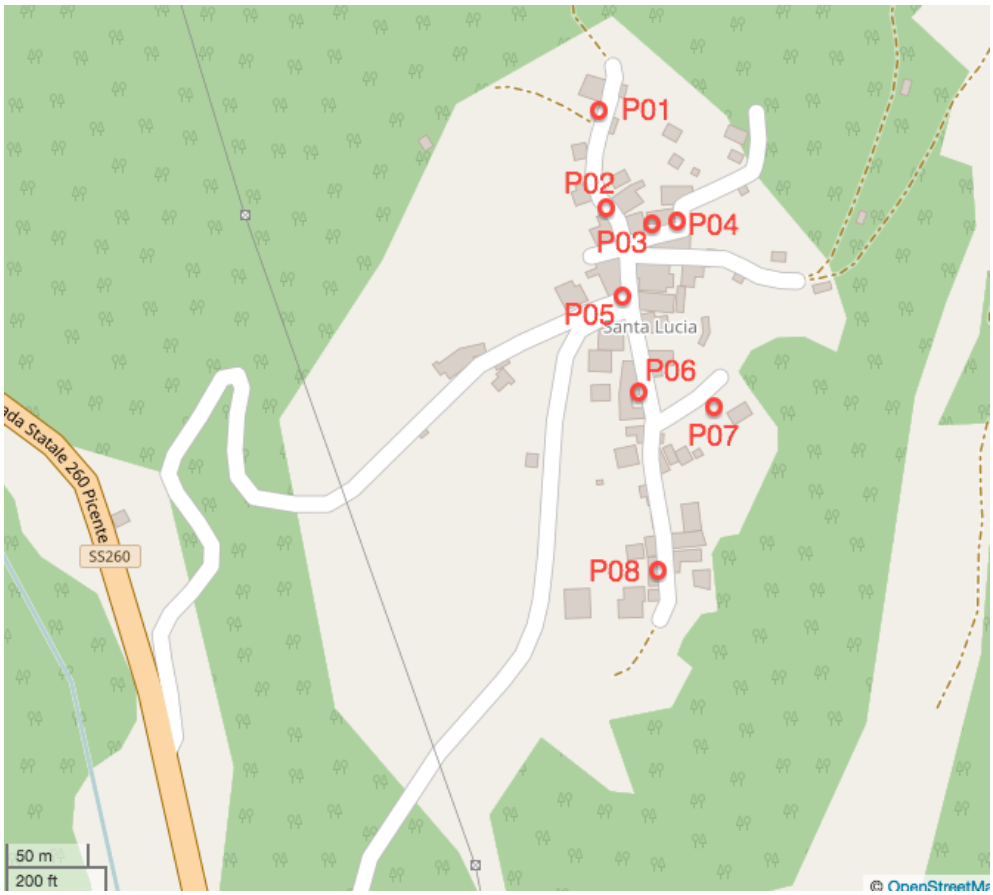

Figure 5.88. Locations of representative structures inspected in Santa Lucia (see Table 5.24 for details).

Table 5.24. Locations of representative structures with damage descriptions.

Picture	DATUM	Location		Damage Level
		Lat.	Long.	
P01	WGS-84	42° 34' 18" N	13° 15' 42" E	D1
P02	WGS-85	42° 34' 18" N	13° 15' 43,998" E	D0
P03	WGS-86	42° 34' 18" N	13° 15' 43,998" E	D1
P04	WGS-87	42° 34' 18" N	13° 15' 42" E	D1
P05	WGS-88	42° 34' 16,998" N	13° 15' 43,002" E	D5
P06	WGS-89	42° 34' 16,998" N	13° 15' 43,002" E	D2
P07	WGS-90	42° 34' 15" N	13° 15' 46,002" E	D3
P08	WGS-91	42° 34' 16,002" N	13° 15' 43,002" E	D2

P01

P02

P03

P04

P05

P06

P07

P08

Figure 5.89. Representative pictures in Santa Lucia (Montereale) (see Table 5.24 for details).

6.0 Performance of Bridge Structures

Principal authors: Luigi Di Sarno, Maria Giovanna Durante, Jonathan P. Stewart

Contributing authors: Anna d'Onofrio, Shideh Dashti, Stefania Sica, Paolo Zimmaro

6.1. Introduction and Reconnaissance Approach

The GEER team worked in close collaboration with the Consortium ReLuis to inspect 12 bridges at the locations shown in Figure 6.1 and Table 6.1. These structures are distributed over a large area that approximately corresponds to the southern zone of the epicentral region. This area includes the two local Regions, namely Lazio and Marche.

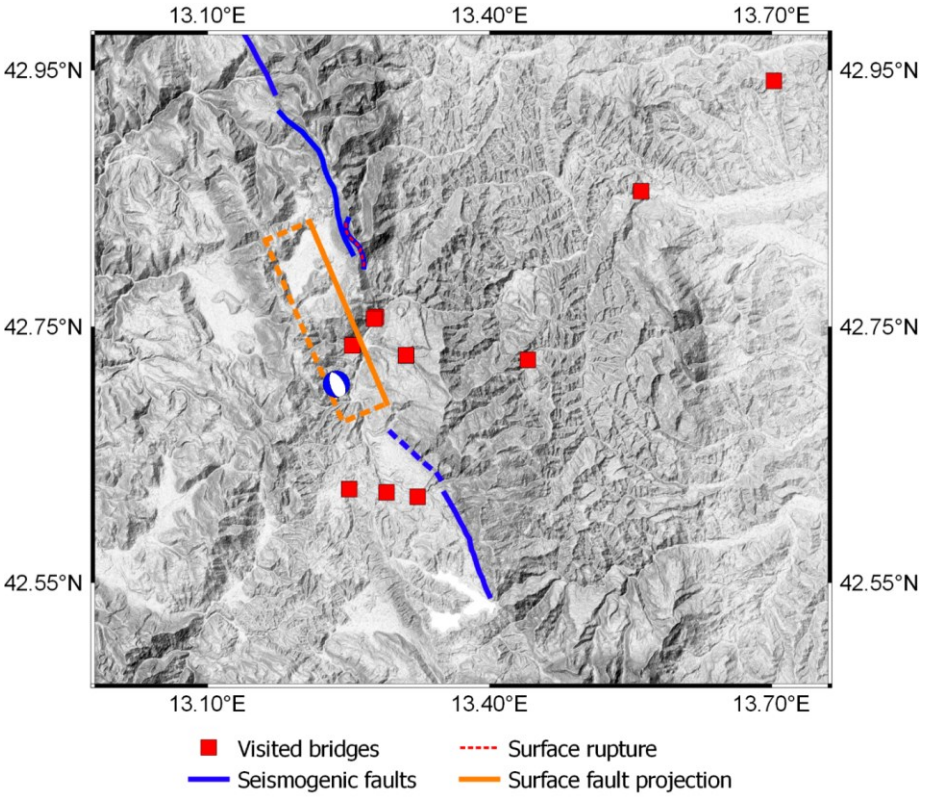

Figure 6.1. Map of epicentral region showing locations of bridge sites visited by the GEER/ReLuis team.

For each inspected bridge, GEER/ReLuis team members were accompanied by officials from the regions Lazio and Marche, respectively. The aim of the on-site work of GEER/ReLuis team was two-fold: (i) documenting the system performance for research applications and (ii) providing technical guidance to local government agencies regarding bridge safety (the latter being a Reluis objective). For a given bridge, the reconnaissance process included checking of the road surface, the main structural elements (such as piers, abutments, joints and supports) and other non-structural elements. We also checked for any evidence of ground failure near foundations or abutments, where these areas were visible or accessible. Due to limited time and lack of access to specialized equipment for rappelling into deep canyons spanned by some

bridges, it was not possible to access all the foundations of piers and abutments. For similar reasons, it was not possible to view the full lengths of bridge columns in some cases, nor the underside portions of deck supports. As a result, for some RC bridges, assessment of hammering phenomena could only be evaluated in an approximate manner by visual inspection of the deck and other readily visible areas.

The inspected bridges were classified according to their age: (1) relative modern viaduct-type bridges, built around the 1960's using reinforced concrete (RC) and/or composite RC and steel members; (2) older masonry arch bridges, which in some cases dated back to the Roman time.

Table 6.1. Details of the inspected bridges

	Type of bridge	Longitude [deg]	Latitude [deg]
SP 20 Colle (km 9+650) – Ponte Ramazzotti	Composite steel and concrete	13.311	42.7276
SP 20 – Colle (km 500)	RC	13.311085	42.727848
SP129 Trisungo-Tufo (km 4+900)	RC	13.278897	42.757709
SP7 Boscomartese (km 16+150)	RC	13.4405	42.7241
SR577 Torrente Rionero	RC	13.3233	42.6172
SS685 Tre Valli Umbre (km 2)	RC	13.277	42.75625
SS4 crossing the Tronto river – Ascoli Piceno	RC	13.560953	42.855762
SP173 – Offida	RC	13.702294	42.941687
Roman-era SP129 Trisungo-Tufo (1 span)	Masonry	13.254862	42.735981
Roman-era SP129 Trisungo-Tufo (3 spans)	Masonry	13.253655	42.73538
SR260 Ponte a Tre Occhi - Amatrice	Masonry	13.290176	42.620668
SR260 Ponte a Cinque Occhi - Amatrice	Masonry	13.250428	42.623178

6.2. Performance of RC and Composite RC bridges

The bridges inspected include:

- Composite steel and concrete bridge along the Strada Provinciale (SP) 20 Colle (km 9+650), also called Ponte Ramazzotti (Figure 6.2);
- RC bridge along the SP20 Colle (km 500);

- RC overpass along the SP129 Trisungo-Tufo (km 4+900);
- RC bridge along the SP7 Boscomartese (km 16+150) (Figure 6.3);
- RC bridge along Strada Regionale (SR) 577, also called Torrente Rionero (Figure 6.4);
- RC bridge along Strada Statale (SS) 685 Tre Valli Umbre (km 2) (Figure 6.5);
- RC bridge along SS4 crossing the Tronto river in Ascoli Piceno;
- RC bridge along SP173 in Offida (Figure 6.6).

Most of the inspected contemporary bridges do not show evidence of seismic induced damage (Figures from 6.2 to 6.4) that, if present, would have required a limitation in bridge utilization.

Figure 6.5 shows the RC bridge along the SS685 Tre Valli Umbre: from the visual inspection it seems that hammering occurs during the earthquake (Figures 6.5b and 6.5c), but it did not affect the functionality of the bridge, which continued to be operational after the event.

Figure 6.6 shows the RC bridge along the SP173 in Offida. This bridge presents significant settlements on the road close to the abutments (Figure 6.6b), that caused damage at the structural elements, as shown in Figure 6.6c. These settlements, which existed before the earthquake, have been amplified by seismic compression of backfill as a result of strong ground motion from the 24 August 2016 mainshock. Thus, it was suggested to limit the maximum load to be carried by the bridge, until specific geotechnical improvements to stabilize the area can be performed.

Figure 6.2. Ponte Ramazzotti - Composite steel and concrete bridge along the SP20 in Colle (42.7276 deg, 13.311 deg): overview of the bridge (a,b), abutment (c) and bridge support (d) details.

Figure 6.3. RC bridge along the SP7 in Boscomartese (42.7241 deg, 13.4405 deg).

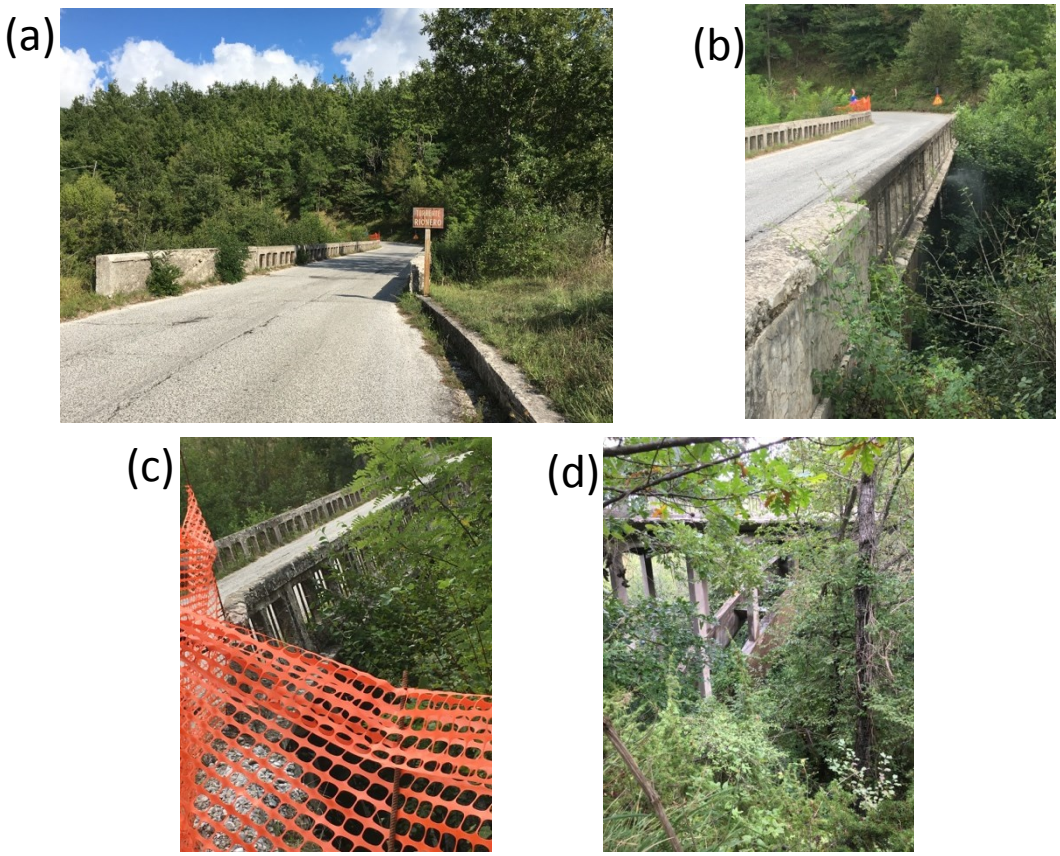

Figure 6.4. RC bridge along the SR577 Torrente Rionero (42.6172 deg, 13.3233 deg): overview of the bridge (a), rupture of the water pipeline on the bridge side (b) and view of the structure (c, d).

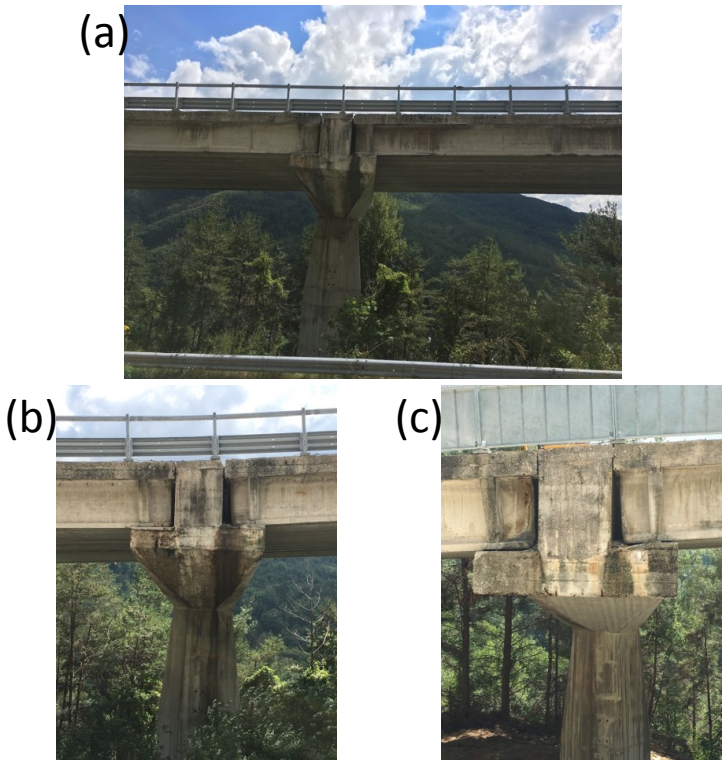

Figure 6.5. RC bridge along the SS685 Tre Valli Umbre (42.75625 deg, 13.277 deg): overview of the bridge (a), details of the hammering evidences (b and c).

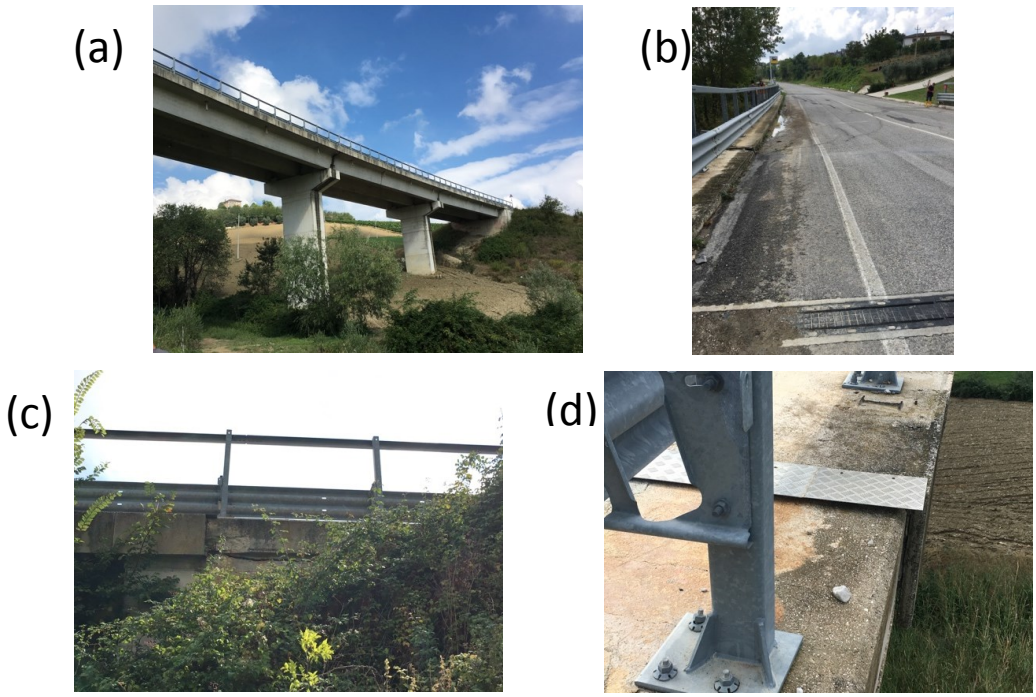

Figure 6.6. RC bridge along the SP173 in Offida (42.941687 deg, 13.702294 deg): overview of the bridge (a), settlement of the road (b) crack (c) and relative displacement of the abutment (d).

6.3. Performance of Masonry Bridges

The bridges inspected include:

- Two arch bridges along the Roman-era SP129 Trisungo-Tufo, located near the village of Tufo (Figures 6.7 and 6.8);
- Ponte a Tre Occhi (Three eyes), located along the SR260 in Amatrice (Figure 6.9);
- Ponte a Cinque Occhi (Five eyes) located along the internal road connecting SS4 (exit of Casale Nibbi) and SR260, in the direction of Amatrice (Figure 6.10).

Two of the inspected masonry bridges showed evidence of seismically induced damage that affected the road surface (Figure 6.7a), typically as a result of differential settlement (Figure 6.9b). These effects caused local officials to limit the use of the SP129 bridge and to close the SR260 bridge, at the time of our site visits.

Figure 6.7 shows one of the two arch bridges inspected along the Trisungo route. It is a single arch bridge. Cracking within load-bearing masonry elements and spalling of surface masonry elements of the interior part of the arch (Figure 6.7d) were observed. Similar effects were observed for the second arch bridge along the Trisungo route (Figure 6.8), formed by three arches. In this case, partial collapse was observed of short walls above the roadway surface (Figures 6.8a and 6.8b), spalling of several elements in the central arch (Figure 6.8c) and significant cracks of some masonry elements on the east support of the central arch (Figure 6.8d). Due to the extensive damage, local officials decided to limit traffic loads over these bridges. It should also be noted that the damage and the partial collapse of masonry elements within the bridge was located in relatively recently added sections of the bridge. The bridge is comprised of an older (Roman era) part and a relatively recent extension; the latter behaved poorly during the earthquake and experienced the severe damage mentioned above.

Figure 6.9 shows the masonry bridge referred to locally as the Ponte a Tre Occhi in Amatrice. This bridge is a critical lifeline for access to Amatrice and was closed on the date of our visit (8 September 2016). The bridge is formed by three arches and the main structure is comprised of *muratura a sacco*, which is a typical method of masonry construction (Giuliani, 1993). This method consists of using regular-shaped masonry elements on the external part of the construction, sometimes with between-element mortar. The interior part of the construction is comprised of relatively irregularly shaped cobbles, usually without mortar. During the earthquake, several sections of the external (regular-shaped) layer collapsed (Figures 6.9a and 6.9c). This resulted in a lack of confinement of the interior, uncemented cobbles, which then underwent lateral relaxation and settlement that was observable on the roadway surface (Figures 6.9a and 6.9b). These diffuse transverse cracks along the road surface have maximum openings of about 5 cm and 2.7 cm horizontally and vertically, respectively. A widespread deformation pattern existed before the mainshock, due to slope instability in the eastern abutment of the Castellano river, as shown in Figure 6.9e and 6.9f (dated December 2011). Moreover, internal cracking was observed on all the arches of the bridge (Figure 6.9d).

Figure 6.7. Masonry bridge along the Trisugo route (42.735981 deg, 13.254862 deg): damages on the road (a), overview of the bridge (b), abutment (c) and partial collapse of the interior part of the arch (d).

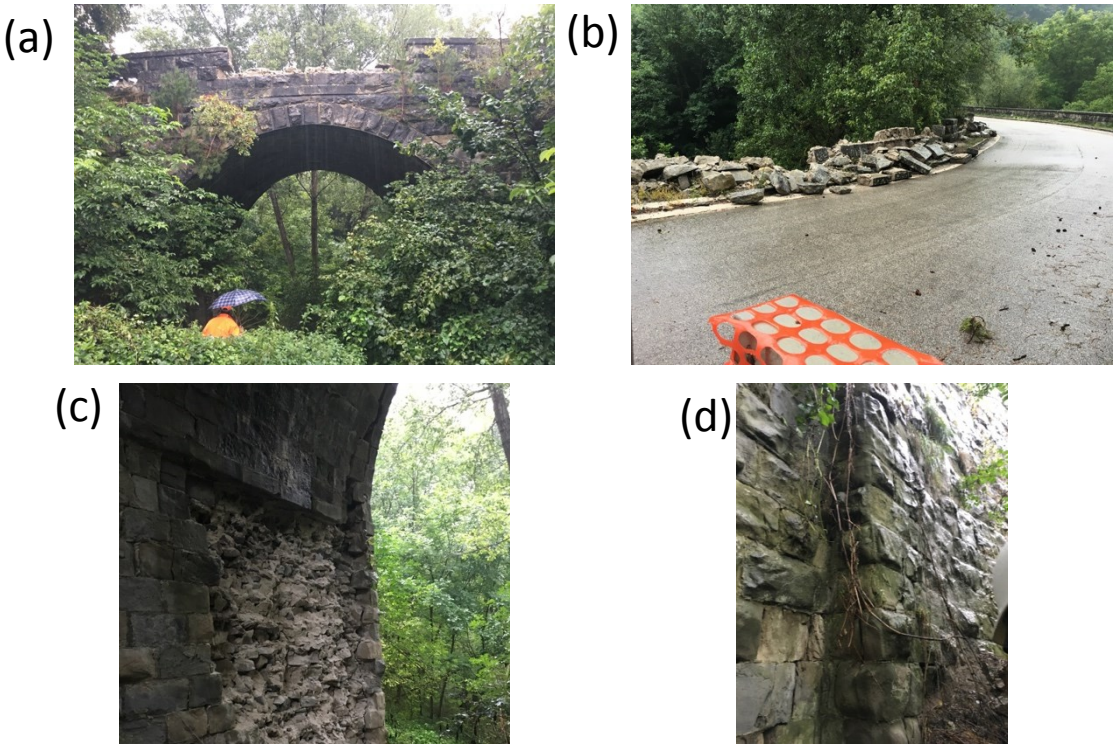

Figure 6.8. Central arch of the three arches masonry bridge along the Trisugo route (42.73538 deg, 13.253655 deg): partial collapse of the railing (a, b) spalling (c) and cracking (d) of some masonry elements.

Figure 6.10 shows the masonry bridge called “Ponte a Cinque Occhi” along the internal road connecting SS4 (from the Casale Nibbio exit) and SR260 along Scandarello lake. The bridge was constructed using the *muratura a sacco* method (similar to “Ponte a Tre Occhi”) and includes five arches. The earthquake caused the collapse of the external masonry panel (Figures 6.10a and 6.10c). Figures 6.10b and 6.10c show structural improvements (retrofits) that cover original masonry elements. Some damage was also observed at the southern abutment (Figure 6.10d). As shown in Figures 6.10b and 6.10c, bridge maintenance was poor.

The Ponte a Cinque Occhi bridge is a critical lifeline for access to Amatrice from the west. The bridge deck surface was not cracked along the road surface nor at abutments. Structural stability was judged to have not been affected by the earthquake and no traffic restrictions were applied.

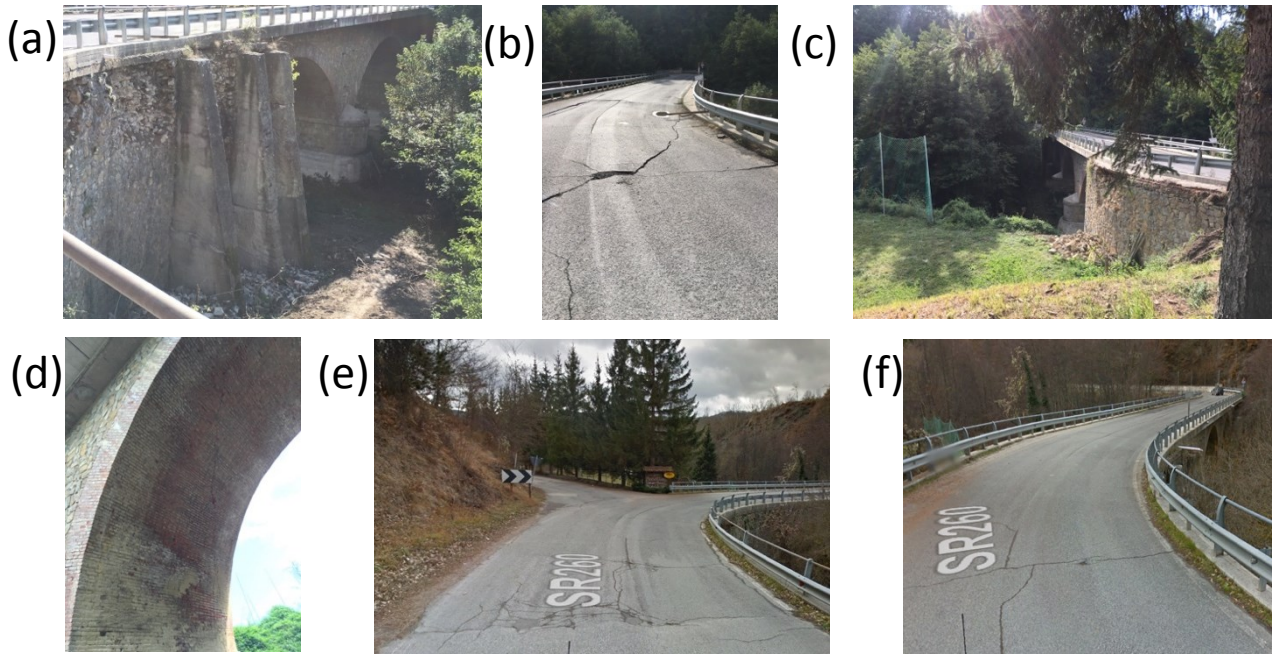

Figure 6.9. Ponte a Tre Occhi - Masonry bridge along the SR260 in Amatrice (42.620668 deg, 13.290176 deg): partial collapse of two side of the bridge (a, c), road settlement (b), cracks on the arch (d), pre-event cracks along the SR260 (e) and bridge-abutment connection (f) (source (e) and (f): Google maps).

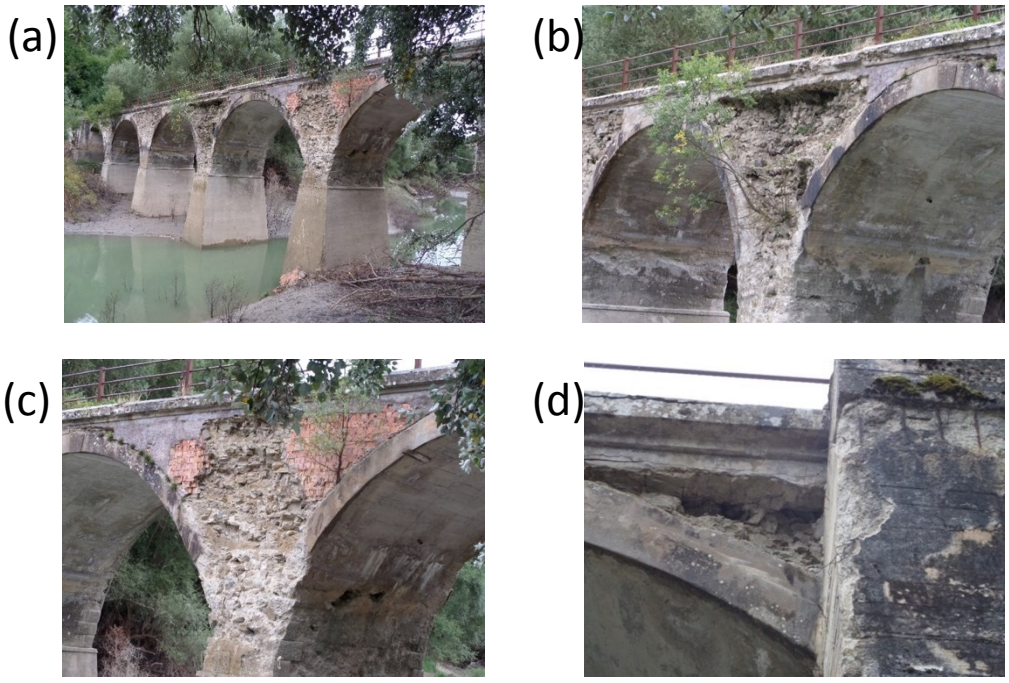

Figure 6.10. Ponte a Cinque Occhi - Masonry bridge (42.623178 deg, 13.250428 deg): (a) view of the 5 bridge arches, (b, c) partial collapse of the bridge masonry with evidence of previous structural interventions, (d) detail of the bridge-abutment connection.

7.0 Other Infrastructure Systems

Principal authors: Francesca Bozzoni, Giuseppe Lanzo, Stefania Sica, Francesco Silvestri

Contributing authors: Stefano Aversa, Michele Mucciacciaro, Paolo Zimmaro

The aim of this chapter is to illustrate the results of observations pertaining to the performance of retaining walls, rockfall barriers and road embankments (Sec. 7.1) as well as to describe the performance of dams (Sec. 7.2) located in the area affected by the August 24, 2016 earthquake.

7. 1 Retaining Walls, Rockfall Barriers, and Road Embankments

In this section, the damage observed on six retaining walls (RW), one rockfall barrier (RB) and three road embankments (RE) will be described. These infrastructure components are located in the municipalities of Amatrice (Figure 7.1a), Arquata del Tronto (Figure 7.1b), and Pescara del Tronto (Figure 7.1c).

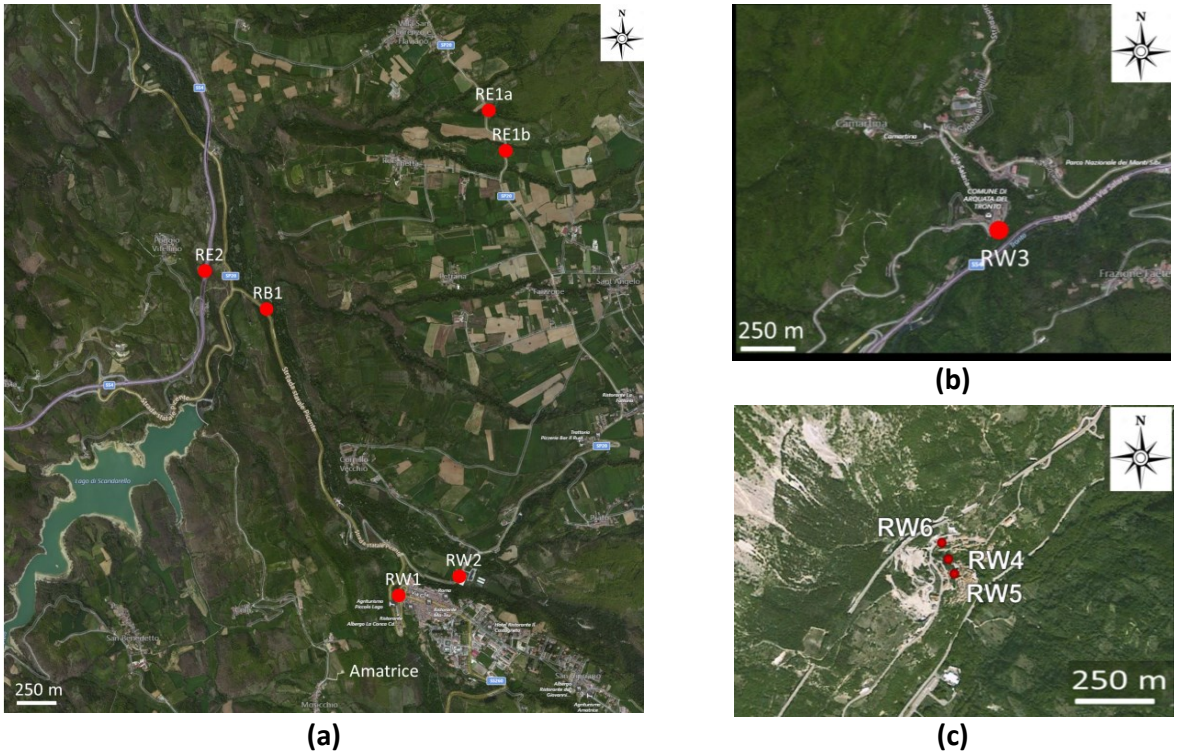

Figure 7.1. Locations of Retaining Walls (RW), Rockfall Barriers (RB) and Road Embankments (RE) observed in the municipalities of Amatrice (a), Arquata del Tronto (b) and Pescara del Tronto (c).

7.1.1 Retaining Walls

Figure 7.2a shows a gravity retaining wall collapsed along and beneath the SS260 road, near the intersection with the village street “Viale Francesco Grifoni”. The wall is constructed of poorly-cemented stone masonry, which is typical of the area (Figure 7.2b). The backfill soil is likely drawn from a pebbly alluvial formation found in in the historical center of Amatrice.

In addition to wall collapse, diffuse cracks along the road surface were observed, which required some asphalt repair. During our reconnaissance (September, 2016), some of these cracks were still evident in the unpaved part of the road (Figure 7.2c). The cracks observed along and across the SS260 road may be linked to displacements of the wall and, probably, also of the slope interacting with it. As shown in Figure 7.2d, pre-event roadway cracks suggest that some deformation may have preceded the mainshock; the photograph shows diffuse cracking along the road surface (along and normal to the direction of travel) and cracking in the brick wall parapet.

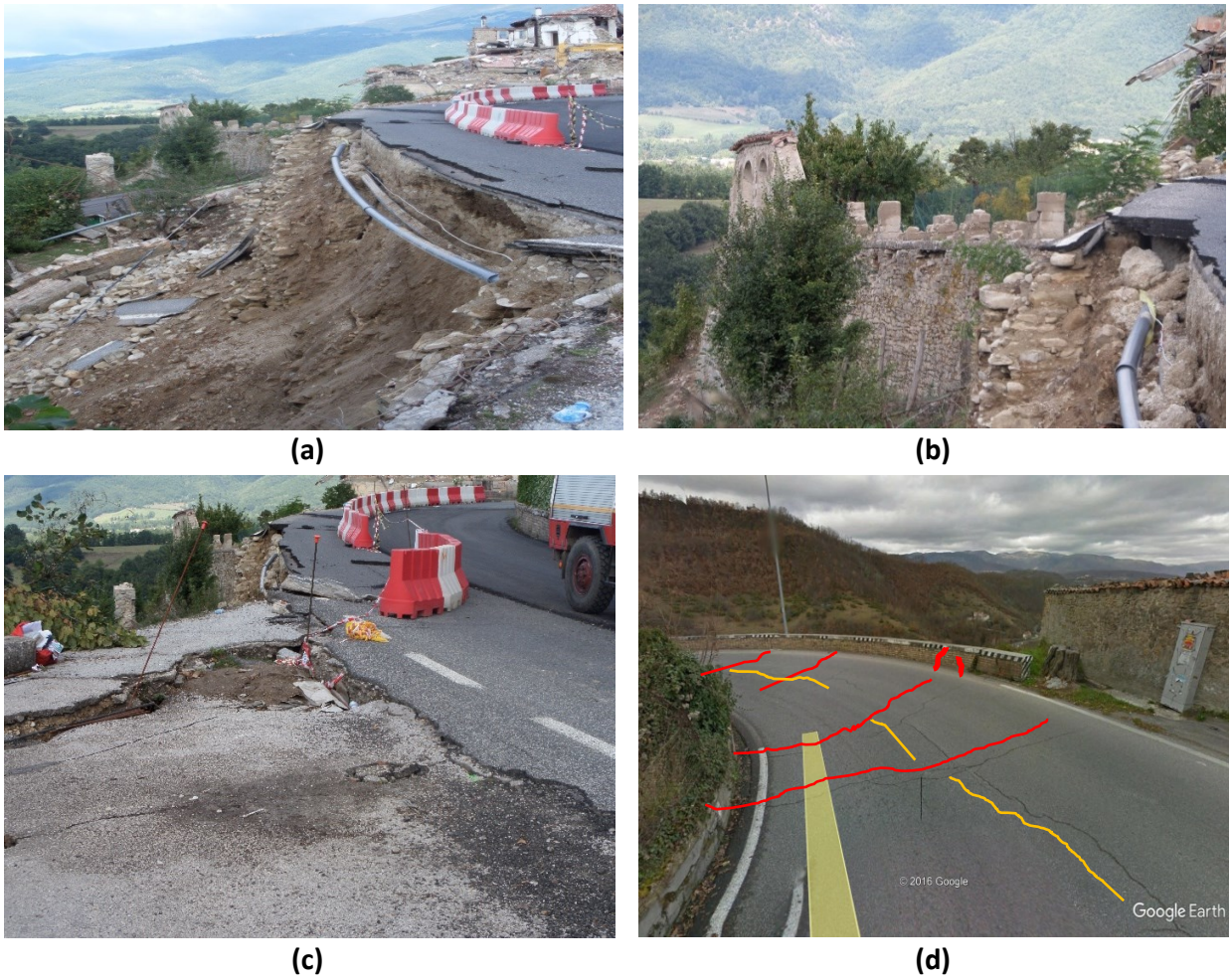

Figure 7.2. Retaining wall along the SS260 road close to Amatrice urban area (42.629533N, 13.286448E): (a) collapse of the wall, (b) detail of the stone masonry texture, (c) cracks along the unpaved portion of the road, (d) Google Earth (July 2011) view of the SS260 road before the earthquake, with evidences of diffuse cracks along the asphalt.

Figure 7.3a shows a collapsed retaining wall supporting a parking lot in the hamlet called "Ponte Sommati", near Amatrice. The lower part of the wall was made of poorly reinforced concrete and the upper part was built with concrete blocks. The images in Figure 7.3b-c indicate the poor quality of the wall, including poor connections between the upper and lower parts.

(a)

(b)

(c)

Figure 7.3. Retaining wall at Ponte Sommati, in the surroundings of Amatrice (42.630662N, 13.291511E): (a) global view of the collapsed wall, (b) side of the wall not collapsed during the earthquake, (c) pre-earthquake image of the retaining structure (Google Earth, July 2011).

Figure 7.4a shows the collapse of the uppermost portion of a masonry wall located along SP129 road near the entry to Arquata del Tronto. The wall has a masonry arch structure, which appears to have been recently restored in the outer face (Figure 7.4b). The soil behind the wall consists of highly fractured marl or marl blocks of maximum size on the order of 1 m (Figure 7.4b-c). Co-seismic relaxation of these marl blocks towards the collapsed wall face contributed to roadway extension and settlement (Figure 7.4d). The cracks along the road surface have maximum openings on the order of 8.0 cm horizontally (Figure 7.4e) and maximum relative vertical displacements of 4 cm. At this site, there was no evidence of any pre-event instability (Figure 7.4f).

Figure 7.5 shows three cases of retaining walls damaged in Pescara del Tronto. In each case, the observed damage may be attributed in part to the poor quality of the retaining structures. Figures 7.5a-b show the collapse of two relatively low masonry walls. The wall in Figure 7.5a is made of concrete blocks connected by mortar, with no evidence of drainage measures having

been installed in the backfill. The wall in Figure 7.5b was erected with a typical dry-stone masonry technique (no mortar between stones) with no foundation. Figure 7.5c-d illustrate the damage to a fence drapery breached by calcarenite rock blocks falling from a slope as high as 8m. No significant damage was observed in the adjacent high concrete wall.

Figure 7.4. Masonry retaining wall in Arquata del Tronto (42.771898N, 13.296715E): (a) partial collapse of the wall parapet, (b) arch masonry structure, (c) marl blocks along the SP129 road, (d) road instability at the top of the wall, (e) opening of the cracks developing along the direction parallel to the road axis, (f) Google Earth view of the site (dated May 2011).

Figure 7.5. Retaining walls in Pescara del Tronto: (a) collapse of a concrete block masonry wall (42.751705N, 13.270562E), (b) collapse of a dry-stone masonry wall (42.751141N, 13.270889), (c) fence drapery breached by calcarenite rock blocks, (d) performance of the adjacent concrete wall (42.752331, 13.270207E).

7.1.2 Rockfall Barriers

Figure 7.6a shows damage to a rockfall barrier along the SS260 road branch that connects Amatrice to the main road SS4 (Salaria). At the time of the reconnaissance, a protection embankment was placed at the toe of the slope (Figure 7.6b). The slope behind the barrier is covered with a hexagonal mesh, which along the failed slope is simply draped with no evidence of reinforcement (Figure 7.6c), while along the stable slope it appears connected to the arenaceous flysch formation by ropes and nails (Figure 7.6d).

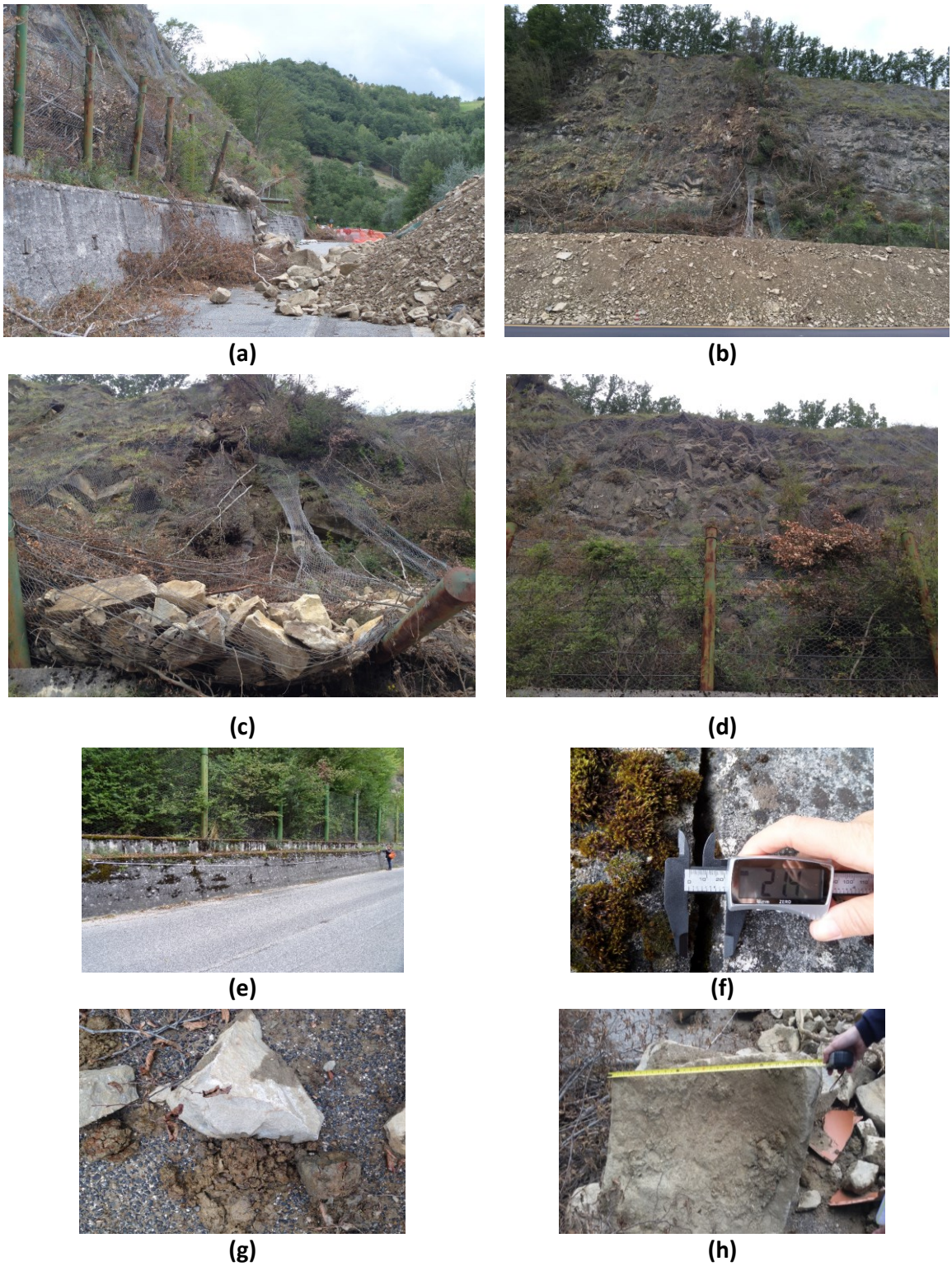

Figure 7.6. Damage to a rockfall protection system along the SS260 road (42.648203N, 13.274285E) in Amatrice municipality: (a) collapsed zone; (b) failed (left) and stable (right) parts of the slope with protection embankment in the foreground; bottom view of the failed (c) vs. stable (d) slope and barrier; concrete wall supporting the barrier (e) and previous crack (f) denoting the absence of reinforcement; (g) arenaceous block with silty matrix and (h) maximum size of the rock blocks fallen.

The rockfall barrier is comprised of a fence with steel horizontal cables connected to vertical cantilever tubular piles anchored to a concrete beam placed upon a 1.4 m tall retaining wall (Figure 7.6e). The concrete wall appears to be unreinforced (Figure 7.6f).

Collapse of the system may be attributed to several factors, among which the lack of anchorage of the mesh panels to the slope and between adjacent panels too, inadequacy of the rockfall barrier with reference to the foundation of the tubular elements, the absence of any retaining cable on the top of the barrier, and the limited strength of both the fence and the horizontal cables. The rockfall barrier was not able to intercept arenaceous blocks up to approximately 30-40 cm in size (Figure 7.6f-g), sliding or falling from a maximum height of about 12 m.

7.1.3 Road Embankments

Longitudinal cracks (Figure 7.7a) were observed in two locations (42.660061N - 13.293697E; 42.657023N - 13.295309E) along SP20 road between Amatrice hamlets San Lorenzo e Flaviano and Sommati. In both cases (RE1a and RE1b in Figure 7.1), differential settlement occurred between a masonry bridge (Figure 7.7b) and an adjacent road embankment. In both locations, the road embankment was probably built after the construction of the small masonry bridges, in order to enlarge the SP20 roadway. A stainless Armco® tube (Figure 7.7c) lies underneath the embankment and the small bridge, apparently acting as a culvert.

The maximum differential settlement observed in the reconnaissance is on the order of 20 cm (Figure 7.7d) at the contact between the bridge and the embankment. Another longitudinal crack parallel to the road axis was observed at the border of the pavement surface (Figure 7.7e) at the outer boundary of the road embankment.

Traces of differential settlements along the road surface were evident before the earthquake as shown in Figure 7.7f (photo dated July 2011; Google Earth image for reference site 42.660061N - 13.293697E). The earthquake appears to have caused seismic compression of the road embankment fill, exacerbating prior settlements, presumably from hydro-compression or similar.

We observed longitudinal cracks (Figure 7.8a-b) at km 133 of main road SS4 (Salaria). Maximum crack widths in the asphalt surface are around 3 cm (Figure 7.8c) and cracking was also observed at the edge of the road pavement (Figure 7.8d). Adjacent to this section of road is a nearly vertical cut. Nearby areas with gentler slopes had no pavement cracking.

Figure 7.7. Embankment instability along the SP20 road between the villages of San Lorenzo e Flaviano and Sommati (42.660061N, 13.293697E): (a) longitudinal crack along the road surface after the earthquake;(b) downstream view of the crossing section; (c) view of the Armco tube underneath the embankment; (d) maximum vertical settlement at the bridge-embankment connection; (e) longitudinal crack at the border of the pavement surface; (f) previous conditions of the road branch before the earthquake (Google image dated July 2011).

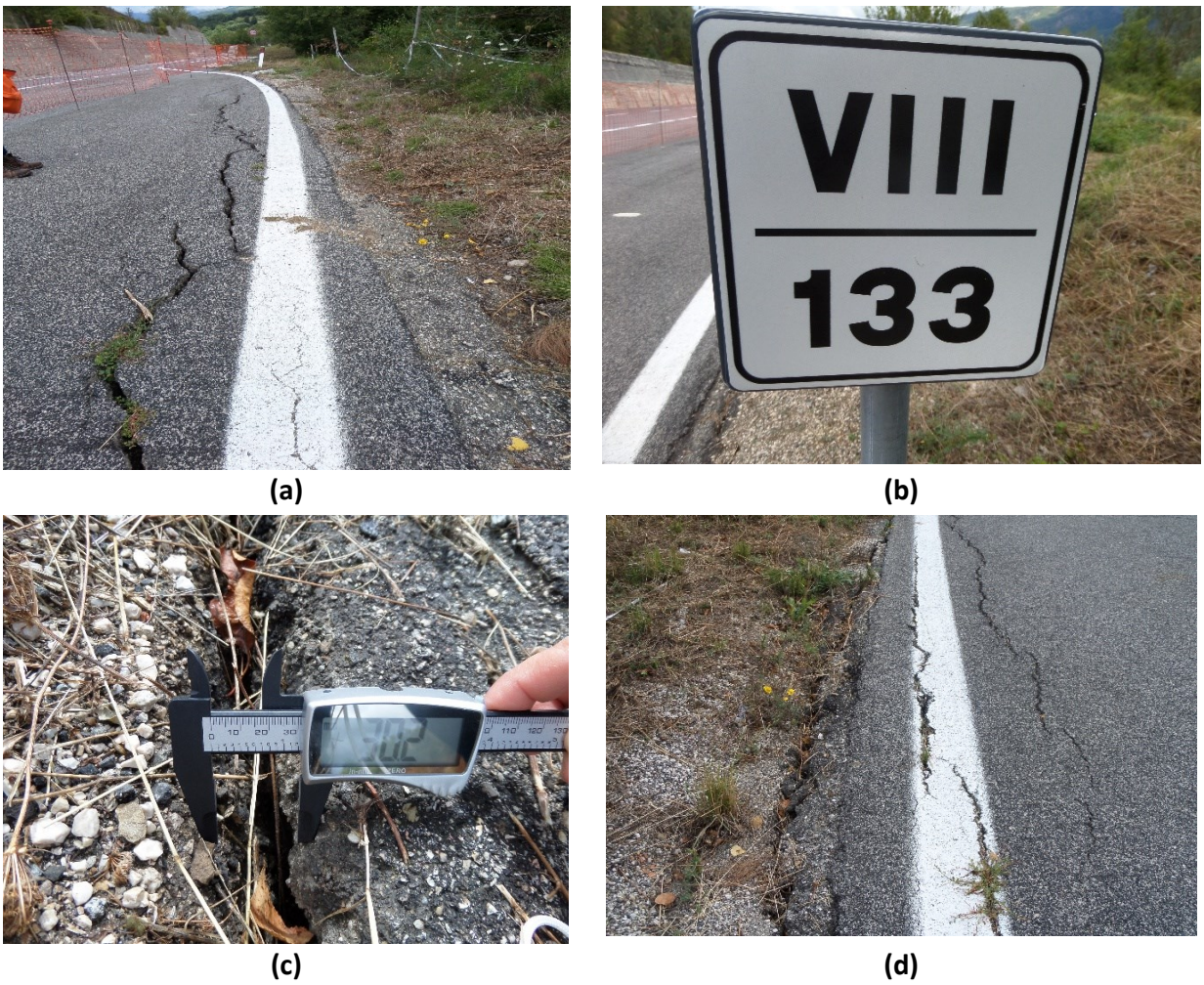

Figure 7.8. Embankment instability along the SS4 road at km 133 (42.650533N - 13.270442E): (a) longitudinal cracks along the whole rest area, (b) identification of the site location by road sign, (c) maximum horizontal opening of the longitudinal crack, (d) disconnection between the lateral slope and the road surface.

7.2 Dams

Figure 7.9 shows the locations of major dams in the epicentral region, along with position of finite fault and event moment tensors. Five dams are in the near-fault region. Table 7.1 lists the dams and their closest distance to the trimmed finite fault model from Chapter 3. These dams are owned and operated by ENEL (Electricity Board of Italy).

One member of the GEER team participated in reconnaissance of the dams jointly with a team representing the French Association for Earthquake Engineering (AFPS), led by Didier Combescure, on October 19, 2016. ENEL did not allow access to the dams prior to this date. Technical visits of four dams, i.e. Scandarello dam and the three dams impounding Campotosto

lake (i.e. Poggio Cancelli, Sella Pedicate, and Rio Fucino) shown in Figure 7.10, were conducted under escort from ENEL technical staff.

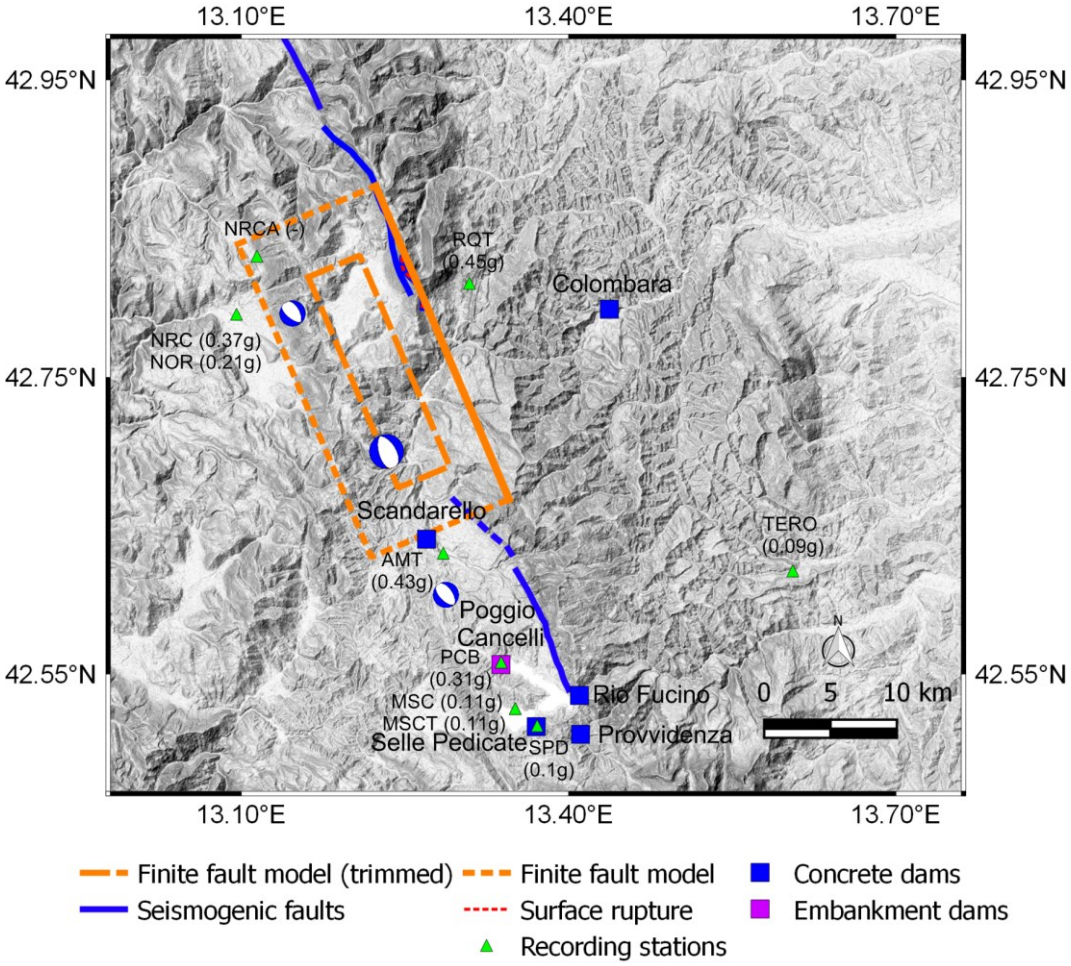

Figure 7.9. Map showing dams in epicentral region relative to position of finite fault and event moment tensors. Seismic stations (green triangles) are also shown with the recorded values of peak ground acceleration (largest horizontal component) in brackets (see Chapter 3).

Table 7.1. Main characteristics (Ministero Infrastrutture e Trasporti, 2009) of the dams located near the August 24, 2016 Central Italy earthquake epicenter.

Dam name	*Dam type*	*Dam height (m)*	*Impounded volume (Mm^3)*	*Epicentral distance (km)*	*Closest distance to the fault - R_{JB} (km)*
Scandarello	concrete gravity	44.0	12.5	7.4	4
Poggio Cancelli	earthfill	27.3	218	18.3	14.7
Sella Pedicate	concrete gravity + earthfill	36.7		23.7	20
Rio Fucino	concrete gravity	36.7		23.4	19
Provvidenza	arch	46.2	2.4	25.9	21.8
Colombara	concrete gravity	19.7	0.5	19.2	15.5

Figure 7.10. Map showing the Campotosto reservoir, dams located in the region (squares), and seismic stations (triangles) with the recorded values of peak ground acceleration in brackets.

According to the Italian Dam Office Regulation, the dam managers are responsible for conducting special safety inspections after an earthquake. These inspections consist of a primary detailed visual survey immediately after the earthquake, followed by a careful check of the data recorded and measured by the monitoring devices installed for safety management. The above controls have been carried out and, according to ENEL staff queried during the survey, all dams withstood ground shaking with no damage. It is worth mentioning that the same dams experienced the 2009 L'Aquila earthquake, showing a very satisfactory seismic response. As a matter of fact, even in this previous strong-motion event none of the dams and their appurtenant structures were damaged by ground shaking (Caruana et al., 2010; Catalano et al., 2013).

A brief description of the dams located in region affected by the August 24 earthquake is provided in the following sub-sections.

7.2.1 Scandarello Dam (Rieti Province)

Scandarello dam is the closest to the epicenter of the August 24 earthquake (Figure 7.9 and Table 7.1). It is a concrete gravity dam with a curved axis located in the Municipality of Amatrice (Rieti Province), along Rio Scandarello, a tributary of Tronto River. The reservoir (Figure 7.11a) with a

capacity of 12.5 Mm^3 is used for hydroelectric power generation in a facility located at the foot of the dam (Figure 7.11b and Figure 7.12). The dam was constructed between 1921 and 1927. Figure 7.13 shows a cross-section (a) and a photo (b) taken during the survey on October 2016 of this dam, 44m high and 199.7m long. The radius of the arch is equal to 150m. The crest of the dam, 6m wide, reaches an elevation of 876.5m a.s.l. The core is monolithic without vertical joints and the base has a thickness of about 40m. The foundation plan is shaped in terraces with an inclination downstream. The foundation substratum is comprised of sandstone and marlstone.

The monitoring system of Scandarello dam has been active since the 1960s and includes various control points at the crest, within the core of the dam, and 15-16m vertically beneath the toe of the dam. Upstream/downstream displacements and the rotation at base of the dam are measured by extensometers and inclinometers. In the immediate aftermath of the August 24 mainshock, only a few millimeters of displacements were measured. More detailed information was not available at the time of the survey. This dam is not instrumented with seismic monitoring devices. The closest seismic station to Scandarello dam is AMT (separated from the dam by 1.7 km). During the August 24 event, the AMT station recorded a peak ground acceleration of about 0.43 g (see Chapter 3.0).

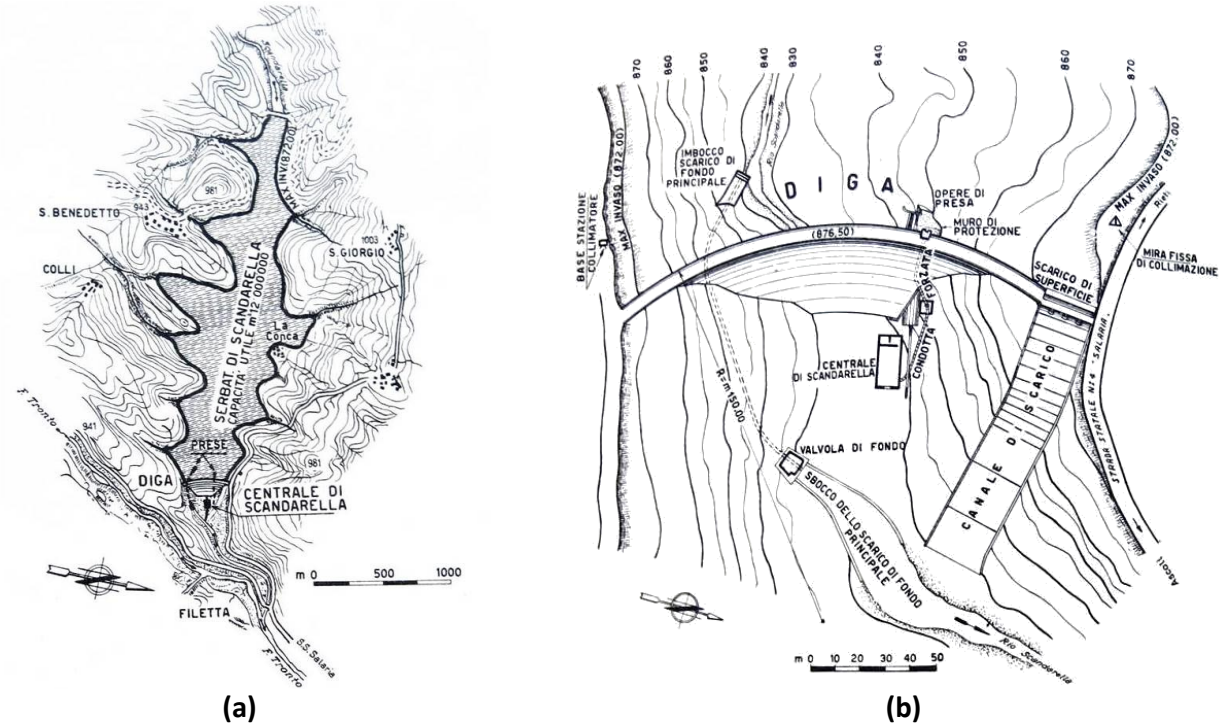

Figure 7.11. Plan view of the reservoir (a) and of the dam of Scandarello (b), located in the Municipality of Amatrice (after ANIDEL, 1951).

Inspections carried out by ENEL staff after the earthquake revealed no damage to Scandarello dam, which we confirmed on October 19, 2016 (Figure 7.12). Furthermore, ENEL staff stated that

no slope instability could be observed along the banks of the reservoir (Figure 7.14). At the time of earthquake, the water was about 5 m below the maximum level, as during the survey on October 19, 2016. When the August, 24 mainshock occurred, the turbine within the station at the foot of the dam stopped operating, which was because of power loss, not damage caused by ground shaking. This turbine is not equipped with a vibration monitoring system.

Figure 7.12. Downstream face of Scandarello dam, with the homonymous station for hydroelectric power generation located at the foot of the dam (October 19, 2016).

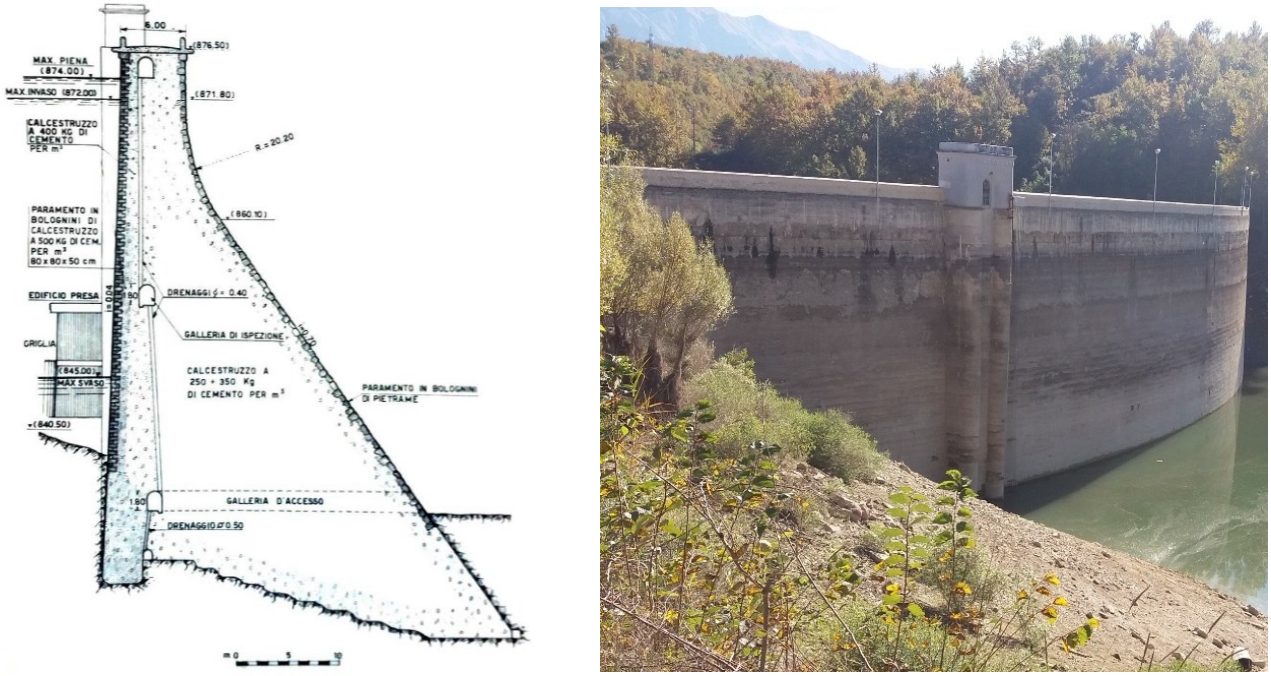

Figure 7.13. Scandarello dam: (a) cross-section (ANIDEL, 1951); (b) photo of the upstream face taken on October 19, 2016 (42.641560°N, 13.269000°E).

Figure 7.14. View of the reservoir from Scandarello dam viewpoint (October 19, 2016): no phenomena of bank instability were observed after the earthquake.

7.2.2 Campotosto Reservoir (L'Aquila province): Dams of Poggio Cancelli, Sella Pedicate and Rio Fucino

Campotosto lake is a man-made reservoir with a capacity of 218 Mm^3, at an altitude of 1313 m a.s.l. It is located within the Province of L'Aquila. As shown in Figure 7.10, the lake is impounded by three dams: Poggio Cancelli, Sella Pedicate and Rio Fucino. Reservoir filling was completed in the 1970s and its water is used for electrical power production.

Poggio Cancelli is a zoned earth dam crossing the Rio Castellano, a tributary of Tronto River. The dam is located about 18 km from the epicenter of the mainshock (Figure 7.9). Figure 7.15, Figure 7.16a and Figure 7.16c respectively show a photo of the dam taken during the GEER survey, the dam cross-section, and material properties from the literature (Jappelli and Silvestri, 2006). The embankment is 27.3m high and 600m long. The original dam was constructed between 1941-51 and is comprised of a central core of low permeability and rockfill shells. The crest of the dam reaches an elevation of 1315m a.s.l. The dam section was subsequently enlarged as shown in Figure 7.16a with the construction of a further embankment between 1964 and 1971. The crest of the current dam is at an elevation of 1327.5m a.s.l.

The core is composed of clayey silt; the upstream shell is composed of calcareous gravel; and the downstream shell has a lower zone made of the same material as the upsteam shell and an upper zone composed of arenaceous gravel. The core of the enlarged dam is located downstream of the original dam and extends horizontally at its base. The upstream shell incorporates the original dam and fully retains the upstream face. The foundation soils are characterized by

coarse-grained alluvial sands and gravels, with lenses of fine grained soils, superimposed on an arenaceous bedrock. The alluvial deposits beneath the clay core were grouted and a concrete cut-off wall was also installed to control seepage through the alluvium below the dam.

Settlements and interior pore pressures of the Poggio Cancelli dam are monitored by a complex system which includes several control points, located at the crest, within the core, vertically beneath the toe of the dam, and downstream of the toe of the dam. By combining the measurements provided by settlement gauges and from differential leveling surveys, the system allows to obtain separately the settlements of the core and in the underlying foundation. In the immediate aftermath of the August 24 mainshock, only a few millimeters of settlements of the crest were measured. More detailed information was not available at the time of the survey. The Poggio Cancelli dam hosts the PCB station (Figure 7.15), which, during the August 24 earthquake, recorded a horizontal peak ground acceleration as high as 0.31 g (Figure 7.10). The installation date is September 28, 1994 according to ITACA (ITalian ACcelerometric Archive, V2.1; http://itaca.mi.ingv.it). Despite the severity of ground motion, the seismic response of Poggio Cancelli dam was satisfactory.

Figure 7.15. Poggio Cancelli embankment dam on the Campotosto reservoir (L'Aquila): photo of the upstream face taken on October 19, 2016 (42.557106°N, 13.338342°E).

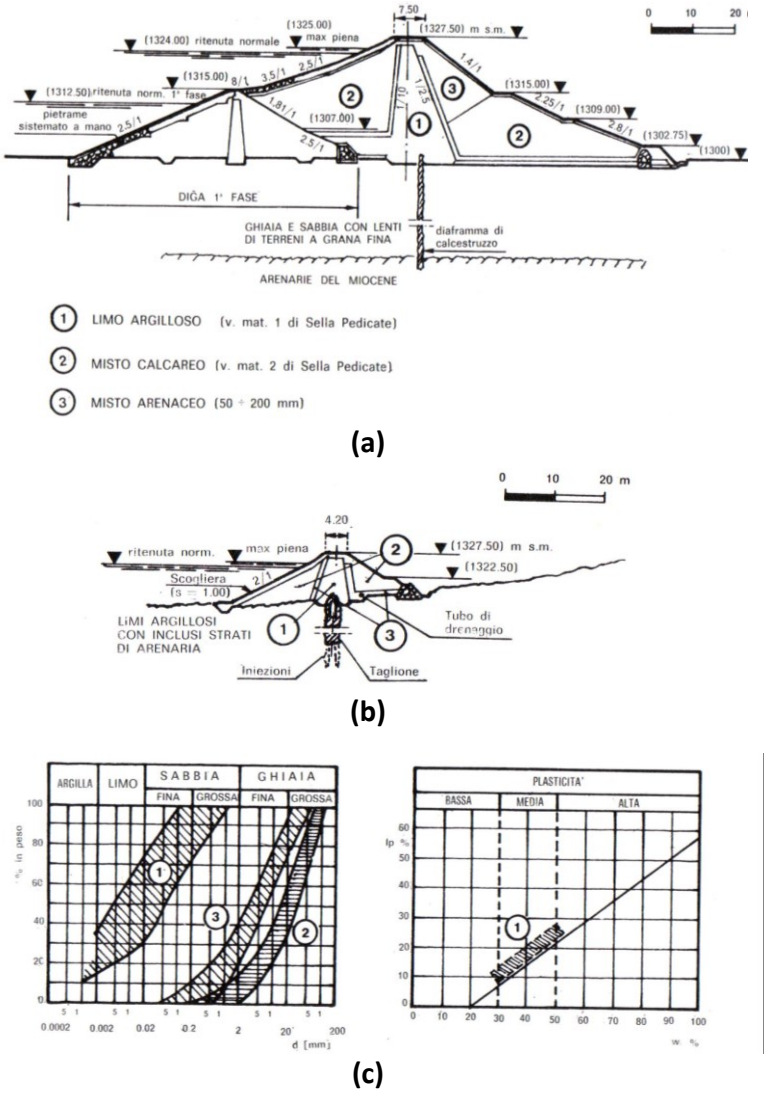

Figure 7.16. Cross-sections of the Poggio Cancelli dam (a) and of one extremity of Sella Pedicate dam (b) with their main geotechnical properties (c) (after Jappelli and Silvestri, 2006).

Figure 7.17. Downstream face of the Poggio Cancelli dam (October 19, 2016) with a close-up view of the light blue box hosting the PCB station (42.558022°N, 13.337990°E), which, during the August 24 earthquake, recorded a peak ground acceleration of about 0.31 g.

Sella Pedicate is a concrete gravity dam along most of its length but with a zoned embankment dam (with a clayey central core and a concrete foundation diaphragm) on the left abutment. The dam was built from 1965 to 1971; it is 20.75m tall and 750m long. Figure 7.18a shows the upstream face of the concrete dam, which is very steep (about 5 horizontal to 1 vertical), while the downstream face has a much milder inclination. The upstream face of the embankment dam is shown in Figure 7.18b, while the cross-section and the material properties are reported in Figure 7.16b and Figure 7.16c, respectively.

It is important to highlight that the SPD seismic station was located within the surveillance station of the dam since April 15, 2009 (after L'Aquila earthquake). During the August 24 earthquake, the SPD station recorded a peak ground acceleration of about 0.11 g. After the mainshock, no damage was observed to Sella Pedicate dam, which is located 23.7 km from the epicenter.

Rio Fucino is a concrete gravity dam with a triangular cross-section and a rectilinear longitudinal axis. The dam encloses the Campotosto basin at the eastern side (Figure 7.10). The maximum impounding level is equal to 39m and the length of crowning is equal to 154m. The body of the dam is subdivided into 12 ashlars through 11 joints located along vertical planes. The height of maximum storage is 1318.15m a.s.l.. A photo of the downstream face and a cross-section of the dam are shown in Figure 7.19a and Figure 7.19b, respectively. Pictures of the upstream face and bell-mouth spillway of the dam are shown in Figure 7.20a and Figure 7.20b,

respectively. The dam was built in two phases: the first started in 1939 and finished in 1955, while a subsequent heightening phase began in 1966 and finished in 1971. In the 1990s, a variation was introduced and completed in 1994. An alternating layering of sandstone and marlstone constitutes the foundation subsoil. Following the seismic code at the time, the dam was designed assuming a level of seismicity S=9 for the site, corresponding to a peak ground acceleration of the order of 0.1g, i.e. close to that recorded at the SPD station, during the August 24 earthquake. The dam is located 23.4 km from the epicenter of the mainshock (Figure 7.9).

The inspections carried out by ENEL staff after the August 24, 2016 earthquake revealed that no damage to Rio Fucino dam was observed.

(a) (b)

Figure 7.18. Photos taken on October 19, 2016 of the upstream face of Sella Pedicate concrete dam (a) and of one of its extremities (b), which is an embankment dam (42.514468°N, 13.370155°E).

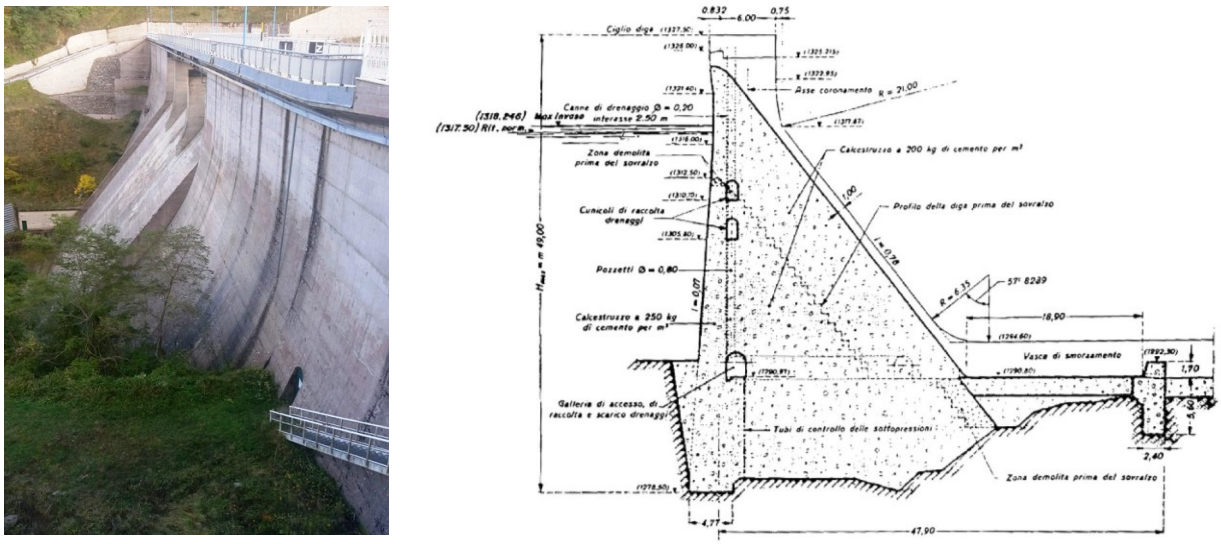

(a) (b)

Figure 7.19. Photo of downstream face taken on October 19, 2016 (42.535681°N, 13.409286°E) and a cross-section (b) of the dam (from FCEM, 1998).

(a) (b)

Figure 7.20. Photo of upstream face (a) and of the bell-mouth spillway (b) of the Rio Fucino dam (October 19, 2016).

7.2.3 Provvidenza Dam (L'Aquila Province)

Provvidenza dam is located at the confluence of the Chiarino creek with the Vomano river. It is a concrete arch dam located in the Municipality of l'Aquila. The reservoir with a capacity of 2.4 Mm^3 is used for hydroelectric power generation. The dam was built in two phases: first 1941-1943 and second 1946-1947. Figure 7.21 and Figure 7.22 show plan and cross-section views of Provvidenza dam. The dam is 46.2m high and 237.7m long at the crest. The crest of the dam reaches an elevation of 1063.2m a.s.l. The dam is founded on sandstone and marlstone formation.

The dam is located about 26 km from the epicenter of the mainshock (Figure 7.9). During the survey on October 19, 2016, the Provvidenza dam was not visited and no specific information on how the dam performed during the August 24, 2016 earthquake was provided.

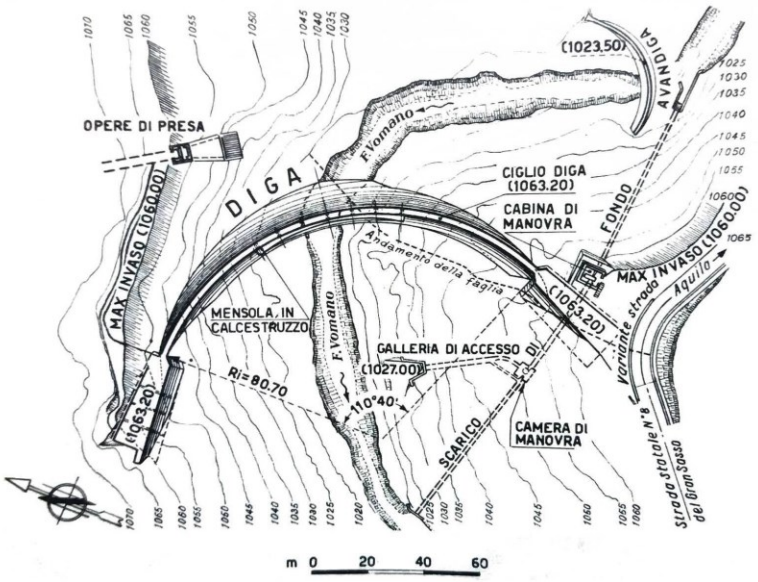

Figure 7.21. Plan view of the Provvidenza dam (from ANIDEL, 1952).

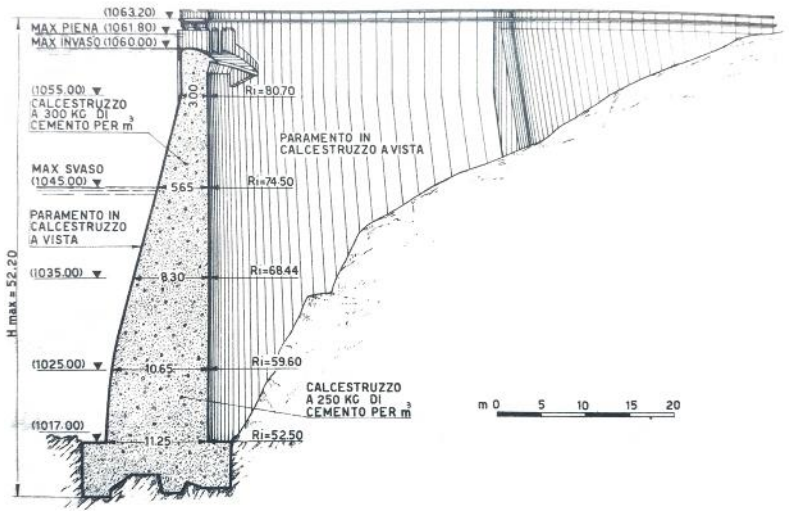

Figure 7.22. Cross-section of Provvidenza dam (from ANIDEL, 1952).

7.2.4 Colombara Dam (Ascoli Piceno Province)

Colombara dam is located on the Tronto river. It is a concrete dam placed in the Province of Ascoli Piceno, between the municipalities of Acquasanta Terme and Roccafluvione. The reservoir has a capacity of about 0.5 Mm^3 and is used for hydroelectric power generation. The dam was built between 1953 and 1955; it is about 20 m high and reaches an elevation of more than 300 m a.s.l. Figure 7.23 shows a plan view of Colombara dam. As shown in Figure 7.10, the Colombara dam is located about 10 km far from RQT station, which, during the August 24 earthquake, recorded a peak ground acceleration of about 0.45 g.

The dam is located about 19.2 km from the epicenter of the mainshock (Figure 7.9). During the survey on October 19, 2016, the Colombara dam was not visited and no specific information on how the dam performed during the August 24, 2016 earthquake was provided.

Figure 7.23. Plan view from Google Earth of Colombara dam.

8.0 Lessons Learned and Next Steps

Jonathan P. Stewart, Giuseppe Lanzo, Francesco Silvestri

Earthquake engineering and engineering seismology are disciplines that are experience-driven to a substantial extent. Post-earthquake reconnaissance, for example as recorded in this report for the 2016 Central Italy earthquake, provides the means by which we develop this experience and document it for use by the broader community. In the case of man-made structures and systems, we examine the effectiveness of our methods and practices. In many cases data gathered during reconnaissance is not from engineered systems but from natural systems (e.g., ground motions, ground failure, etc.); such data plays a fundamental role in the development of engineering methods for seismic risk forecasting (e.g., ground motions, ground failure hazards).

In this report we present the results of reconnaissance and related data processing activities undertaken over approximately a one month period following the mainshock event on 24 August 2016. As a GEER team, our primary mission was reconnaissance related to ground failures (surface rupture, landslides, other ground deformations), soil-structure interaction (e.g., retaining wall failures), and indicators of local site response effects (such as damage patterns). However, upon deployment to the field, we soon discovered that our mission should broaden to include documentation of structural performance for a variety of reasons including: (1) it supported our mission of evaluating damage patterns; (2) the structural performance data was indeed perishable, and as the first reconnaissance team in many of the visited areas, we felt a duty to document our observations. As a result, the reader can find in this report elements of traditional GEER reports combined with considerable detail on structural performance, particularly in relation to masonry building damage patterns and bridge performance.

With some humility well expressed by Italian-American Yogi Berra ("It's tough to make predictions, especially about the future"), we anticipate several features of this event will impact future research and modelling efforts:

1. Earthquake probabilities: When a large earthquake occurs, there are two schools of thought regarding its effect on the risk of subsequent large events. One is that stress release lowers earthquake rates relative to the long-term (Poisson) rate until stresses can again build-up on the fault. Another is that stress release on one portion of the fault may increase stress on adjoining portions of the same fault segment or adjacent segments. This would tend to increase earthquake rates (and hence short-term probabilities) relative to the long-term rate. This subject is of substantial practical significance for regional risk assessment. As shown in Figure 8.1, the August 2016 and October 2016 events occupy a gap along the NW striking Apennine chain between the locations of the 1997 Umbria-Marche and 2009 L'Aquila events. The occurrence of this cluster of earthquakes suggest that latter (probability increasing) mechanism may be in play here. This subject will certainly be studied and debated moving forward.

2. Faults as seismic sources: The portions of the Apennines affected by these earthquakes have numerous fault segments, many of which are well expressed at the ground surface (Chapter 2). Despite this, seismic source models used for Italian hazard studies in many cases do not take into consideration known attributes of these segments, often relying instead on seismic source zones or composite faults. We encourage the use of planar fault sources for seismic source characterization; the clear association of recent events with known faults may provide some momentum in this regard.

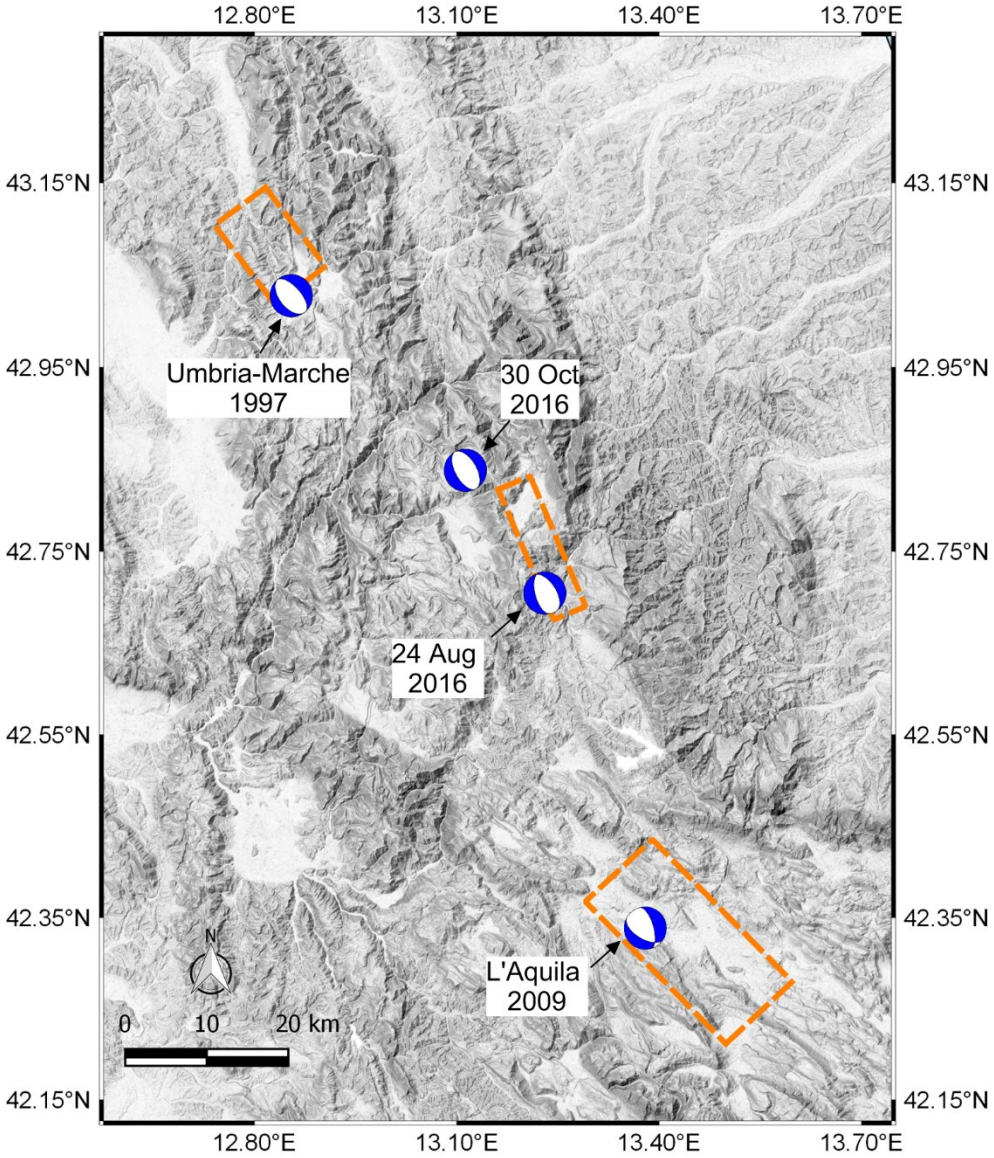

Figure 8.1. Map of central Italy showing moment tensors of major earthquakes since 1997 and the intermediate gap areas. Finite fault models from Chiaraluce et al. (2004; 1997 Umbria-Marche event), Piatanesi and Cirella (2009; 2009 L'Aquila event), and Tinti et al. (2016, 24 August mainshock). Moment tensor for 30 October 2016 earthquake is also shown.

3. Multi-segment rupture: When fault segments are considered as seismic sources, an important question is whether single earthquake events can rupture multiple segments. It appears the 24 August 2016 event ruptured both the Mt. Vettore and Laga Mountains faults, which is an important observation to inform the modeling of multi-segment ruptures in Italy.
4. Surface fault rupture: The data on surface faulting from this earthquake will be a valuable resource for statistical models of surface rupture characteristics of normal fault earthquakes.
5. Ground motions: For the most part, the ground motions arising from the August 2016 event sequence are compatible with expectation from ground motion models that are customized for known fast-attenuation features in Italy. Hence, to a large extent, the event itself and the ground shaking that it produced were not a surprise. The ground motions generated by these events will significantly extend the world-wide inventory of normal fault ground motions in tectonically active regions, as used for the example in NGA-West projects (e.g., Bozorgnia et al. 2014).
6. Masonry structure fragility: Data on structural performance during earthquake events can be used to develop empirical fragility curves, which are used for seismic vulnerability and risk assessment. Several Italy-specific models have been published including Sabetta et al. (1998) (using data for 50,000 structures examined following the 1980 Irpinia and 1984 Abruzzo earthquakes) and Rota et al. (2008) (using data for 150,000 structures from various events between 1980 and 2002). One of the principle advantages of the data collected in this event, relative to many prior events, is better constraint on ground motion characteristics due to multiple near-field sensors (Chapter 3). We anticipate that fragility models will be re-evaluated in consideration of the data from these events.
7. Retrofit effectiveness: Lack of retrofit in masonry structures, combined with strong shaking, too often led to high collapse rates. Where present and well implemented, retrofit typically saved structures (and their occupants) from collapse. While in some cases these same structures appear to have collapsed in subsequent events, the retrofitting did its job by saving the lives of building occupants. The effectiveness of various retrofit measures, or lack thereof, will likely be investigated.
8. Other findings: Landslides consisted mainly of rockfalls, which were not great in number. This performance has been documented, and can later be compared to much greater landslide occurrence from the October 2016 events. Bridges performed well for the most part, although several masonry bridges suffered significant damage. Dams performed well and some road embankments suffered settlement, apparently from seismic compression.

As noted in the introduction, this report has documented the effects of the 24 August 2016 main shock and two immediate aftershocks. For the most part, we do not discuss the late October events to the north, which will be the subject of a future report.

References

Abrahamson N. A., W.J. Silva, R. Kamai, 2014. Summary of the ASK14 ground motion relation for active crustal regions. *Earthquake Spectra*, **30**, 1025-1055.

Aki K., P.G. Richards, 2002. Quantitative Seismology. *University Science Books*, Sausalito, CA.

Akinci A., F. Galadini, D. Pantosti, M.D. Petersen, L. Malagnini, D.M. Perkins, 2009. Effect of the time-dependence on probabilistic seismic hazard maps and deaggregation for the central Apennines, Italy. *Bull. Seismol. Soc. Am.*, **99** (2A), 585-610.

Ameri G., D. Bindi, F. Pacor, F. Galadini, 2011. The 2009 April 6, Mw 6.3, L'Aquila (central Italy) earthquake: finite-fault effects on intensity data. *Geophys. J. Int.*, **186** (2), 837-851, http://doi.org/10.1111/j.1365-246X.2011.05069.x

ANIDEL, 1951. Associazione Nazionale Imprese Distributrici di Energia Elettrica, Milano. Le dighe di ritenuta degli impianti idroelettrici italiani, Vol. 5 (in Italian).

ANIDEL, 1952. Associazione Nazionale Imprese Distributrici di Energia Elettrica, Milano. Le dighe di ritenuta degli impianti idroelettrici italiani, Vol. 6 (in Italian).

Aringoli D., B. Gentili, M. Materazzi, G. Pambianchi, 2010. Mass movements in Adriatic Central Italy: activation and evolutive control factors in Landslides: Causes, types and effects. © *2010 Nova Science Publishers, Inc.* Editors: Ernest D. Werner et al., pp. 1-71. ISBN: 978-1-60741-258-8.

Ausilio E., P. Zimmaro, 2016. Landslide characterization using a multidisciplinary approach. *Measurement*, In Press. DOI: http://dx.doi.org/10.1016/j.measurement.2016.01.009

Bagnaia R., A.M. Blumetti, G. De Luca, A. Gorini, S. Marcucci, P. Marsan, G. Milana, R. Salvucci, E. Zambonelli, 1996. Morfotettonica dei rilievi a nord della conca aquilana. *Il Quaternario*, **9**, 287-292.

Baiocchi V., C. Pesaresi, 2015. GIS4RISKS: Geographic Information System for Risk Image–Safety Key. A methodological contribution to optimise the first geodynamic post-event phases and to face emergencies. *J-Reading-Journal of Research and Didactics in Geography*, **(2)**.

Baker J.W., 2007. Quantitative classification of near-fault ground motions using wavelet analysis. *Bull. Seismol. Soc. Am.*, **97** (5), 1486-1501.

Basili R., C. Bosi, P. Messina, 1999. Paleo-landsurfaces and tectonics in the upper Aterno valley (central Apennines). *Z. Geomorph. N.F.*, Suppl. Bd. **118**, 17-25.

Bindi D., F. Pacor, L. Luzi, R. Puglia, M. Massa, G. Ameri, R. Paolucci, 2011. Ground motion prediction equations derived from the Italian strong motion database. *Bull Earthq Eng*, **9**: 1899-1920.

Blumetti A.M., 1995. Neotectonic investigations and evidence of paleoseismicity in the epicentral area of the January-February 1703, Central Italy, earthquakes. In: Serva, L. & Slemmons, D. B.,

(eds.): *Perspectives in paleoseismology. Association of Engineering Geologists*, spec. publ. **6**, 83-100.

Blumetti A.M., F. Dramis, B. Gentili, G. Pambianchi, 1990. La struttura di M. Alvagnano-Castel Santa Maria nell'area nursina: aspetti geomorfologici e sismicità storica. *Rend. Soc. Geol. It.*, **13**, 71-76.

Blumetti A.M., G.P. Cavinato, M. Tallini, 1996. Evoluzione plio-quaternaria della Conca di L'Aquila - Scoppito: studio preliminare. *Il Quaternario*, **9**, 281-286.

Boccardo P., F. Chiabrando, F. Dutto, F. G. Tonolo, A. Lingua, 2015. UAV deployment exercise for mapping purposes: Evaluation of emergency response applications. *Sensors*, **15** (7), 15717-15737.

Boncio P., A. Pizzi, F. Brozzetti, G. Pomposo, G. Lavecchia, D. Di Naccio, F. Ferrarini, 2010. Coseismic ground deformation of the 6 April 2009 L'Aquila earthquake (central Italy, Mw 6.3). *Geophys. Res. Lett.* **37**.

Boncio P., G. Lavecchia, B. Pace, 2004a. Defining a model of 3D seismogenic sources for Seismic Hazard Assessment applications: the case of central Apennines (Italy). *J. Seism.*, **8**, 407–425.

Boncio P., G. Lavecchia, G. Milana, B. Rozzi, 2004b. Improving the knowledge on the seismogenesis of the Amatrice-Campotosto area (central Italy) through an integrated analysis of minor earthquake sequences and structural data. *Ann. Geophys.,* **47**, 1723–1742.

Boore D.M., J. P. Stewart, E. Seyhan, G.M. Atkinson, 2014. NGA-West 2 equations for predicting PGA, PGV, and 5%-damped PSA for shallow crustal earthquakes. *Earthquake Spectra*; **30**: 1057-85.

Bozorgnia Y., N.A. Abrahamson, L. Al Atik, T.D. Ancheta, G.M. Atkinson, J.W. Baker, et al., 2014. NGA-West2 Research Project. *Earthquake Spectra*, **30**: 973-87.

Bray J.D. and J.P. Stewart: coordinators, 2000. Chapter 8: Damage patterns and foundation performance in Adapazari. Kocaeli, Turkey Earthquake of August 17, 1999 Reconnaissance Report, T.L. Youd, J.P. Bardet, and J.D. Bray, eds., *Earthquake Spectra*, Supplement A to Vol. **16**, 163-189.

Brozzetti F., G. Lavecchia, 1994. Seismicity and related extensional stress field; the case of the Norcia seismic zone (central Italy). *Annales Tectonicae,* **8**, 36–57.

Cacciuni A., E. Centamore, R. Di Stefano, F. Dramis, 1995. Evoluzione morfotettonica della conca di Amatrice, *Studi Geol. Camerti*, vol. spec. **1995/2**, 95–100.

Calamita F., A. Pizzi, 1992. Tettonica quaternaria nella dorsale appenninica umbro-marchigiana e bacini intrappenninici associati. *Studi Geologici Camerti*, vol. spec. **1992/1**, 17-25.

Calamita F., A. Pizzi, A. Romano, M. Roscioni, V. Scisciani, G. Vecchioni, 1995. La tettonica quaternaria nella dorsale appenninica umbro-marchigiana: una deformazione progressiva non coassiale. *Studi Geol. Camerti*, vol. spec. **1995/1**, 203-223.

Calamita F., M. Coltorti, D. Piccinini, P.P. Pierantoni, A. Pizzi, M. Ripepe, V. Scisciani, E. Turco, 2000. Quaternary faults and seismicity in the Umbro-Marchean Apennines (central Italy). *Journal of Geodynamics,* **29**, 245-264.

Calamita F., M. Coltorti, G. Deiana, F. Dramis, G. Pambianchi, 1982. Neotectonic evolution and geomorphology of the Cascia and Norcia depression (Umbria-Marche Apennine). *Geografia Fisica e Dinamica Quaternaria*, **5**, 263-276.

Calamita F., M. Coltorti, P. Pieruccini, A. Pizzi, 1999. Evoluzione strutturale e morfogenesi plio-quaternaria dell'appennino umbro-marchigiano tra il preappenino umbro e la costa adriatica. *Bollettino della Società Geologica Italiana*, **118**, 125-139.

Campbell K.W., Y. Bozorgnia,2014. NGA-West2 ground motion model for the average horizontal components of PGA, PGV, and 5% damped linear acceleration response spectra. *Earthquake Spectra*, **30**, 1087-1115.

Carminati E., C. Doglioni, 2012. Alps vs. Apennines: The paradigm of a tectonically asymmetric Earth. *Earth-Science Reviews*, **112**, 67–96.

Caruana R., A. Catalano, G. Spogli, 2010. Behaviour of the dams involved in seismic sequence occurred in April 2009 in Abruzzo (Italy). *8th ICOLD European Club Symposium*, Innsbruck, Austria, 22-23 September 2010.

Castelli V., F. Galadini, P. Galli, D. Molin, M. Stucchi, 2002. Caratteristiche sismogenetiche della srogente della Laga e relazione con il terremoto del 1639. *Proc. 21st meeting of Gruppo Nazionale di Geofisica della Terra Solida*.

Catalano A., R. Caruana, F. Del Gizzi, A. De Sortis, 2013. Observed behaviour of Italian dams under historical earthquakes. *9th ICOLD European Club Symposium*, April 10-12, 2013, Venice Italy.

Cavinato G.P., P. De Celles, 1999. Extensional basins in the tectonically bimodal central Apennines fold-thrust belt, Italy: Response to corner flow above a subducting slab in retrograde motion. *Geology*, **27** (10), 955-958.

Cello G., G. Deiana, P. Mangano, S. Mazzoli, E. Tondi, L. Ferreli, L. Maschio, A.M. Michetti, L. Serva, E. Vittori, 1998. Evidence for surface faulting during the september 26, 1997, Colfiorito (Central Italy) earthquakes. *Journal of Earthquake Engineering*, **2**, 1-22.

Cello G., S. Mazzoli, E. Tondi, E. Turco, 1997. Active tectonics in the Central Apennines and possible implications for seismic hazard analysis in peninsular Italy. *Tectonophysics*, **272**, 43-68.

CERI working group: S. Martino, P. Caporossi, M. Della Seta, C. Esposito, A. Fantini, M. Fiorucci, R. Iannucci, G.M. Marmoni, P. Mazzanti, S. Moretto, S. Rivellino, R.W. Romeo, P. Sarandrea, F. Troiani, C. Varone, 2016. Sisma Amatrice Effetti- Interazione rete infrastrutturale. Available at http://www.ceri.uniroma1.it/ , last accessed October 19, 2016.

Chiarabba C., Amato A., Anselmi M., Baccheschi P., Bianchi I., Cattaneo M., Cecere G., Chiaraluce L., Ciaccio M.G., De Gori P., De Luca G., Di Bona M., Di Stefano R., Faenza L., Govoni A., Improta L., Lucente F.P., Marchetti A., Margheriti L., Mele F., Michelini A., Monachesi G., Moretti M.,

Pastori M., Piana Agostinetti N., Piccinini D., Roselli P., Seccia D., Valoroso L., 2009. The 2009 L'Aquila (central Italy) Mw 6.3 earthquake: main shock and aftershocks. Geophys. Res. Lett. 36, 1–6.

Chiarini E., E. La Posta, F. Cifelli, C. D'Ambrogi, V. Eulilli, F. Ferri, M. Marino, M. Mattei, L.M. Puzzilli, 2014. A multidisciplinary approach to the study of the Montereale Basin (Central Apennines, Italy). *Rend. Fis. Acc. Lincei*, **25** (Suppl 2), S177–S188. DOI: 10.1007/s12210-014-0311-3.

Chiou B.S.-J., R.R. Youngs,2014. Update of the Chiou and Youngs NGA model for the average horizontal component of peak ground motion and response spectra. *Earthquake Spectra*, **30**, 1117-1153.

Choi J.-K., J.-S. Won, S. Lee, S.-W. Kim, K.-D. Kim, H.-S. Jung, 2011. Integration of GIS and SAR interferometry for a coal mine subsidence hazard map in Taebaek, Korea. *Int. J. Remote Sens.*, **32** (23), 8161–8181.

Cinti F.R., D. Pantosti, P.M. De Martini, S. Pucci, R. Civico, S. Pierdominici, L. Cucci, C.A. Brunori, S. Pinzi, A. Patera, 2011. Evidence for surface faulting events along the Paganica Fault prior to the April 6 2009 L'Aquila earthquake (Central Italy). *Journal of Geophysical Research, J. Geophys. Res.*, **116** (B07), 2156-2202, DOI: 10.1029/2010JB007988.

Civico R., A.M. Blumetti, E. Chiarini, F.R. Cinti, E. La Posta, F. Papasodaro, V. Sapia, M. Baldo, G. Lollino, D. Pantosti, 2016. Traces of the active Capitignano and San Giovanni faults (Abruzzi Apennines,Italy). *Journal of Maps*, http://dx.doi.org/10.1080/17445647.2016.1239229

Coltorti M., P. Farabollini, 1995. Quaternary evolution of the Castelluccio di Norcia Basin. *Il Quaternario*, **8**, 149-166.

Cosentino D., P. Cipollari, P. Marsili, D. Scrocca, 2010. The Geology of Italy, 2010. In: Beltrando, Marco, Peccerillo, Angelo, Mattei, Massimo, Conticelli, Sandro, Doglioni, Carlo (Eds.), Electronic edition, *Journal of the Virtual Explorer1441-8142* volume **36** (paper 11).

D'Agostino N., 2014. Complete seismic release of tectonic strain and earthquake recurrence in the Apennines (Italy). *Geophys. Res. Lett.* DOI: 10.1002/(ISSN)1944-8007.

D'Agostino N., J.A. Jackson, F. Dramis, R. Funiciello, 2001. Interactions between mantle upwelling, drainage evolution and active normal faulting: an example from the central Apennines (Italy), *Geophys. J. Int.*, **147**, 475–479.

D'Agostino N., S. Mantenuto, E. D'Anastasio, R. Giuliani, M. Mattone, S. Calcaterra, P. Gambino, L. Bonci, 2011. Evidence for localized active extension in the central Apennines (Italy) from global positioning system observations. *Geology*, **39**, 291-294.

Department of Civil Protection (DPC): Website of the Italian Civil Protection Department - Presidency of the Council of Ministers.

Devoti R., A. Esposito, G. Pietrantonio, A.R. Pisani, F. Riguzzi, 2011. Evidence of large scale deformation patterns from GPS data in the Italian subduction boundary. *Earth Planet. Sci. Lett.*, **311**, 230-241. http://dx.doi.org/10.1016/j.epsl.2011.09.034 .

DISS Working Group, 2015. Database of Individual Seismogenic Sources (DISS), Version 3.2.0: A compilation of potential sources for earthquakes larger than M 5.5 in Italy and surrounding areas. http://diss.rm.ingv.it/diss/ , Istituto Nazionale di Geofisica e Vulcanologia; DOI: 10.6092/INGV.IT-DISS3.2.0.

EMERGEO Working Group, 2010. Evidence for surface rupture associated with the Mw 6.3 L'Aquila earthquake sequence of April 2009 (central Italy). *Terra Nova*, **22**, 43-51

EMERGEO Working Group, 2016. Terremoto di Amatrice del 24 agosto 2016: Effetti Cosismici. DOI: 10.5281/zenodo.61566

EMERSITO working group, 2016. Rapporto preliminare sulle attività svolte dal gruppo operativo EMERSITO a seguito del terremoto di Amatrice Mw 6.0 (24 agosto 2016, Italia centrale). DOI: 10.5281/zenodo.151655.

ESM working group, 2015. Engineering Strong-Motion database, version 1.0, DOI: 10.13127/ESM.

Falcucci E., S. Gori, E. Peronace, G. Fubelli, M. Moro, M. Saroli, B. Giaccio, P. Messina, G. Naso, G. Scardia, A. Sposato, M. Voltaggio, P. Galli, F. Galadini, 2009. The Paganica fault and surface coseismic ruptures due to the April 6, 2009 earthquake (L'Aquila, Central Italy). *Seismological Research Letters*, **80** (6), 940-950.

Falcucci E., S. Gori, F. Galadini, G. Fubelli, M. Moro, M. Saroli, 2016. Active faults in the epi-central and mesoseismal Ml 6.0 24, 2016 Amatrice earthquake region, central Italy. Methodological and seismotectonic issues. *Annals of geophysics*, **59**, Fast Track 5, 2016. DOI: 10.4401/ ag-7266.

FCEM, 1998. Servizio Nazionale Dighe. Foglio di condizioni per l'esercizio e la manutenzione, Diga di Rio Fucino in comune di Campotosto (AQ). Concessionario: ENEL S.p.A., Gestore: Divisione Produzione, Redazione: ing. Gianfranco Saraca. *Ufficio Periferico di Perugia* (in Italian).

Fielding E.J., M. Talebian, P.A. Rosen, H. Nazari, A. Jackson, M. Ghorashi, R. Walker, 2005. Surface ruptures and building damage of the 2003 Bam, Iran, earthquake mapped by satellite synthetic aperture radar interferometric correlation. *J. Geophys. Res.* **110**, B3, B03302.

Fubelli G., 2004. Evoluzione geomorfologica del versante tirrenico (Italia Centrale). *Phd thesis, University of Roma Tre*, Rome, Italy.

Fubelli G., S. Gori, E. Falcucci, F. Galadini, P. Messina, 2009. Geomorphic signatures of recent normal fault activity versus geological evidence of inactivity: Case studies from the central Apennines (Italy). *Tectonophysics*, **476**, 252-268.

Galadini F., 2006. Quaternary tectonics and large-scale gravitational deformations with evidence of rock-slide displacements in the central Apennines. *Geomorphology*, **82**, 201-228.

Galadini F., P. Galli, 1999: The Holocene paleoearthquakes on the 1915 Avezzano earthquake faults (central Italy): implications for active tectonics in Central Apennines, *Tectonophysics*, **308**, 143-170.

Galadini F., P. Galli, 2000. Active tectonics in the Central Apennines (Italy) - Input data for seismic hazard Assessment. *Natural Hazards*, **22**, 225-270.

Galadini F., P. Galli, 2003. Paleoseismology of silent faults in the Central Apennines (Italy): the Mt. Vettore and Laga Mts. Faults. *Annals of Geophysics*, **46** (5), 815-836, ISSN 2037-416X.

Galadini F., P. Galli, I. Leschiutta, G. Monachesi, M. Stucchi, 1999. Active tectonics and seismicity in the area of the 1997 earthquake sequence in central Italy: a short review. *Journal of Seismology*, **3**, 167-175.

Galadini F., P. Messina, 2001. Plio-Quaternary changes of the normal fault architecture in the central Apennines (Italy). *Geodinamica Acta*, **14**, 321-344.

Galadini F., P. Messina, B. Giaccio, A. Sposato, 2003. Early uplift history of the Abruzzi Apennines (central Italy): available geomorphological constraints, *Quat. Int.*, **101/102**, 125-135.

Galli P., B. Giaccio, P. Messina, 2010. The 2009 central Italy earthquake seen through 0.5 Myr-long tectonic history of the L'Aquila faults system. *Quaternary Science Review*, **29**, 3768-3789.

Galli P., B. Giaccio, P. Messina, E. Peronace, G.M. Zuppi, 2011. Palaeoseismology of the L'Aquila faults (central Italy, 2009, Mw 6.3 earthquake): implications for active fault linkage. *Geophys. J. Int.* **187**, 1119–1134. DOI: 10.1111/j.1365-246X.2011.05233.x

Galli P., E. Peronace, A. Tertulliani, 2016. Rapporto sugli effetti macrosismici del terremoto del 24 Agosto 2016 di Amatrice in scala MCS. Roma, *rapporto congiunto DPC, CNR-IGAG, INGV*, 15 pp. DOI: 10.5281/zenodo.161323.

Galli P., F. Galadini, D. Pantosti, 2008. Twenty years of paleoseismology in Italy. *Earth Science Reviews*, **88**, 89–117.

Galli P., F. Galadini, F. Calzoni, 2005. Surface faulting in Norcia (central Italy): a "paleoseismological perspective". *Tectonophysics*, **403**, 117-130.

Galli P., R. Camassi, R. Azzaro, F. Bernardini, S. Castenetto, D. Molin, E. Peronace, A. Rossi, M. Vecchi, A. Tertulliani, 2009. Il terremoto aquilano del 6 aprile 2009: rilievo macrosismico, effetti di superficie ed implicazioni sismotettoniche. *Il Quaternario (Italian Journal of Quaternary Sciences)*, **22** (2), 235-246.

Giuliani C.F., 1993. L'edilizia nell'antichità, *La Nuova Italia Scientifica*, Roma.

Gori S., E. Falcucci, S. Atzori, M. Chini, M. Moro, E. Serpelloni, G. Fubelli, M. Saroli, R. Devoti, S. Stramondo, F. Galadini, S. Salvi, 2012. Constraining primary surface rupture length along the Paganica fault (2009 L'Aquila earthquake) with geological and geodetic (DInSAR and GPS) data. *Italian Journal of Geosciences (Boll. Soc. Geol. It.)*, **131** (3), 359-372.

Gori S., F. Dramis, F. Galadini, P. Messina, 2007. The use of geomorphological markers in the footwall of active faults for kinematic evaluations: examples from the central Apennines. *Bollettino della Società Geologica Italiana*, **126**, 365-374.

Gregor N., W. Silva, R. Darragh, 2002. Development of attenuation relations for peak particle velocity and displacement. *A PEARL report to PG&E/CEC/Caltrans*, June 12, 2002.

Gruppo di Lavoro INGV sul terremoto di Amatrice, 2016. Secondo rapporto di sintesi sul Terremoto di Amatrice Ml 6.0 del 24 Agosto 2016 (Italia Centrale). DOI: 10.5281/zenodo.154400.

Guidoboni E., G. Ferrari, D. Mariotti, A. Comastri, G. Tarabusi, G. Valensise, 2007. CFTI4Med, Catalogue of Strong Earthquakes in Italy (461 B.C.-1997) and Mediterranean Area (760 B.C.-1500), INGV-SGA, http://storing.ingv.it/cfti4med/

INGV Working Group "GPS Geodesy (GPS data and data analysis center)", 2016. Preliminary co-seismic displacements for the August 24, 2016 ML6, Amatrice (central Italy) earthquake from the analysis of continuous GPS stations, DOI: 10.5281/zenodo.61355.

INGV Working Group, 2016. Secondo rapporto di sintesi sul terremoto di amatrice ML6.0 del 24 agosto 2016 (Italia Centrale). September 19th, 2016.

INGV, 2016. Terremoto di Amatrice. Effetti cosismici. Version of September 4th 2016.

INQUA Team, 2016. The August 24, 2016, Amatrice earthquake (Mw 6.0): field evidence of on-fault effects, PRELIMINARY REPORT http://www.isprambiente.gov.it/files/notizie-ispra/notizie-2016/sisma-italia-centrale/REPORT_Amatrice_en_2016_09_16.compressed.pdf

IREA-CNR and INGV working group, 2016. Sequenza sismica di Amatrice: aggiornamento delle analisi interferometriche satellitari e modelli di sorgente. DOI: 10.5281/zenodo.61682. *(In Italian)*

ISPRA, 2016. http://193.206.192.231/carta_geologica_italia/tavoletta.php?foglio=139/132

ISPRA, 2016. Report attività svolta da ISPRA in data 25-26/08/2016, A (in Italian). Available at http://www.isprambiente.gov.it/files/notizie-ispra/notizie-2016/sisma-italia-centrale/ReportattivitsvoltadaISPRAindata26.pdf. , last accessed October 19, 2016).

Jappelli R., T. Silvestri, 2006. Rassegna dei materiali sciolti adoperati nelle dighe costruite in Italia nel periodo 1950-1975. *Questioni di Ingegneria Geotecnica - Scritti in onore di Arturo Pellegrino, Vol. II*, pp. 429-524. Hevelius, Benevento (in Italian).

Jo M.-J., J.-S. Won, S.-W. Kim, H.-S. Jung, 2010. A time-series SAR observation of surface deformation at the southern end of the San Andreas fault zone. *Geosci. J.*, **14** (3), 277-287.

Jung H.-S., Z. Lu, J. S. Won, M.P. Poland, A. Miklius, 2011. Mapping three-dimensional surface deformation by combining multiple-aperture interferometry and conventional interferometry: Application to the June 2007 eruption of Kilauea volcano, Hawaii. *IEEE Geosci. Remote Sens. Lett.*, **8** (1), 34-38.

Kaklamanos J., L.G. Baise, D.M. Boore, 2011. Estimating unknown input parameters when implementing the NGA ground-motion prediction equations in engineering practice. *Earthq. Spectra*, **27**: 1219-1235.

Keefer D.K., R.C. Wilson, 1989. Predicting earthquake-induced landslides with emphasis on arid and semi-arid environments. *Publication of the Inland Geological Society*, **2**, 118-149.

Lai C.G., M. Corigliano, M. Agosti, 2009. Dams and Earthquakes: the Case of L'Aquila Seism. *Progettazione Sismica*. Vol. **1**, No. 3, September-December 2009. pp. 179-201.

Lavecchia G., F. Ferrarini, F. Brozzetti, R. de Nardis, P. Boncio, L. Chiaraluce, 2012. From surface geology to aftershock analysis: constraints on the geometry of the L'Aquila 2009 seismogenic fault system. *Ital. J. Geosci. (Boll. Soc. Geol. It.)*, **131** (3), 330-347. DOI: 10.3301/IJG.2012.24.

Lavecchia G., P. Boncio, F. Brozzetti, F. De Nardis, D. Di Naccio, F. Ferrarini, A. Pizzi, G. Pomposo, 2010. The April 2009 Aquila (central Italy) seismic sequence (Mw 6.3): a preliminary seismotectonic picture. In: Guarnieri, P. (Ed.), *Recent Progress on Earthquake Geology*, Nova Publisher, 1-18.

Lee W., Z. Lu, J.-S. Won, H.-S. Jung, D. Dzurisin, 2013. Dynamic deformation of Seguam Island, Alaska, 1992–2008, from multi-interferogram InSAR processing. *J. Volcanol. Geotherm. Res.*, **260**, 43-51.

Martino S., A. Prestininzi, R.W. Romeo, 2014. Earthquake-induced ground failures in Italy from a reviewed database. *Natural Hazards and Earth System Sciences*, **14**, 799-814.

Messina P., C. Bosi, M. Moro, 2003. Sedimenti e forme quaternari nell'alta valle dell'Aterno (L'Aquila). *Il Quaternario*, **16**, 231-239.

Messina P., P. Galli, E. Falcucci, F. Galadini, B. Giaccio, S. Gori, E. Peronace, A. Sposato, 2009. Evoluzione geologica e tettonica quaternaria dell'area interessata dal terremoto aquilano del 2009. *Geoitalia*, **28**, 24-29.

Michetti A.M., L. Serva, 1990. New data on the seismotectonic potential of the Leonessa fault area (Rieti, central Italy). *Rend. Soc. Geol. It.*, **13**, 37-46.

Ministero delle Infrastrutture e dei Trasporti, 2009. Eventi sismici aprile 2009 nella zona dell'aquilano. Controllo della sicurezza delle grandi dighe. *Direzione generale per le dighe e le infrastrutture idriche ed elettriche*. Maggio 2009 (in Italian).

Ministry of the Infrastructures, 2018. Norme 867 Tecniche per le Costruzioni. Decreto Ministeriale 868 D.M. 14 gennaio 2008. *Gazzetta Ufficiale della Repubblica Italiana*, **29**. *(In Italian)*

Montone P., M.T. Mariucci, 2016. The new release of the Italian contemporary stress map. *Geophysical Journal International*, **205**, 1525-1531.

Moretti M., L. Margheriti, A. Govoni, 2016. Rapid response to earthquake emergencies in Italy: temporary seismic network coordinated deployments in the last five years. in: *D'Amico S. (Ed): Earthquakes and their impacts on Society*, Springer.

Moro M., E. Falcucci, S. Gori, M. Saroli, F. Galadini, submitted. New paleoseismologic data in the sector between the 2016 Amatrice and 2009 L'Aquila seismic sequences (central Apennines): the Mt. Marine Fault. *Ann. Geophys*.

Moro M., S. Gori, E. Falcucci, M. Saroli, F. Galadini, S. Salvi, 2013. Historical earthquakes and variable kinematic behaviour of the 2009 L'Aquila seismic event (central Italy) causative fault, revealed by paleoseismological investigations. *Tectonophysics*, **583**, 131-144.

Moro M., V. Bosi, F. Galadini, P. Galli, B. Giaccio, P. Messina, A. Sposato, 2002. Analisi paleosismologiche lungo la faglia del M. Marine (alta valle dell'Aterno): risultati preliminari. *Il Quaternario*, **15**, 267-278.

Pagliaroli A., A. Avalle, E. Falcucci, S. Gori, F. Galadini, 2015. Numerical and experimental evaluation of site effects at ridges characterized by complex geological setting. *Bulletin of Earthquake Engineering*, **13**: 2841-2865.

Patacca E., P. Scandone, E. Di Luzio, G.P. Cavinato, M. Parotto, 2008. Structural architecture of the central Apennines: interpretation of the CROP 11 seismic profile from the Adriatic coast to the orographic divide. *Tectonics*, **27**, TC3006, 36 pp.

Piatanesi A., A. Cirella, 2009. Rupture Process of the 2009 Mw6.3 L'Aquila (Central Italy) Earthquake from Nonlinear Inversion of Strong Motion and GPS Data. *Istituto Nazionale di Geofisica e Vulcanologia (INGV)*, Rome, Italy.

Pierantoni P., G. Deiana, S. Galdenzi, 2013. Stratigraphic and structural features of the Sibillini Mountains (Umbria-Marche Apennines, Italy). *Italian Journal of Geosciences*, **132**(3), 497-520.

Pizzi A., F. Calamita, M. Coltorti, P. Pieruccini, 2002. Quaternary normal faults, intramontane basins and seismicity in the Umbria-Marche- Abruzzi Apennine ridge (Italy): contribution of neotectonic analysis to seismic hazard assessment. *Boll. Soc. Geol. It., Spec. Publ.*, **1**, 923-929.

Pizzi A., F. Galadini, 2009. Pre-existing cross-structures and active fault segmentation in the northern-central Apennines (Italy). *Tectonophysics*, **476**, 304-319.

Pizzi A., V. Scisciani, 2000. Methods for determining the Pleistocene–Holocene component of displacement on active faults reactivating pre-Quaternary structures: examples from the central Apennines (Italy). *Journal of Geodynamics,* **29**, 445-457.

Regione Lazio, 2013. Microzonazione sismica del Comune di Accumoli. Attuazione art. 11 legge n.77/2009. Approvato dalla Regione Lazio ai sensi della DGR 545/2010. Available at: http://www.regione.lazio.it/prl_ambiente/?vw=uas

Regione Lazio, 2016. Microzonazione sismica del Comune di Amatrice. Attuazione art. 11 legge n.77/2009. In corso di approvazione da parte del DPC ai sensi OPCM 4007/2012.

Regione Marche, 2014. Microzonazione sismica del Comune di Arquata del Tronto. Attuazione art. 11 legge n.77/2009. OCDPC n. 52/2013. Approvato dalla Regione Marche.

Regione Marche, 2015. Microzonazione sismica del Comune di Montegallo. Attuazione art. 11 legge n.77/2009. OCDPC n. 171/2014. Approvato dalla Regione Marche.

Roberts G.P., A.M. Michetti, 2004. Spatial and temporal variations in growth rates along active normal fault systems: an example from the Lazio-Abruzzo Apennines, central Italy. *J. Struct. Geol.*, **26**, 339-376.

Rota M., A. Penna, C.L. Strobbia, 2008. Processing Italian damage data to derive typological fragility curves. *Soil Dynamics and Earthquake Engineering*, **28**, 933-947.

Rovida A., M. Locati, R. Camassi, B. Lolli, P. Gasperini (eds.), 2016. CPTI15, Catalogo parametrico dei terremoti italiani, http://emidius.mi.ingv.it/CPTI15-DBMI15/. DOI: http://doi.org/10.6092/INGV.IT-CPTI15

Sabetta F., A. Goretti, A. Lucantoni, 1998. Empirical fragility curves from damage surveys and estimated strong ground motion. *Proceedings: Eleventh European Conference on Earthquake Engineering*, Paris, France.

Scasserra G., J.P. Stewart, R.E. Kayen, G. Lanzo, 2009. Database for earthquake strong motion studies in Italy. *Journal of Earthquake Engineering*, **13** (6), 852-881.

Scisciani V., E. Tavarnelli, F. Calamita, 2002. The interaction of extensional and contractional deformations in the outer zones of the central Apennines, Italy. *Journal of Structural Geology*, **24**, 1647-1658.

Shahi S.K., J.W. Baker, 2014. An efficient algorithm to identify strong velocity pulses in multi-component ground-motions. *Bull. Seismol. Soc. Am.*, **104** (5), 2456-2466.

Silvestri F., G. Forte, M. Calvello, 2016. Multi-level approach for zonation of seismic slope stability: Experiences and perspectives in Italy. *Panel report. 12th International Symposium on Landslides, Napoli (Italy), 12-19 June 2016 'Landslides and Engineered Slopes. Experience, Theory and Practice'* (Eds: Picarelli L., Scavia C., Aversa S., Cascini L.), 1:101-118. London: Taylor and Francis Inc., ISBN: 978-113802988-0.

Silvestri F., V. Aiello, A. Barile, A. Costanzo, R. Puglia, T.S. Pescatore, E. Lo Russo, F. Pinto, D. Tornesello, 2006. Analisi e zonazione della stabilità dei pendii in condizioni sismiche: applicazioni di metodi tradizionali ed avanzati ad un'area di studio. *Questioni di Ingegneria Geotecnica – Scritti in onore di Arturo Pellegrino* **2**, 617-660. Benevento: Hevelius (in Italian).

SISMIKO working group, 2016. Rapporto preliminare sulle attività svolte dal gruppo operativo SISMIKO a seguito del terremoto di Amatrice Mw 6.0 (24 agosto 2016, Italia centrale). DOI: 10.5281/zenodo.157546.

Stewart J.P., G. Lanzo, A. Pagliaroli, G. Scasserra, G. Di Capua, S. Peppoloni, R. Darragh, N. Gregor, 2012. Ground Motion Recordings from the Mw 6.3 2009 L'Aquila Earthquake in Italy and their Engineering Implications. *Earthquake Spectra*, **28**, 317-345.

Storti F., F. Balsamo, A. Koopman, M. Mozafari, J. Solum, R. Swennen, C. Taberne, 2016. Superimposed positive and negative inversion of the syn-rift fault networkpreserved in the Montagna dei Fiori Anticline, Central Apennines, Italy. *EGU General Assembly 2016*, 17-22 April, 2016 in Vienna, Austria, p.3057Vienna, Volume: EGU2016-3057

Suziedelyte Visockiene J., R. Puziene, A. Stanionis, E. Tumeliene, 2016. Unmanned Aerial Vehicles for Photogrammetry: Analysis of Orthophoto Images over the Territory of Lithuania. *International Journal of Aerospace Engineering*, **2016**, Article ID 4141037, 9 pages. doi:10.1155/2016/4141037.

Tertulliani A., A. Rossi, L. Cucci, M. Vecchi, 2009. L'Aquila (Central Italy) earthquakes: the predecessors of the April 6, 2009 event. *Seismological Research Letters*, **80** (6), 1008-1013.

Tertulliani A., F. Galadini, F. Mastino, A. Rossi, M. Vecchi, 2006. Studio macrosismico del terremoto del Gran Sasso del 5 settembre 1950: implicazioni sismotettoniche. *Il Quaternario*, **19**, 195-214.

Tinti E., L. Scognamiglio, A. Michelini, M. Cocco, 2016. Slip heterogeneity and directivity of the ML 6.0, 2016, Amatrice earthquake estimated with rapid finite-fault inversion, *Geophysical Research Letters*, accepted for publication. DOI: 10.1002/2016GL071263.

Tinti, E., L. Scognamiglio, A. Michelini, M. Cocco, 2016. Slip heterogeneity and directivity of the ML 6.0, 2016, Amatrice earthquake estimated with rapid finite-fault inversion, *Geophysical Research Letters*, accepted.

Vallet J., F. Panissod, C. Strecha, M. Tracol, 2011. Photogrammetric performance of an ultra light weight swinglet UAV. In *UAV-g* (No. EPFL-CONF-169252).

Vittori E., P. Di Manna, A.M. Blumetti, V. Comerci, L. Guerrieri, E. Esposito, A.M. Michetti, S. Porfido, L. Piccardi, G.P. Roberts, A. Berlusconi, F. Livio, G. Sileo, M. Wilkinson, K.J.W. McCaffrey, R.J. Phillips, P.A. Cowie, 2011. Surface faulting of the 6 april 2009 Mw 6.3 L'Aquila earthquake in central Italy. *Bulletin of the Seismological Society of America*, **101** (4), 1507-1530.

Walker J.P., G.P. Roberts, P.R. Sammonds, P. Cowie, 2010. Comparison of earthquake strains over 102 and 104 year timescales: insights into variability in the seismic cycle in the central Apennines, Italy. *Journ. Geophys. Res.*, **115**, B10418, DOI: 10.1029/2009JB006462.

Wills C. J., K.B. Clahan, 2006. Developing a map of geologically defined site-condition categories for California. *Bulletin of the Seismological Society of America*, **96**(4a), 1483-1501.

Yun S., E.J. Fielding, M. Simons, P. Rosen, S. Owen, F. Webb, 2011. Damage proxy map of M 6.3 Christchurch earthquake using InSAR coherence. *Fringe Workshop, Advances in the science and applications of SAR interferometry from ESA and 3rd party missions*. Frascati, Italy, https://earth.esa.int/documents/10174/1567329/Yun_FRINGE2011.pdf.

Yun S., K. Hudnut, S. Owen, F. Webb, M. Simons, P. Sacco, E. Gurrola, G. Manipon, C. Liang, E.J. Fielding, P. Milillo, H. Hua, A. Coletta, 2015. Rapid Damage Mapping for the 2015 Mw 7.8 Gorkha Earthquake Using Synthetic Aperture Radar Data from COSMO–SkyMed and ALOS-2 Satellites. *Seismological Research Letters*, **86** (6), 1549-1556

Zhang L., Z. Lu, X. Ding, H.-S. Jung, G. Feng, C.-W. Lee, 2012. Mapping ground surface deformation using temporarily coherent point SAR interferometry: Application to Los Angeles Basin. *Remote Sens. Environ.,* **117**, 429-439.

Zimmaro P., J.P. Stewart, 2015. Probabilistic seismic hazard analysis for a dam site in Calabria (southern Italy). UCLA SGEL Report No.: **2015/02**, *University of California, Los Angeles, Structural and Geotechnical Engineering Laboratory*. Available at www.escholarship.org/uc/item/8fm3h6rj.